

AFRL-IF-RS-TR-2002-270
Final Technical Report
October 2002



**MIXED-DIMENSIONALITY VLSI-TYPE
CONFIGURABLE TOOLS FOR VIRTUAL
PROTOTYPING OF BIOMICROFLUIDIC DEVICES
AND INTEGRATED SYSTEMS**

CFD Research Corporation

Sponsored by
Defense Advanced Research Projects Agency
DARPA Order No. G220 & J406

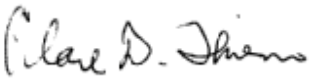
APPROVED FOR PUBLIC RELEASE; DISTRIBUTION UNLIMITED.

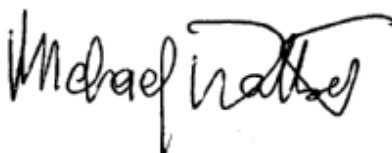
The views and conclusions contained in this document are those of the authors and should not be interpreted as necessarily representing the official policies, either expressed or implied, of the Defense Advanced Research Projects Agency or the U.S. Government.

**AIR FORCE RESEARCH LABORATORY
INFORMATION DIRECTORATE
ROME RESEARCH SITE
ROME, NEW YORK**

This report has been reviewed by the Air Force Research Laboratory, Information Directorate, Public Affairs Office (IFOIPA) and is releasable to the National Technical Information Service (NTIS). At NTIS it will be releasable to the general public, including foreign nations.

AFRL-IF-RS-TR-2002-270 has been reviewed and is approved for publication

APPROVED: 
CLARE D. THIEM
Project Engineer

FOR THE DIRECTOR: 
MICHAEL L. TALBERT, Maj., USAF
Technical Advisor, Information Technology Division
Information Directorate

REPORT DOCUMENTATION PAGE

Form Approved
OMB No. 074-0188

Public reporting burden for this collection of information is estimated to average 1 hour per response, including the time for reviewing instructions, searching existing data sources, gathering and maintaining the data needed, and completing and reviewing this collection of information. Send comments regarding this burden estimate or any other aspect of this collection of information, including suggestions for reducing this burden to Washington Headquarters Services, Directorate for Information Operations and Reports, 1215 Jefferson Davis Highway, Suite 1204, Arlington, VA 22202-4302, and to the Office of Management and Budget, Paperwork Reduction Project (0704-0188), Washington, DC 20503

1. AGENCY USE ONLY (Leave blank) **2. REPORT DATE**
October 2002 **3. REPORT TYPE AND DATES COVERED**
Final Jun 98 – Aug 01

4. TITLE AND SUBTITLE
MIXED-DIMENSIONALITY VLSI-TYPE CONFIGURABLE TOOLS FOR VIRTUAL PROTOTYPING OF BIOMICROFLUIDIC DEVICES AND INTEGRATED SYSTEMS

5. FUNDING NUMBERS
C - F30602-98-2-0152
PE - 63739E
PR - E117
TA - 00
WU - 36

6. AUTHOR(S)
Vinod B. Makhijani and Andrzej J. Przekwas

7. PERFORMING ORGANIZATION NAME(S) AND ADDRESS(ES)
CFD Research Corporation
215 Wynn Drive, 5th Floor
Huntsville Alabama 35805

8. PERFORMING ORGANIZATION REPORT NUMBER

9. SPONSORING / MONITORING AGENCY NAME(S) AND ADDRESS(ES)
Defense Advanced Research Projects Agency AFRL/IFTC
3701 North Fairfax Drive 26 Electronic Parkway
Arlington Virginia 22203-1714 Rome New York 13441-4514

10. SPONSORING / MONITORING AGENCY REPORT NUMBER
AFRL-IF-RS-TR-2002-270

11. SUPPLEMENTARY NOTES
AFRL Project Engineer: Clare D. Thiem/IFTC/(315) 330-4893/ Clare.Thiem@rl.af.mil

12a. DISTRIBUTION / AVAILABILITY STATEMENT
APPROVED FOR PUBLIC RELEASE; DISTRIBUTION UNLIMITED.

12b. DISTRIBUTION CODE

13. ABSTRACT (Maximum 200 Words)
Computer-aided design of microfluidic systems often necessitates the use of multi-physics simulation tools with the flexibility to develop models at various resolution levels. High-fidelity models (2D, 3D) are needed for the design and optimization of particular components and devices, where as system-level models allow for VLSI-scale simulation of integrated systems. Mixed-dimensionality software capabilities were developed, validated and demonstrated for virtual prototyping and design of biomicrofluidic devices and integrated systems during the course of this project. The effort included development of multiphysics high-fidelity and reduced-order models for microfluidic flows, electrochemistry, free-surface flows and biochemistry, along with mixed-dimensionality (3D-ID-OD) and multiscale analyses capabilities. A methodology for automated generation of models (solids, meshes, boundary conditions, etc.) from layouts and process was also developed. The system-level mixed-dimensionality software was linked with a both a layout-solids-fabrication optimization tool as well as with a network simulator, SPICE. Parametric microfluidic device model libraries using PYTHON-based scripting, and a simulation manager for automated numerical design analysis and optimization were also developed. The simulation capabilities were incorporated into CFD Research Corporation's commercial software suite, CFD-ACE+, and were applied for device-level and system-level analysis of various biomicrofluidic problems of interest to both the defense industry and commercial market.

14. SUBJECT TERMS
Computer-Aide Design (CAD), Multiscale, Multiphysics, System-Level Analysis, Biomolecular Reactions, Electrochemistry, Microfluidics, Liquid Filling, Layout to Solids to Mesh, Microsystem Fabrication Simulation, Reduced-order Models, Optimization

15. NUMBER OF PAGES
186

16. PRICE CODE

17. SECURITY CLASSIFICATION OF REPORT
UNCLASSIFIED

18. SECURITY CLASSIFICATION OF THIS PAGE
UNCLASSIFIED

19. SECURITY CLASSIFICATION OF ABSTRACT
UNCLASSIFIED

20. LIMITATION OF ABSTRACT
UL

TABLE OF CONTENTS

	<u>Page</u>
1. INTRODUCTION	1
1.1 Background.....	1
1.2 Project Motivation	2
1.3 Project Objectives	3
1.4 Summary of Accomplishments.....	3
1.4.1 Building the Model - From Layouts to Models	3
1.4.2 Hierarchy of Simulation Models.....	4
1.4.3 Multiphysics Models in CFD-ACE+	5
1.4.4 Applications for Biomicrofluidics Devices and Integrated Systems	6
2. CFD-MICROMESH	7
2.1 Basic Approach for Geometric Modeling.....	7
2.2 Software Features.....	7
2.3 Demonstration Case using Voxel-Based Approach.....	8
2.4 Geometric Modeling and Structured Grid Generation in Micro-Mesh	9
2.5 CFD-Micromesh-Tet.....	13
3. MICROSYSTEM FABRICATION PROCESS SIMULATIONS	14
3.1 Solids-Layout Geometry and Mesh Development.....	14
3.2 Development of Layout to Simulation and Reverse Interfaces	16
4. BIOMOLECULAR REACTIONS SIMULATION MODULE	21
4.1 Software Overview	21
4.2 Surface-Immobilized Enzyme Kinetics	21
4.2.1 Theory	21
4.2.2 Model Validation and Parametric Study.....	23
4.3 Volumetric Protein-Ligand Cooperative Binding.....	24
4.3.1 Theory	24
4.3.2 Model Validation and Parametric Study.....	26
4.4 Biomolecular Surface Adsorption.....	28
4.4.1 Theory	29
4.4.2 DNA Filtration Application	30
4.4.3 Competitive Multi-Protein Adsorption.....	32
4.4.4 Receptor Immobilization in Microfluidic SPR Biosensor	37
4.5 Biomolecular Receptor-Ligand Surface Binding.....	41
4.5.1 Theory	41
4.5.2 Receptor-Ligand Binding in a Microfluidic Biosensor	41
4.5.3 Simulation of Displacement Assays	44
4.6 Virtual Sequences Programming Capability.....	46
4.6.1 Software Options	46
4.6.2 Demonstration of Capability.....	47
5. ELECTROCHEMISTRY SIMULATION MODULE	49
5.1 Modified Treatment of Zeta Potential at the Wall	49
5.1.1 Mathematical Formulation.....	49
5.1.2 Validation Test Case	50
5.2 Ionization Model.....	51

5.2.1	Theory	52
5.2.2	Model Validation and Demonstration	52
5.3	ECHEM Graphical-User Interface	54
5.4	Further Validation Cases	55
5.4.1	Electroosmotic Capillary Flow with Non-Uniform Zeta Potential	55
5.4.2	Electrochemical Transport Model Validation	57
6.	FABRICATION AND CHARACTERIZATION OF MICROFLUIDIC TEST STRUCTURES	60
6.1	Flow Apparatus for Microfluidic Measurements	60
6.1.1	Typical Problems with Syringe Pumps	60
6.1.2	Development of an Improved Fluid Delivery System	60
6.2	Microchannel Test Structures	62
6.2.1	Microchannel Blood Flow Experiments	62
6.2.2	Model Validation for Dilute Blood Flow in Straight Microchannels	63
6.2.3	Model Validation for Whole Blood Flow in Various Microchannels	65
6.3	Microneedle Structures	67
6.3.1	Experimental Blood Flow Measurements	67
6.3.2	Microneedle Pressure-Flow Characteristics and Apparent Viscosity	67
6.3.3	Clogging Phenomenon in Microfilter Needles	69
6.4	Micromixer System and Component Microvalves	69
6.4.1	Micromixer System Performance	69
6.4.2	Microvalve Characterization	71
7.	REDUCED-ORDER MODELS AND MIXED DIMENSIONALITY	73
7.1	One-Cell Model for Incompressible Pressure-Driven Microfluidic Flows	73
7.1.1	Theory	73
7.1.2	Model Application for Straight Channel Flow	74
7.1.3	Model Application for Flow in a Spiral Microchannel	77
7.1.4	Model Application for Flow Through a 90 Degree Bend	78
7.1.5	Reduced-Order Model Library for Flows in Bends	80
7.1.6	Model Applications for Flow Through Microfluidic Valves	82
7.2	One-Cell Model for Electrokinetic Flows	84
7.2.1	Model Application for Straight Channels	84
7.2.2	Model Application for Double S-Shaped Channels	84
7.2.3	Model Applications for a Bent Square Pipe	86
7.3	One-Cell Model for Free Surface Flows	87
7.3.1	Model Description	87
7.3.2	Validation Test Case	87
7.3.3	Comparison Between 1-D and High-Fidelity Simulations	88
7.3.4	Hybrid One-Cell and Multi-Cell Model Capability	89
7.4	Filament Model	90
7.4.1	Theory	90
7.4.2	Filament Application for Fluid Heating in Microreactor	91
7.4.3	Model Application for a Continuous-Flow PCR System	91
7.4.4	Filament Application for Branching Microfluidic Channels	92
7.5	Serial Coupling Between Multi-Cell and Single-Cell Domains	94
7.5.1	Model Application for Pressure-Driven Microfluidic Flows	94

7.5.2	Model Application for Liquid Filling Problem.....	95
7.6	Mixed-Dimensionality Coupled Multi-Cell and 0-D Point Model Simulations.....	96
7.6.1	Coupling between CFD-ACE+ and Analogy SABER	97
7.6.2	Coupling Between CFD-ACE+ and SPICE.....	98
8.	PARAMETRIC MODELS, SCRIPTING AND OPTIMIZATION	102
8.1	Parametric Microfluidic Device Models Using Python Scripting.....	102
8.1.1	Python Scripting.....	102
8.1.2	Parametric Model of Tesla Valve Geometry	102
8.1.3	Parametric Model of Helical Microfluidic Mixing Chamber	103
8.1.4	Python Scripting in CFD-Micromesh	104
8.2	Simulation Manager for Automated Numerical Design Analysis	105
8.2.1	Manual Design Analysis Procedures	105
8.2.2	Automated Script-Driven Simulation Methodologies	105
8.2.3	Simulation Templates	106
8.2.4	Application of Simulation Manager for Parametric Simulations	107
8.3	Numerical Optimization of Tesla Valve.....	108
8.4	Numerical Optimization of the DNA Biochip Device.....	110
8.4.1	Problem Description	110
8.4.2	Customized GUI for DNA Chip Optimization Problem.....	110
8.4.3	Model Setup.....	110
8.4.4	Solution Procedure.....	113
8.4.5	Optimization Results.....	114
9.	DEMONSTRATION AND APPLICATION FOR BIOMICROFLUIDIC DEVICES AND INTEGRATED SYSTEMS	115
9.1	CANARY B-Cell Biosensor	115
9.1.1	Problem Description	115
9.1.2	Stage I Studies.....	116
9.1.3	Stage II Studies	117
9.1.4	Conclusions.....	119
9.2	Electrokinetic Sample Injection and Pinching in a Cross-Channel	119
9.2.1	Problem Description	119
9.2.2	Method of Approach.....	120
9.2.3	Results and Discussions.....	122
9.2.4	Summary of Results.....	124
9.3	Electrokinetic DNA Chip.....	124
9.3.1	Problem Description	124
9.3.2	Method of Approach.....	125
9.3.3	Sample Results and Discussion	125
9.3.4	Summary and Conclusions	127
9.4	Stacking of Species in a Glass Microchannel.....	127
9.4.1	Problem Description	127
9.4.2	Method of Approach.....	128
9.4.3	Sample Results and Discussion	128
9.4.4	Summary of Results.....	131
9.5	Impact of Sheath Flow on Electrokinetic Sample Transport.....	131
9.5.1	Problem Description	131

9.5.2	Method of Approach	131
9.5.3	Results and Discussion	132
9.6	Continuous Micromixer System Analysis	134
9.6.1	Coupled 3-D/1-D/0-D Simulation using ACE+ and SABER	134
9.6.2	System-Level Simulation using ACE+ and SPICE	136
9.7	Capillary Array Electrophoresis Chip	137
9.7.1	Problem Description	137
9.7.2	Method of Approach	138
9.7.3	Sample Results	138
9.8	Protein Labchip System	138
9.8.1	Problem Description	138
9.8.2	Method of Approach	139
9.8.3	Sample Results	140
9.9	Microfluidic Biodiagnostic System	140
9.9.1	Study Objective	140
9.9.2	Background	142
9.9.3	Geometric Modeling and Mesh Generation	143
9.9.4	Model Parameters	144
9.9.5	Model Assumptions	145
9.9.6	Solution Procedure	146
9.9.7	Results and Discussion	147
9.9.8	Conclusions and Recommendations	152
10.	PROJECT SUMMARY	154
10.1	Software Capabilities Developed	154
10.2	Commercialization and Technology Transfer	155
10.2.1	Software Commercialization Efforts	155
10.2.2	Software Commercialization Success	157
10.2.3	Software-Based Commercial Services	158
10.2.4	Projects and Success Stories Resulting from Consulting Services	160
10.2.5	In-House Applications	162
10.3	Plans for Further Research, Development and Improvement	163
	REFERENCES	164

LIST OF FIGURES

Fig. 1.1 CFD-ACE+ Multiphysics Simulation Environment for Bio Microfluidic Devices and Integrated Systems	2
Figure 1.2: Automated geometry, mesh, and model generation in CFD-Micromesh for multiphysics simulations of biofluidic microsystems. Example design path is shown for a two fluid static micromixer	4
Figure 1.3. ACE+ filament capability for modeling heat transfer in a biochip device	5
Figure 1.4: Agilent’s DNA LabChip System that was analyzed using CFD-ACE+	6
Figure 2.1: Graphical-User Interface for CFD-Micromesh	9
Figure 2.2: Application of CFD-Micromesh for a static microfluidic mixer	9
Figure 2.3: Layout of a microfluidic device	10
Figure 2.4: Automatic generation of 3-D model of the device	11
Figure 2.5: Coarse structural mesh for microfluidic device	12
Figure 2.6: Finer structural mesh, with 1-D mesh inside channels	12
Figure 2.7: Fine structural mesh for the microfluidic device	12
Figure 2.8: Solid model and corresponding surface mesh for microbead array	13
Figure 3.1: Standard etch operation in CFD-Micromesh Program	15
Figure 3.2: Physical etch simulation data imported into CFD-Micromesh Program	16
Figure 3.3: Algorithm for synthesis of mask-layouts to create desired shapes	17
Figure 3.4: Example of mask-layout and fabrication process synthesis	18
Figure 3.5: Evolution Convergence Profile	18
Figure 3.6: Tesla valve (Isotropic Etch)	18
Figure 3.7: Robust mask-layout synthesis	19
Figure 3.8: Robust mask-layout synthesis verification	19
Figure 4.1. Schematic of flow domain for enzyme-catalyzed reaction problem	22
Figure 4.2: Velocity vectors in the flow domain	23
Figure 4.3: Mass fraction contours of FXa in the flow domain (figure scale = 150y)	23
Figure 4.4: Normalized FX concentration versus channel height	24
Figure 4.5: Schematic of the T-channel flow domain	25
Figure 4.6: Transient variation in O ₂ saturation at fixed location in common branch	27
Figure 4.7: Non-dimensionalized concentration contours of unbound oxygen	27
Figure 4.8: Non-dimensionalized concentration contours of unbound oxygen	28
Figure 4.9: Spatial variation in HbO ₂ concentration along channel width at the exit	28
Figure 4.10: Geometric model of DNA extraction chip with unstructured surface mesh	31
Figure 4.11: Flow patterns along the central plane in the DNA extraction chip	31
Figure 4.12: Normalized solution DNA concentration contours through the chip	32
Figure 4.13: Schematic of processes occurring during protein adsorption	34
Figure 4.14: Comparison of ACE+ (solid lines) and published (symbols) theoretical results on competitive multi-protein adsorption	34
Figure 4.15: Effect of flow on multiprotein adsorption in a 2-D flow channel	35
Figure 4.16 Schematic of flow over a microbead assay (dimensions in microns)	36
Figure 4.17: Site-specific protein binding on a microbead array in the presence of flow	36
Figure 4.18: Competitive multi-protein binding on a microfluidic bead array	37

Figure 4.19: The TI-SPREETA Biosensor System.....	38
Figure 4.20. Biosensor calibration data	39
Figure 4.21: Flow velocity vectors in the SPREETA flow cell.....	40
Figure 4.22. Computational grid, flow field and binding site location in SPREETA	40
Figure 4.23: Neutravidin-Gold surface binding in SPREETA Biosensor Flow Cell	41
Figure 4.24: Effect of flow rate on surface binding in the SPREETA System.....	43
Figure 4.25: Effect of receptor surface density on surface binding in the SPREETA.....	43
Figure 4.26: Effect of adsorption rate constant on surface binding in the SPREETA.....	44
Figure 4.27: Different stages of the displacement assay.....	45
Figure 4.28: Transient variation in (a) antigen surface concentration and (b) labeled antigen flux	46
Figure 4.29: Transient processes and steps in a binding assay	47
Figure 4.30: Surface concentration profile of bound analyte during the entire assay	48
Figure 5.1: Computational domain geometry and grid for electrokinetic test case	50
Figure 5.2: Electroosmotic velocity vectors in flow domain.....	51
Figure 5.3: Electroosmotic velocity distribution normal to the wall	51
Figure 5.4: Contour levels of sample (Picric Acid) concentration is shown at 1 and 6 minutes into the simulation for initial concentrations of 0.02, 1.0 and 10 mM.	53
Figure 5.5: Comparison of experimental (Ermakov and Righetti, 1994) and simulated (present study and Ermakov and Righetti, 1994) Electropherogram for Picric Acid (Initial Conc. = 0.02 mM).....	54
Figure 5.6: Sample GUI windows from the ECHEM Module	54
Figure 5.7: Schematic of capillary with varying surface potential along the axis. The anticipated velocity profiles away from the junction of two regions are shown.....	55
Figure 5.8: (a) Pressure distribution along the capillary, and (b) Comparison of velocity profiles in region 2 (Solid Lines: CFD-ACE+, Symbols: Experimental Data).....	56
Figure 5.9: Comparison of numerical (left) and experimental (right) results on normalized dye concentration for 10% EOF suppression.	57
Figure 5.10: Computational domain geometry used in 1-D open-tube plug flow. The dye concentration was monitored at locations 1, 2, 3, and 4, which were 0.75, 1.75, 9.75 and 19.75mm, respectively, from concentration interface at time $t = 0$	58
Figure 5.11. Temporal variations in ion concentration at various downstream locations based on CFD-ACE+ and analytical predictions (low pecelet number case).....	58
Figure 5.12: Temporal variations in ion concentration at various downstream locations based on CFD-ACE+ and analytical predictions (high pecelet number case).....	59
Figure 6.1: Standard deviation of pressure signal as a function of flow rate for plastic and glass syringes.	61
Figure 6.2: (a) Schematic of the flow apparatus; (b) Pressure signal at steady flow rate using the old syringe pump (Cole Parmer) and the new pump (Parker). The period of fluctuations corresponds to 1 rotation of the pump lead screw.	61
Figure 6.3: Microfabricated flow structures showing: (a) typical channel configurations including straight channels, 90° bends, and sudden contractions; and (b) electron micrographs of a bend and a contraction channel.....	62
Figure 6.4: Dependence of blood viscosity on shear rate	63
Figure 6.5: Fluid pressure in microchannel for 1/5 dilution (10 μ L/min flow rate).....	64

Figure 6.6: Comparison of experimental and model predictions of volumetric flow rate to pressure drop ratio for dilute blood flow in rectangular microchannels.....	64
Figure 6.7: Experimental and simulated (Power Law Model) pressure vs. flow rate relationships	66
Figure 6.8: Simulated pressure vs. flow rate relationships based on one-variable Walburn-Schneck Power Law.....	66
Figure 6.9: Experimental and analytical pressure drop vs. flow rate plots (right) for various microneedle configurations (left).....	67
Figure 6.10: Comparison of flow rate as a function of blood dilution at fixed pressure heads for straight needle (left) and filter needle (right).....	68
Figure 6.11: Apparent viscosity of blood in different microneedles	68
Figure 6.12: Micromixer System Schematic	70
Figure 6.13: Mixing of fluorescein and colored water at 1.5 ml/min flow rate.....	70
Figure 6.14: Concentration as a function of downstream distance for fluorescein in the Micromixer System.	71
Figure 6.15: Experimental (left) and numerical flow visualization for Microvalve.....	72
Figure 7.1: Channel geometry and grid for the one-cell and multi-cell simulations	75
Figure 7.2: Pressure distribution (in Pa) along duct (scaled in Y direction) for one-cell (top) and multi-cell (bottom) models	76
Figure 7.3: Pressure variation along the microchannel length for 3-D flow case.....	77
Figure 7.4: Pressure distribution along a spiral microchannel.....	78
Figure 7.5: Channel geometry and mesh for the bent channel simulations	78
Figure 7.6: Pressure distribution in the microchannel bend	79
Figure 7.7: Pressure variation along the microchannel length.....	79
Figure 7.8: Pressure distribution in the microchannel bend predicted with the one-cell model modified to account for bending losses	80
Figure 7.9: Pressure loss (ΔP , Y-axis) due to a bend as a function of U_{\max}^2 (X-axis).....	81
Figure 7.10: Schematic of a miter bend. The momentum resistance is applied in the area of the channel shown inside the box.	82
Figure 7.11: Tesla valve geometry and dimensions.....	83
Figure 7.12: Multi-cell and single-cell grids for the Tesla valve model.....	83
Figure 7.13: Simulated (3-D and 1-D models) and experimental pressure-flow characteristics for Tesla valve	83
Figure 7.14: 1-D Geometric model for electrokinetic channel flow.....	84
Figure 7.15: Electroosmotic transport of charged sample at different time instants	84
Figure 7.16: Channel geometry and 1-D/2-D grids for the double S-shaped channel.....	85
Figure 7.17: 1-D solutions of A+ concentration contours at different instants (in secs.).....	85
Figure 7.18: 1-D solution of B+ concentration contours at different instants (in secs.).....	86
Figure 7.19: 2-D Solutions of B+ concentration contours at different instants (in secs.).....	86
Figure 7.20: Bent square channel geometry and initial location of sample A+.....	86
Figure 7.21: Sample locations at different time instants (in secs.) in bent square pipe.....	87
Figure 7.22: 1-D model validation for surface tension-driven liquid filling problem	88
Figure 7.23: Comparison of 1-D and 2-D simulation for microchannel liquid filling	89
Figure 7.24: Geometric model and mesh for a bifurcating microchannel (45 μm height)	89
Figure 7.25: Surface tension-driven liquid filling simulation with hybrid model	90
Figure 7.26: Simulation of flow and heat transfer in a microreactor system using filaments	91

Figure 7.27: Computational domain for continuous flow PCR system.....	92
Figure 7.28: Simulation results for continuous flow PCR system.....	92
Figure 7.29: (a) T-junction between filaments, and (b) Network of T-junction branches.....	93
Figure 7.30: Heat transfer between reservoirs and interconnecting channels in a biochip device	93
Figure 7.31: Geometry of the microchannels and 1-D filament grid.....	94
Figure 7.32: Temperature distribution in microchannel network and cooling base	94
Figure 7.33: Geometric model and mesh for a static micromixer test case.....	95
Figure 7.34: Fluid mixing patterns in the static micromixer	95
Figure 7.35: Simulation of liquid filling (in red) using a coupled 3-D/1-D approach.....	96
Figure 7.36: Schematic representation of coupling between ACE+ and SABER.....	97
Figure 7.37: Fluidic circuit in SABER coupled with 3-D ACE+ model of Tesla valve (left) and simulated pressure-flow characteristics (right).....	97
Figure 7.38: Schematic showing coupling between SPICE and CFD-ACE+.....	99
Figure 7.39: ACE+ and SPICE simulation with two-level Newton-Raphson Algorithm	100
Figure 8.1: Construction windows of Python-generated parametric Tesla valve Models.....	102
Figure 8.2: (a) Parametric geometry creation set-up; (b) Baseline mixing coil; (c) Mixing coil with 2.5 times pitch; (d) Mixing coil with half the tube diameter	103
Figure 8.3: CFD-Micromesh GUI showing parametric models of microchannel network	104
Figure 8.4: Hierarchy of processes controlled by scripting.....	105
Figure 8.5: Schematic of the steps involved in the design processes	107
Figure 8.6: Configuration of 2-D planar microchannel and beam.....	107
Figure 8.7: Temperature contours in the microchannel.....	108
Figure 8.8: Tesla valve optimization using the Simulation Manager.....	109
Figure 8.9: Tesla valve angle optimization (left) based on cost function (right).....	109
Figure 8.10: Customized template designed for the DNA biochip problem. The 2 panels below show fields for entering geometric parameters as well as model options.....	111
Figure 8.11: Optimizer-GUI image shows GUI for running general optimization simulations	112
Figure 8.12: Geometry of the DNA chip and computational mesh.....	112
Figure 8.13: Flowchart for the DNA chip optimization process	113
Figure 8.14: Plot of cost function and cost function components during optimization.....	114
Figure 8.15: Target DNA concentration in the optimized biochip	114
Figure 9.1: Contours illustrating the convective-diffusive motion of antigen from the inlet chamber into the flow chamber.....	116
Figure 9.2: Effect of flow injection protocol (stopped vs. continuous buffer flow) on surface binding	116
Figure 9.3: B-Cells on fin-type obstacle.....	117
Figure 9.4: Helical snake geometry	117
Figure 9.5: Post geometry with surface coverage.....	117
Figure 9.6: Comparison of surface coverages. Post and cup designs show maximum signal....	117
Figure 9.7: Antigen transport - no lateral force	118
Figure 9.8: Antigen transport under lateral force.....	118
Figure 9.9: Binding enhancement due to lateral force -slow flow.....	118
Figure 9.10: Binding enhancement due to lateral force- fast flow.	118
Figure 9.11: Hydrodynamic forcing - 45 degree	119
Figure 9.12: Hydrodynamic forcing - 90 degree	119

Figure 9.13: Effect of forcing flow ratios on surface coverage	119
Figure 9.14: Effect of forcing flow angle on surface coverage	119
Figure 9.15: Cross-channel system for sample injection and pinching	120
Figure 9.16: Potential distribution along the axis of the separation channel	122
Figure 9.17: Sample filling in cross during step 1	122
Figure 9.18: Sample pinching in the cross-channel during step 2	123
Figure 9.19: Sample injection in the cross-channel during step 3	123
Figure 9.20: (a) Schematic illustration of DNA transport and hybridization on a DNA Chip; (b) Geometry of the flow cell chip (provided by Nanogen)	124
Figure 9.21: (a) Distribution of DNA concentration at the anode; (b) DNA concentration contours near the anode at $T = 1$ second	126
Figure 9.22: H^+ concentration along the electrode plane at different time instants for the fixed potential simulations	126
Figure 9.23: Radial variation of electric field components E_R and E_Z along the electrode plane for $T=0.5s$	127
Figure 9.24: Initial concentration of TAPS and sample in straight channel	128
Figure 9.25: Spatial variation in (a) sample concentration ($Kgmol/m^3$), and (b) electrical conductivity (S/m) along the channel axis at 0.2 secs.	129
Figure 9.26: Spatial variation in (a) sample concentration ($Kgmol/m^3$), and (b) electrical conductivity (S/m) along the channel axis at 0.6 secs.	130
Figure 9.27: Spatial variation in (a) sample concentration ($Kgmol/m^3$), and (b) electrical conductivity (S/m) along the channel axis at 5.0 secs.	130
Figure 9.28: Spatial variation in (a) sample concentration ($Kgmol/m^3$), and (b) electrical conductivity (S/m) along the channel axis at 10 secs.	130
Figure 9.29: Schematic of sample transport in a capillary inside a channel	131
Figure 9.30: Sample dispersion in the domain for the 0.01 Pa case. The time instants and peak sample concentrations are shown adjacent to each plot	132
Figure 9.31: Sample dispersion in the domain for the 1.0 Pa case. The time instants and peak sample concentrations are shown adjacent to each plot	133
Figure 9.32: Electric field contours and flow vectors in the domain for the 1 Pa case.	133
Figure 9.33: Sample dispersion in the domain for the 40 Pa case. The time instants and peak sample concentrations are shown adjacent to each plot	134
Figure 9.34: (a) Schematic representation of micromixer system model, and (b) Computational domain and mesh used in the analysis	135
Figure 9.35: Preliminary results from coupled ACE+ and SABER system-level micromixer simulations	136
Figure 9.36: Coupled 3-D and 0-D model of Berkeley micromixer system	136
Figure 9.37: Sample ACE+ and SPICE results for the Berkeley micromixer showing pressure- flow variations in the system	137
Figure 9.38: (a) Capillary array electrophoresis chips designed and fabricated by UC-Berkeley; (b) Structured one-cell simulation mesh generated by CFD-Micromesh.	137
Figure 9.39: Positions of Species C (left) and Species E (right) at $T=25s$ in the capillary electrophoresis chip	138
Figure 9.40: Layout of Agilent chip used in demonstration simulations	139
Figure 9.41: Solid model and mesh for the protein Labchip	139
Figure 9.42: Locations of inlets 1 and 3, and outlets 2 and 4 in the Biochip system	140

Figure 9.43: Simulated sample pinch-off in the Agilent Biochip.....	140
Figure 9.44: Schematics showing the assembled ISTAT biomicrofluidic diagnostic cartridge (left) as well as the sub-assemblies (right).....	141
Figure 9.45: See-through solid model of I-STAT cartridge assembly showing blood gas and ion selective electrodes	142
Figure 9.46: Top View of Sensor Half of I-STAT Cartridge	143
Figure 9.47: Same View of Meshed Results from CFDRC’s CFD-Micromesh.....	144
Figure 9.48: Temperature Distribution in Cartridge at 15 Seconds and 2 Minutes after Calibrant Heating in the Channel. The plots show horizontal planes through the sensor and through the channel.	148
Figure 9.49: Transient Temperature Profiles during Calibrant Fluid Heating.....	149
Figure 9.50: Transient Temperature Profiles in Channel during Calibrant Flushing and Sample Introduction.....	150
Figure 9.51: Transient Temperature Profiles during Sample Heating in Channel	151
Figure 10.1: Advertisement for CFD-ACE+ Multiphysics Software	157
Figure 10.2: CFDRC’s biofluids lab facility.....	160
Figure 10.3: Glucose monitoring system analyzed for Medisense (left) and sample results from multiscale vein filter analysis for J&J Cordis (right).....	161
Figure 10.4: Design analysis of APDS-II biosensor system being developed at LLNL	162
Figure A.1: Comparison Between 1 st Order and Higher Order Scheme for Static Micromixer Case.....	167

LIST OF TABLES

		<u>Page</u>
Table 4.1	Comparison of numerical and experimental data	23
Table 6.1	Experimental Flow Rate-Pressure Drop Data and Calculated Viscosity for Dilute Blood Flow Through Microchannels	62
Table 7.1	Pressure Gradient Along the Microchannel for 2-D Channel Flow	74
Table 7.2	Pressure Gradient Along the Microchannel for 3-D Channel Flow	74
Table 7.3	Comparison of Pressure Drop and Shear Force Along Spiral Microchannel for Various One-Cell Models with Analytical Solutions	75
Table 7.4	Comparison of 1-D Model with Momentum Resistance and 2-D Simulations	80
Table 9.1	Applied Voltage (V) and Time (sec) During Injection Process	118
Table 9.2	Material properties used in the I-STAT simulations	142

ACKNOWLEDGEMENTS

During the course of this project, the authors received help, encouragement and advice from a number of individuals without which this project would not have been a success.

The authors would like to thank several DARPA Project Managers, Drs. Heather Dussault and Anantha Krishnan, for their enthusiastic support, guidance and patience. Thanks are also due to Messrs. Joseph Beasock, Air Force Research Laboratory/IFTB and Clare Thiem, Air Force Research Laboratory/IFTC for their work in the role of project monitors and for their helpful suggestions for improvements.

This work would not have been possible without the extensive support and help provided by a number of CFDRC personnel. Thanks are due to Dr. Ashok Singhal for technical direction, for help with synergizing this effort with other on-going programs at CFDRC and for providing IR&D support for commercialization of the developed capabilities. Various individuals provided valuable help with different aspects of the project: Mr. Jag Raghavan and Dr. Shankar Sundaram for biochemistry modeling and related demonstration studies; Drs. Z. J. Chen, Jerry Feng and S. Krishnamoorthy for the electrokinetics simulations; Drs. Z. Tan and Michal Furmanczyk for the CFD-Micromesh development and SABER-ACE+ coupling; Drs. Yu Jiang, Deming Wang and Sami Bayyuk for the numerical algorithms and VOF modeling; Ms. Anna Garrison and Dr. Jerry Jenkins for the script-based optimization studies; Dr. Nathan Hariharan for the SPICE and CFD-ACE+ coupling and Drs. Hui Ding and Maciej Pindera for the filament model development efforts. Software group personnel, including Mr. Milind Talpallikar, Winston Jiang and Shaoping Li helped out with the GUI and other software support. Finally, the Graphics group worked on adapting CFD-VIEW for one-cell model visualization, for which thanks are due to Dr. Jeroen van der Zijp. Thanks are also due to Ms. Jennifer Swann and Ms. Misty Gravette for their help with the documentation work.

The authors would also like to thank our project partners from the California Institute of Technology (Dr. Erik Antonnson), U. C. Berkeley (Dr. Dorian Liepmann) and Tanner Research Inc. (Dr. Barry Dyne), as well as Mr. Donald Verlee for their valuable inputs and fruitful collaboration during the course of the project.

1. INTRODUCTION

1.1 Background

This report presents results of a DARPA/MTO Composite CAD Project aimed to develop a comprehensive microsystem CAD environment, **CFD-ACE+ Multiphysics**, for bio and microfluidic devices and complete microsystems. The project began in July 1998, and was a three-year team effort between CFD Research Corporation, California Institute of Technology (CalTech), University of California, Berkeley (UCB), and Tanner Research, with Mr. Don Verlee from Abbott Labs participating as a consultant on the project.

The overall objective of this project was to develop, validate and demonstrate several applications of a user-configurable VLSI-type mixed-dimensionality software tool for design of biomicrofluidics devices and integrated systems. The developed tool would provide high fidelity 3-D multiphysics modeling capability, 1-D fluidic circuits modeling, and SPICE interface for system level simulations, and mixed-dimensionality design. It would combine tools for layouts and process fabrication, geometric modeling, and automated grid generation, and interfaces to EDA tools (e.g. Cadence) and MCAD tools (e.g. ProE).

All of the major tasks and activities in this program were organized to take advantage of the expertise of each team member:

- **CFDRC:** (Drs. Vinod Makhijani and Andrzej Przekwas) project coordination, development of new high-fidelity, reduced-order and mixed-dimensionality multiphysics capabilities in system-level software, implement virtual-sequence programming and software configurability, software validation, demonstration, application and commercialization.
- **CalTech:** (Dr. Erik Antonnson) develop methodology to synthesize mask-layout and fabrication process-sequence for desired microflow function, create “meshing-ready” solid models, facilitate two-way coupling of layout-solids-fabrication tools with CFDRC’s software.
- **U. C. Berkeley** (Dr. Dorian Liepmann) design, fabricate and experimentally characterize parametric batches of microfluidic device building blocks for model validation.
- **Tanner Research** (Barry Dyne) provide layout editor (L-Edit) and technical user support to Cal Tech for data management, geometric rendering and feature extraction for MEMS mask-layout synthesis program.
- **Consultant** (Mr. Don Verlee) consultation on CAD tool design specifications, identification of bio-microfluidic test cases for demonstrating software applicability, software evaluation.

Figure 1.1 schematically illustrates the resulting CFD-ACE+ Multiphysics simulation environment for Biomicrosystems simulations and design. The report documents the work performed during the three years of the project.

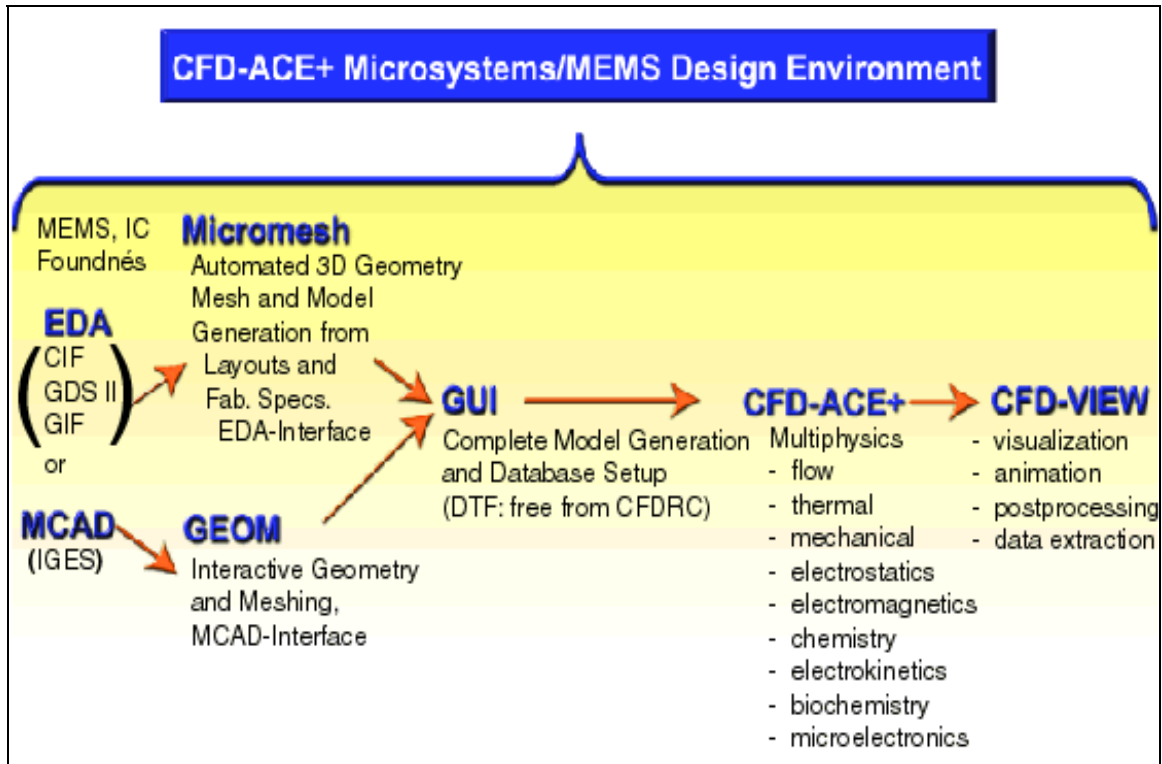


Fig. 1.1 CFD-ACE+ Multiphysics Simulation Environment for Bio Microfluidic Devices and Integrated Systems

1.2 Project Motivation

It is generally recognized the microsystems technology will be the focus of intense international competition, and a variety of exciting new MEMS-based products will drive the commercial markets [McWhorter, 1999]. The new generation of microfluidic chips will host mechanical devices, fluidic channels, chemical mixers and reactors, bioanalytical devices, photonic devices and circuits, and a myriad of others, all integrated with the electronics. The success of the bio microsystems industry, to a large extent, will be determined by the availability of Computer Aided Design (CAD) tools. High prototyping costs, long product development cycles, and time-to-market pressure create acute demands for sophisticated, commercial quality design tools.

Biofluidic microsystems incorporate several microfluidic, electronic, and mechanical devices. The operation of such systems entails complex computer controlled procedures. The complexity of fluidic, thermal, electrokinetic, biochemical, and electronic devices requires advanced modeling and design tools for each of the individual devices that make up the system. To be accepted by the industry, however, the biomicrofluidics CAD tools have to provide essential functionality and accuracy of the simulation results. Moreover they have to support device-level, system-level and mixed-level simulations. Increasingly used by non-CFD experts, they have to offer ease-of-use, and intuitive geometry and model setup, resembling the fabrication process.

1.3 Project Objectives

The objective of this project was to develop, validate and demonstrate several applications of a user-configurable VLSI-type mixed-dimensionality software tool for design of biomicrofluidics devices and integrated systems. The software tool would enable:

- Multiphysics (biochemistry, electrochemistry, multiphase flows), mixed-dimensionality (3-D/1-D/0-D) analyses
- Dynamic simulation of multi-step biomicrofluidic process sequences
- Automated generation of models (solids, meshes, boundary conditions, volume conditions ..) from layouts and process
- Direct integration and two-way coupling of VLSI-type software with layout-solids-fabrication-optimization tools.

The proposed work is divided into three consecutive well-defined annual phases:

Phase I (1st year): Design and development of base technology

Phase II (2nd year): Technology integration, validation and demonstration

Phase III (3rd year): Process automation, technology transfer and commercialization

All of the project accomplishments, summarized in the next section, and described in further detail in Section 2.10, were aimed at fulfilling the above-stated objectives.

1.4 Summary of Accomplishments

Biomicrofluidics systems have been evolving so rapidly that the physics modeling capabilities planned at the beginning of the project had to be upgraded and improved several times during the project. Originally planned interface between ACE+ and SABER has been developed but discontinued due to unavailability of SABER (acquired by Avant). Instead, a robust CORBA-based direct interface to SPICE has been established. CFDRC plans further development and support of the SPICE module in ACE+ for mixed level simulations. It offers a cost effective and convenient option to customers. Also, due to the organizational changes and shift of corporate focus at Tanner Research during the course of the project, they ended up participating only in a very limited role during the first year of the project by providing the team with their L-Edit software package. This package was used to import the MEMS designs (in GDSII or CIF format) from other institutions into CFDRC's design environment. Ledit also allowed us to process very large designs, which can not be handled using CFD-Micromesh.

In the following section, we briefly discuss the most important accomplishments, categorized by their role in contributing to the main objective of the project.

1.4.1 Building the Model - From Layouts to Models

Simulation process of microsystems involves two challenging steps: geometric modeling and mesh generation. Since geometrical configurations of microsystems are often very complex, typically the grid generation task is performed manually with mechanical CAD tools, which is a tedious and time-consuming effort. In this project a fully automated mesh generation procedure from 2-D layouts and fabrication process specifications has been developed and implemented in

CFD-Micromesh. Figure 1.2 illustrates a sample 2-D layout of a micro mixer and the resultant 3-D mesh. The layouts are imported in standard micro fabrication formats (CIF, GDSII, and DXF). However, image formats (GIF, JPG) can also be used. The code generates a 3-D model using operations (deposition, etching, bonding,...) specified by the fabrication process data.

A 3-D finite element (FEM) or finite volume (FVM) mesh with tagged material properties, boundary and volume conditions is then automatically generated. The complete model description is saved in a standard DTF format. The automatic generation of the 3-D model and mesh typically takes a couple of minutes on a current PC machine.

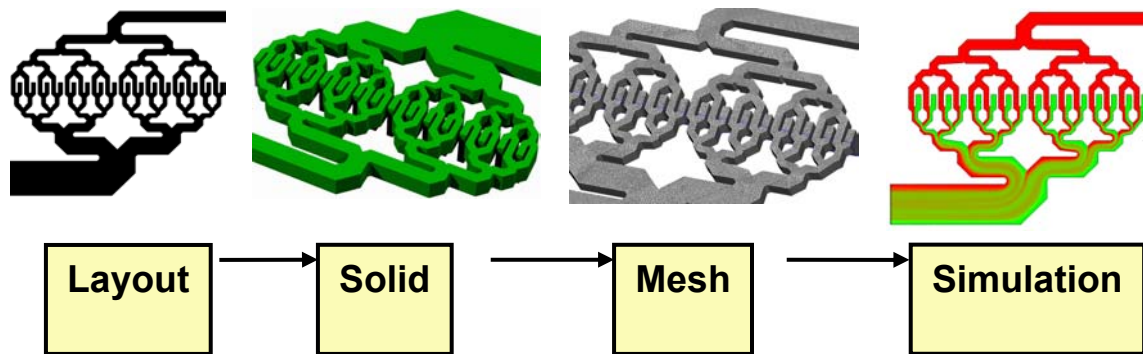


Figure 1.2: Automated geometry, mesh, and model generation in CFD-Micromesh for multiphysics simulations of biofluidic microsystems. Example design path is shown for a two fluid static micromixer.

1.4.2 Hierarchy of Simulation Models

Simulation and design of microfluidic systems requires at least two levels of modeling:

- **High-fidelity models** (usually three-dimensional finite element or finite volume) for multiphysics design and optimization of particular elements and devices (e.g. their geometrical structure); and
- **System-level models** for simulation of complete microsystems integrated from a large number of devices, for which reduced or compact models are necessary to make such system simulations computationally feasible.

Generation of compact models for microfluidic devices is one of the most challenging and time consuming tasks in the design process. The difficulties arise from the nonlinearity of physical processes, and from the coupling between physical disciplines e.g. structures, fluid, electrostatic, thermal. There are several approaches to generating compact models ranging from simplified analytic description with algebraic expressions, to functional curve fits to experimental performance characteristics, to equivalent electrical (RLC) circuit models. Compact models can be generated from experimental data for existing devices or from detailed parametric simulations using high fidelity models. A comprehensive library of reusable compact models for electronic, fluidic, and mechanical devices will have to be established for system-level simulations such as SPICE. Circuit models for fluidic channels, valves, pumps, mechanical membranes, comb drives, micro heaters, and others have been demonstrated. For example, circuit models of air damping,

for inertial sensors, and for synthetic jets have been recently demonstrated by CFDRC. 3-D models can be used for modeling larger components of fluidic microsystems but computational time (hours per case) will limit the number of design parameters. Circuit models, once validated, allow for rapid parametric simulations of a large number of designs.

For some processes (e.g. mixing and diffusion), there is no clear way to generate compact models. In those cases a **mixed-dimensionality** modeling technique can be used. CFD-ACE+ environment allows to link 3-D device models, point models described with algebraic/differential equations, and circuit (SPICE) models to perform system level simulations. Coupling between the simulation levels is facilitated by integrating boundary conditions of the 3-D model and using them as contact I/O signals for the system level simulator. CFD-ACE+ offers a direct (CORBA) link to SPICE. The Simulation Manager scripting, developed at CFDRC, can be used to customize the design process.

In many designs, the circuit models cannot represent the complexity of 3-D device and interconnect topology. To enable fast simulations within the 3-D framework of ACE+, a novel concept of a **Filament** has been developed in the project. Filaments are essentially 3-D structures represented as a length-wise polyhedral mesh embedded in a surrounding macroscopic domain or they can join several different domains. In modeling fluidic microsystems filaments can be used for microchannels, integrated micro heaters, beams, and other devices coupled to fully meshed 3-D devices. Advantage of using filaments are enormous: ease of geometric modeling and automated meshing, fast fully implicit solution, good accuracy (thanks to locally analytic solutions), and natural visualization. Figure 1.3 illustrates the use of the filament for modeling heat transfer in a biochip device.

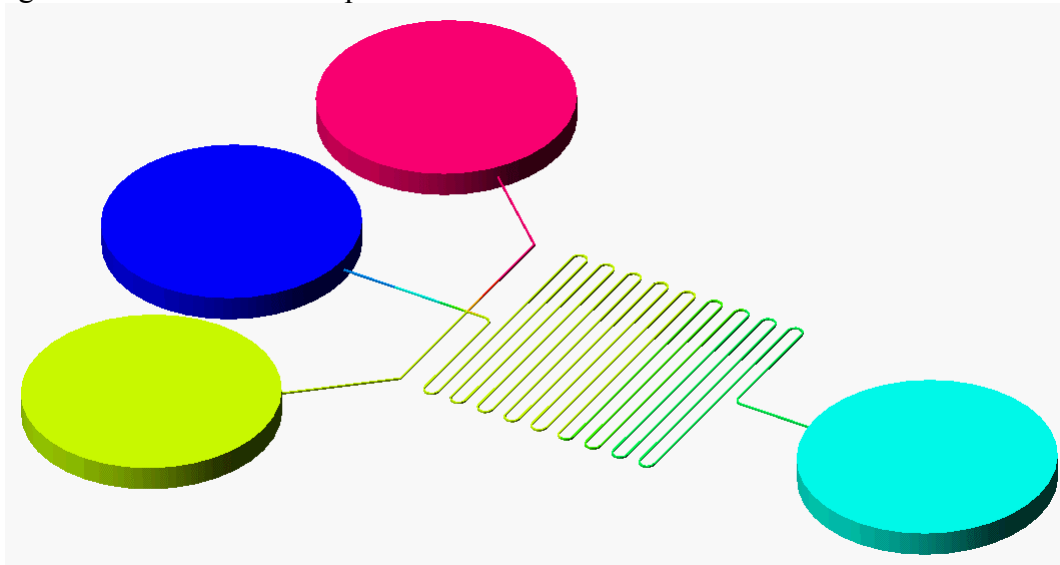


Figure 1.3. ACE+ filament capability for modeling heat transfer in a biochip device.

1.4.3 Multiphysics Models in CFD-ACE+

Fluidic microsystems in bioanalytical and biodiagnostic applications include a broad range of devices such as valves, pumps, mixing chambers, electrokinetic channels, detection devices, and several types of microreactors (e.g. PCR, hybridization). Computational design of such systems requires multiphysics modeling capability.

In this project, the CFD-ACE+ environment has been significantly upgraded to fully multiphysics level with emphasis on electrokinetic, biochemical, and electrochemistry disciplines. The new Bio-Electrochemistry features added to CFD-ACE+ on this project are:

- Biochemical reaction kinetics, which include enzyme-catalysis, cooperative ligand-binding, non-competitive and competitive receptor-ligand binding (both reversible and irreversible);
- Improved wall zeta potential model;
- Sample stacking in a multiple ionic species system;
- Ionization model to simulate acid-base equilibrium reactions, autoionization of water and ionization equilibria involving ampholytes;

A detailed description of mathematical models, numerical methods, validation results, etc., is presented in the remaining chapters of this report.

1.4.4 Applications for Biomicrofluidics Devices and Integrated Systems

In this project, the comprehensive multiphysics modeling tools developed at CFDRC have been applied for both device-level and system-level design studies on various types of biomicrofluidics systems. Application examples include electronic DNA chips, optical and cell-based biosensor systems, various types of electrokinetic separation and sample stacking devices, electrophoretic biochips, microfluidic mixers and lab-on-a-chip systems for blood diagnostics. Figure 1.4 shows one of the lab-on-a-chip systems that was analyzed using the developed system-level CAD capabilities. Section 9 of this report demonstrates the modeling approaches and outlines the simulation results obtained during the analysis of these devices.

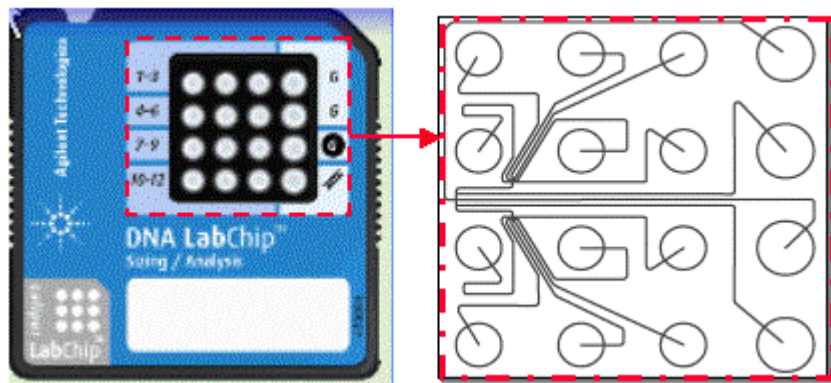


Figure 1.4: Agilent's DNA LabChip System that was analyzed using CFD-ACE+

2. CFD-MICROMESH

A new software tool was developed at CFDR during the course of the project for fast geometric modeling and mesh generation for 3-D microfluidics devices and systems simulations. The software, called CFD-Micromesh, generates grids for simulation of electrical, thermal, and mechanical behavior of the devices. Since geometrical configurations of microsystems are often very complex, typically the grid generation task is performed manually with mechanical CAD tools, which is a tedious and time-consuming effort. CFD-Micromesh addresses the need for fully automated mesh generation from 2-D layouts and fabrication process specifications.

2.1 Basic Approach for Geometric Modeling

The input for CFD-Micromesh consists of a mask file (such as CIF or GDSII) and a processing file. The mask file specifies the masks in which a material is deposited or etched. The processing file specifies the order and the metric (such as the thickness) of the deposition and etching processes. The deposition/etching processes are simulated using a 3-D array consisted of 'nx' by 'ny' by 'nz' voxels. The size of the voxels determines the resolution of the simulation. However, because of efficient internal compressions, the memory required is not related to the number of the voxels. For example, a simulation using 800x400x320 voxels consumes only 8MB space. The time is roughly proportional to the number of voxels.

Because of the large number of voxels involved, visualization using polygon-based approach (such as CFD-VIEW or VRML) is not feasible. Therefore, a special ray tracer is provided. It consumes little memory and runs at decent speed, typically 30 to 200 seconds, when 3 lights are used, to generate an 800x800 image. The user can control which material (including the air) to show

2.2 Software Features

CFD-Micromesh can import standard layout formats (CIF, GDSII), or even images (GIF, JPG), and generate a 3-D model using operations specified by the process data or the user. A 3-D finite volume mesh with tagged boundary and volume conditions is then automatically generated. The automatic generation of 3-D model and mesh takes typically a couple of minutes on a current PC machine. The geometry/meshing engines and user interfaces are described below:

GUI: CFD-Micromesh has a very intuitive graphical user interface (GUI) designed for microsystems and microelectronics engineers with little or no CFD experience (see Figure 3.1 below).

Modeler: The model is internally represented by encoded voxels. The encoding allows high-resolution representation of complex geometries. Based on a user input, the following geometric operations are allowed:

- a) *Deposition:* Simulates the deposition process in fabrication;
- b) *Etching:* Mimics the etching process;
- c) *Diffusion:* Simulates the diffusion process of semiconductor fabrication;

- d) *Insertion*: Inserts a solid material into the existing model at an arbitrary position (useful when final shape of the objects is known); and
- e) *Replacing*: Replaces an existing material with a new one.

The input geometry can be 2-D masks (including CIF and GDSII), bitmaps, and standard primitives (polygons and ellipses) drawn by the user directly in the CFD-Micromesh graphical user interface (GUI) shown in Figure 2.1. User can also input 3-D primitives (bricks, spheres, and cylinders) and 3-D b-reps (in STL format). The resulting model is visualized by an efficient ray-tracer.

Mesher: The meshing module generates a 3-D finite volume grid. The voxel data is projected onto an XY-plane to obtain a 2-D image. A 2-D triangular grid is then generated. The triangulator is written to allow: a) vectorization of the 2-D image; b) high-quality triangulation; and c) mesh adaptation. The grid size distribution for the adaptation step is controlled by another user-specified image (layout). The triangles are then extruded into prisms, which can be further processed to obtain grids of mixed prismatic-hexahedral or pure hexahedral type. The grid is the Cartesian product of a triangular grid and a set of cross planes in the z-direction. The user specifies the maximum number of cross planes and the expected triangle size. The cross planes and triangles are generated automatically. Besides, a conformal surface triangulation can also be generated. The triangulation is nearly optimal to represent the geometry (including material interfaces).

DTF Output: The user can choose to split the boundary conditions further into top, bottom and side types. This allows more flexible BC assignment.

2.3 Demonstration Case using Voxel-Based Approach

The CFD-Micromesh tool has been demonstrated on a range of microsystem applications, including fluidic micromixers, valves and pumps. Figure 2.2 below shows one example for a micromixer. The grid generation process takes a few seconds. The figure shows the prismatic grid. The air elements have been removed for visualization.

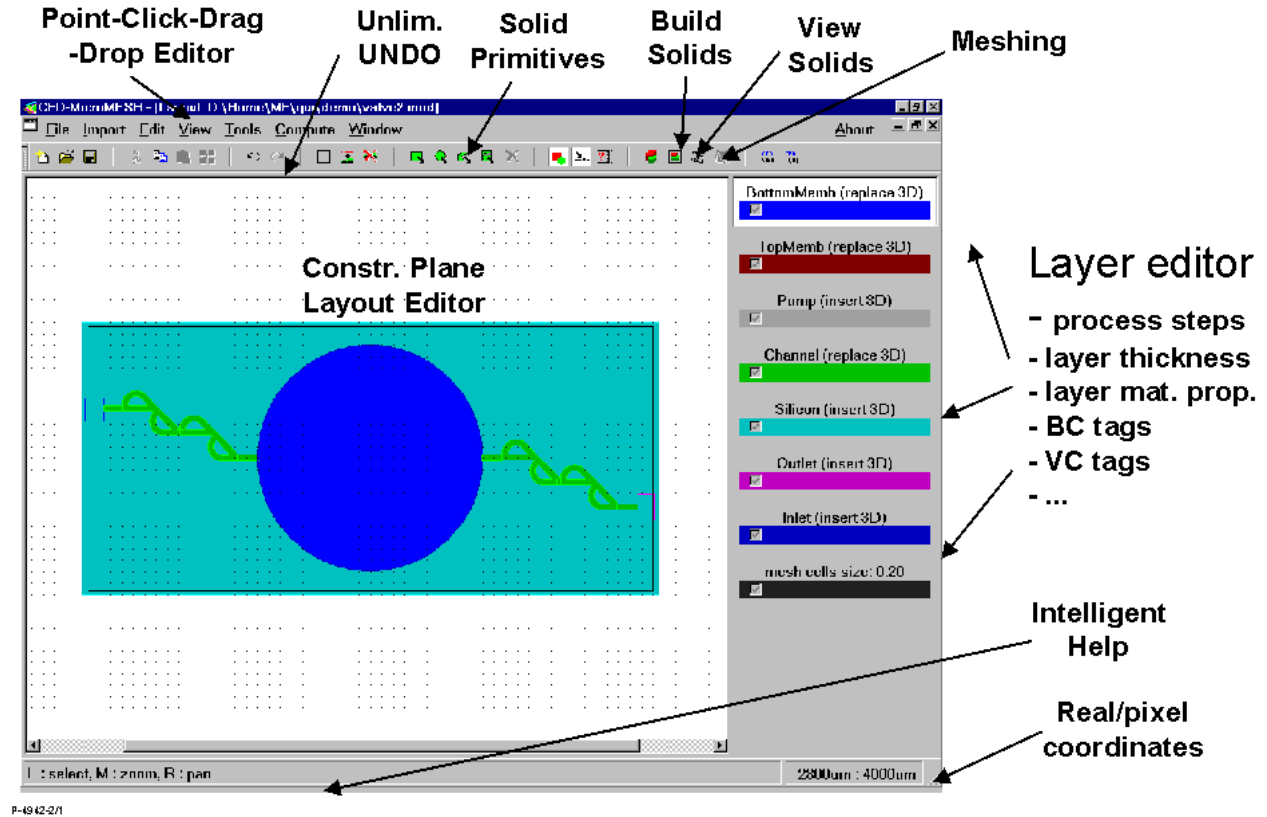


Figure 2.1: Graphical-User Interface for CFD-Micromesh

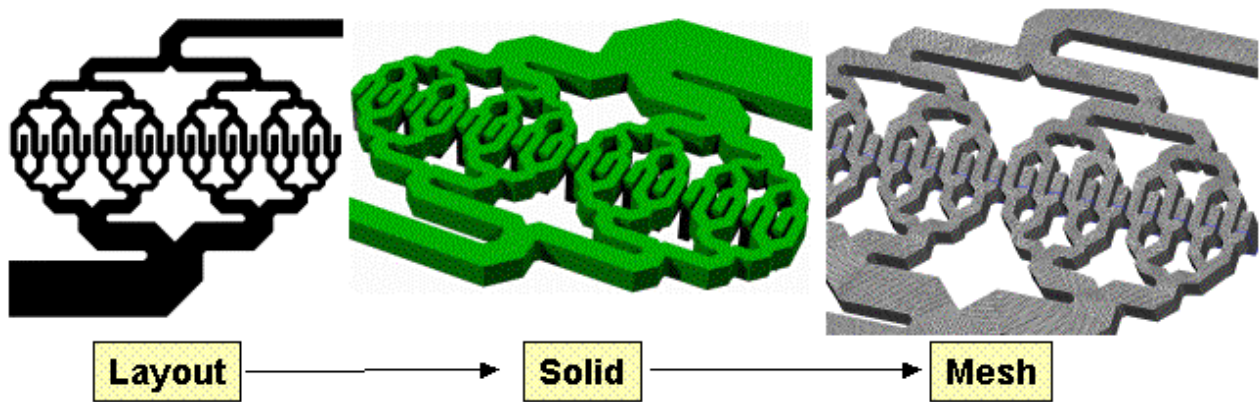


Figure 2.2: Application of CFD-Micromesh for a static microfluidic mixer

2.4 Geometric Modeling and Structured Grid Generation in Micro-Mesh

Geometric Modeling of Solids: The voxel-based technology of solid modeling is just right for a small and complex shape. Modeling of non-complex shapes for large structures, however, requires a different approach. A new geometrical modeling technology has been developed to handle this problem.

Features of Voxel-based modeling:

- Complex, non-planar shapes, like accurate simulation of physical deposition or etching
- Ratio of the total model size comparing to the smallest detail cannot be bigger than few thousands

Features of Geometry-based modeling:

- Currently, we can handle only rectangular shapes, but we plan to extend it for any 2-D polygons. Only planar structures will be supported in this technology.
- This technique can handle much bigger projects with any ratio of model size comparing to smallest detail. The model size is limited only by number of elements in layouts.

Those features make these two technologies complementary, and the possibility to use them in the same program allows for solving much bigger set of problems.

Geometric modeling of structures described by layouts and process description requires development of procedures to describe blocks and topology at every step of model creation, and to predict the effect of each new operation on the existing model. This technique has been implemented in CFD-Micromesh. The new approach was used to generate a solid model for the microfluidic structure presented in Figure 2.3. The ratios of channels length to width make it impossible to model this structure using the earlier voxel technique.

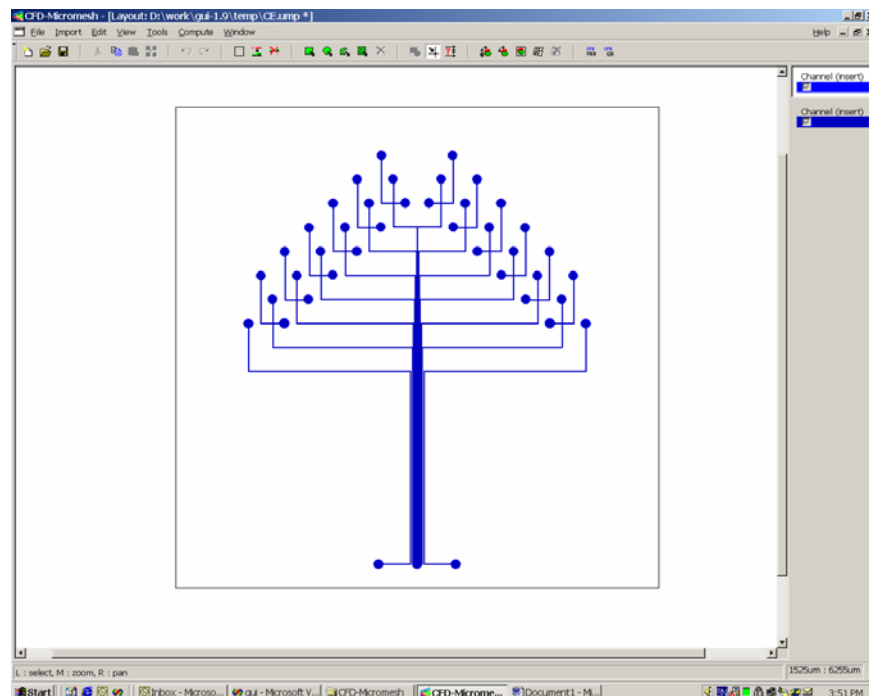


Figure 2.3: Layout of a microfluidic device

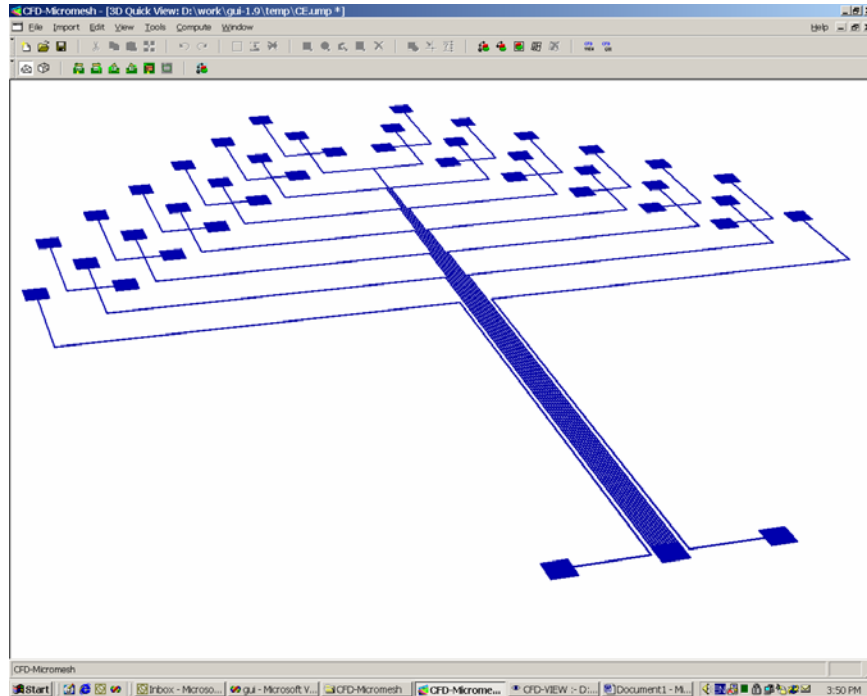


Figure 2.4: Automatic generation of 3-D model of the device

Another advantage of the new method is computation speed. The model building time of silicon micro-valve presented in Figure 2.4 was less than 1 second for the geometry-based method, and 45 seconds for the voxel-based method. Even bigger time reduction was achieved for mesh generation described later. The time, of course, is highly dependent on the type of modeled shapes.

Structural mesh for 3-D Model: Prior to this project CFD-Micromesh relied on voxel-based geometries and could generate only unstructured meshes, e.g. triangle based prisms. In this project, a new mesh generation technology was developed for the geometry-based method. The generated mesh is fully structural, i.e., structured hexahedrals, which makes it especially good for fluid flow problems. This new mesh building procedure requires the development of methods to automatically create a mesh in each block and ensures mesh matching at any two adjacent blocks.

Using the presented method, three different meshes were built for a fluidic structure presented earlier in Figure 2.4. Figure 2.5 shows the coarsest mesh. Figure 2.6 shows a finer mesh, with 1-D meshes inside the channels. Figure 2.7 shows the finest mesh with multiple cells per channel width.

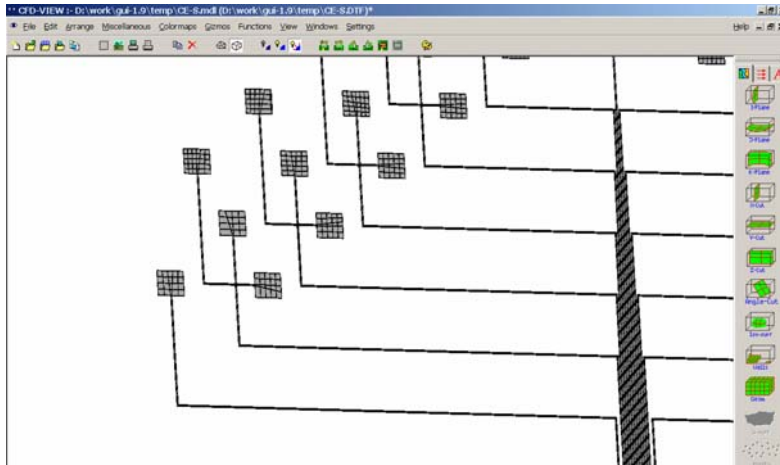


Figure 2.5: Coarse structural mesh for microfluidic device

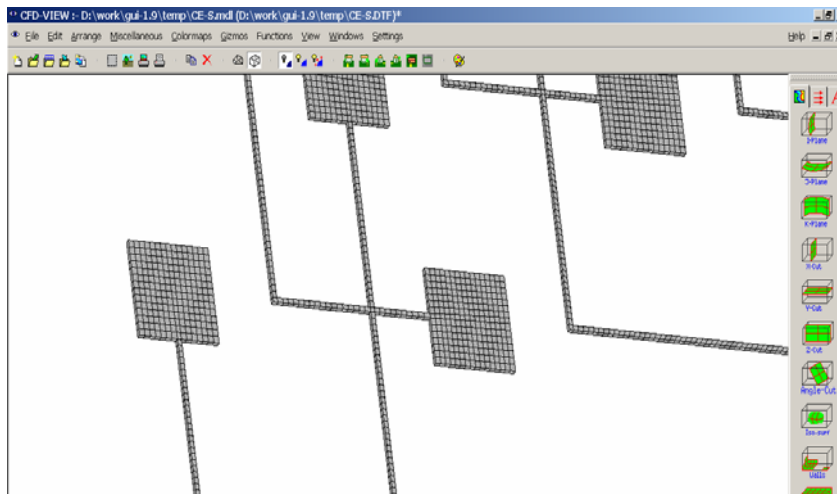


Figure 2.6: Finer structural mesh, with 1-D mesh inside channels

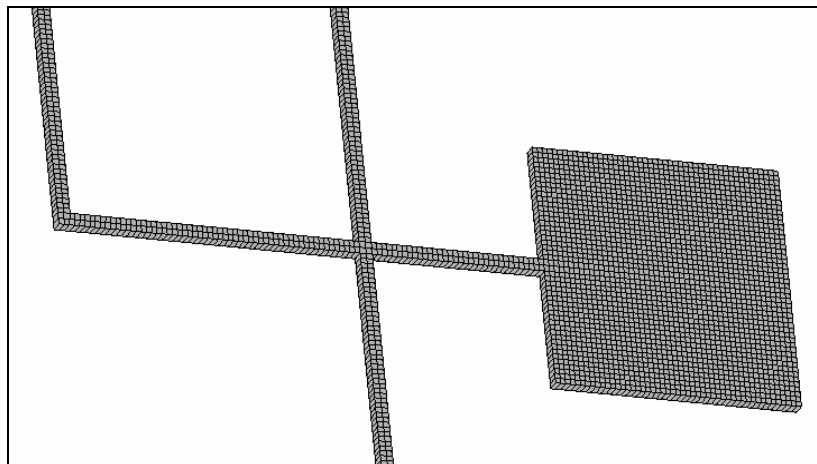


Figure 2.7: Fine structural mesh for the microfluidic device

2.5 CFD-Micromesh-Tet

CFDRC also started work on the development of CFD-Micromesh-Tet, which enables development of geometric models and meshes for microfluidic structures with 3-D shapes/configurations. The underlying methodology used here is as follows:

Solid modeling: CFD-Micromesh-Tet uses fractional volume of materials in each cell, instead of binary (0 and 1) representations. This results in more accurate geometry. Also, most of the operations allowed in the other version of CFD-Micromesh are allowed here as well: deposition, etching, diffusion, insertion, removing and replacing.

Grid generation: Tetrahedral elements are generated here. Marching cube and marching “tet” algorithms are used to generate basic tetrahedra. Several operations (swapping, smoothing etc) are implemented to improve the quality of the mesh.

Interactive visualization of solids: This version is improved to include an interactive 3-D solid visualization capability. It begins by generating a surface triangulation just sufficient to represent the geometry and shows the surface in OpenGL.

Example: Application of CFD-Micromesh-Tet for the microbead array problem (described later in the report) is presented here. The channel shown in Figure 2.8 has a cross sectional area of $50\ \mu\text{m} \times 50\ \mu\text{m}$. 25 micro beads of diameter $5\ \mu\text{m}$ are packed along the lower channel wall. CFD-Micromesh-Tet was used to create the solid model and tetrahedral mesh. The mesh was generated by initially create an octree grid, which was then split into tetrahedral elements using marching cube and marching tetrahedron methods. Quality improvement procedures were then applied to the tetrahedral mesh, to reduce bad shaped elements. The solid model and corresponding surface mesh are shown below.

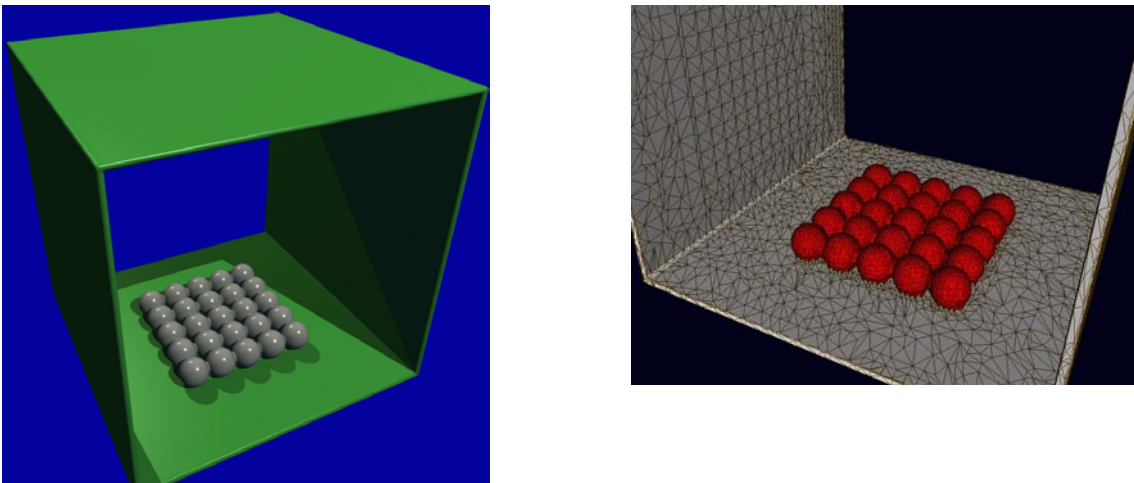


Figure 2.8: Solid model and corresponding surface mesh for microbead array

3. MICROSYSTEM FABRICATION PROCESS SIMULATIONS

This section describes the development of a fabrication process simulator for MEMS applications that was developed to work in conjunction with CFDRC's software module. All of the work described in this section was carried out by Prof. Erik Antonsson and his graduate students at the California Institute of Technology

3.1 Solids-Layout Geometry and Mesh Development

Objective: The objective here was to:

- (a) Integrate the Caltech etch-simulation program ("SEGS") with the CFDRC software;
- (b) Complete the renewal of Caltech's cellular automata fabrication simulation method, and complete the integration of this simulator with CFDRC's data format;
- (c) Complete the development of etch and deposition computational algorithms (models) for integration with the level-sets software; and
- (d) Initiate validation of the results of these simulations.

Method of Approach: A graduate student from Caltech attended a week-long training session at CFDRC in Huntsville, Alabama, to become familiar with the software. The interface to the CFDRC software was investigated by Caltech, so that the integration could be accomplished in a straightforward way.

CFDRC provided the input and output data format (and examples) to Caltech, and they developed input and output filters to permit the SEGS etch simulator to be used to generate solids and meshes for the CFDRC analysis software. Because CFDRC used a pixel-based input format and a voxel-based output format, creating an interface between Caltech's vector- and surface-based formats was not trivial. A filter was successfully created to convert from Caltech's surface format to CFDRC's voxel format. However, this effort strongly suggested that Caltech retain a pixel/voxel representation in their simulation (rather than convert from pixels to vectors and from surfaces to voxels), and utilize the approach of one of their earlier generation of simulators based on cellular automata. This approach had the benefits of geometric robustness, and avoided the need of the conversions mentioned above. Geometric accuracy was limited by the size of the voxels, but since CFDRC was already utilizing this format, this was not a serious limitation in this application.

In addition to the high-performance multi-process anisotropic etch simulator (SEGS) developed earlier by Caltech, a level-sets "engine" (computer program) provided by CFDRC to Caltech, was used to develop the necessary 3-D etch and deposition algorithms for this computing environment. It was expected that this approach would permit the Caltech etch simulator to be used to generate solids and meshes for the CFDRC simulation and analysis software, and physically and geometrically accurate simulations of many fabrication processes could be conducted, including etching and deposition. Caltech completed their etch rate and deposition rate modeling procedure, and interfaced this model to the CFDRC level sets computational "engine".

Testing of the integrated modeler and level sets engine led to some serious questions as to the accuracy of the level sets engine (simple isotropic depositions were inaccurately simulated). Furthermore, the level sets engine was too computationally expensive. These computational problems with the level-sets "engine", therefore, led Caltech to abandon this approach.

Results and Discussions: The interface of the Caltech fabrication process simulation code ("SEGS") with CFDRC's modeling and analysis software has been completed. Transfer of the Caltech software to CFDRC was conducted by a graduate student from Caltech who spent a week at CFDRC. During this time, the software was compiled and initial testing and demonstrations were conducted at CFDRC to ensure interoperability of the code generated at each location. Included in this work is the etch rate and deposition rate modeling procedure. The Caltech code ("SEGS") is now integrated seamlessly into CFDRC's CFD-Micromesh application as the wet etch process simulator, which significantly extends CFDRC's capability for simulating vertical etch only or uniform etch in each direction (compare Figures 3.1 and 3.2).

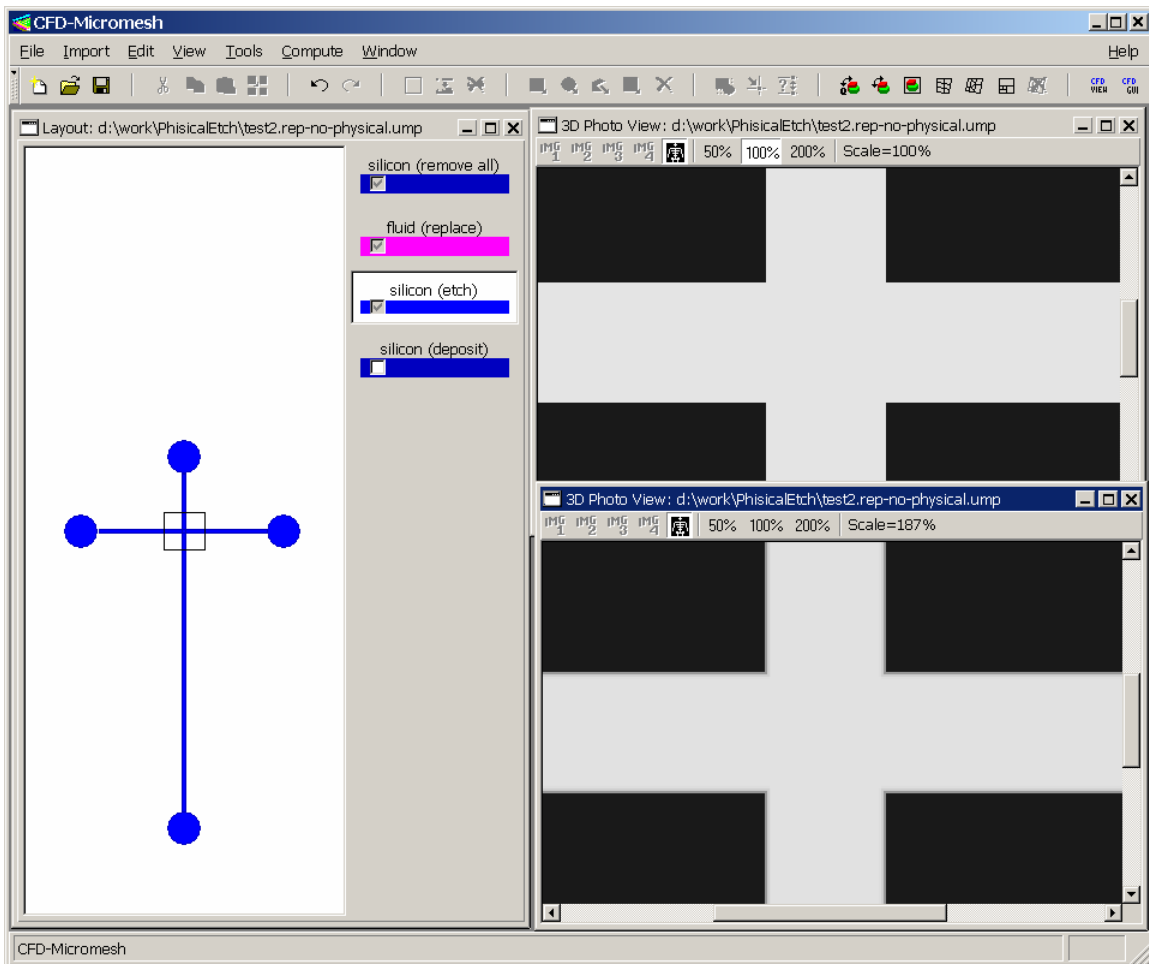


Figure 3.1: Standard etch operation in CFD-Micromesh Program

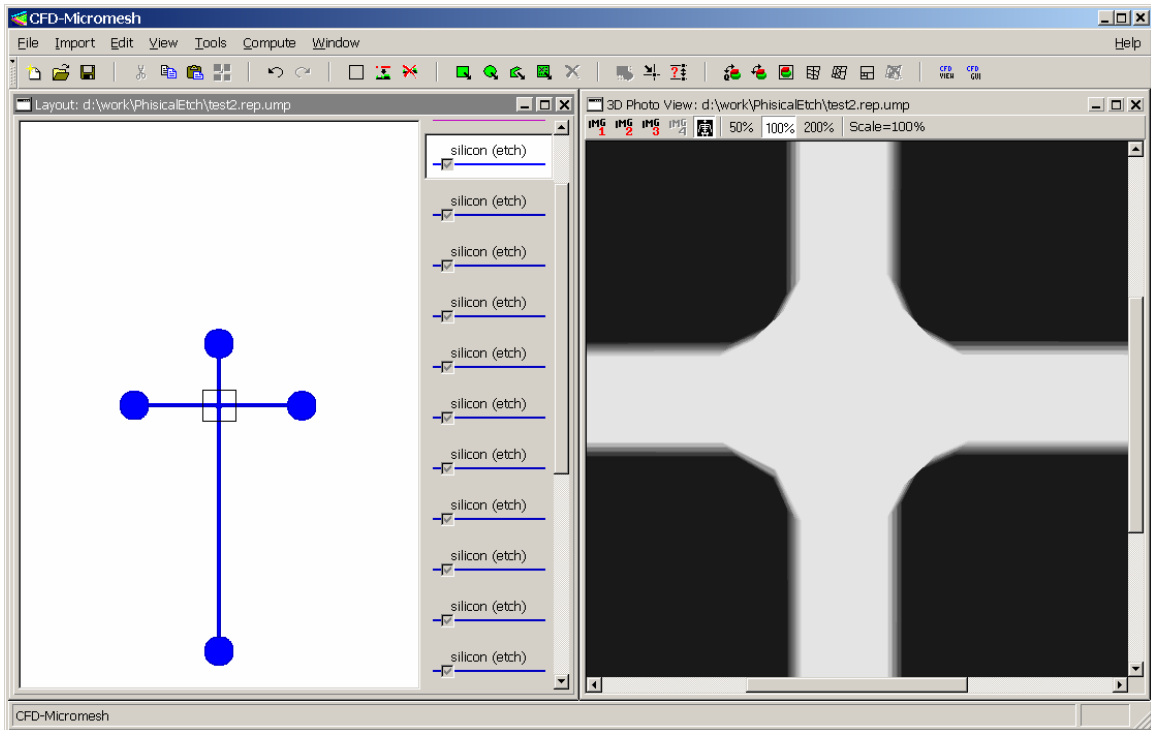


Figure 3.2: Physical etch simulation data imported into CFD-Micromesh Program

A significant component of the testing is validation with experiment. To do so, Caltech mounted an effort to have masks made and then etched shapes fabricated from those masks. Caltech then inspected the fabricated shapes and compared them to the predicted shapes produced by the simulation. Earlier experimental validation demonstrated the correctness of several of the previous fabrication simulation methods.

3.2 Development of Layout to Simulation and Reverse Interfaces

Objectives: The work objectives here were to:

- Complete the initial iterative method for synthesizing mask-layouts; and
- Introduce synthesis of the fabrication process.

Method of Approach: This method utilizes the high-performance anisotropic etch simulator developed previously by Caltech. The mask-synthesizer utilizes a stochastic exploration method (a genetic algorithm) in an iterative loop to identify and refine mask-layouts that produce shapes close to the desired shape. Running this procedure through several iterations (generations) produces convergence towards a mask-layout that produces the etched shape closest to the desired shape (Figure 3.3).

The iterative loop works in the following way. An initial (random) population of valid mask-layouts and fabrication processes is produced. The fabrication of these masks with their associated processes is simulated with a computationally efficient and geometrically accurate 3-D etching simulation (SEGS). The 3-D results of the fabrication simulation are compared to the desired 3-D shape. According to the closeness values of each individual (mask-layout and

process) in the population, a genetic algorithm (GA) is applied with selection, crossover and mutation operators to introduce variations into the mask-layouts and processes. The robustness of the GA produces subsequent generations with better performance. The iterations are repeated and the simulated shapes converge to the desired shape.

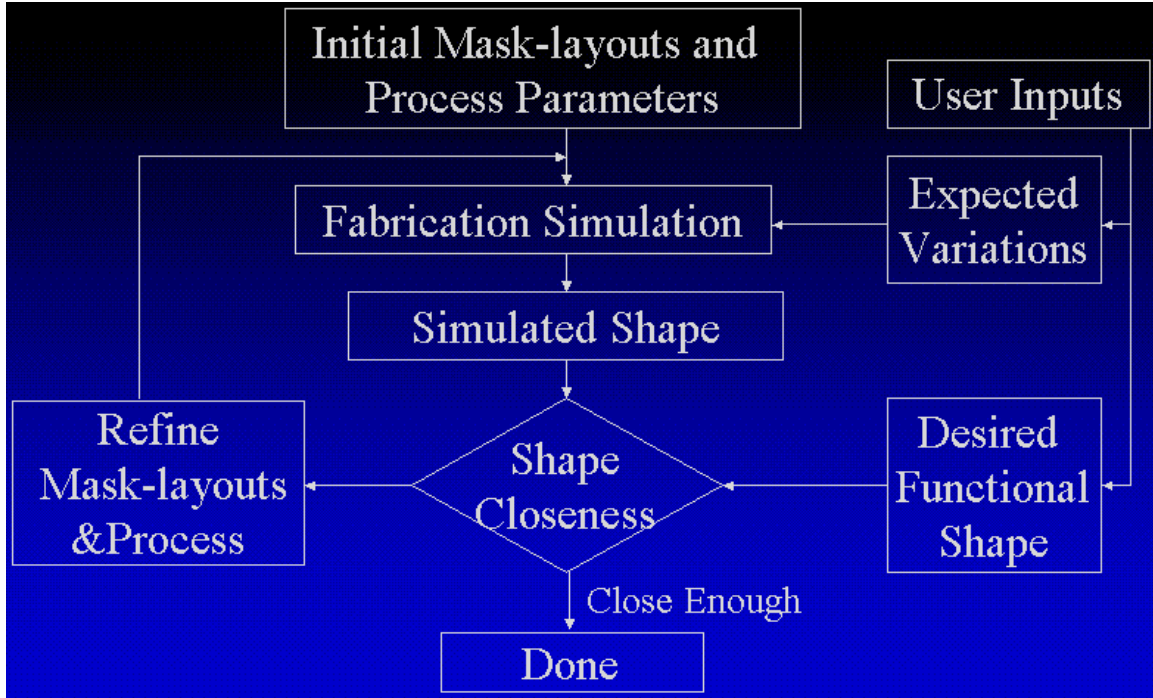


Figure 3.3: Algorithm for synthesis of mask-layouts to create desired shapes

This initial mask-layout synthesis work was extended to also synthesize the fabrication process. Caltech was able to include the duration of each of two dissimilar etchants into the stochastic optimization. With multiple etchants (processes), the universe of shapes that can be created by this process was greatly enlarged, and the corresponding importance of an automated method for synthesizing both mask-layout and fabrication process was demonstrated. Figure 3.4 shows an example case in which the desired 3-D shape is in the lower right corner. The best individual from the genetic algorithm population is shown in each frame, with the mask layout shown by a thin black line. After 46 generations, the best shape in the population is essentially identical to the desired shape. The rate of convergence, based on the 3 measures of shape closeness (shape, size and slope mismatch), as the algorithm proceeds, is shown in Figure 3.5.

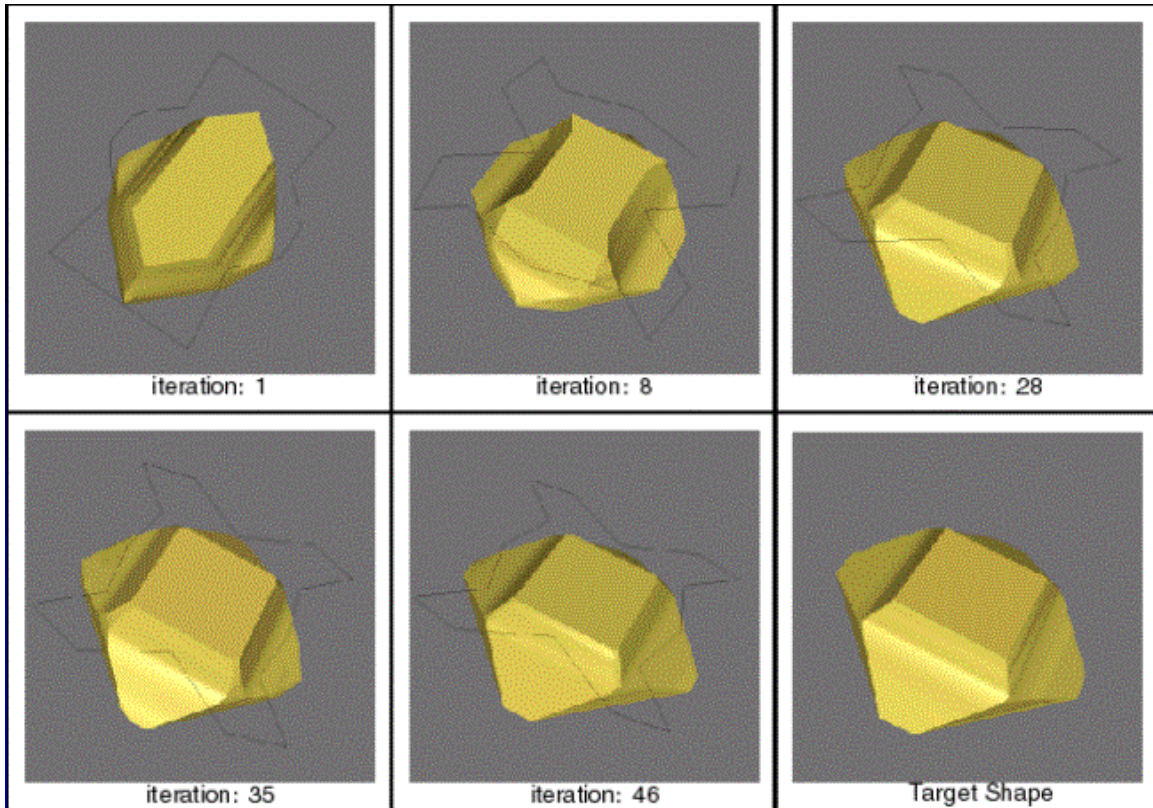


Figure 3.4: Example of mask-layout and fabrication process synthesis

Results and Discussions: Caltech expanded the capability of this approach to multiple etchants, and tested the method on increasingly challenging desired shapes, including two shapes directly of interest in microfluidics: intersecting channels (shown in Figure 3.2), and a Tesla valve (Figure 3.6). They also expanded the capability of the genetic algorithm to include a variable number of sides in the mask-layout polygons, through the creation of a variable gene-length genetic algorithm, which was integrated with the multi-process SEGS etch simulator. The procedure, which utilized a variable length genetic algorithm (to permit the synthesis of mask-layouts with variable geometric complexity), was demonstrated to produce a (compensated) mask-layout and process sequence to produce a desired 3-D shape.

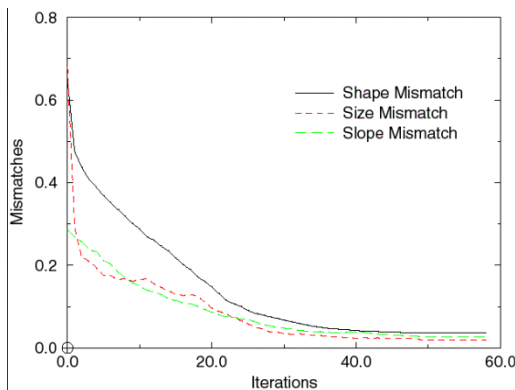


Figure 3.5: Evolution Convergence Profile



Figure 3.6: Tesla valve (Isotropic Etch)

The capability was later extended to include uncontrolled variations, and the genetic algorithm synthesis procedure produced mask-layouts that were robust (insensitive) to these variations. The initial uncontrolled variation that was demonstrated was ± 6 degrees of mask misalignment. Subsequently, robust synthesis of mask-layouts with other uncontrolled variations was also demonstrated (see Figure 3.7), including both global etch rate variations and etch rate model inaccuracy in particular directions. Using this approach, it has been shown that the genetic algorithm synthesis procedure produces mask-layouts that are robust (insensitive) to these variations (Figure 3.8).

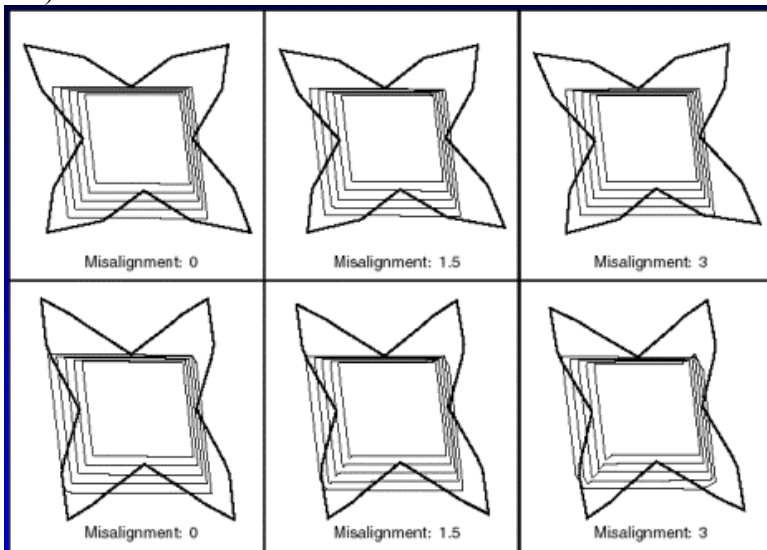


Figure 3.7: Robust mask-layout synthesis

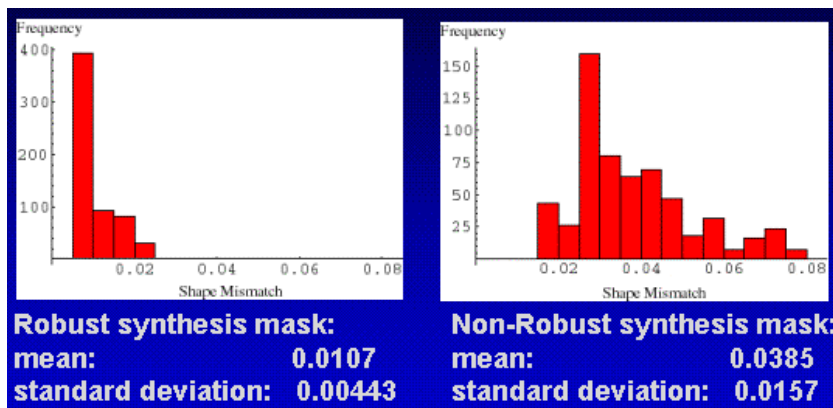


Figure 3.8: Robust mask-layout synthesis verification

Also to demonstrate the potential of the synthesis approach, other evaluation criteria were used in addition to shape matching, and the synthesis procedure was shown to produce mask-layouts and processes, which met the user-specified design requirements. For example, by utilizing the dimension of the mask-layouts as one of the evaluation criteria, mask-layouts with small dimensions (small areas) were synthesized. Using such mask-layouts can improve the device density on the wafer. Thus, the synthesis approach has been demonstrated on a set of complex 3-

D shapes. Also, mask-layouts that are robust to uncontrolled variations have been synthesized and tested.

4. BIOMOLECULAR REACTIONS SIMULATION MODULE

4.1 Software Overview

A new Biomolecular Reactions simulation module (henceforth referred to as the Biochem module) has been developed within the framework of the CFD-ACE+ multiphysics software suite. The model enables simulation of various kinds of biochemical reaction phenomena typically encountered during the development of biomicrofluidics devices and processes. The module enables process design for various kinds of biomolecular assays and other phenomena (e.g. selective adsorption) involving proteins, enzymes, DNA and antigen-antibodies.

The capability for simulating the following kinds of biochemical phenomena and processes was incorporated into CFD-ACE+:

1. **Surface-immobilized enzyme-catalyzed reactions**, useful for design studies on biosensors in which the interactions of biological elements (e.g.. enzymes) with transducers (electrochemical, optical, etc.) are converted to measurable signals;
2. **Cooperative protein-ligand volumetric reactions** (e.g.. hemoglobin-oxygen binding kinetics, useful for design of microfluidic blood-gas chemistry sensing devices);
3. **Biomolecular surface adsorption** (first-order and second-order kinetics; competitive and non-competitive binding; reversible and irreversible binding), encountered during DNA filtration, non-specific protein binding on biomaterial surfaces, derivatization of biosensor surfaces with biomolecule receptors, etc;
4. **Biomolecular receptor-ligand surface interactions** (first-order and second-order kinetics; non-competitive binding; cross-reactivity; reversible and irreversible binding) encountered during antigen-antibody binding in immunosensors, protein-ligand binding, DNA hybridization, etc.

The theoretical basis for the models, validation studies and sample model application test cases are presented in the following section. Applications of the Biochem module for solving practical biomicrofluidics problems of interest to the BioMEMs community are presented later in Section 9.

4.2 Surface-Immobilized Enzyme Kinetics

4.2.1 Theory

Enzymes are a class of proteins that act as biological catalysts for certain reactions and can bind itself to specific substrates to form a product. Numerical simulation capabilities have been developed for enzyme-catalyzed surface reactions within the framework of CFD-ACE+. The underlying theory and governing equations are illustrated by describing a sample test case, which involves modeling the conversion of the zymogen, factor X (FX) to the serine protease, factor Xa (FXa), in the presence of the tissue factor-factor VII catalytic complex (TF-FVIIa) in a parallel-plate flow channel.

Problem Description: The catalyst was assumed to be present in a layer of rat vascular smooth muscle cells along the lower surface of the flow channel. Figure 4.1 shows the schematic of the flow domain with channel dimensions. The simulation accounted for the convective-diffusive

transport of both FX and FXa. The enzymatic conversion of FX to FXa was modeled by simulating enzyme-catalysis along the lower wall.

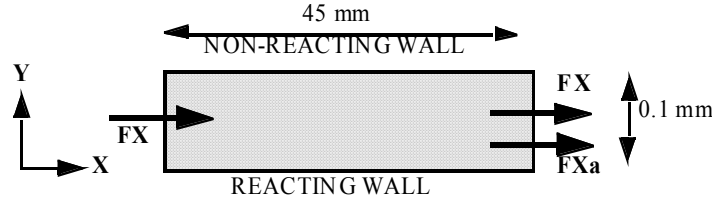


Figure 4.1. Schematic of flow domain for enzyme-catalyzed reaction problem

Governing Equations: Mass transfer occurs by both convective and diffusive transport. Therefore, the flow velocities needed to describe convective transport of the species were obtained by solving the Navier-Stokes equation shown in vector form in Equation 4.1. The mass fractions of the two species, FX and FXa, were computed by solving the conservation of mass equation within the flow domain (Equation 4.2).

$$\rho \vec{U} \cdot \nabla \vec{U} + \nabla P - \mu \nabla^2 \vec{U} = 0 \quad (4.1)$$

$$\vec{U} \nabla C - D \nabla^2 C = 0 \quad (4.2)$$

where ρ is the fluid density (taken as 1 g/cm^3), \vec{U} is the velocity vector, C represents the species concentration and D is the species diffusivity (taken as $5 \times 10^{-7} \text{ cm}^2/\text{s}$). The conversion ratio of FX to FXa in the enzymatic reaction stoichiometry was assumed as 1:1.

The flow boundary conditions for the problem include uniform inlet velocity, fixed exit pressure (taken as zero) and zero-slip conditions along the bounding walls. The mass transport boundary conditions include uniform inlet FX concentration ($C=C_0 = 100 \text{ nM}$) and zero flux condition at the non-reacting wall (Equation 4.3). Since there is a reaction along the lower plate where there is conversion of FX to FXa, the effect of this reaction on bulk flow mass transport was incorporated through appropriate source and sink terms for FXa and FX, respectively, at the boundary cells along the wall.

The enzymatic reaction was modeled based on the simplified Michaelis-Menten kinetics (Equation 4.4), which describes the formation of a single product from a single reactant through a single intermediate (Marshall, 1978). Equation 4.4 assumes that the enzyme concentration is small compared with the initial concentration of the substrate and the equilibrium concentration of the product and that the formation of the product is irreversible (valid during the initial part of the reaction before significant amount of product has formed). Most importantly, it is valid for the “steady-state” part of the reaction progress curve, when the concentration of the intermediate species is almost constant, which is valid for cases where the reactant is largely in excess of the enzyme.

$$D \frac{dC}{dy} = 0 \quad \text{at } y = y_{\max} \quad (4.3)$$

$$-D \frac{dC}{dy} = V_{\max} \left[\frac{C_w}{K_m + C_w} \right] \quad \text{at } y = 0 \quad (4.4)$$

where K_m is the Michaelis constant ($= 36 \text{ nM}$), V_{\max} is the maximum rate of FXa formation (in $\text{fmole}/\text{min}/\text{cm}^2$), C_w is the near wall concentration of FX and y_{\max} is the chamber height. All the model parameters used here were based on a previous study by Hall *et al.* (1998).

4.2.2 Model Validation and Parametric Study

Solution Procedure: A two-dimensional geometric model was created for the flow domain shown in Figure 4.1 using CFDRC's geometric modeling/mesh generation software, CFD-GEOM. A body-fitted structured grid was used to discretize the flow domain into approximately 4,000 computational cell volumes. The SIMPLEC algorithm (Van Doormal and Raithby 1984) in CFD-ACE+ along with the second order upwind-differencing scheme for spatial discretization was used to obtain the flow solutions. Flow was modeled as steady laminar incompressible, Newtonian flow. Simulations were carried out for various inlet flow conditions corresponding to physiologic wall shear rates ($10 - 1300 \text{ s}^{-1}$) encountered in the human vasculature. To study the influence of reaction kinetics on the biochemical process occurring in the flow system, different values of the reaction rate constant V_{\max} ($124 - 4000 \text{ fmole}/\text{min}/\text{cm}^2$) were used in the study. A grid sensitivity study was also done to ensure that numerical solutions were not influenced by the grid density.

Sample Simulation Result: Fully developed flow solutions corresponding to the different wall shear rates were obtained prior to solving for mass transport. Figure 4.2 shows the velocity vectors for a wall shear rate of 100 s^{-1} . Figure 4.3 shows the FXa concentration contours in the flow domain. (The figure has been scaled 150 times in the y direction).

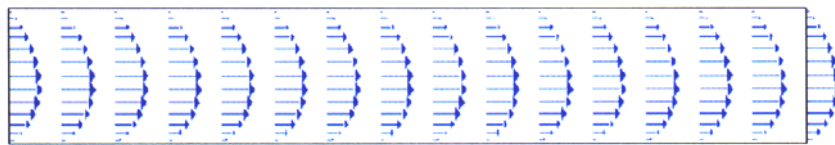


Figure 4.2: Velocity vectors in the flow domain

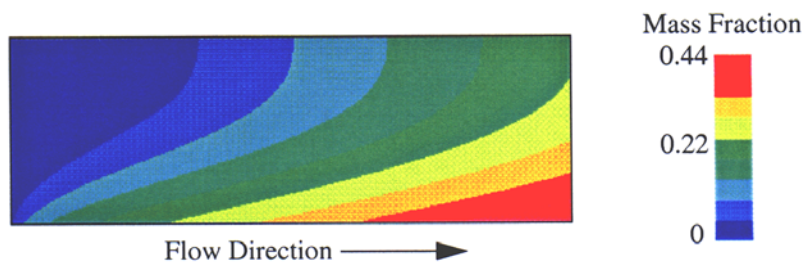


Figure 4.3: Mass fraction contours of FXa in the flow domain (figure scale = $150y$)

Model Validation: Table 4.1 shows a comparison of numerical predictions on the mean value of FXa outflux for different values of V_{max} and wall shear rates with corresponding experimental data from Hall *et al* (1998). The numerical fluxes predicted by CFD-ACE+ are in close agreement with the experimental data,

Effect of Flow Rate on FX Conversion: V_{max} was set constant at 4000 fmole/min/cm² and the wall shear rates (or rather flow rates) were varied from 10 to 1000 s⁻¹. Figure 4.4a shows the normalized mass fraction profiles of FX at the chamber midpoint (22.5 cm). At low flow rates, due to the increased residence time of FX in the channel, we see more conversion of FX to FXa, which results in lower FX concentration at the channel midpoint. At high flow rates, most of the FX in regions away from the reacting surface seems largely unaffected by the presence of the enzyme, and hence FX concentration is higher.

Effect of Reaction Rate on FX Conversion: Figure 4.4b shows the effect of surface reaction rate on the FX concentration at the chamber midpoint at a fixed value of wall shear rate (20 s⁻¹). As expected, the plots show a higher consumption, and hence lower concentration of FX near the reacting wall at higher reaction rates.

Table 4.1 Comparison of numerical and experimental data

V_{max} (fmole/min/cm ²)	Wall shear rate (s ⁻¹)	Numerical flux (fmole/min/cm ²)	Experimental mean flux (fmole/min/cm ²)
792	1280	532.5	593 ±32
200	80	138.9	138 ±33
124	20	85.5	95 ±20

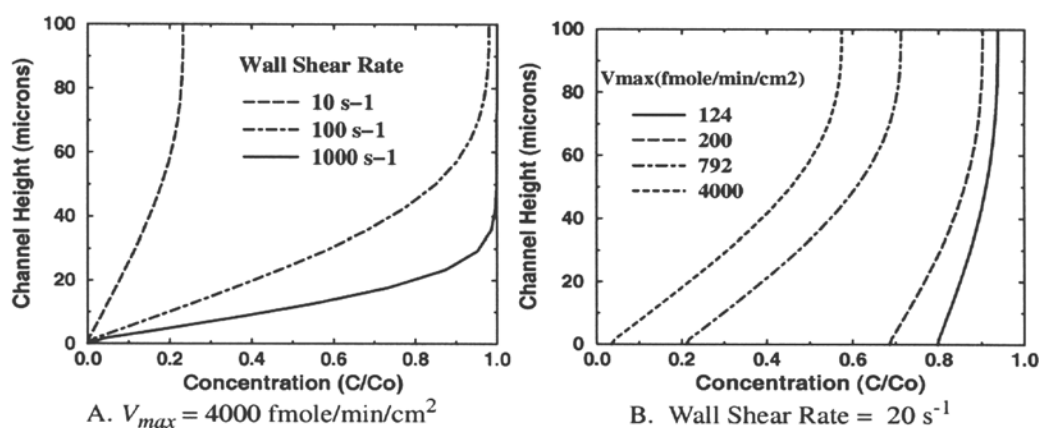


Figure 4.4: Normalized FX concentration versus channel height

4.3 Volumetric Protein-Ligand Cooperative Binding

4.3.1 Theory

The capability to simulate volumetric reactions between an allosteric protein and a ligand, for which the ligand binding is cooperative, was developed in CFD-ACE+. Cooperativity refers to

the facilitation of binding of subsequent ligand molecules after the first ligand has bound to the oligomer. The underlying theory and governing equations are outlined through a sample test case described below.

Problem Description: The sample problem describes the mixing of co-flowing streams of oxyhemoglobin (HbO₂) and deoxyhemoglobin (Hb) in a T-shaped microchannel (500 microns width). The simulation accounted for convection and diffusion of Hb, HbO₂ and oxygen in addition to the oxygen-hemoglobin reaction kinetics, which display cooperativity. The model described a facilitated diffusion system with association-dissociation reactions involving the three species.

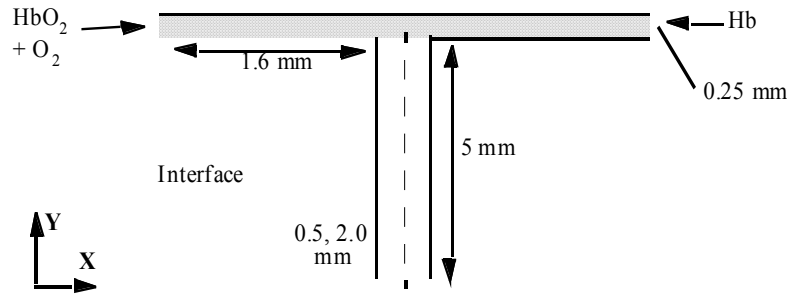


Figure 4.5: Schematic of the T-channel flow domain

Governing Equations: Time-varying mass fractions of the three species (HbO₂, Hb and O₂) at different locations in the flow domain were obtained by solving the conservation of mass equations given in Equations 4.5 – 4.7. N_i , and F_i , are the concentrations, and fluxes (convective + diffusive), of species “i”, respectively, and “t” refers to time. Γ is the reaction term, which describes the oxygen-hemoglobin binding kinetics. The binding of oxygen (ligand) to hemoglobin (allosteric protein) is cooperative. A hemoglobin molecule consists of four peptide chains, each with an incorporated heme group to which an oxygen molecule binds. Binding of an oxygen molecule results in a conformational change in the hemoglobin molecule, and affects its ability to further bind oxygen molecules. Oxygen-hemoglobin kinetics have been defined by either the complex four-step Adair reaction scheme, or by the simpler one-step approximation in which each hemoglobin molecule is replaced by four independent heme groups (Popel, 1989). The latter approach was used in the present study. The reaction mechanism term (Equation 4.8) was chosen such that it reduces to the Hill equilibrium model when the rate term is set to zero (Makhijani *et al.*, 1990).

$$\frac{\partial N_o}{\partial t} = -\nabla F_o - \Gamma \quad (4.5)$$

$$\frac{\partial N_{HO}}{\partial t} = -\nabla F_{HO} + \Gamma \quad (4.6)$$

$$\frac{\partial N_H}{\partial t} = -\nabla F_H - \Gamma \quad (4.7)$$

$$\Gamma = K \left[N_H \left(\frac{N_O}{N_{50}} \right)^n - N_{HO} \right] \quad (4.8)$$

N_{50} is the concentration of oxygen in equilibrium with hemoglobin at 50% fractional oxygen saturation, which can be expressed as $Bu * P_{50}$ where Bu is the Bunsen solubility coefficient of oxygen and P_{50} is the oxygen partial pressure at 50% fractional oxygen saturation. K is the dissociation rate constant for oxyhemoglobin and n is the dimensionless Hill coefficient.

4.3.2 Model Validation and Parametric Study

Solution Procedure: A two-dimensional geometric model was generated for the flow domain shown in Figure 4.5 using CFD-GEOM and discretized into approximately 2100 cells using a body-fitted structured grid. A zero-flux mass boundary condition and no-slip velocity condition was applied along all walls. A fixed exit pressure condition was used for the flow equations. Steady-state flow solutions were obtained using CFD-ACE+ using the same procedure described in Section 4.2.2.

Grid sensitivity studies were carried out to ensure that the model predictions were insensitive to grid density. Simulations were then done for the case in which the common branch of the T-channel had a width of 2 mm. Model validation was done through comparison of the results with published experimental data from Vay (1986). Finally, the model was used to analyze the effects of flow rate and reaction rate on the diffusional mixing of HbO_2 and Hb .

Model Validation: This simulation was done under no flow conditions. The following model parameters were chosen to enable comparison of simulation results with published experimental data (Vay, 1986): $P_{50} = 7.0$ Torr, $Bu = 1.45 \times 10^{-3}$ mM/ Torr, $n = 2.5$, $K = 39.49 \text{ s}^{-1}$, hemoglobin diffusivity = oxyhemoglobin diffusivity = $9.375 \times 10^{-7} \text{ cm}^2/\text{s}$, oxygen diffusivity = $1.51 \times 10^{-5} \text{ cm}^2/\text{s}$, total heme concentration = 7.21 mM. The initial condition chosen was 100% fractional oxygen saturation in the left-half of the flow domain ($N_H = 0$) and 0% on the right side ($N_{HO} = 0$). The corresponding initial equilibrium concentrations of O_2 in the domain were calculated from the Hill equation by setting $\Gamma = 0$ in Equation 4.8. The simulation was carried out for 420 seconds with a time step of 0.03 sec.

The transient variation predicted in the oxygen saturation (oxyhemoglobin/total hemoglobin concentration) 100 microns to the left of the channel midpoint shows close agreement with the experimental data (see Figure 4.6). The saturation at this location decreases with time as oxyhemoglobin diffuses to the right side of the channel and also dissociates to form unbound O_2 , which also diffuses to the right

Effect of O_2 -Hb Reactions on the Diffusive Mixing Process: The remaining simulations were done for a common channel width of 500 microns. The total duration of the transient simulations was 25 seconds with a time step of 0.005 sec. The effect of the oxygen-hemoglobin reaction terms on the diffusive mixing of oxygen in the T-channel was studied by performing simulations with and without the reaction terms. The convective terms were turned on in these simulations. The density and kinematic viscosity of the hemoglobin solution was taken as 1170 kg/m^3 and $2.99 \times 10^{-6} \text{ m}^2/\text{s}$, respectively.

Figure 4.7 shows oxygen concentration profiles (non-dimensionalized with respect to the total heme concentration) at end of 20 seconds in the domain. (The common channel has been scaled in the X-direction for clarity). In absence of an association reaction with hemoglobin (which essentially acts as a sink term), we see higher concentrations of unbound oxygen transported across the interface.

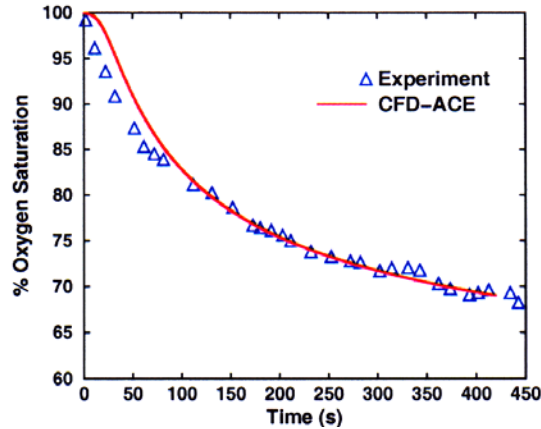


Figure 4.6: Transient variation in O₂ saturation at fixed location in common branch

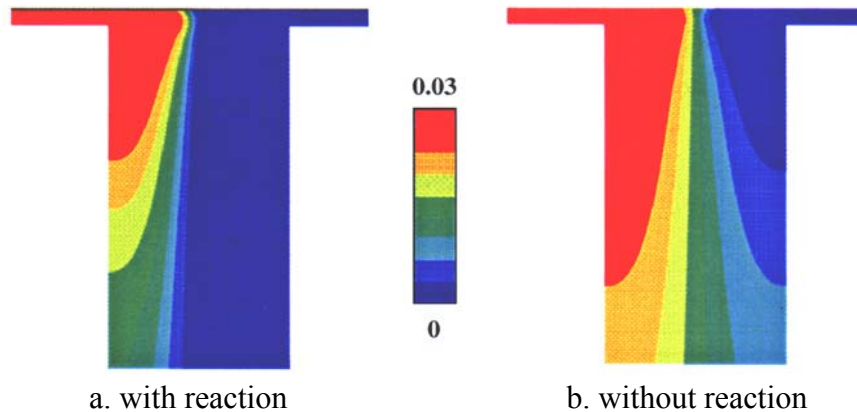


Figure 4.7: Non-dimensionalized concentration contours of unbound oxygen

Effect of Convection on the Diffusive Mixing Process. The effect of the convective terms on the diffusive mixing process was studied by performing simulations with, and without, the convective terms. Here, the initial conditions specified were 95% oxygen saturation on the left side and 5% saturation on the right side. The corresponding equilibrium values of HbO₂ and Hb were also used as the initial conditions. Non-dimensionalized concentration contours of free oxygen in the channel at $t=20$ seconds are shown in Figure 4.8. There is clearly more diffusive mixing of free oxygen on the left and right sides of the channel in the absence of convection.

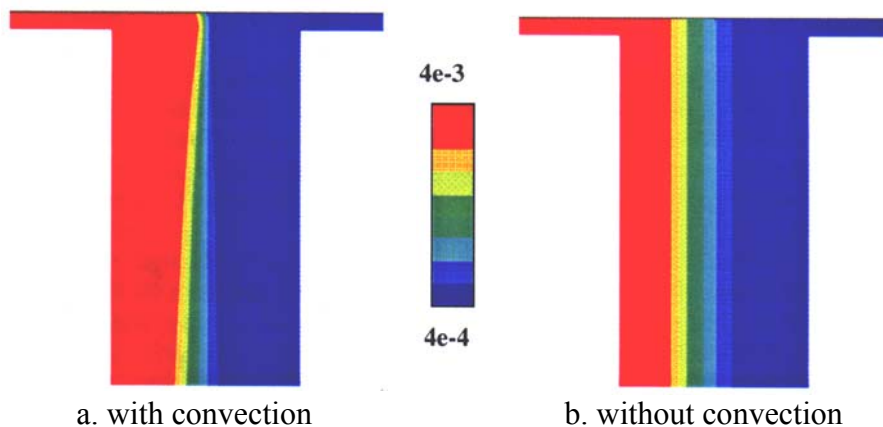


Figure 4.8: Non-dimensionalized concentration contours of unbound oxygen

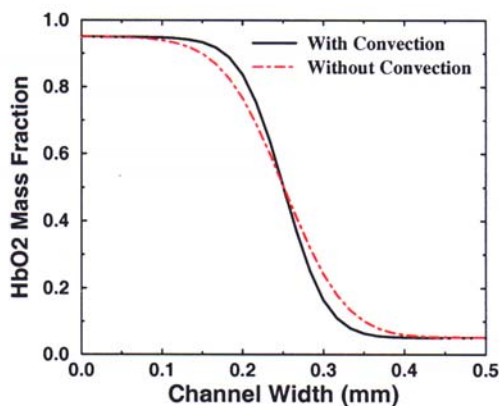


Figure 4.9: Spatial variation in HbO₂ concentration along channel width at the exit

Figure 4.9 shows the effect of convection on the spatial profile of HbO₂ along the channel width at the exit of the T-junction at $t=20$ seconds. HbO₂ concentrations are higher in the oxygenated (left) side of the T-junction and lower in the deoxygenated side. This indicates that the convective washout of HbO₂ from the flow channel decreases the residence time of this species in the channel, which results in a smaller amount of HbO₂ dissociation, and Hb and O₂ association, on the left, and right sides, respectively.

4.4 Biomolecular Surface Adsorption

Biomolecular surface adsorption is an important phenomenon that influences the performance of various kinds of biomicrofluidics devices. It describes the adsorption of biomolecules on to binding sites on a biomaterial surface either through physical or chemical adsorption. This phenomenon can be viewed as desirable, or undesirable, depending on the specific application of the biochip devices. The process of DNA filtration/purification, through adsorption on silica-coated surfaces, and the non-specific adsorption of proteins along the channel walls, leading to loss of sample, in a protein biochip, are two examples which illustrate the positive, and negative effects of surface adsorption, respectively.

4.4.1 Theory

We have developed the capability to simulate non-specific and specific, competitive and non-competitive, reversible and irreversible biomolecular surface adsorption based on the second-order binding kinetics. The reaction mechanism and the governing equations for surface binding model is as follows.



$$\frac{dC_B}{dt} = K^a C_w C_p - K^D C_B - K^r C_B \quad (4.9b)$$

where C_w is the “target” specie concentration at the wall, C_p is the “probe” concentration bound to the wall, C_B is the irreversibly bound complex (target + probe) concentration, and C_B^* is the irreversibly bound complex.

For multiple species and multiple (probes and targets) binding a more general, non-dimensional form has been implemented in CFD-ACE+.

$$\frac{d\theta_i}{dt} = K_i^a C_{iw} (1 - \theta - \phi) - K_i^d \theta_i - K_i^r \theta_i \quad (4.10)$$

where $\theta = \sum_i \theta_i$ and $\phi = \sum_i \phi_i$. This equation describes the reversible adsorption of multiple biomolecular species competing for the same binding sites on a biomaterial surface. Here, θ_i and ϕ_i = fraction of available binding covered by reversibly and irreversibly adsorbed biomolecule specie, “i”, respectively. C_i and C_{iw} = species concentration in bulk solution and near wall solution, respectively. K_i^a and K_i^d represent the adsorption and desorption rate constants, respectively. The surface reaction for irreversible adsorption is as follows:

$$\frac{d\phi_i}{dt} = K_i^r \theta_i \quad (4.11)$$

K_i^r is the rate constant for conversion of a reversibly adsorbed molecule to an irreversibly-bound state. Equations 4.10 and 4.11 together can be used to simulate the non-specific competitive binding of multiple protein species on to a biomaterial surface where, after a certain time-period, due to denaturation or some other phenomenon, the adsorbed molecules become unavailable for desorption and remain irreversibly bound to the surface. This model is applicable only for monolayer formation along the surface.

Various applications of the surface binding models outlined in section 4.4.1 are described in the following sections.

4.4.2 DNA Filtration Application

Problem Description: Here, the flow and surface reactions that describe the extraction of DNA from a sample flowing through a microfluidic DNA filtration chip (see Figure 4.10) were simulated using the first-order binding kinetics model in CFD-ACE+. The filtration chip consisted of inlet and outlet ports and an interior reaction/extraction chamber with multiple pillars. The top and bottom walls of the chamber as well as the pillars were made of a DNA binding material. The geometry of the device was similar to that of the Cepheid chip (Christel et al., 1998). The pillar diameters, however, were larger, and the number of pillars were also much lower than in the Cepheid chip. The resulting DNA binding surface area was 0.16 cm^2 as compared to 0.36 mm^2 in the Cepheid chip.

Method of Approach: Flow was modeled as steady, laminar, incompressible and Newtonian. The mass fractions of the DNA in different regions of the flow domain were computed by solving the conservation of mass equation for a passive scalar. The DNA diffusivity, D , was taken approximately equal to $10^{-7} \text{ cm}^2/\text{s}$, based upon molecular weight considerations for a DNA mixture with an average strand length of 500 base pairs, and the corresponding diffusivity for other macromolecules (e.g. hemoglobin) in water. Since the binding reaction results in DNA removal from the flow sample, the effect of this reaction on the bulk flow DNA transport was modeled by adding appropriate sink terms to the transport equation at the boundary cells along the reacting walls.

The flow boundary conditions for the problem include uniform inlet velocity, fixed exit pressure (taken as zero) and zero-slip conditions along the bounding walls. The mass transport boundary conditions include uniform inlet DNA concentration ($C=C_0 = 1000 \text{ ng/ml}$) and zero flux condition at the non-reacting side walls. On the DNA binding surface,

$$-D \frac{dC}{dn} = K_d C_w \quad \text{at binding surface} \quad (4.12)$$

where K_d is the binding rate constant, n describes the normal direction to the binding surfaces and C_w is the near wall DNA concentration.

Simulations were initially carried out to determine K_d through comparison of simulation results with DNA deposition data measured by Christel et al. (1998). Once $K_d (= 7 \times 10^{-5} \text{ cm/s})$ was obtained, parametric studies were carried out to study the effect of DNA flow rate and chamber geometry on the chip capture efficiency.

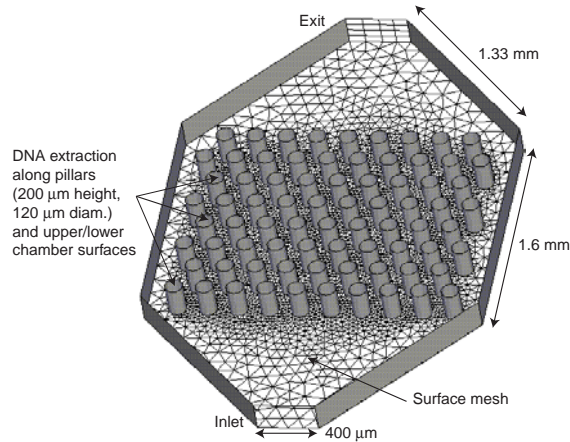


Figure 4.10: Geometric model of DNA extraction chip with unstructured surface mesh

Flow Patterns in the Extraction Chamber. Figure 4.11a shows the flow velocity contours along the mid-plane of the extraction chamber. The velocity vectors are shown in the vicinity of the pillars in Figure 4.11b. Results show a symmetric distribution of fluid velocities (and pressures) due to the system layout. Because the Reynolds number is very low, there is minimal recirculation around the pillars.

Effect of Chamber Geometry on Capture Efficiency: To demonstrate the enhancement of capture surface area due to the pillars, a simulation was carried out under the baseline flow conditions for the “flat chip” configuration in which the pillars were absent. The normalized DNA concentration contours along the lower surface of the chamber are shown in Figure 4.12b. The model predicts a lower capture efficiency of 0.84% for the flat chip configuration, which is consistent with its reduced capture surface area (0.12 cm^2 as compared to 0.16 cm^2). Similar results have been reported by Christel et al. (1998).

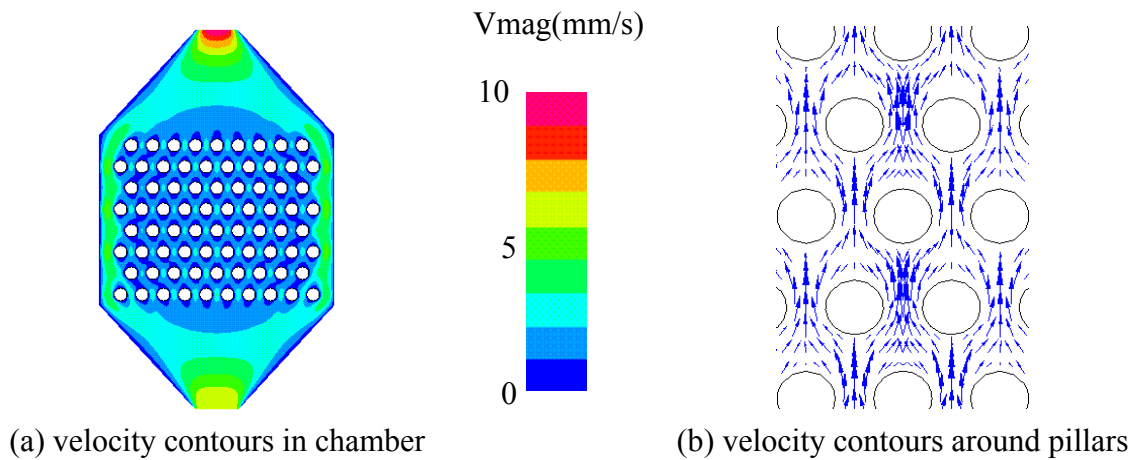


Figure 4.11: Flow patterns along the central plane in the DNA extraction chip

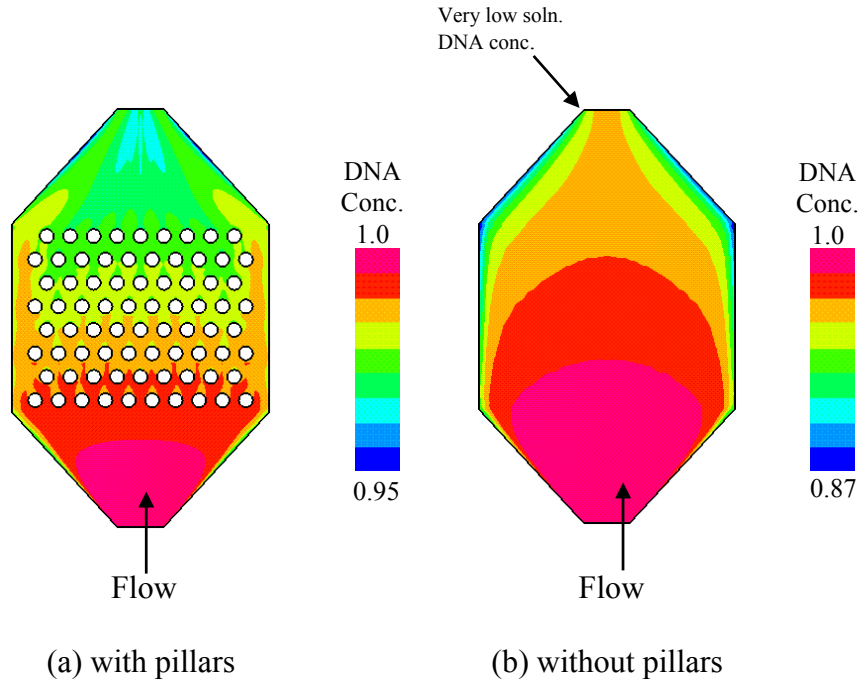


Figure 4.12: Normalized solution DNA concentration contours through the chip

Effect of Flow Rate on Capture Efficiency: Parametric studies were carried out to determine the effect of sample flow velocity on the DNA capture efficiency. Two different flow rates were used: 5 ml/s and 0.05 ml/s. The DNA concentration in the sample was maintained at 1000 ng/ml. The model predicted a decrease in DNA capture efficiency from 1.25% to 0.128% when the flow rate was increased. Christel et al. (1998) have similarly reported a decrease in capture efficiency from 10 to 5% when they increase their flow rate from 0.5 $\mu\text{l/s}$ to 5 $\mu\text{l/s}$ for a DNA concentration of 100 ng/ml. This can be attributed to the decreased residence time of the DNA strands in the extraction chamber due to increased convective transport, which reduces the potential for completion of the surface binding reaction. For the case with the decreased flow rate, as expected, the model predicted an increased capture efficiency of 11.2%. In the measurements reported by Christel et al, (1998), a decrease in DNA flow rate from 0.5 $\mu\text{l/s}$ to 0.1 $\mu\text{l/s}$ resulted in the same capture efficiency. The discrepancy between their experimental data and our simulation results could be attributed to factors such as differences in the chip geometry and the assumption of first-order binding kinetics.

4.4.3 Competitive Multi-Protein Adsorption

Problem Description: This sample problem describes the convective-diffusive transport of three proteins, Albumin (Alb), Immunoglobulin-g (Ig-g), and Fibrinogen (Fib) from the bulk solution (dilute plasma) to a biomaterial surface as well as competitive adsorption and displacement kinetics on the surface. The schematic of the problem is shown in Figure 4.13. Surface adsorption occurs in a very thin, microscopic “near wall” (boundary) layer. Transport of the biomolecules from the bulk solution to this near wall layer occurs purely due to diffusion. (Convective transport of analyte from the bulk solution to this boundary layer is not possible unless the binding surface is permeable to the sample). The model simulates sequential protein adsorption and desorption from the surface (Vroman effect). This process is important in

situations where blood comes in contact with biomaterials and results in formation of adsorbed layers, which control cellular events like thrombosis and infection.

Method of Approach: At the material surface, we assume second-order kinetics for surface adsorption and first-order kinetics for desorption (Equation 4.10), and conversion to irreversibly adsorbed state. The net (diffusive) flux of each protein species from the bulk solution towards the near wall layer equals the sum of the increase of reversibly and irreversible adsorbed protein, as shown in Equation 4.13.

$$-D_i \frac{\partial C_i}{\partial y} = K_i^a C_{iw} P_s (1 - \theta - \phi) - K_i^d P_s \theta_i \quad (4.13)$$

where P_s = maximum surface protein concentration in the monolayer.

The transient Navier Stokes equation (4.14) was solved along with the transient mass conservation equations for all 3 protein species in the bulk flow (Equation 4.15).

$$\rho \frac{\partial \vec{U}}{\partial t} + \rho \vec{U} \cdot \nabla \vec{U} + \nabla P - \mu \nabla^2 \vec{U} = 0 \quad (4.14)$$

where ρ = solution density, \vec{U} = velocity vector, and P = pressure.

$$\frac{\partial C_i}{\partial t} + \vec{U} \cdot \nabla C_i - D_i \nabla^2 C_i = 0 \quad (4.15)$$

where t = time and D_i = species diffusivity. Zero mass flux boundary conditions were prescribed along all non-binding surfaces. Equation 4.13 was used as the mass flux boundary condition along the binding surface. The input parameters used in the problem are as follows:

- Adsorption rate constants ($\text{cm}^3 \text{g}^{-1} \text{s}^{-1}$): $K_{\text{Alb.}}^a = 0.005$, $K_{\text{Ig.}}^a = 0.03$, $K_{\text{Fib.}}^a = 0.8$
- Rate constants for desorption (s^{-1}): $K_{\text{Alb.}}^d = 0.1$, $K_{\text{Ig.}}^d = 0.05$, $K_{\text{Fib.}}^d = 9 \times 10^{-5}$
- Irreversible rate constants (s^{-1}): $K_{\text{Alb.}}^r = 3 \times 10^{-5}$, $K_{\text{Ig.}}^r = K_{\text{Fib.}}^r = 5 \times 10^{-5}$
- Diffusivity of proteins (cm^2/s): $D_{\text{Alb.}} = 8.5 \times 10^{-7}$, $D_{\text{Ig.}} = 4 \times 10^{-7}$, $D_{\text{Fib.}} = 2 \times 10^{-7}$
- Initial protein conc. in bulk solution (g/cm^3): $C_{\text{Alb.}} = 60$, $C_{\text{Ig.}} = 15$, $C_{\text{Fib.}} = 3$
- Maximum possible surface protein concentration (g/cm^2): $P_s = 0.18$
- Inlet velocity (mm/s): $V_{\text{in}} = 10$

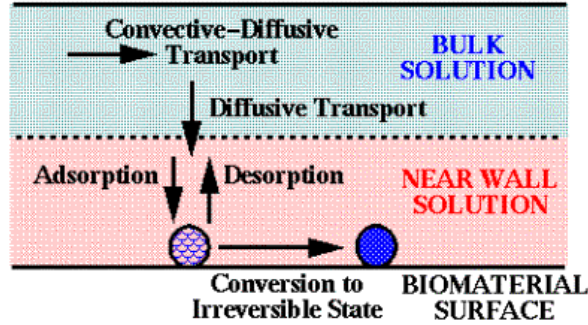


Figure 4.13: Schematic of processes occurring during protein adsorption

Model Validation: CFD-ACE+ simulation results for a case without irreversible adsorption and convection using above parameters are compared with published simulation results from Lu et al. (1994) in Figure 4.14a. Model predictions on time-varying surface concentrations for all 3 proteins shows good match with the published values. As expected, the protein with highest diffusivity, albumin, gets adsorbed first followed by immunoglobulin and fibrinogen. The desorption process starts almost immediately with albumin desorbing at a higher rate than the other proteins.

Simulations were also performed for a case with both reversible and irreversible adsorption in the absence of convection. Here, the initial protein concentrations were reduced by a factor of 2, and adsorption constants were reduced by a factor of 10. As seen in Figure 4.14b, once again the results compared well with corresponding results from Lu et al. (1994).

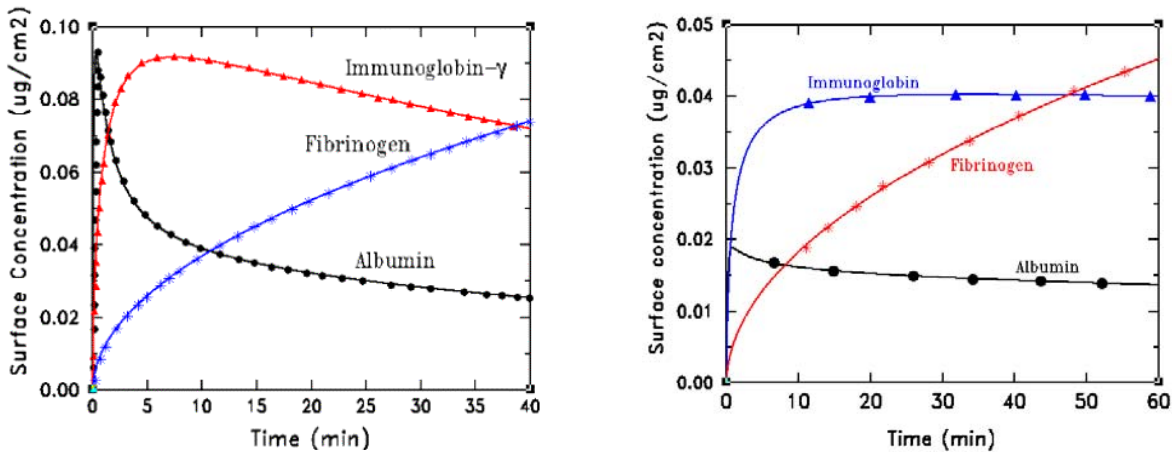


Figure 4.14: Comparison of ACE+ (solid lines) and published (symbols) theoretical results on competitive multi-protein adsorption

Site-Specific Surface Adsorption in the Presence of Flow: The simulations shown in Figure 4.14a were repeated in the presence of flow. The flow domain schematic is shown in Figure 4.15a. Here, surface adsorption occurs in only a portion of the flow channel. Figure 4.15b compares time-varying (spatially-averaged) protein surface concentrations in the presence and absence of flow. Flow provides a continuous supply of proteins in the regions above the adsorption surface, and replenishes the amount of protein removed from the bulk solution due to

surface adsorption. The net effect of convection is to slightly increase the rate of cumulative surface deposition of protein within the time period of this simulation. The effects on the individual protein surface concentrations, however, are much more pronounced even at this very small flow rate ($10 \mu\text{m/s}$).

The multi-protein adsorption capabilities were extended for 3-D analysis along irregular surfaces. This capability was demonstrated for an on-chip bioassay system based upon the microbead array technology, which enables implementation of different types of binding assays in a parallel format. In this system, a cluster of beads ($5 \mu\text{m}$ diameter) chemically encoded for different types of binding assays is arranged in a tightly-packed configuration within a cubical microfluidic chamber (see Figure 4.16). When the sample containing the analytes flows through the chamber, biochemical reactions occur on the bead surfaces. Once the sample has passed through the chamber, the reaction products on the beads can be post-processed for simultaneous detection of the various analytes in a parallel manner. Sample results from this study, in which the input parameters and flow rate were the same as in Figure 4.15, are shown in Figure 4.17.

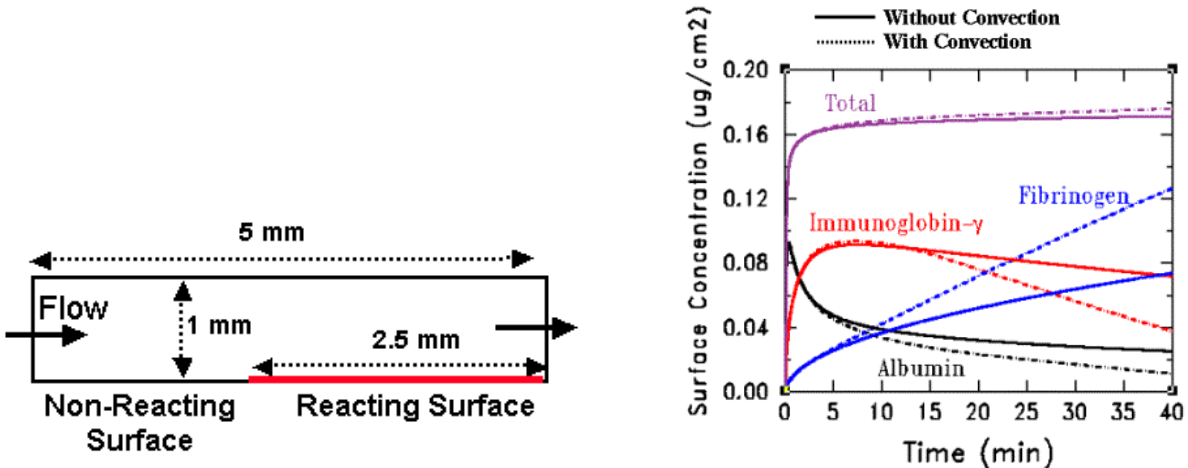


Figure 4.15: Effect of flow on multiprotein adsorption in a 2-D flow channel

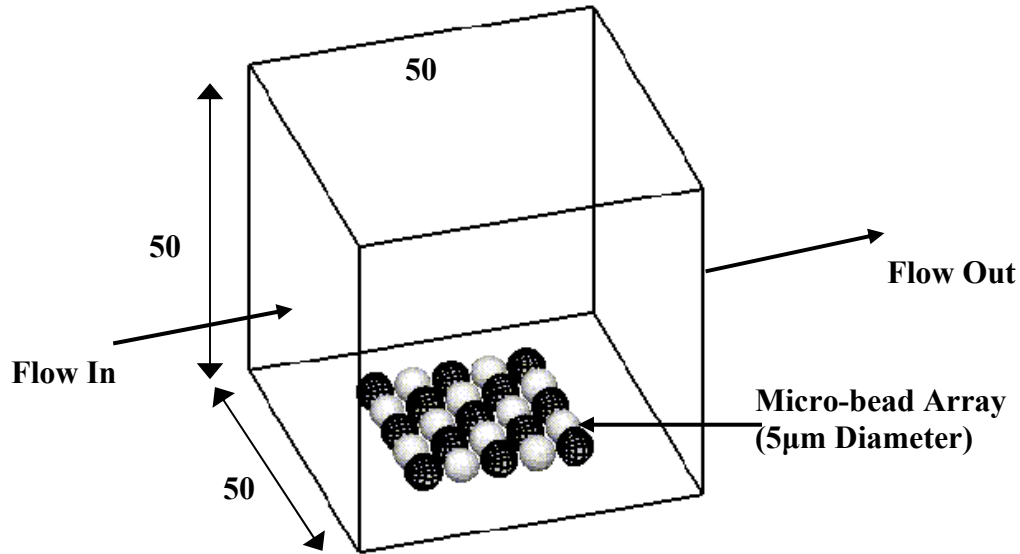


Figure 4.16 Schematic of flow over a microbead assay (dimensions in microns)

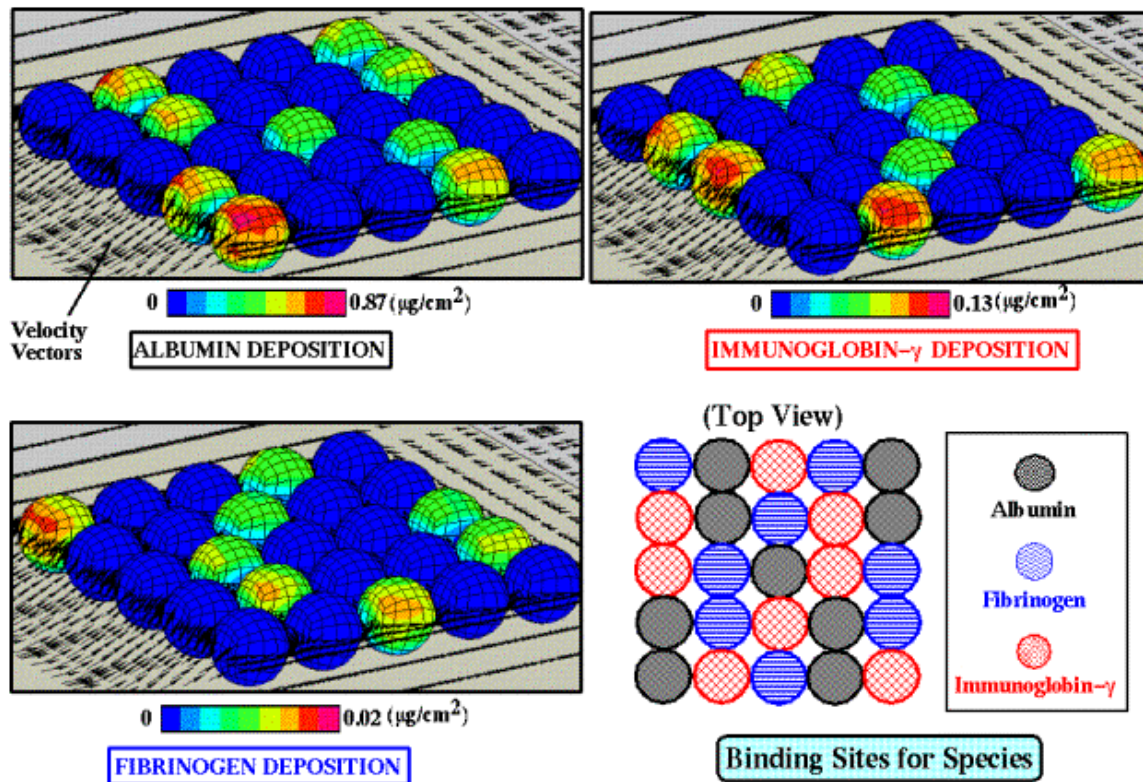


Figure 4.17: Site-specific protein binding on a microbead array in the presence of flow

Competitive Multi-Protein Adsorption on a Microbead Array: The phenomenon of competitive non-specific surface binding of the 3 protein species on a micro-bead array was simulated in this study. Both reversible and irreversible surface binding were considered. The

computational domain was the same as in Figure 4.16. Flow provided a continuous supply of proteins in the regions adjacent to the spheres.

Figure 4.18 shows the time-varying (spatially-averaged) protein surface concentrations for all three proteins. Albumin, which has a high diffusivity, is adsorbed along the spherical surfaces at a much faster rate than the other two proteins as indicated by its higher concentration levels. Fibrinogen, which has the lowest diffusivity, just begins to get deposited along the bead surfaces resulting in low surface concentration levels. The figure also shows the surface concentration contours at time = 140s for all three proteins. Albumin shows the highest deposition followed by Immunoglobulin- γ . Only trace amounts of Fibrinogen are seen on the bead surfaces at this time instant. We see greater deposition of protein along the beads upstream because of higher availability and continuous supply of protein due to convection.

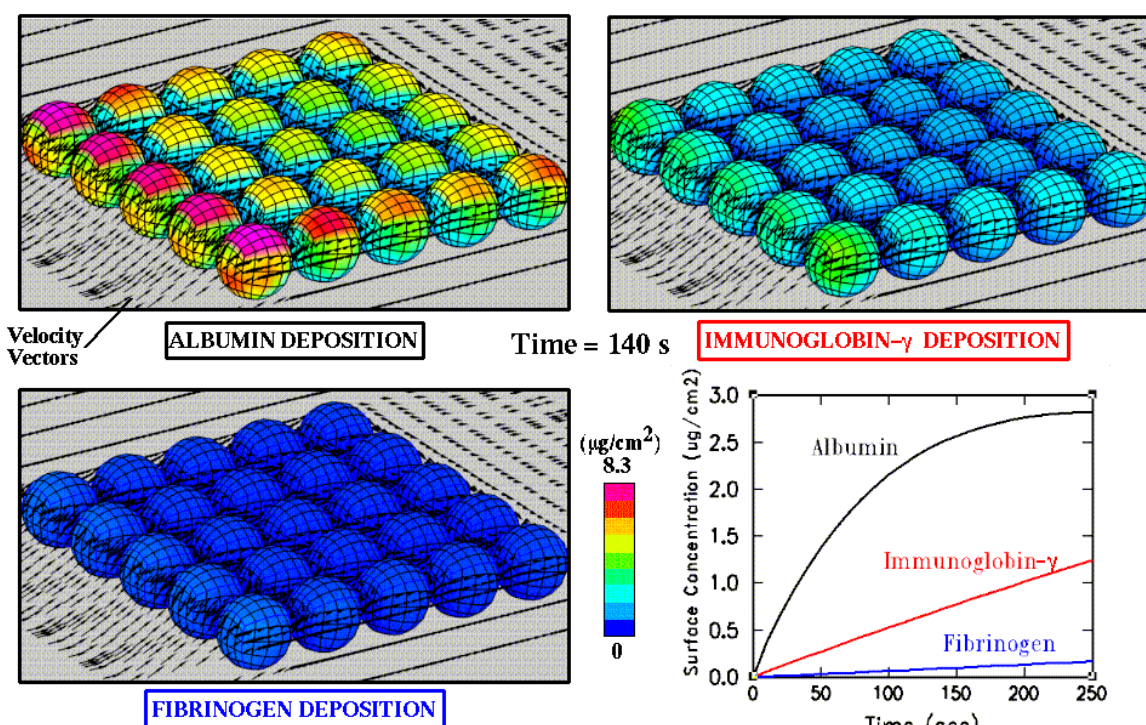


Figure 4.18: Competitive multi-protein binding on a microfluidic bead array

4.4.4 Receptor Immobilization in Microfluidic SPR Biosensor

Problem Description: The protein adsorption model was applied for:

- Studing the non-competitive adsorption of Neutravidin on the gold sensor in the microfluidic flow cell of SPREETA, a Surface Plasmon Resonance Biosensor;
- Extracting intrinsic binding kinetics for Neutravidin adsorption on gold; and
- Using extracted kinetics parameters to validate the biomolecular adsorption model in CFD-ACE+.

SPREETA Biosensor: The SPREETA evaluation module manufactured by Texas Instruments was added to the CFDRC Bio-fluids laboratory. The Spreeta is a SPR-based biosensor. Near-infrared light (840 nm) from a light emitting diode (LED) is polarized to enhance surface

plasmon resonance. The sensor is a finely gold coated surface. Spreeta is also equipped with a flow cell which can help in flowing different analytes (buffers, proteins, RNA, DNA) or even cells. The TI-SPREETA system is shown in Figure 4.19 along with a schematic of the flow cell.

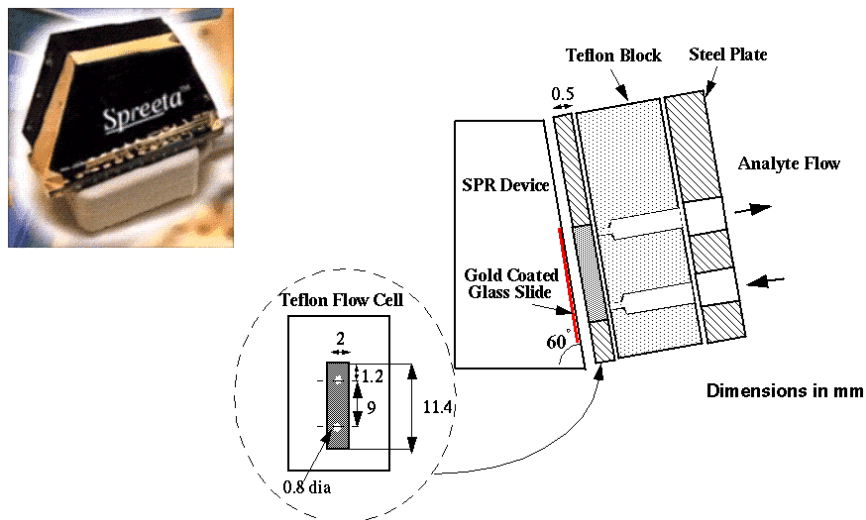


Figure 4.19: The TI-SPREETA Biosensor System

The sample containing the analyte passes through orifices in a steel plate and a Teflon block before entering the Teflon flow cell through a circular inlet port. The bottom surface of the Teflon flow cell is a gold-coated glass slide on which the receptor molecules are attached. When this surface is exposed to the sample, the analyte molecules bind to the sensor's surface via their specific interaction with the binding molecules. The binding event is detected by the SPR device. The instrument needs calibration before it can be used for biomolecular binding detection. A plot of the change in signal vs. pixel # is shown in Figure 4.20. After a couple of random fluctuations, the signal stabilizes. SPREETA comes with a software package for analyzing the data acquired by the change in refractive index. The biosensor has been shown to be effective in determining the association and dissociation rate parameters of different substrates.

Experimental Protocol: The sensor was initialized in air followed by phosphate buffer saline (PBS) at a flow rate of 300 $\mu\text{l}/\text{min}$. Once a stable baseline refractive index was established, neutravidin at a concentration of 5 $\mu\text{g}/\text{ml}$ was introduced into the system. Following adsorption of neutravidin onto the gold surface, which lead to a stable refractive index, PBS buffer was introduced to wash off unbound neutravidin. The experiment was then repeated at higher neutravidin concentrations of 20 and 40 $\mu\text{g}/\text{ml}$.

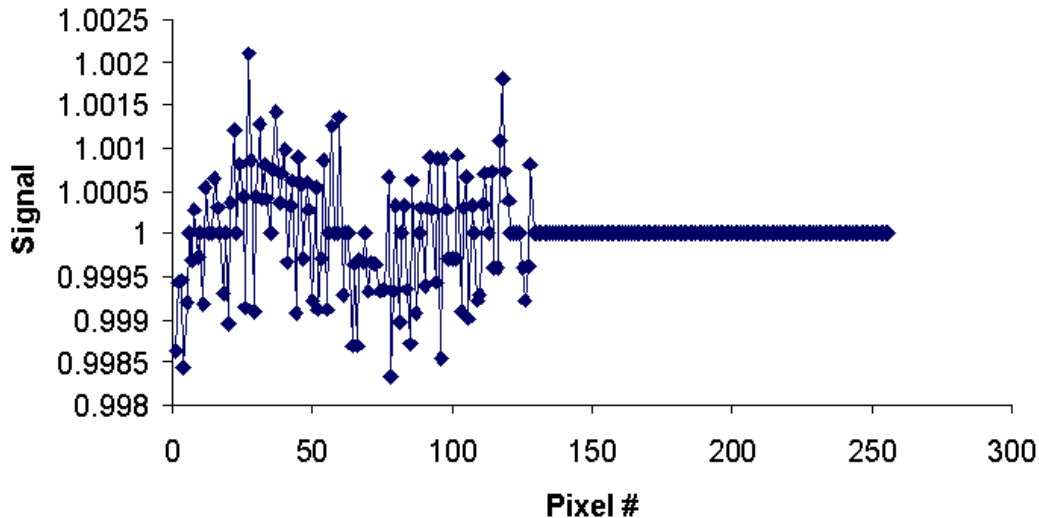


Figure 4.20. Biosensor calibration data

Simulation Procedure: A 3-D geometric model of the TI-SPR flow cell described in Figure 4.19 was developed using CFDRC's geometric modeling and mesh generation software, CFD-GEOM. The model included a portion of the inflow and outflow orifices in the Teflon block. The flow domain was discretized into approximately 17,700 computational cell volumes with the help of a 3-D body-fitted mesh. CFD-ACE+ was used to solve the governing flow, mass transport and second-order adsorption kinetics equations. Flow was modeled as laminar, incompressible, Newtonian. The diffusion constant of avidin was set to $4\text{E-}11 \text{ m}^2/\text{s}$.

The SIMPLEC algorithm in CFD-ACE+ along with a second order differencing scheme for spatial discretization were used to first obtain flow solutions at discrete time intervals of 5 seconds. The flow boundary conditions included uniform inlet mass flow rate, fixed exit pressure (taken as zero) and zero-slip conditions along the bounding walls. Zero-flux mass transport boundary conditions were prescribed on all non-binding walls. Along the gold surface, the diffusive flux of the protein was set equal to the net rate of surface adsorption (Equation 4.13). The initial conditions for flow calculations were the steady-state analyte flow field. For mass transport equations, the initial condition were chosen as zero concentrations to mimic the transient filling of neutravidin in the flow cell.

The flow solutions were then used as an input to solve the transient mass transport and surface reaction equations at each time step. The surface adsorption equations were solved in each of surface cells along the reacting surfaces. The flow rate was maintained the same as that in the experiments ($300 \mu\text{l}/\text{min}$). The binding occurred in a small central patch $4\text{mm} \times 0.05 \text{ mm}$. The flow velocity vectors, flow traces and the binding area of the TI-SPREETA are shown in Figures 4.21 and 4.22.

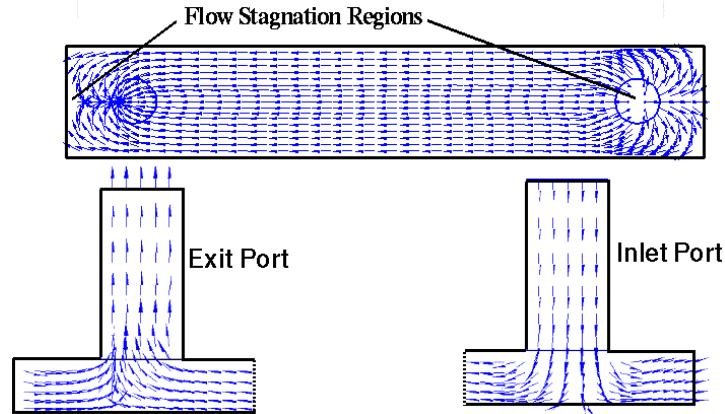


Figure 4.21: Flow velocity vectors in the SPREETA flow cell

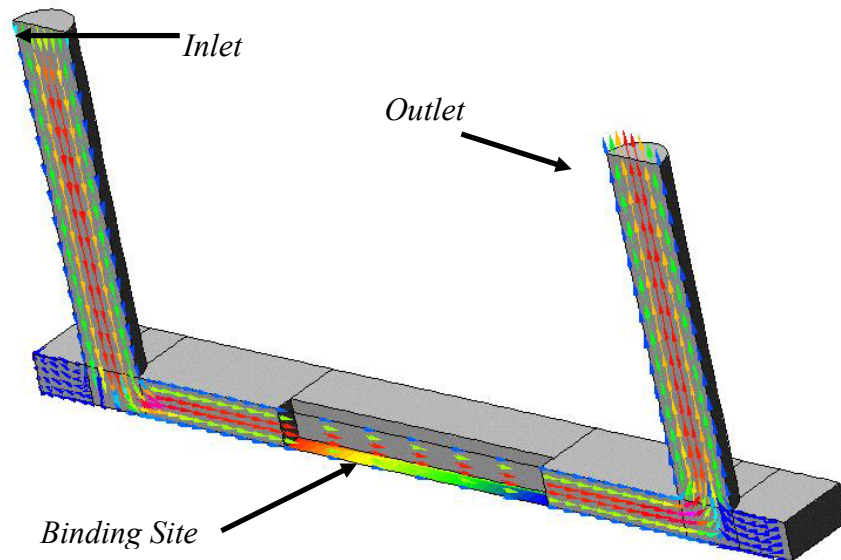


Figure 4.22. Computational grid, flow field and binding site location in SPREETA

Extraction of Binding Kinetics Parameters: Following the gathering of experimental data, ACE+ simulations were performed to extract the binding kinetics parameters from the data. The idea was to obtain *the kinetic constants that describes the data satisfactorily*. Inspection of experimental data. reveals that saturation binding levels (independent of inlet concentration of 40 $\mu\text{g/ml}$) is reached at the two higher concentration levels used in the present set of experiments. Assuming Langmuir Type I adsorption behavior, the coincidence of binding saturation levels leads to the conclusion that desorption is insignificant at these concentrations i.e. the binding response at the highest concentration is influenced mainly by the adsorption rate. Therefore, several values of K_a and peak surface density, P_{max} , were utilized in the simulations until the predicted binding curve agreed well with the biosensor data at 40 $\mu\text{g/ml}$. From the fitted curve, *the adsorption constant K_a was found to be $5.31E+06 \text{ M}^{-1}\text{s}^{-1}$* , and *the maximum surface concentration was found to be $6.4E-12 \text{ moles/m}^2$* .

Model Validation: The extracted binding kinetics data was then used in subsequent simulations (5 and 20 $\mu\text{g/ml}$ inlet concentrations) to test the validity of the surface adsorption model. As shown in the figure 4.23, simulation results agree quite well with corresponding experimental surface binding data.

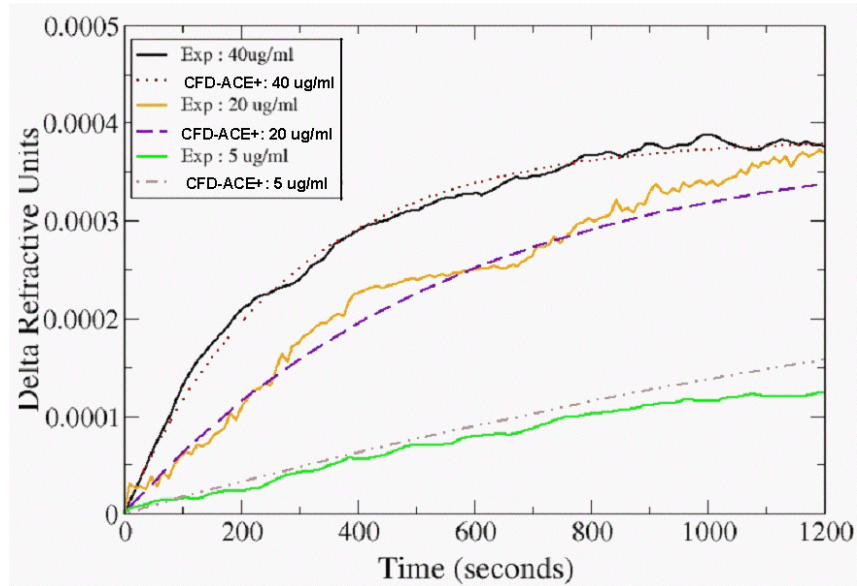


Figure 4.23: Neutravidin-Gold surface binding in SPREETA Biosensor Flow Cell

4.5 Biomolecular Receptor-Ligand Surface Binding

4.5.1 Theory

The second-order kinetics model presented earlier in Section 4.4.1 can be also used to describe receptor-ligand surface interactions for cases where 1 mole of the receptor binds to 1 mole of the ligand. Here, θ represents the fraction of the derivatized receptor molecules that have already bound to the ligand, and P_s represents the receptor surface concentration (in molar units). This simulation capabilities for ligand-receptor binding kinetics can be applied for design and analysis of the following types of binding assays: direct binding, competitive binding and displacement. Displacement assays are essentially a form of competitive binding in which the competition is not between two or more different species, but rather between labeled and unlabelled molecules of the same species.

4.5.2 Receptor-Ligand Binding in a Microfluidic Biosensor

Problem Description: The receptor-ligand surface interaction model was applied for analyzing the effect of mass transport on the surface binding kinetics of an analyte (Beta Galactosidase Antigen in Phosphate Buffered Saline, PBS) to a receptor (Neutravidin derivatized onto a gold surface) in the TI-Spreeta system. Here, the receptor was assumed to be already derivatized on the sensor surface.

Method of Approach: The following model parameters were used in the analysis:

- Association rate constant ($\text{M}^{-1} \text{s}^{-1}$): $K^a = 10^5$
- Rate constant for dissociation (s^{-1}): $K^d = 0.001$
- Initial analyte concentration in bulk solution (ppm): $C_o = 5$

- Maximum possible surface analyte concentration ($\mu\text{g}/\text{cm}^2$): $P_s = 0.2$
- Inlet flow rate for TI-SPR system ($\mu\text{L}/\text{min}$) = 50, 300, 600

PBS was assumed to have the same density and viscosity of water, and therefore:

- Density of sample (kg/m^3): = 1000
- Viscosity of sample (m^2/s): = 0.86×10^{-6}

The molecular weight of the analyte is 115,000. By assuming the molecules are spherical and that volume of the sphere is proportional to the molecular weight, the diffusion coefficient is inversely related to $1/3$ power of the species' molecular weight (inversely proportional to the radius by the Stokes-Einstein equation, Bird et al., 1960). Based on this assumption and published diffusivity data on the zymogen Factor X ($5 \times 10^{-7} \text{ cm}^2/\text{s}$, molecular weight = 59,000), we estimate the analyte diffusivity to be $D = 4 \times 10^{-7} \text{ cm}^2/\text{s}$.

The method of approach for the simulations with flow turned on was similar to that described in the previous section for neutravidin adsorption. Simulations were also performed for the no-flow cases in which analyte transport was purely diffusion-driven.

Well-Mixed Binding Model: Equation 4.10 is often simplified for the non-competitive binding case by reducing it to a first order reaction in which the near wall analyte concentration, C_w , is assumed constant. In this simplified form, it can be solved to obtain an exact analytical expression for the relative amount of bound analyte as a function of time. Results for the simplified model were compared with corresponding results from the detailed model to assess the validity of the assumption of constant near wall analyte concentration.

Effect of Flow Rate on Biomolecular Binding: The effect of flow rate on the simulated surface binding process is shown in Figure 4.24. A comparison of results from the detailed high-fidelity simulation with corresponding results based on the simplified well-mixed model is also shown. The plot shows that during the initial stages of the surface binding process, when the binding kinetics proceed rapidly, there are significant differences in surface concentrations of the bound analyte predicted based upon the simplified and CFD solutions. After about 20 minutes (0.33 hours), the concentration of bound analyte becomes more or less constant. At this stage, the analytical results agrees well with the simulation results. The model also indicates appreciable differences during the initial part of the binding process between the no-flow, 50 and 300 $\mu\text{L}/\text{min}$ cases, although as the flow rate increases, the difference becomes less and less. This indicates that beyond a certain flow rate, the binding phenomenon isn't mass transport-limited any more. The 300 and 600 $\mu\text{L}/\text{min}$ cases show very little difference.

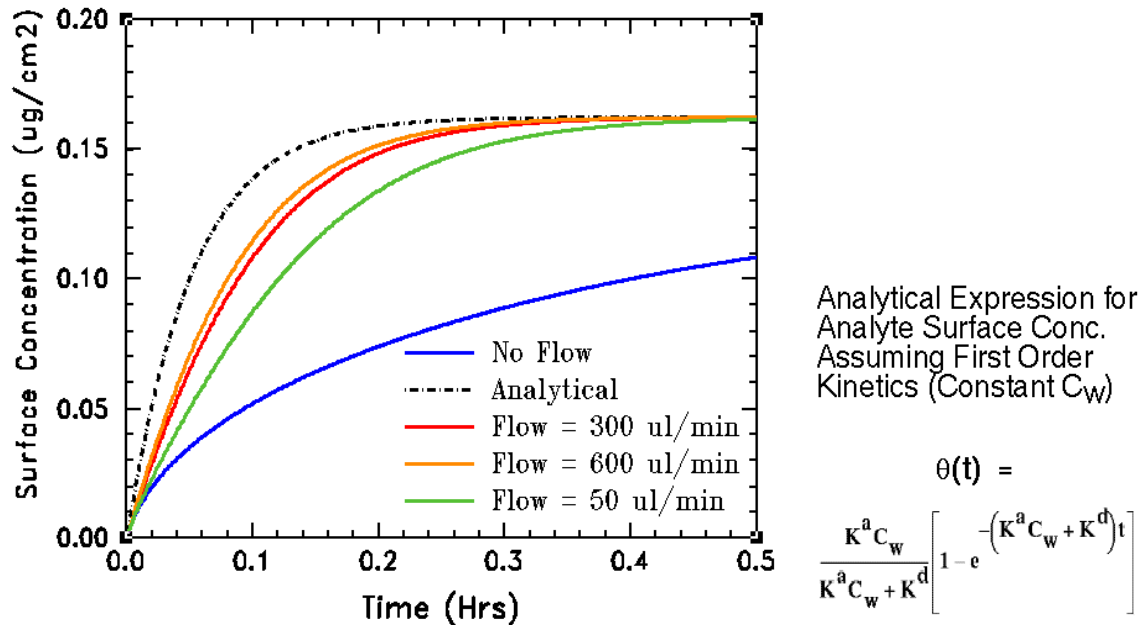


Figure 4.24: Effect of flow rate on surface binding in the SPREETA System

Effect of Receptor Surface Density on Surface Binding: Parametric studies were performed to analyze the effect of surface receptor density on the binding process. Two values of P_s , that were either two orders of magnitude lower or higher than the baseline value of $0.2 \mu\text{g}/\text{cm}^2$, were used. These correspond to cases where the surface density of immobilized receptors in the biosensor is either much lower, or much higher, than the baseline case respectively. The no-flow and flow simulations for the TI system were repeated with these values of P_s . The surface concentration of bound analyte, normalized with respect to P_s , for each case is shown in Figure 4.25.

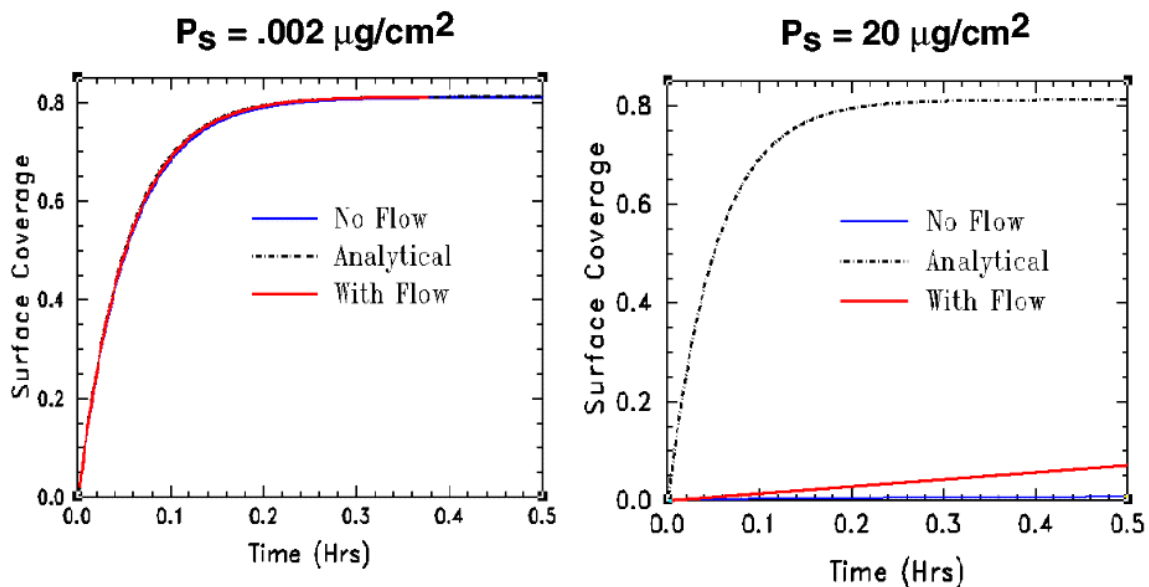


Figure 4.25: Effect of receptor surface density on surface binding in the SPREETA

For the case with a very low $P_s = 0.002 \text{ mg/cm}^2$, there is very little difference between the analytical solution, based on the assumption of constant near-wall analyte concentration, and the flow and no flow cases. Here, although the reaction rate is the same as in the baseline case, the mass of analyte removed from the sample per unit time during the course of the entire binding reaction is much lower than before. Therefore very little replenishment of the analyte near the reaction surface is necessary to complete the binding reaction. Hence, the results are quite similar for the flow and no-flow cases.

Conversely, when the P_s value used is $20 \text{ }\mu\text{g/cm}^2$, the analyte mass removed from the sample per unit time becomes significantly higher than in the baseline case. Due to the rapid depletion of analyte from the near-wall layer, the replenishment of analyte is insufficient even in the presence of flow with the current analyte flow rate. This tends to slow down the reaction significantly in comparison with the case where an infinite supply of analyte is assumed to be available for the binding (the analytical case). As expected, the no-flow case makes the situation even worse.

Effect of Association Rate Constant on Surface Binding: The effect of an increase in the association rate constant from $10^5 \text{ M}^{-1} \text{ s}^{-1}$ to $10^6 \text{ M}^{-1} \text{ s}^{-1}$ on the surface reaction was studied. This represents a case where receptors with a higher affinity to the analyte are used in the biosensor. Figure 4.26 shows the transient surface concentration profiles for the two cases studied. The simulation with a higher association constant predicted higher analyte deposition in shorter periods of time for both the flow and no flow cases. As expected, the equilibrium surface concentration of analyte, which is governed by the ratio of K^a/K^d , was also higher for this case. These results indicate a strong influence of the rate constant on the entire surface binding process and highlights the need to accurately determine these constants for use in experimental analyses.

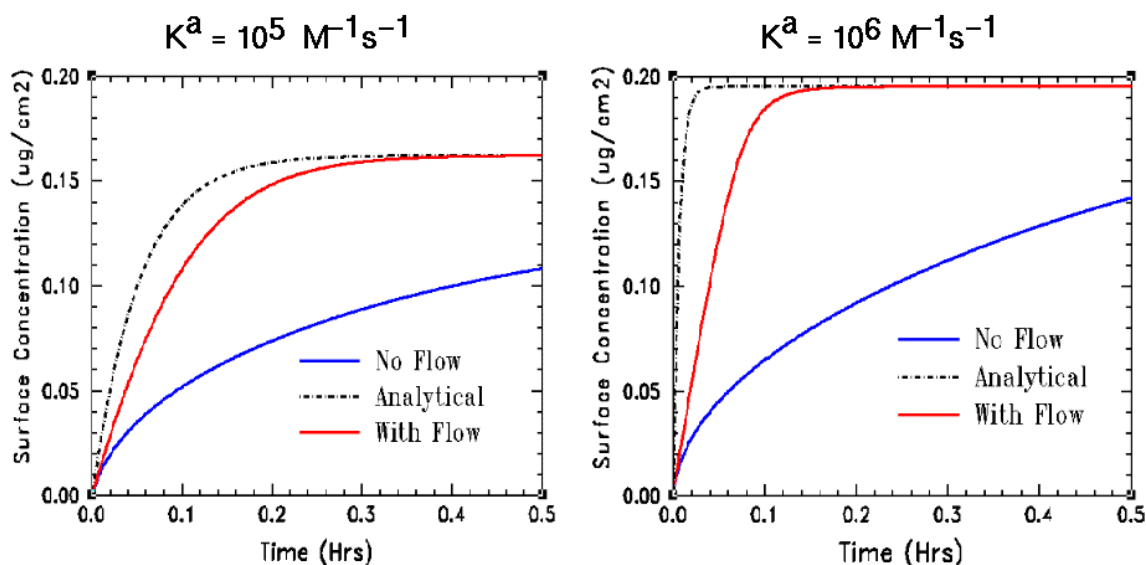


Figure 4.26: Effect of adsorption rate constant on surface binding in the SPREETA

4.5.3 Simulation of Displacement Assays

Problem Description: A displacement assay was simulated in a microfluidic environment, in which antigen and buffer solution was flown between two parallel plates in a rectangular channel. The lower plate represented the reacting surface with the antibody receptors. The

different stages of the assay are shown schematically in Figure 4.27. In Stage I, the flow of labeled antigen is maintained along the receptor sites for a fixed period of time. The labeled antigen particles bind to some of the receptor sites while others are carried with the bulk flow. During Stage II, the labeled antigen flow is turned off and a buffer solution is sent over the binding sites. This buffer flow removes loosely bound or unbound antigen particles from the system. Finally, in Stage III, sample containing unlabeled antigen is passed over the binding sites. The unlabeled antigen particles bind to free antibody receptor sites and also displace labeled antigen from the receptor into the bulk solution. The labeled antigen exiting the system is then sensed at a location downstream of the binding sites. The presence of labeled antigen in the flow at this stage indicates a positive assay.

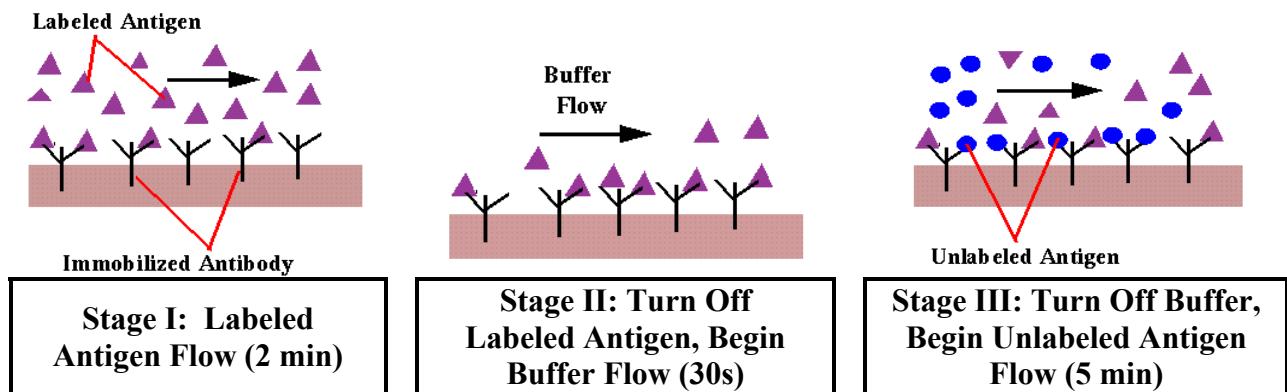


Figure 4.27: Different stages of the displacement assay

Method of Approach: A 2-D structured grid generated using CFD-GEOM was used in this analysis. The input data for the problem was as follows:

1. Reversible adsorption rate constant ($\text{cm}^3 \text{g}^{-1} \text{s}^{-1}$): $K_a = 0.005$
2. Rate constants for desorption (s^{-1}): $K_d = 0.1$
3. Diffusivity of antigen (cm^2/s): $D = 8.5 \times 10^{-7}$,
4. Inlet antigen concentration in bulk solution (Stage1) (g/cm^3): $C_o = 60$
5. Maximum possible surface antigen concentration (g/cm^2): $P_s = 0.18$
6. Inlet velocity (mm/s): $V_{in} = 100$
7. Viscosity of solution (m^2/s): $\nu = 0.86 \times 10^{-6}$
8. Density of solution (kg/m^3): $\rho = 1000$

Simulation Results: Figure 4.28a shows the average surface concentration profiles for both the labeled and unlabeled antigen. During stage 1, the labeled antigen binds to the antibody receptors and its surface concentration increases till it reaches an equilibrium value at about 75 s. After 120s, the labeled antigen flow is turned off and the buffer flow is turned on, which results in desorption of labeled antigen from the surface leading to a decrease in its surface concentration. During stage 3, the buffer flow is turned off and the unlabeled antigen flow is started (after 150s). The surface concentration of unlabeled antigen increases as it starts to bind to the available receptor sites along the reacting surface and also displaces the bound labeled antigen. When the desorption constant was increased from 0.1 s^{-1} to 0.8 s^{-1} , it results in a lower surface concentration for both labeled and unlabeled antigens. Figure 4.28b shows the amount of

antigen sensed at the downstream location for the two desorption rates. Labeled antigen flux measured downstream was higher at the lower desorption rate.

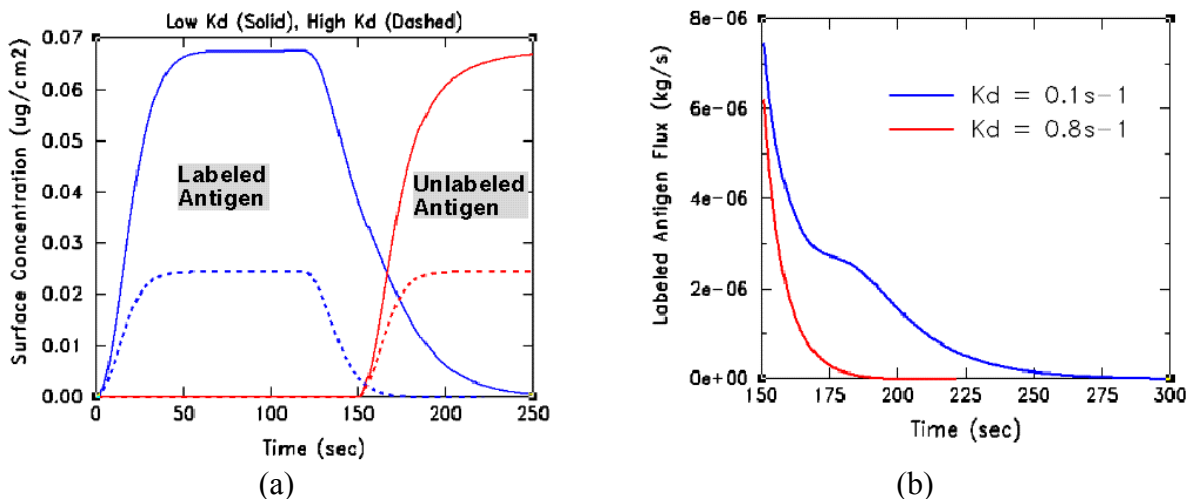


Figure 4.28: Transient variation in (a) antigen surface concentration and (b) labeled antigen flux

4.6 Virtual Sequences Programming Capability

The reacting surface inside a biosensor or bio-diagnostic device is exposed to different types of fluids (analytes, buffer solutions, reagents). These solutions are passed through the biosensor in a sequential format during analysis. The flow rates and species concentrations in these solutions can vary considerably depending on the application and assay protocol. We term the simulation of different processes in a binding assay as virtual sequencing. This capability is introduced into CFD-ACE+ through user-prescribed variations in the flow and mass transport boundary conditions.

4.6.1 Software Options

The “Biochem” module in CFD-ACE+ was modified to enable simulation of a complete assay sequence without the need to stop and restart the simulation after adjusting boundary conditions at different stages of the assay. This is a more user-friendly approach as the user does not have to monitor the simulation constantly, save data, and restart the simulation during every stage of the assay. The user can prescribe boundary conditions via user subroutines, or through the GUI, using the following options:

Constant values: The user can set constant flow velocities or species concentrations through the GUI.

Profile Along X, Y, and Z Directions: This feature allows the user to specify boundary conditions as a function of location. The user needs to specify the number of data points, their coordinate location and enter the variable values at those locations.

Profile in Time: The inlet flow and concentration boundary conditions can be prescribed as a function of time. The user has to enter a number of data points for time and the dependent

variable value at each time instant through the GUI. (The only limitation here is that a linear fitting algorithm is not available at the moment to fit a series of data points. The solver therefore curve-fits every data set using the spline option, even though a particular set may have linear variations during a portion of the assay. The linear fitting algorithm will be available shortly.)

Read Data From a File: Inlet flow or species concentration profiles can also be read from a data file. This would be an easier than the above two options if the user has a lot of data points.

User-Defined Boundary Conditions: This feature allows the user to specify different kinds of functions to prescribe the time dependent flow or species concentration boundary conditions. For example, periodic, (sine, cosine...etc), polynomial, spline, and more complex functions can be set using simple user_routines. In these routines, the user has to obtain the required boundary and variable indexes before applying the function for that variable along the boundary.

4.6.2 Demonstration of Capability

The beta galactodase-neutravidin binding assay within the flow cell the TI-Spreeta system was used as a demonstration test case. Here, analyte binding occurs when the analyte sample is passed through the flow cell. The flow cell is then flushed with buffer solution and the dissociation reaction is monitored. The user-defined BC option was used to define all six stages of the assay as shown in Figure 4.29. The stages 1, 3 and 5 were input as user_defined functions and constant values for the flow variable were set for stages 2, 4 and 6 in the user_routines. The analyte concentration remained constant during the simulation. Figure 4.30 shows the results of the sample simulation performed on the TI-SPREETA biosensor with this profile as an inlet flow boundary condition.

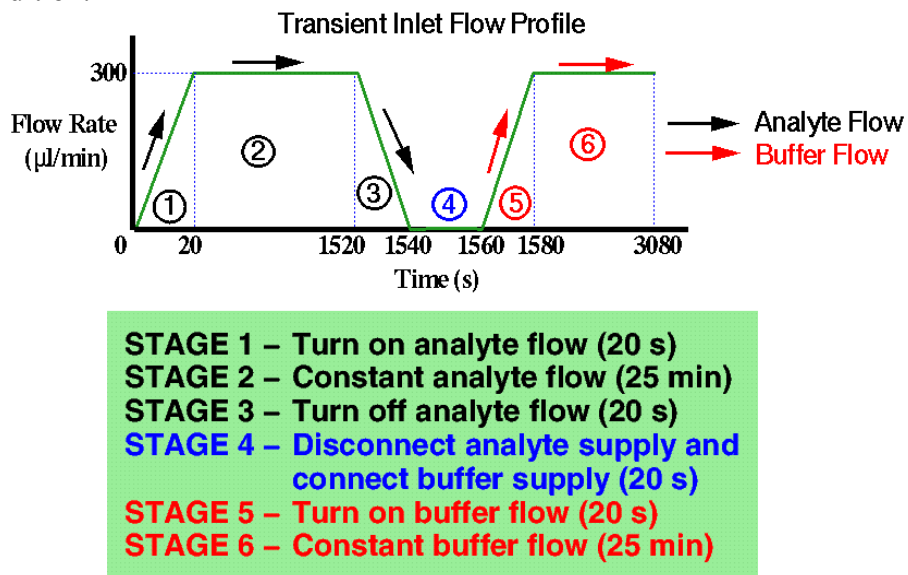


Figure 4.29: Transient processes and steps in a binding assay

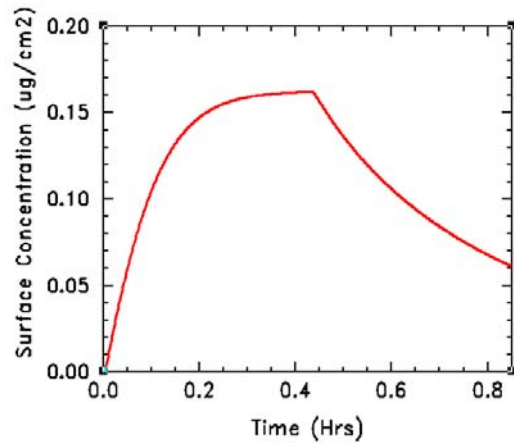


Figure 4.30: Surface concentration profile of bound analyte during the entire assay

5. ELECTROCHEMISTRY SIMULATION MODULE

The electrokinetics module in CFD-ACE+, originally developed on a previous DARPA SBIR project, was significantly refined, reformulated and upgraded into a full-fledged electrochemistry (ECHEM) module. Primary refinements include modification of the mathematical treatment of the zeta potential, incorporation of the ionization model to simulate electrochemical reactions and extension of the module to allow for spatially-varying zeta potential. All of these refinements along with a series of model validation test cases are outlined in the following sections.

5.1 Modified Treatment of Zeta Potential at the Wall

5.1.1 Mathematical Formulation

While simulating electroosmotic flows, it is difficult to generate a mesh that also resolves the double-layer region, since the thickness of the double layer (Debye thickness) is in between 0.1 μm to 0.1 nm. There are two approaches to deal with the double layer in CFD simulations: (a) through a wall velocity term, and (b) through source terms in the momentum equation. The previous electrokinetics module adopted the first approach. Here, we explain how the second approach works.

In physics, the effect of double layer is modeled by ζ potential at the wall, which contributes to the force exerted on the fluid. The momentum equation, which accounts for such force can be written as:

$$\frac{\partial}{\partial t} \rho \mathbf{u}_i + C(\mathbf{u}_i) = -\nabla p + D(\mathbf{u}_i) + \varepsilon \kappa^2 \zeta \nabla \phi \quad (5.1)$$

where, C and D are convection and diffusion terms, ε is permittivity, $\delta = \kappa^{-1}$ is the Debye thickness, ζ is potential near the wall and ϕ is potential away from double layer. It should be pointed out that the following assumption of electrical potential Φ is used here:

$$\Phi = \phi + \zeta \quad (5.2)$$

Since the ζ potential is only valid inside the double layer, we can propose the following equation for it (Patankar and Hu, 1998):

$$\nabla \zeta = \kappa^2 \zeta \quad (5.3)$$

Due to the extremely small thickness of the double layer, the above equation can be solved exactly in a 1-D form in the following manner:

$$\zeta = \zeta_0 e^{-\kappa y} \quad (5.4)$$

where, ζ_0 is potential at the wall, y is the normal distance from the wall. The boundary condition $y = \infty, \zeta = 0$ has been used. Substituting the solution of ζ into the momentum equation above and integrating it in a control volume, we have

$$S = \int_V \epsilon \kappa^2 \zeta (\nabla \phi) dV = A \epsilon \kappa^2 (\nabla \phi) \int_0^\delta \zeta_0 e^{-\kappa y} dy = A \epsilon \kappa (\nabla \phi) \zeta_0 (1 - e^{-1}) \quad (5.5)$$

where A is cell face area. The term S is put into the momentum equation source term.

Next, we need to modify the shear stress near the wall. In order to do this, we integrate the momentum equation once along the direction normal to the wall, neglecting the convection term and pressure gradient in capillary flows:

$$\mu \frac{\partial u}{\partial y} = - \int_0^\delta \epsilon \kappa^2 \zeta_0 (\nabla \phi) e^{-\kappa y} dy \quad (5.6)$$

The result gives

$$\mu \frac{\partial u}{\partial y} = \frac{\epsilon (\nabla \phi) \zeta_0}{\delta e / (1 - e)} \quad (5.7)$$

Therefore, if we assign the new wall distance parameter to be $\delta \frac{e}{1 - e}$, we should be able to calculate the correct shear stress near the wall.

5.1.2 Validation Test Case

In order to verify the current approach, we set up a 2-D test case in which the analytical solution of the flow velocity outside the double layer can be found (Probstein, 1989). The domain geometry is 2cm long and 0.02 cm high. The potential at both ends are 100 V and 0 V respectively. The relative permittivity is 78.4, the wall potential ζ_0 is -1. Figure 5.1 shows the geometry and grids. Figure 5.2 shows the velocity vectors. Figure 5.3 shows the velocity distribution normal to the wall.

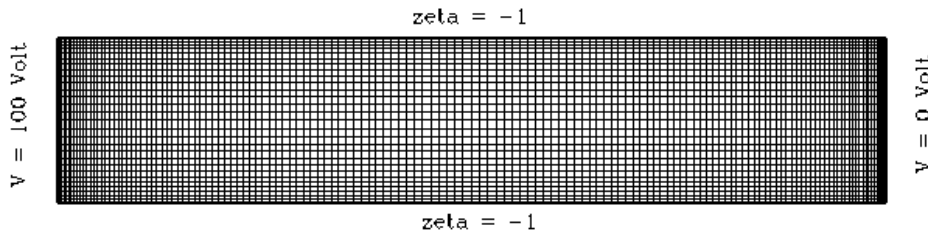


Figure 5.1: Computational domain geometry and grid for electrokinetic test case

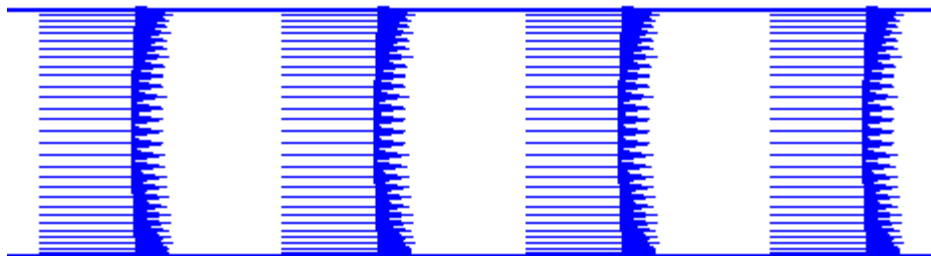


Figure 5.2: Electroosmotic velocity vectors in flow domain

The computed velocity at the edge of the double layer is compared below with the analytical value:

Analytical Solution	3.4708E-3 (m/s)
CFD-ACE+ Solution	3.4663E-3 (m/s)

From the comparison, we can see that the solution based on the current approach matches the analytical solution quite well.

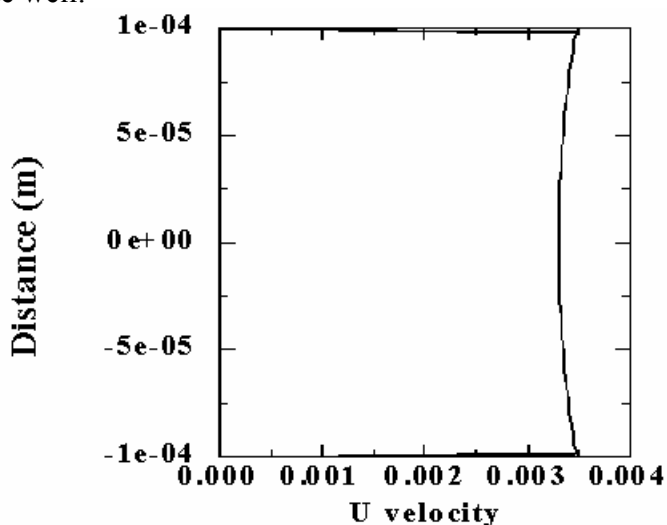


Figure 5.3: Electroosmotic velocity distribution normal to the wall

5.2 Ionization Model

The ionization modeling capability has been developed within the framework of the EChem module in CFD-ACE+, which allows users to simulate acid-base equilibrium reactions along with autoionization of water. Besides, it can also model ionization equilibria involving ampholytes. This new feature will enable the simulation of various physical phenomena such as:

- Capillary electrophoresis
- Isoelectric focusing
- Moving boundary electrophoresis
- Isotachopheresis

Besides, the user will be able to model phenomena such as stacking, pH gradient generation using ampholyte stacking, etc. All of these phenomena are relevant to the upcoming field of proteomics.

5.2.1 Theory

An implicit finite-volume numerical scheme has been developed to solve the three-dimensional transport equations along with fully-coupled ionization equilibria in acid/base systems. The scheme solves conservation equations for mass and momentum while satisfying the electroneutrality condition in a sequential fashion until convergence is achieved. The electric field is computed based on current conservation formulation. The scheme has been suitably implemented so that it also works in conjunction with the one-cell model of CFD-ACE⁺.

Governing Equations: We assume that an aqueous solution contains monovalent acids (HA_n) and bases (B_m), for which association-dissociation reactions can be represented by



where A_n^- and H^+B_m are the conjugate bases. These reactions are described by the association/dissociation equilibrium constants and degrees of dissociation. Given the concentration of various acids and bases, and their equilibrium constants, at any given time, the system should satisfy the electroneutrality condition.

5.2.2 Model Validation and Demonstration

Problem Description: The ionization model was used to study the time evolution of a sample containing several analytes in a capillary electrophoresis microchip. The phenomena of sample stacking and tailing due to conductivity differences and the effect of degree of ionization were analyzed and compared with experimental data of Ermakov and Righetti (1994).

Method of Approach: All the domain walls were assumed insulated and a no-flux boundary condition was applied. Voltages were specified at the inlet and outlet of the channel. The pH value and acid/base concentrations of the buffer solution were defined as initial conditions. Location and concentration of the sample were also initially defined. The geometry considered in this case was a capillary tube similar to the one used in the experimental and computational studies of Ermakov and Righetti (1994). An isothermal condition was assumed since the experiments were performed in the range of 26-28°C. A weak monovalent picric acid was chosen as sample species. Buffer solution consisted of 20 mM acetic acid titrated with NaOH to a pH of 5.0. The concentration of the sample species was varied from 0.02-10 mM. An electric potential of 0 V was applied at the inlet while 10,000 V were applied at the outlet. Initially, the capillary tube was filled with the acetate buffer and a sample volume of 20.6 nl was introduced into the system. The simulation was performed in a transient manner over a long period of time.

Model Validation and Sample Results: In Figure 5.4, the contour levels of the sample at two time intervals, ($t = 1$ and 6 minutes), for three different initial concentrations, ($C_o = 0.02, 1.0$ and

1.0 mM) of the sample are shown. At low concentration, there was not much dispersion and the sample stayed narrow and focused. As the initial concentration increased, we observed that:

- The sample dispersed more as it traveled downstream towards the anode
- The difference in the electrical conductivity between the sample and the buffer created a nonuniform electric field that led to sample stacking. The sample attained a triangular shape at larger concentration as shown in Figure 5.4 (f) while maintaining a Gaussian profile at lower concentration as shown in Figure 5.5.

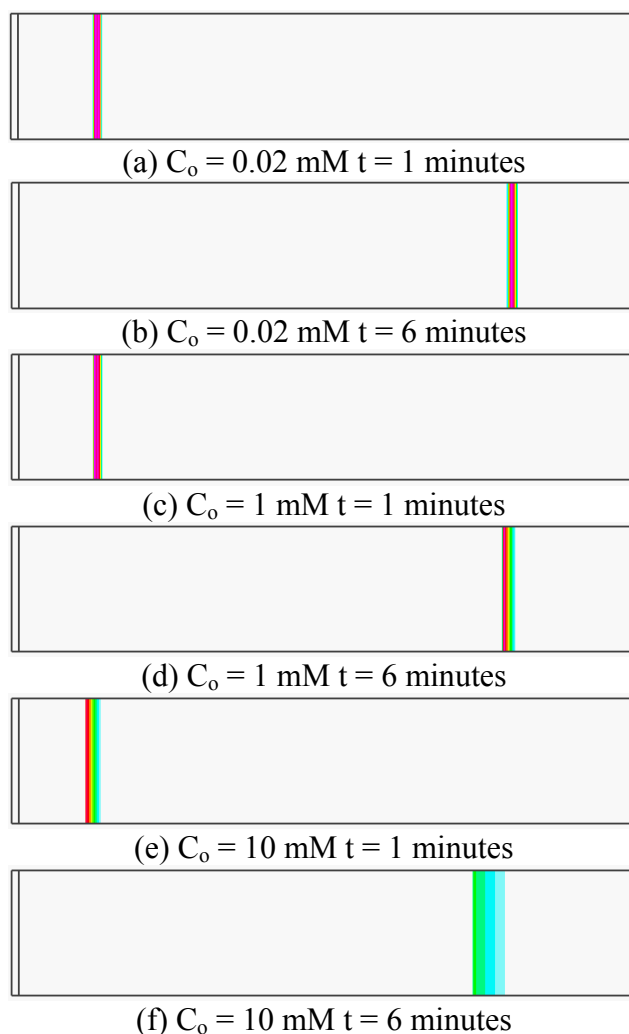


Figure 5.4: Contour levels of sample (Picric Acid) concentration is shown at 1 and 6 minutes into the simulation for initial concentrations of 0.02, 1.0 and 10 mM.

An electropherogram, taken at the location 30 cm from the inlet as predicted by the computer simulation was compared with the experimental data (Ermakov & Righetti, 1994) in Figure 5.5. We observe that there was a good qualitative and quantitative agreement in shape of the concentration profile, the migration time and the maximum concentration of the sample. With a sample concentration of 0.02 mM, which is very low compared to that of the buffer, the sample tends to maintain a Gaussian profile with the maximum concentration almost the same as that of

the initial concentration. This suggests that the system is subjected to diffusional dispersion only. At higher concentration, ($C = 1.0 \text{ mM}$), the conductivity difference between sample zone and background electrolyte caused sample stacking and the sample shape became triangular as observed in the experiments.

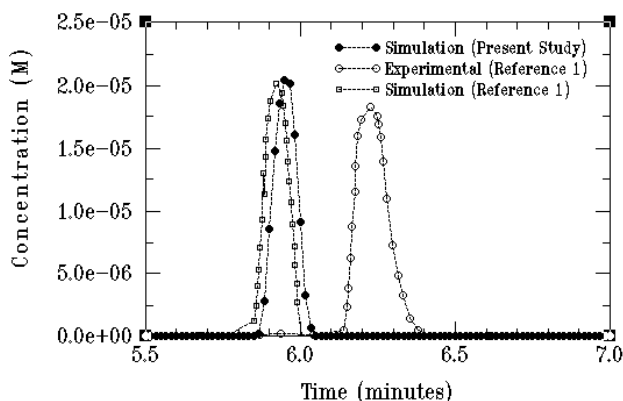


Figure 5.5: Comparison of experimental (Ermakov and Righetti, 1994) and simulated (present study and Ermakov and Righetti, 1994) Electropherogram for Picric Acid (Initial Conc. = 0.02 mM).

5.3 ECHM Graphical-User Interface

A new Graphical User Interface (GUI) window set for ECHM has been developed, tested and documented. This interface enables the use of ECHM for 3-D high fidelity simulations, for reduced 1-D modeling (described later in Section 7) and for generation of compact models of electrochemical devices. Figure 5.6 presents selected GUI windows of the ECHM module. The GUI windows demonstrate:

- User setup for specie (neutrals and ions) names for boundary conditions
- Reaction mechanisms setup for liquids; and
- Electrochemical properties.

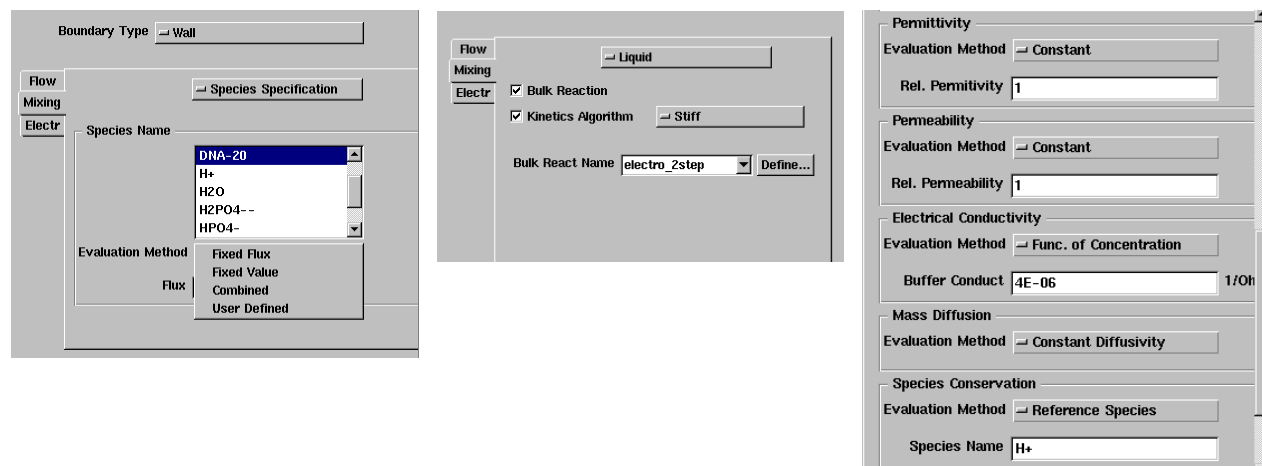


Figure 5.6: Sample GUI windows from the ECHM Module

5.4 Further Validation Cases

5.4.1 Electroosmotic Capillary Flow with Non-Uniform Zeta Potential

Some recent experimental work has been done to investigate the hydrodynamics and sample dispersion in electroosmotic capillary flow with non-uniform zeta potential [Herr et al., 1999 and 2000]. This is an important study since it is directly relevant to the design of electroosmotic flow (EOF) control scheme as well as to the design of integrated microfluidic systems.

Problem Description: A schematic illustration of the problem is shown in Figure 5.7.

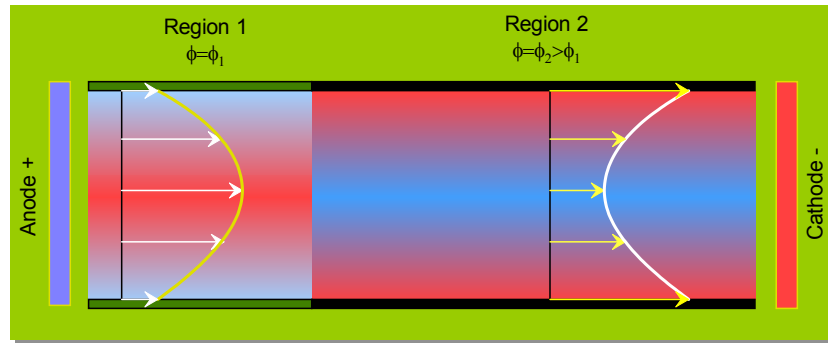


Figure 5.7: Schematic of capillary with varying surface potential along the axis. The anticipated velocity profiles away from the junction of two regions are shown.

Two regions of different zeta potential are shown. Detailed analysis indicates that the disturbance of the discontinuity decays very fast. A couple of capillary diameters away from the junction, the velocity profiles are fully developed and independent of axial position [Long et al, 1998]. The basic feature of fluid flow in this complex capillary is the combination of electroosmosis with induced pressure driven flow due to the surface inhomogeneity. We are also interested in species dispersion in both regions of the capillary flow. The numerical model accounts for the complex variation of surface and species properties, flow conditions and electric field.

The capillary considered here has total length of 50cm and diameter of 75 μ m. The surface zeta potential is replaced by the equivalent electroosmotic mobility, which is either 2E-4 m/sV in region two or zero in region 1. The zero electroosmotic mobility means that the EOF is totally suppressed. However, in order to compare the present results and the experimental measurements of velocity profile obtained using 40% active silanol groups in the EOF-suppressed region 1, we choose an electroosmotic mobility in region 1 as 0.8E-4m/sV. The local electric field strength is prescribed as 100V/m.

Pressure and Velocity Comparison: The simulation results are shown in Figure 5.8a for pressure distribution and in Figure 5.8b for velocity profiles. The pressure distribution exhibits linearity in almost the entire portion of region 1 or region 2. The transition is localized to within a small region comparable with the capillary diameter, where flow exhibits sudden expansion in order to preserve flux continuity. Three sets of curves corresponding to 10, 50 and 80% EOF suppression are shown in Figure 5.8b. The pressure induced by zeta potential jump will in turn

contribute to the velocity profile, which is anticipated to be a plug flow in capillary of uniform zeta potential. The pressure gradient in each region can be well approximated by

$$\left. \frac{\partial p}{\partial x} \right|_i = \frac{8E_x \varepsilon}{R_0^2} (\bar{\zeta} - \zeta_i), \bar{\zeta} = \frac{\sum_i L_i \zeta_i}{\sum_i L_i} \quad (5.11)$$

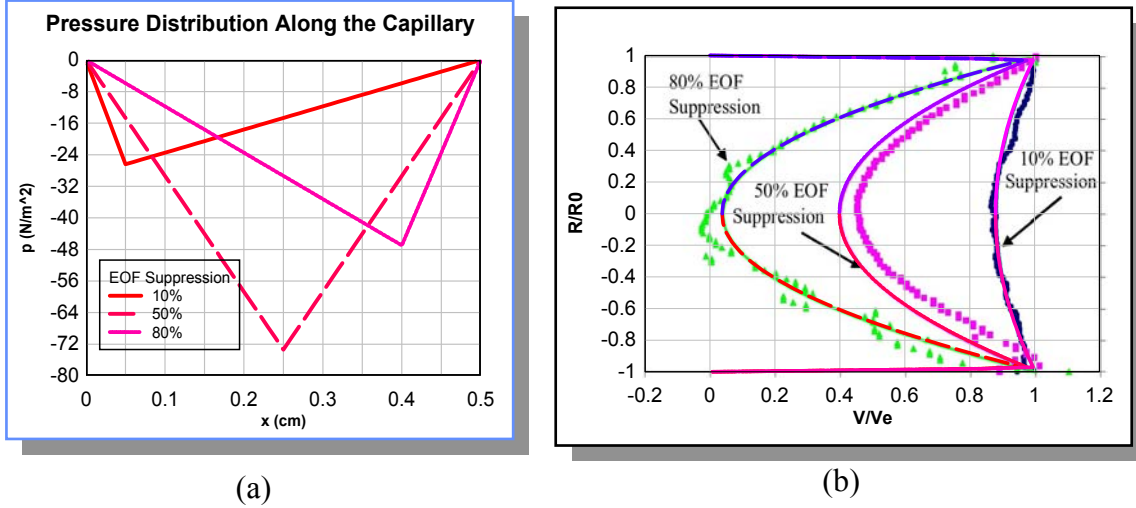


Figure 5.8: (a) Pressure distribution along the capillary, and (b) Comparison of velocity profiles in region 2 (Solid Lines: CFD-ACE+, Symbols: Experimental Data)

Figure 5.8 compares the simulated velocity profile in the EOF supporting region 2 with experimental measurements from Herr et al. (1999, 2000). Note that we have applied no-slip boundary conditions on the capillary wall in contrast to the slip EOF boundary condition in the double layer. The velocity increases sharply across the double layer, which is of the order of nanometers. The velocity profile predicted by approximate pressure gradient for each region is given in terms of the electroosmotic mobility by

$$u_i(R) = \omega_i \left[1 + 2 \left(\frac{\bar{\zeta}}{\zeta_i} - 1 \right) \left(1 - \frac{R^2}{R_0^2} \right) \right] \quad (5.12)$$

Sample Dispersion Comparison: Top study species dispersion in the capillary tube, an initial dye mark of width $25\mu\text{m}$ is placed 10 cm away from the zeta potential discontinuity in region 2. Due to the lack of physical properties of the dye, here we assumed the dye consists of small neutral particles and the diffusivity is chosen as $5E-9 \text{ m}^2/\text{s}$. The normalized dye concentration contours predicted numerically are compared with experimental results in Figure 5.9 for 10% EOF suppression. Five events are presented from the initial conditions until a time duration of 264 ms. The agreement between the numerical and experimental results on the position of maximum dye concentration is reasonable. However, the experiments indicate that the dye diffuses more dramatically as time elapses in comparison with model predictions. Potential sources of discrepancy could be attributed to: (1) Errors in diffusion constant used in the analysis; (2) Incorrect assumption of 40% active silanol groups in region where complete EOF

suppression supposedly takes place; (3) Non-uniform initial concentration of dye. These factors warrant further investigation.

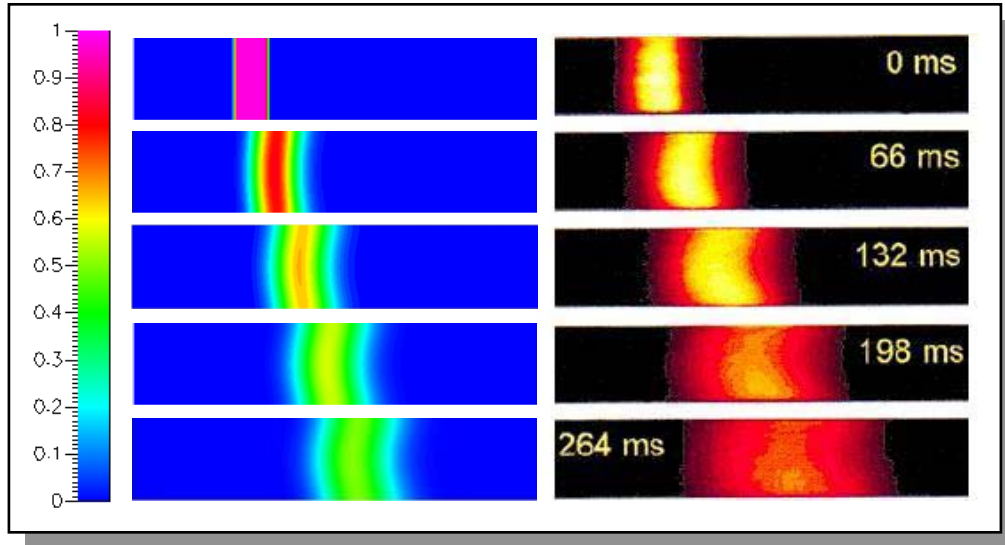
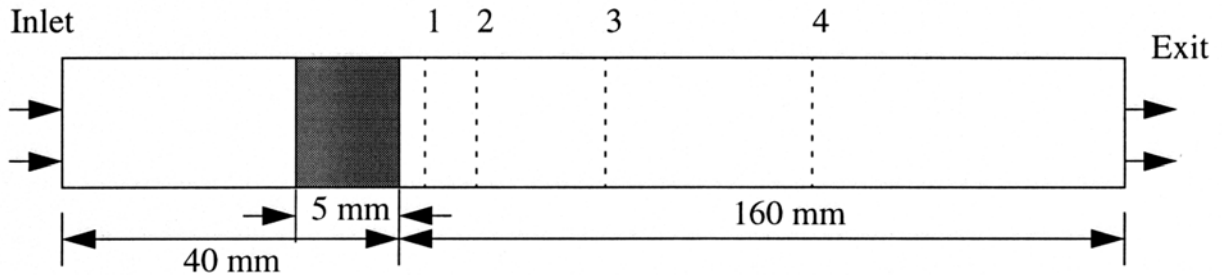


Figure 5.9: Comparison of numerical (left) and experimental (right) results on normalized dye concentration for 10% EOF suppression.

5.4.2 Electrochemical Transport Model Validation

A simple one-dimensional advection diffusion problem was set up to address issues such as numerical dispersion, which can significantly influence simulation results involving sample transport. CFD-ACE+ results were compared with corresponding results based on an analytical solution.

Problem Description: The problem involved the transport of 1-D plug of finite width as shown in Figure 5.10. The 1-D advection-diffusion transport equation was solved for sample migration under an electric field. Model parameters used were: $D_i = 6.7e-10 \text{ m}^2/\text{s}$; $w_i = D_i e / T k = 2.5917e-08 \text{ m}^2/\text{V}\cdot\text{s}$, where D_i is the diffusion coefficient of the sample, e is the electric charge, k is Boltzman constant and T is room temperature. The ion is assumed positively charged. We fix inlet potential to 5.4587 V and exit to zero, so that the ion will experience a constant electrophoretic velocity of $7.0736E-7 \text{ m/s}$. The channel is 1 mm wide and 200 mm long with the initial concentration interface positioned at $t = 0$ (“0” station). The plug has a finite width of 5 mm. Four monitoring stations, numbered 1, 2, 3 and 4 in Figure 5.10, are chosen arbitrarily. They are located at 0.75 mm, 1.75 mm, 9.75 mm and 19.75 mm, respectively, from concentration interface at time $t = 0$. The dye concentration is initialized to 1 to the left of “0” station and up to -5mm (shaded region in Figure 5.10), and to zero on the right. We use a uniform grid size of 0.5mm thick. The time for the integration is set to 1 sec, corresponding to a CFL number of $1.4e-03$. Crank-Nicholson time stepping scheme with a factor of 0.5 and a second-order upwind scheme with a blending factor of 0 are used for time and spatial discretizations, respectively.



(Figure Not to Scale)

Figure 5.10: Computational domain geometry used in 1-D open-tube plug flow. The dye concentration was monitored at locations 1, 2, 3, and 4, which were 0.75, 1.75, 9.75 and 19.75mm, respectively, from concentration interface at time $t = 0$.

Analytical Model: Dye is convected and diffused into the unshaded region. For any station, located at a distance x from the initial interface, it can be shown that

$$C(x; t) = 0.5 \left[\operatorname{erf} \left(\frac{1}{2} \sqrt{\operatorname{Pe}_1} \frac{\{1D\tau_1\}}{\sqrt{\tau_1}} \right) \operatorname{Derf} \left(\frac{1}{2} \sqrt{\operatorname{Pe}_2} \frac{\{1D\tau_2\}}{\sqrt{\tau_2}} \right) \right] \quad (5.13)$$

where C is the concentration, $\operatorname{Pe}_1 = (U_0 x / D)$ and $\operatorname{Pe}_2 = (U_0 (x+w) / D)$ are the Peclet numbers, and $t_1 (= t U_0 / x)$ and $t_2 (= t U_0 / (x+w))$ are the nondimensional time scales. Here, w represents the width of the plug.

Comparison at Low Peclet Number: The concentration of the dye as predicted by ACE+ is compared with the analytical solution in Figures 5.11. The Peclet numbers are 0.75, 1.75, 9.75 and 19.75 at the monitored locations 1, 2, 3, and 4, respectively. There is an excellent quantitative agreement between present simulation and analytical results.

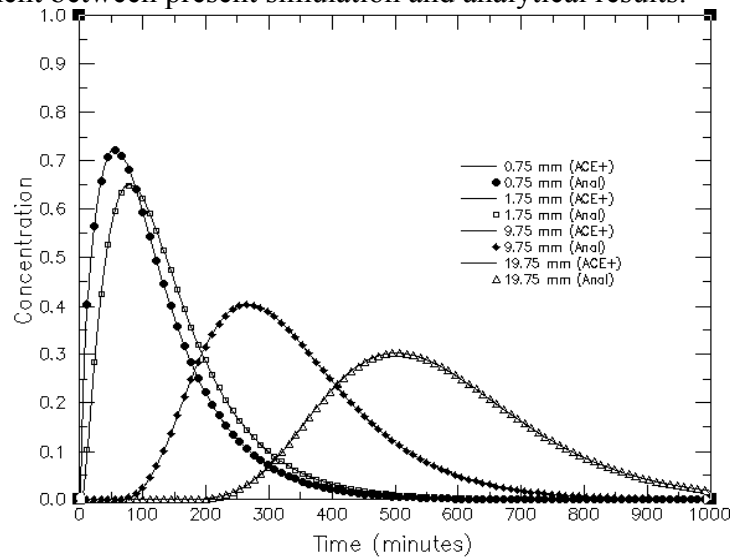


Figure 5.11. Temporal variations in ion concentration at various downstream locations based on CFD-ACE+ and analytical predictions (low peclet number case).

Comparison at Peclet Numbers: To understand the performance of ACE+ for high Peclet number flows, we reduce the diffusion coefficient of the sample from $6.7\text{e-}10\text{ m}^2/\text{s}$ to $6.7\text{e-}12\text{ m}^2/\text{s}$, so that the Peclet number at these locations will be 75, 175, 975 and 1975. The results from the simulation are shown in Figure 5.12. This figure clearly illustrates that initially when the interface is approaching the monitor position, ACE+ overpredicts the concentration, by 8%. Hence, the user is cautioned to interpret the ACE+ solutions when the Peclet number of the flow is very high (above 50).

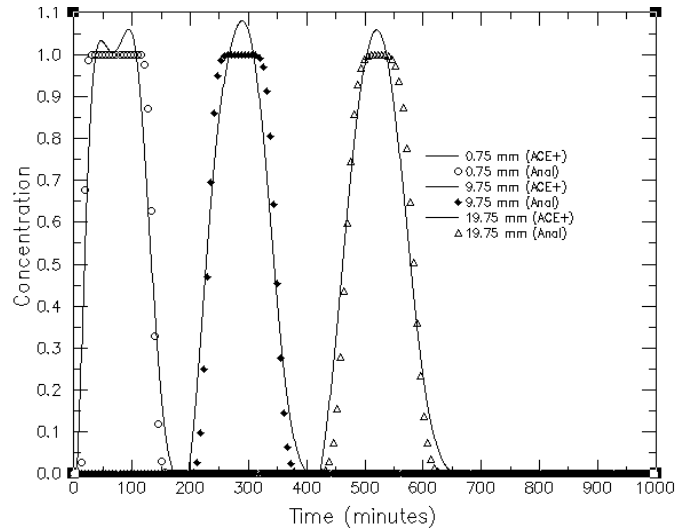


Figure 5.12: Temporal variations in ion concentration at various downstream locations based on CFD-ACE+ and analytical predictions (high peclet number case).

6. FABRICATION AND CHARACTERIZATION OF MICROFLUIDIC TEST STRUCTURES

This section describes the work done on fabrication, and subsequent characterization, of the various types of microfluidic test structures (microchannels, microneedles, microvalves and micromixers) through experimental measurement of their performance, which was performed at UC Berkeley. It also outlines numerical model validation work performed at both UC Berkeley and CFDRRC using the measured data and CFD-ACE+.

6.1 Flow Apparatus for Microfluidic Measurements

6.1.1 Typical Problems with Syringe Pumps

The characterization of micro fluids devices requires the availability of an experimental setup that allows determining the relation between flow rate and pressure drop. Previously, experiments have been performed using a commercially available syringe pump (Cole Parmer P-74900-20) to impose a flow rate and an unamplified pressure sensor (Honeywell 26PC series) to measure the pressure drop. In addition to a relatively low output signal (100 mV nominal range) high fluctuations made the reading very difficult. Therefore, a set up was to be designed that allows for flow measurements with a high flexibility in applications, automated control of the measurements and data acquisition by a computer.

6.1.2 Development of an Improved Fluid Delivery System

If the formerly used plastic syringes are replaced by glass syringes, the flow rate becomes steadier resulting in a more stable output signal as shown in Figure 6.1. The 60 Hz noise of the output signal can be reduced by two orders of magnitude using shielded cable. A stepper motor with a linear slider (both Parker) is being used in closed loop feed back control as main component of a self made syringe pump. The fluctuation of the flow rate due to mechanical imperfections of the actuation can be reduced by half an order of magnitude compared to the commercial syringe pump.

An electric circuit has been built based on an instrumentation amplifier (Burr Brown, INA122) in order to amplify the output signal of the pressure transducer to a nominal range of 5V, increasing the resolution possibilities of the signal. The syringe pump is now controlled through a computer using HPVEE. Measurement data is acquired and preprocessed using an A/D board and HPVEE. The ultimate goal is to integrate electric circuitry into a box that will convert signals from 4 pressure transducers, 3 current signals and 1 temperature signal into 0-5V signals that can be recorded through HPVEE. Binary output signals generated in HPVEE will actuate relays that can be used to power heaters (part of some microfluidics devices) or valves that are part of the set up. Such valves can be used to automatically refill the syringes when they are empty in order to guarantee a continuous measurement procedure.

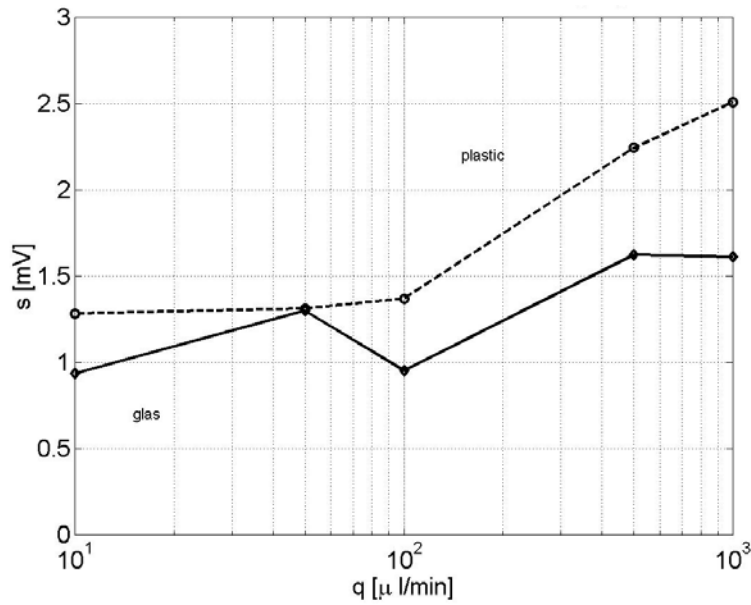


Figure 6.1: Standard deviation of pressure signal as a function of flow rate for plastic and glass syringes.

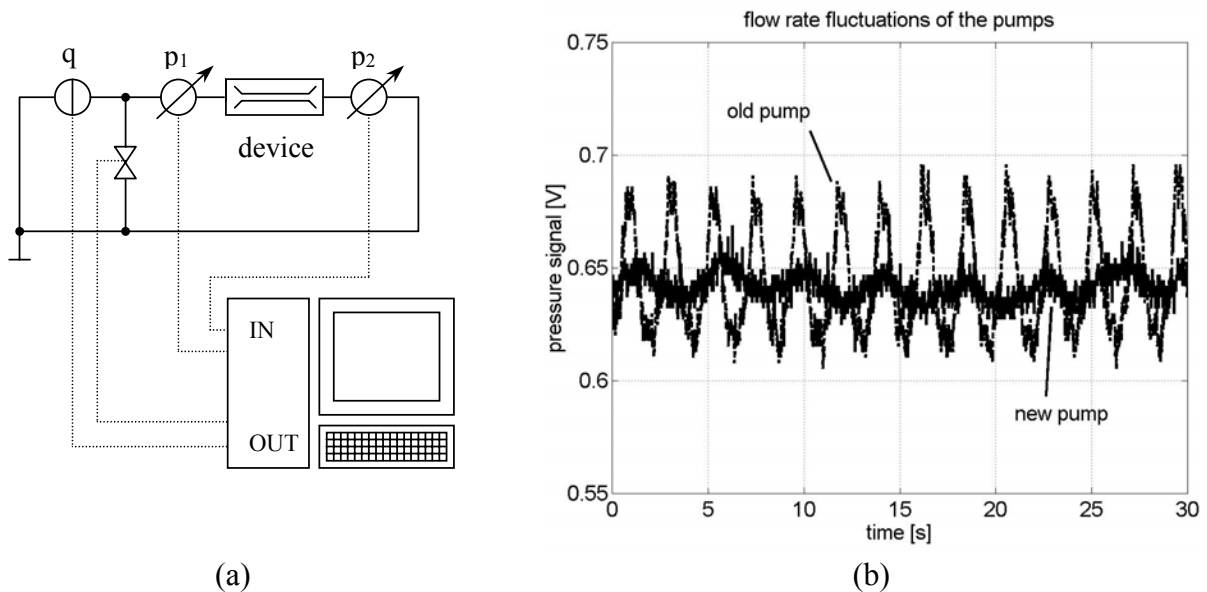


Figure 6.2: (a) Schematic of the flow apparatus; (b) Pressure signal at steady flow rate using the old syringe pump (Cole Parmer) and the new pump (Parker). The period of fluctuations corresponds to 1 rotation of the pump lead screw.

Development of the new fluid delivery system has been completed (see schematic in Figure 6.2a). Validation of the new syringe pump system has shown much better performance compared with syringe pumps, although there is still a period fluctuation in the fluid flow (Figure 6.2b). In addition to the new delivery system, a new data acquisition system for microfluidic systems has also been constructed. The new system includes the capability acquire data from two pressure transducers, control delivery by a syringe pump and refill syringes when needed. The latter is critical to keep bubbles out of the system and for accurate and rapid investigation of

blood flow through micro-devices. A computer program has also been developed for data acquisition and fluidic control.

6.2 Microchannel Test Structures

6.2.1 Microchannel Blood Flow Experiments

Blood flow experiments were performed at various dilutions (hematocrit) from pure saline to whole blood through prototype microchannels. Channels for flow testing were fabricated in silicon using deep reactive ion etching (DRIE) to create rectangular cross-section trenches (Figure 6.3). Straight channels, channels with sudden contractions, and channels with 90° bends were all etched 60µm deep into the silicon and had total lengths of 12mm, regardless of configuration. Both the straight channel and 90° bend were patterned with 200µm widths, while in the channel with sudden contraction, a 200µm wide, 6mm long channel fed into a 100µm wide, 6mm long channel.

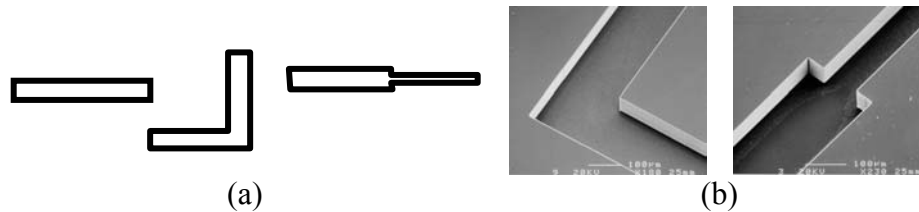


Figure 6.3: Microfabricated flow structures showing: (a) typical channel configurations including straight channels, 90° bends, and sudden contractions; and (b) electron micrographs of a bend and a contraction channel.

Defibrinated blood of 45% hematocrit was diluted with saline in various volume fractions to obtain different levels of dilution. Viscometry was performed on the dilute blood samples by a Vilastic 3 Viscoelastic Analyzer (Vilastic Scientific, Inc.), which measures fluid parameters of a sample as it is oscillated in a small tube. Defibrinated sheep blood is a shear thinning fluid, with the viscosity dropping from 5.4×10^{-3} to just under 4.9×10^{-3} Pa·s over the shear rate range of 80 to 400s^{-1} (see Figure 6.4). These values are comparable to the measurements of blood viscosity in the literature.

The pressure was explicitly controlled in the experiments. The pressure vs. flow rate relationships for all of the channel configurations were roughly linear, though the flow resistances were somewhat higher for lower flow rates than for higher flow rates, as would be expected for a shear-thinning fluid. For the $200\mu\text{m} \times 60\mu\text{m} \times 12\text{mm}$ straight channel, the first-order estimation of flow resistance for blood was about $1.3 \times 10^{13} \text{ kg}/(\text{s}\cdot\text{m}^4)$ roughly 3.5 times that for water. The addition of the ninety degree bend midway through the channel increases the flow resistance to about $1.8 \times 10^{13} \text{ kg}/(\text{s}\cdot\text{m}^4)$, while with a sudden contraction midway and subsequent width reduction to $100\mu\text{m}$, the flow resistance was about $2.5 \times 10^{13} \text{ kg}/(\text{s}\cdot\text{m}^4)$.

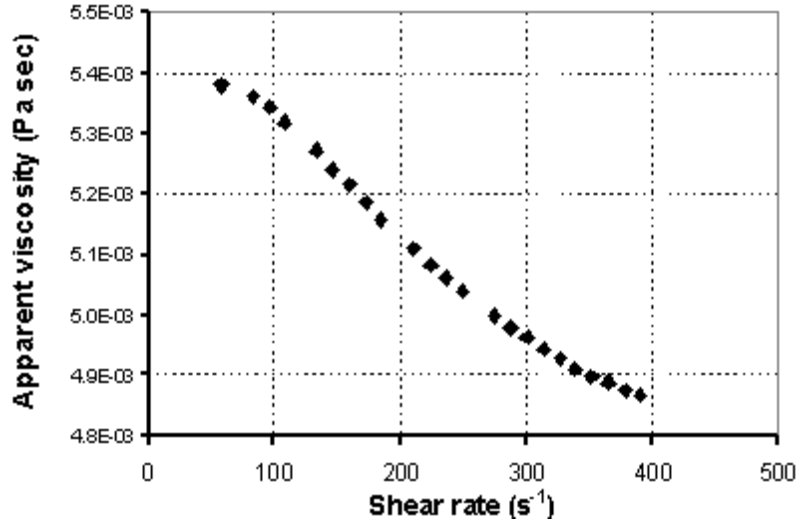


Figure 6.4: Dependence of blood viscosity on shear rate

6.2.2 Model Validation for Dilute Blood Flow in Straight Microchannels

Experimental data on pressure drop-flow rate ratios for dilute blood flow experiments in prototype microchannels was used to validate corresponding numerical simulations using CFD-ACE+. The data chosen was for a straight channel of 3.64 mm length and 42 x 25 micron cross section. The equivalent diameter (D_e) of the channel was first calculated as 4 times the hydraulic radius of the channel, i.e. 4 times the ratio of flow area to wetted perimeter of the channel (= 31.34 microns). Pressure drop variation as a function of flow rate, Q , for a rectangular channel is calculated as follows:

$$\Delta P = \frac{8\lambda\mu L}{\pi D_e^4} Q \quad (6.1)$$

where λ is the friction coefficient that depends upon the aspect ratio of the channel cross section. The value of this coefficient was determined computationally by simulating flow through a rectangular channel with dimensions identical to those mentioned above using water as a test fluid. Using the obtained value of λ (=10.95), the apparent viscosity of the blood for various dilutions was calculated for the experimental data.

Table 6.1: Experimental Flow Rate-Pressure Drop Data and Calculated Viscosity for Dilute Blood Flow Through Microchannels

Dilution (volume fraction)	$Q/\Delta P$ ($\mu\text{L}/\text{min kPa}$)	Apparent Viscosity (Pa s)
Saline	0.68	8.38e-4
1/25	0.59	9.66e-4
1/10	0.53	1.08e-3
1/5	0.52	1.1e-3

Flow simulations were performed in the microchannels for the various dilutions mentioned above using the laminar flow model for an incompressible, Newtonian fluid. Non-Newtonian effects were assumed negligible at the chosen dilution levels. The apparent viscosity calculated

earlier was used and the density was computed as a volume average of the two fluids – saline and blood. The variation of pressure drop across the channel was reported as a function of flow rate for fully developed flow in the channel. Variation of pressure along the length of channel is shown in Figure 6.5. A comparison of experimental and computed results is shown in Figure 6.6. There is excellent agreement (within 0.1%) between the computed pressure drop and the experimental data. As the volume fraction of blood in the samples increases, the pressure drop across the length of the channel for a given flow rate reaches a constant value.

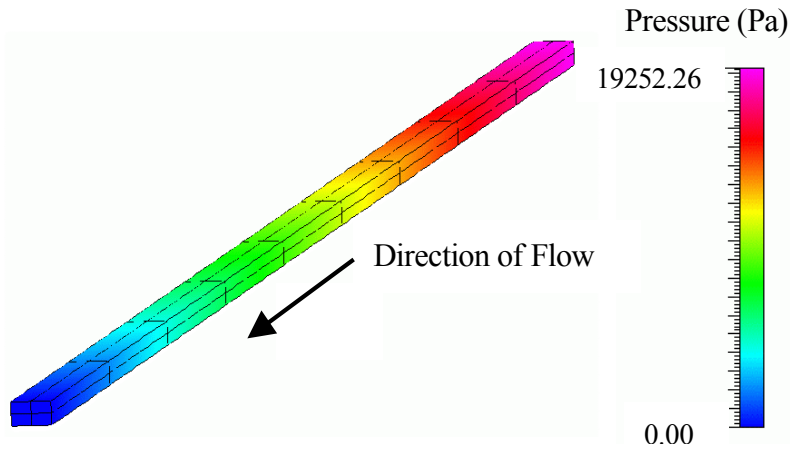


Figure 6.5: Fluid pressure in microchannel for 1/5 dilution (10 $\mu\text{L}/\text{min}$ flow rate)

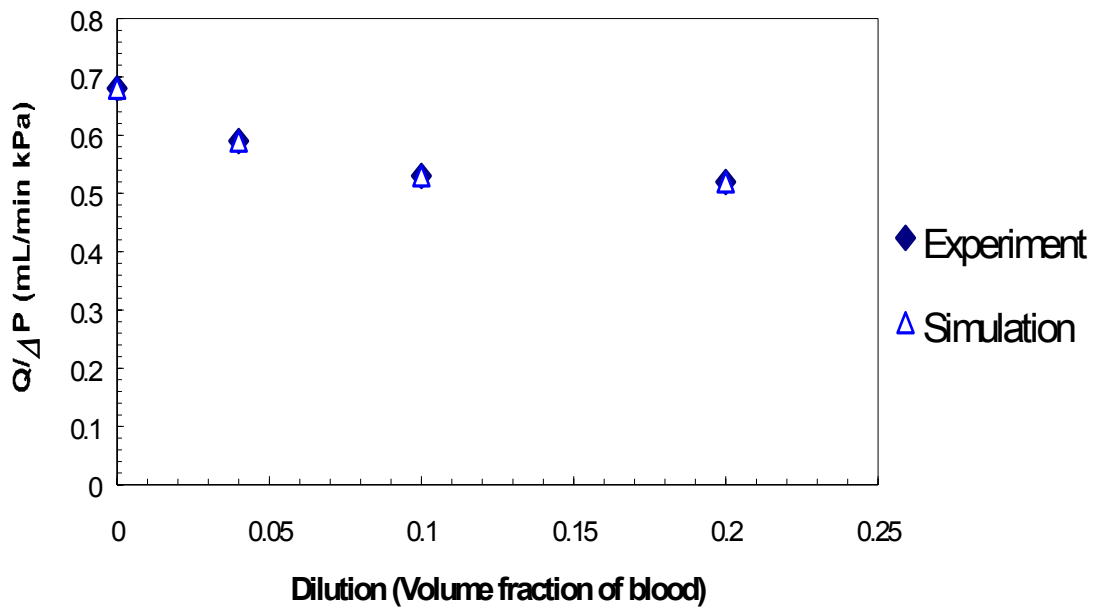


Figure 6.6: Comparison of experimental and model predictions of volumetric flow rate to pressure drop ratio for dilute blood flow in rectangular microchannels.

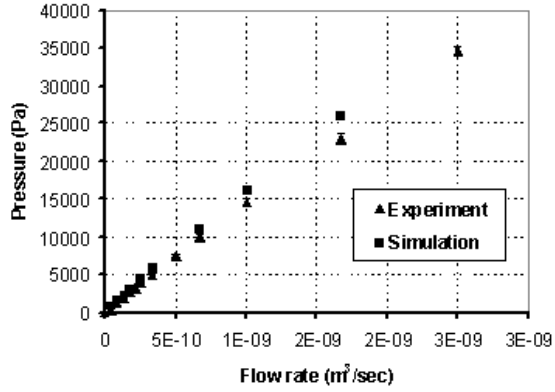
6.2.3 Model Validation for Whole Blood Flow in Various Microchannels

Non-Newtonian Models Used in the Study: Flow simulations for whole blood were performed for straight microchannels, contracting microchannels and channels with a 90 degree bend. The constitutive equation chosen for this study was the power law equation, which has the form:

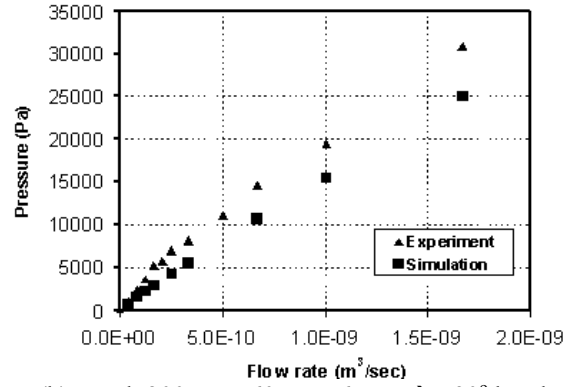
$\tau = k(\dot{\gamma})^n$. The specific parameters for blood (defibrinated sheep blood of 41% hematocrit) used in this study were determined from a least squares fit of the log-log relation between shear rate and shear stress. For the chosen blood samples, the values obtained for the power law parameters were: $k = 0.00733 \text{ Pa}\cdot\text{s}^n$, and $n = 0.932$. To provide a comparison between an established constitutive model and the non-Newtonian model formulated specifically for this study, simulations of blood flow through the straight channel and channel with 90° bend were also performed using the “one variable” power law of Walburn and Schneck, which had the parameters $n=0.785$ and $k=0.0134 \text{ Pa}\cdot\text{s}^n$, obtained at 37°C. The Walburn-Schneck model has a greater degree of non-Newtonian character than the power law model developed in this study.

Comparison of Numerical Predictions with Experimental Data: Steady-state flows based on both power-law models and a Newtonian reference were numerically simulated for each of the flow geometries using CFD-ACE+. The resulting pressure generated between inlet and outlet of the flow structure was computed. These simulations predicted pressure vs. flow rate relationships that were similar to the trends and magnitude of the experimental data. As with the experimental measurements, the computed relationships between pressures vs. flow rates were roughly linear. With both the straight channel and the channel with sudden contraction, results of numerical simulations closely matched the experimental measurements (Figure 6.7a,c). Simulations of the flow through the channel with the bend, however, predicted pressure drops that were consistently smaller than the pressure drops measured during flow experiments (Figure 6.7b).

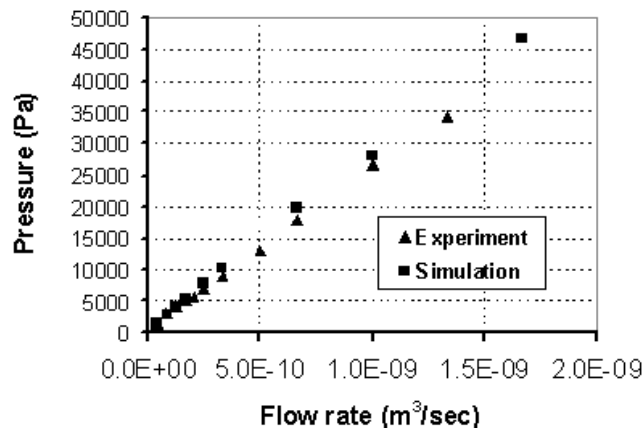
Not surprisingly, simulations using the Walburn-Schneck model for blood flow through the straight channel and channel with bend produced pressure vs. flow relationships that deviated more from linear than relationships produced with our power law model. Hydrodynamic resistances (slopes in Figure 6.8) were visibly lower for higher flow rates than they were for lower flow rates. Overall, the flow resistance were much lower for the Walburn-Scheck model than for our model, since the high shear viscosity predicted the former are much lower.



(a) Straight channel: $200\mu\text{m} \times 60\mu\text{m} \times 12\text{mm}$

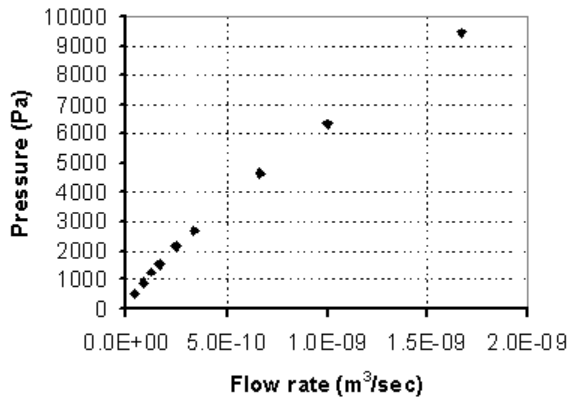


(b) Bend: $200\mu\text{m} \times 60\mu\text{m} \times 6\text{mm} \rightarrow 90^\circ$ bend
 $200\mu\text{m} \times 60\mu\text{m} \times 6\text{mm}$

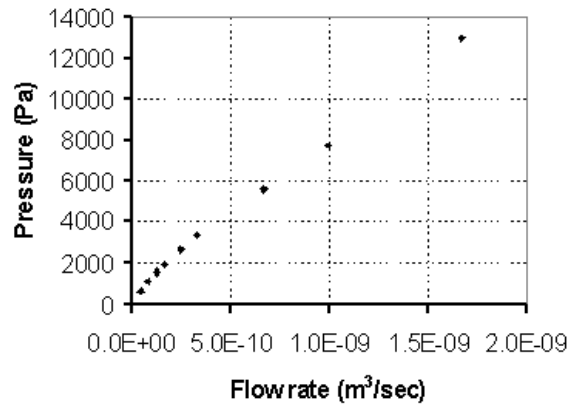


(c) Sudden contraction: $200\mu\text{m} \times 60\mu\text{m} \times 6\text{mm} \rightarrow 100\mu\text{m} \times 60\mu\text{m} \times 6\text{mm}$

Figure 6.7: Experimental and simulated (Power Law Model) pressure vs. flow rate relationships



(a) Straight channel: $200\mu\text{m} \times 60\mu\text{m} \times 12\text{mm}$



(b) Bend: $200\mu\text{m} \times 60\mu\text{m} \times 6\text{mm} \rightarrow 90^\circ$ bend \rightarrow
 $200\mu\text{m} \times 60\mu\text{m} \times 6\text{mm}$

Figure 6.8: Simulated pressure vs. flow rate relationships based on one-variable Walburn-Schneck Power Law.

6.3 Microneedle Structures

Microneedles can be used for sample extraction or injection for biomedical applications. It is important to understand how complex biological fluids behave within the needles because non-Newtonian effects have been associated with fluid flow of concentrated biological solutions. The following sections outline some of the blood flow experimental studies conducted on microneedles of various different configurations.

6.3.1 Experimental Blood Flow Measurements

Various microneedle structures, comprising straight and bent needles as well as needles with a filter, were fabricated (see Figure 6.9). Dilute blood flow measurements were made in all needle configurations. Different concentrations of sheep blood diluted with phosphate buffered saline (PBS) were investigated in different needle geometries. The pressure drop was measured as a function of flow rate through the needles at varying fluid flow rate (5-30 $\mu\text{l}/\text{min}$). The fluid exits into an infinite bath and enters from a housing, which is several times the needle diameter. In addition, the fluid in the filter needle enters at the tip and exits at the base (the fluid sees an expansion not a contraction). However, the fluid exits from the tip of the bent needle. Since the straight needle is symmetric, the orientation of that needle does not matter.

A comparison of experimental results with analytical estimates of pressure drops based on the assumption of laminar flow through rectangular ducts with no entrance, exit or geometry losses is shown in Figure 6.9. The large discrepancy between the data and theoretical estimates indicates that pressure losses and non-Newtonian effects in these microneedle structures warrant further investigation.

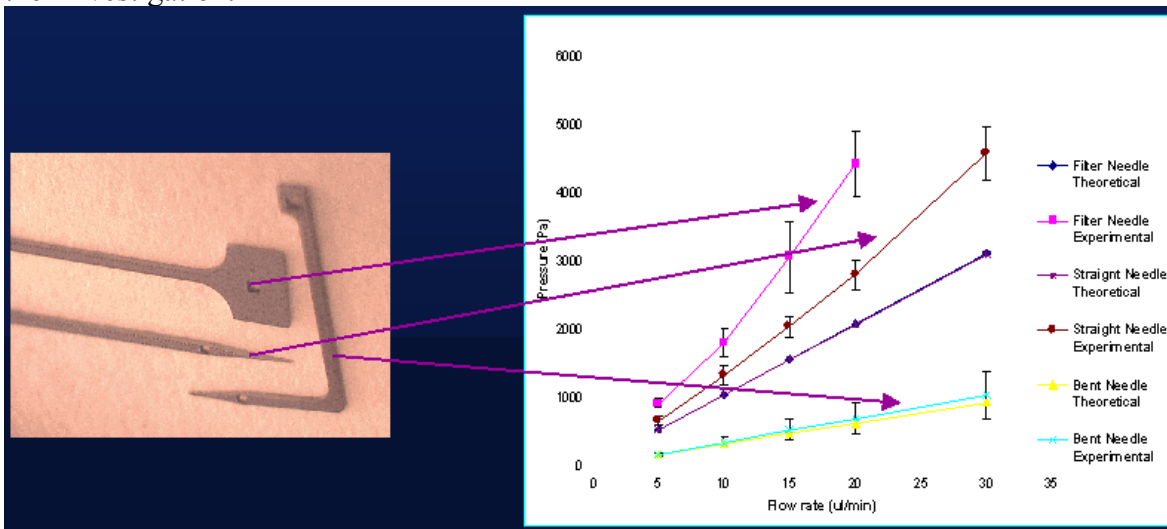


Figure 6.9: Experimental and analytical pressure drop vs. flow rate plots (right) for various microneedle configurations (left).

6.3.2 Microneedle Pressure-Flow Characteristics and Apparent Viscosity

Additional pressure-flow data for the straight and microfilter needles are shown in Figures 6.10. The flow rate is lower for the filter needle as RBC's tend to clog up the filter. Figure 6.11 shows the apparent viscosity of blood in the straight and filter needles. The viscosity for the straight needles is almost constant until high blood concentrations. The viscosity in the filter needle

seems to rise even at low blood concentrations. This could probably be attributed to clogging in the filter.

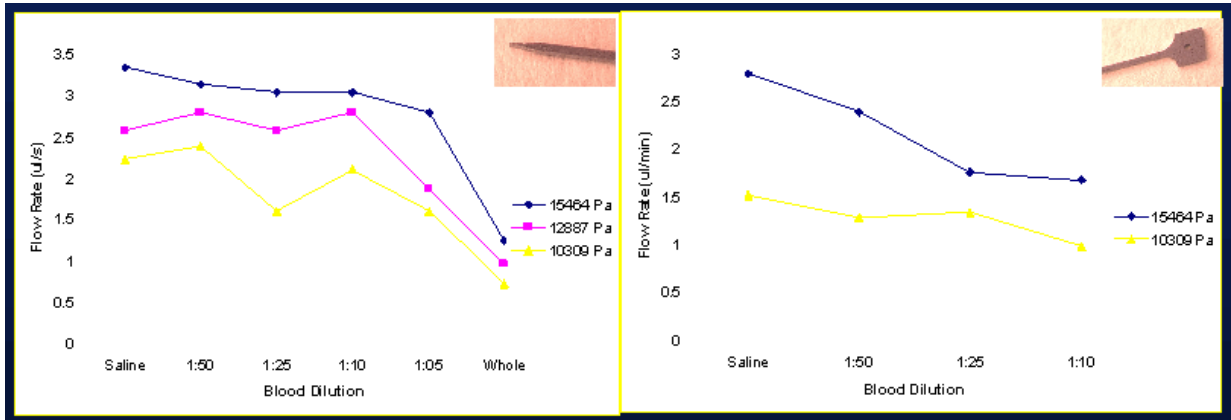


Figure 6.10: Comparison of flow rate as a function of blood dilution at fixed pressure heads for straight needle (left) and filter needle (right)

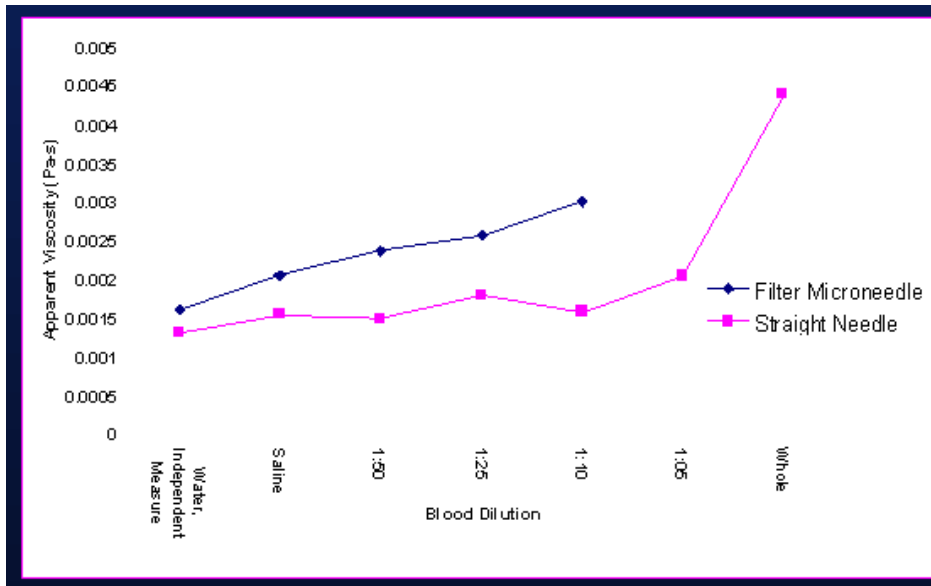


Figure 6.11: Apparent viscosity of blood in different microneedles

Only slight shear thinning behavior was observed in these experiments, and only slight changes in apparent viscosity were recorded even at higher hematocrit levels. This is hypothesized to be a result of the Fahraeus effect in which cells are excluded from the wall regions in small channels. Microneedles with complex features clogged easily, whereas needles with larger hydraulic radii allowed higher concentrations of blood to flow through them. However, at higher hematocrit levels (>25%), even the lower resistance needle clogged.

Flow resistance to blood through the microneedles was highly dependent on needle geometry (see Figure 6.10). Microneedles with complex features such as microfilters clogged easily at moderate blood concentrations (>1:25 dilution), even if the filter spacing was much larger (80 microns) than the size of the blood cells (8 microns). Even at lower blood concentrations,

clogging was very apparent and care had to be taken during data collection. Needles with simpler geometries, such as a larger hydraulic radii “bent” microneedles, allowed higher concentrations of blood to flow through them. However, at higher concentrations of blood, even the lower resistance needle clogged. Whole blood (~45% hematocrit) could flow at very high pressures, but the pressures required for flow was highly variable between needles due to different amounts of clogging in each needle.

Little change in apparent viscosity was seen as blood dilutions were increased. The viscosity change, as a function of blood dilution, is very gradual. Literature values for water is 0.001 pa-s. Blood viscosity is a function of hematocrit level. Whole blood (45% hematocrit) is about 4 times as viscous as water. At a 1:5 dilution of blood should have an apparent viscosity of about 0.0018 Pa-s (Fung , 1993), but the apparent viscosity of the 1:5 dilution flowed though the bent needle is only about 0.0012 Pa-s. It is hypothesized that the small change in viscosity is the result of the Fahraeus effect. Thus, the blood hematocrit levels flowing through the needle is much lower than in the bulk solution. In addition, since there is a lower concentration of cells in the device, the shear thinning properties of blood are not observed since the cell suspensions appear more Newtonian at lower concentrations.

6.3.3 Clogging Phenomenon in Microfilter Needles

The clogging behavior of the needles is hypothesized to be the result of two mechanisms. First, proteins are very easily adsorbed onto silicon surfaces. Once a thin layer of proteins are adsorbed, cellular adhesion is promoted. Secondly, some cells shear as a result of high shear flow. Thus sheared cells will stick and aggregate in a random orientation which leads to clogging. Clogging was most apparent in the microfilter needles. This is probably due to the microfilter structure rather than a smaller hydraulic diameter, since a straight needle with the same hydraulic diameter did not clog as readily (data not shown). When the fluid enters the filter head, there is a complicated entrance flow. The microfilter also presents very localized regions of high shear. Thus cells and sheared cells may aggregate between the filter rungs, causing a clog. This can be confirmed experimentally by observing the spread of data as flow rate increases. As the flow rate increases through needles, the spread of the data becomes a larger percentage of the measured value. This is hypothesized to be because of the higher shear rates at higher flow rates, which results in “mini” clogs. These clogs cause the pressure to increase in the device until sufficient pressure is reached to force the clog through the device at which time the pressure falls. This phenomenon of random pressure fluctuation was seen during all phases of the blood flow experiments and was attributed to small clogs forming and then clearing. Adhesion reducing coatings, such as heparin or a thin layer of TeflonTM may decrease the clogging of needles with cellular solutions.

6.4 Micromixer System and Component Microvalves

6.4.1 Micromixer System Performance

An active micromixer system, which utilized microbubble pumps and one-way check valves, was developed at U. C. Berkeley to facilitate fluid mixing in microchannels. A schematic micromixer system, showing the micropumps and microvalves, is presented in Figure 6.12. The two bubble pumps function sequentially, 180 degrees out-of-phase with one another. While the bubble in one pump is expanding (and pushing liquid out), the other pump is drawing liquid in during bubble contraction. This asynchronous pumping results in pulsating flow within the

mixing chamber, which enhances mixing. Sample images of the mixing of fluorescein and colored water are shown in Figure 6.13. Initial quantitative data on the mixing rates is shown in Figure 6.14. System-level micromixer simulation results are presented later in Section 9.

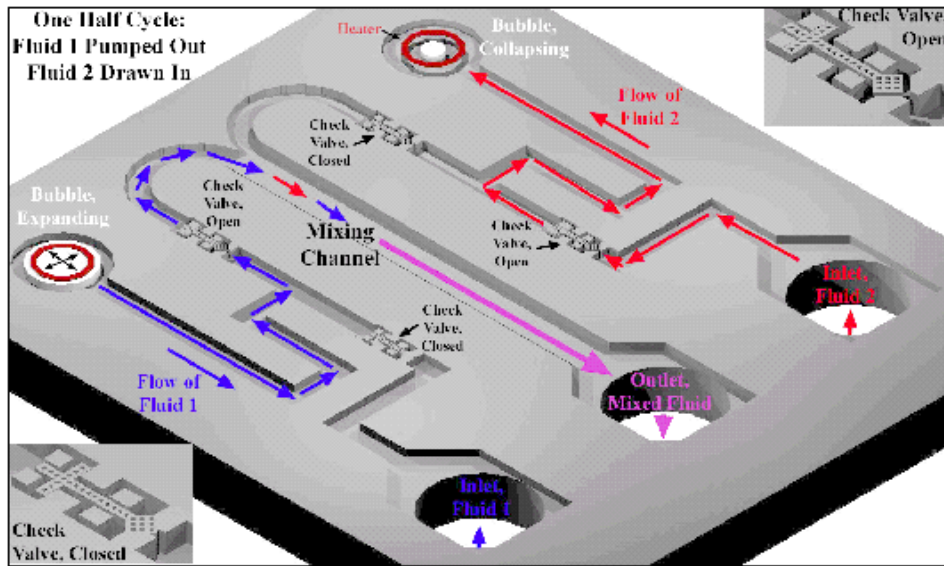


Figure 6.12: Micromixer System Schematic

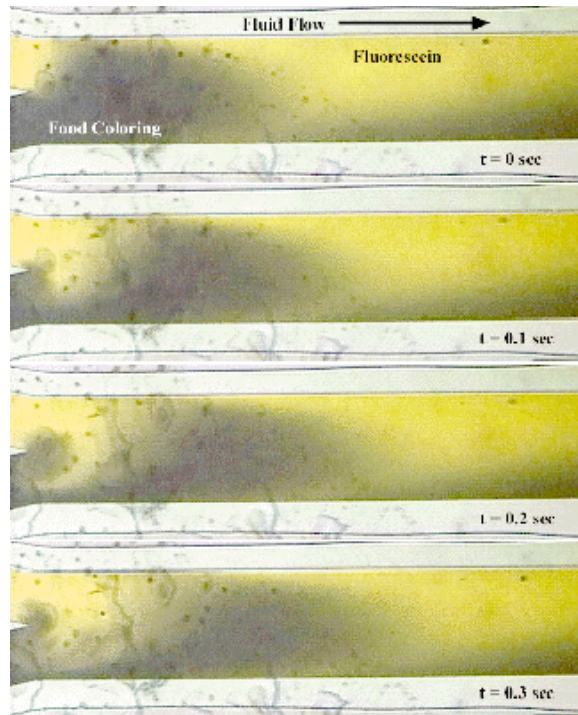


Figure 6.13: Mixing of fluorescein and colored water at 1.5 ml/min flow rate

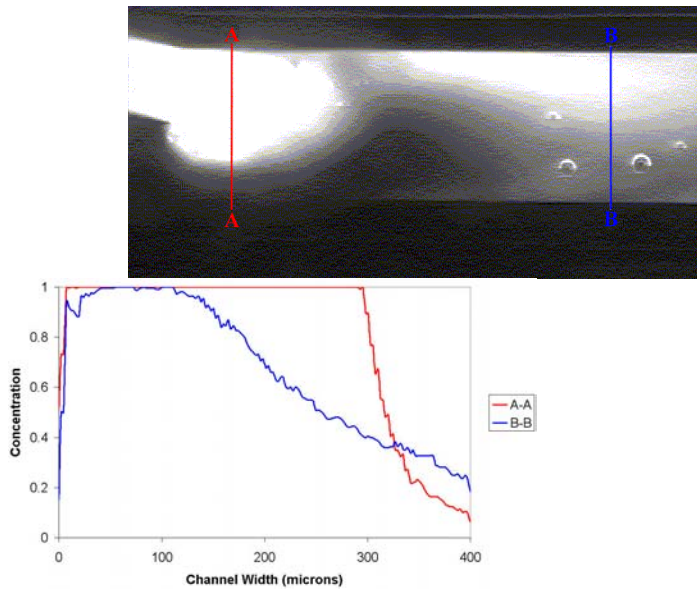


Figure 6.14: Concentration as a function of downstream distance for fluorescein in the Micro-mixer System.

6.4.2 Microvalve Characterization

Check valves are required for the micromixer system to work. The check valve design that has been developed has been tested to measure the difference in flow resistance for the open and closed direction. A syringe pump was used to deliver a known flow rate and a pressure transducer used to determine the resulting pressure drop (and hence flow resistance). The ratio of resistances for the closed and open directions for water has been measured at around 100:1.

CFD-ACE+ was used to numerically simulate Newtonian fluid flow through the microvalve. Model predictions showed good agreement with corresponding experimental flow visualization data as shown in Figure 6.15. Experimental investigation of non-Newtonian flows through the micro-fluidic valves were also conducted. The flow of DNA-laden fluids through the micro-check valves was studied. The check valves provided a platform to investigate the effects of complex geometries on fluid flow patterns as well as the effects of these flows on DNA. The experimental data shows significant elongation of the DNA molecules through several parts of the check valve as well as areas of recirculation where the DNA is able to recoil. The DNA never completely coils while in the flow apparatus because of the long relaxation time. However, this research indicates that micro-fluidic controls structures will have significant effects on large molecules and have to be designed with these aspects in mind.

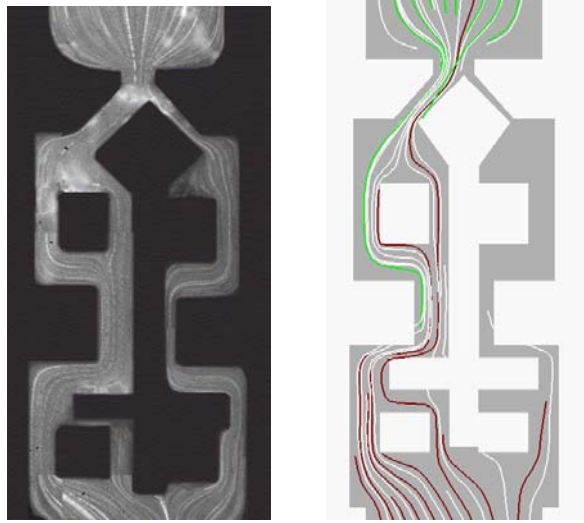


Figure 6.15: Experimental (left) and numerical flow visualization for Microvalve

7. REDUCED-ORDER MODELS AND MIXED DIMENSIONALITY

A reduced-order modeling capabilities has been developed within the framework of CFD-ACE+. It is a key capability required for extending the multiphysics CFD-ACE+ software suite for system-level simulations. Reduced-order (one-cell) models have been developed for pressure-driven incompressible microfluidics flow, electrokinetic transport and free-surface flows. The mixed-dimensionality capability which allows for coupling of multi-cell models with the one-cell model, or 0-D (network-type) point models, is another key capability developed in CFD-ACE+ for system-level analysis. The following types of mixed-dimensionality simulations are possible:

- Serial coupling between 3-D/2-D and 1-D/0-D elements: Important when certain regions necessitate high-fidelity simulations while other portions can be accurately described using one-cell or lumped-parameter point models;
- Hybrid 2-D/3-D and 1-D models (1 1/2-D or 2 1/2-D models): Important when one-dimension (say channel height) is significantly smaller than the other two dimensions so that multiple cells aren't needed across that dimension to accurately resolve physical phenomenon; and
- Embedded 1-D models within 2-D/3-D models (Filament Capability): Enables multi-scale simulations in situations where there are disparate, overlapping geometric length scales within the same computational domain.

Example test cases that demonstrate the utility of the reduced-order models as well as the mixed-dimensionality capabilities are presented in the following sections.

7.1 One-Cell Model for Incompressible Pressure-Driven Microfluidic Flows

7.1.1 Theory

Channel flows have some specific characteristics. For certain low range of Reynolds number, flows create laminar boundary layers near the wall regions. If the channel aspect ratio (channel length divided by height) is large enough, the flow inside the channel is fully developed. It is possible for CFD software to simulate such flows with help of theoretical analysis. The one-cell wall model for incompressible is developed for this purpose.

Model Assumptions: One cell model assumes that the flow velocity distribution between two walls facing each other (parallel or not) achieves a parabolic profile between these walls. This assumption is derived from fully developed channel flows and is true for laminar flow between straight parallel walls. It is approximately true for flows between bending walls. However, if the walls change their shapes smoothly, this assumption will not create much difference. It should be pointed out that in order to capture the correct flow quantities, such as pressure gradient, shear force, etc., between sharper turned walls, we may need other numerical models to account for the pressure loss in the bend.

Model Description: Let us assume laminar flow passing through between two walls. The flow boundary conditions are: $U = U^1$, at wall 1; and $U = U^2$, at wall 2. Since the velocity distribution is parabolic, we prescribe a parabolic profile for velocity as:

$$U = a * y^{**2} + b*y + c \quad (7.1)$$

where a, b and c are constants and y is local distance normal to the wall. The shear stress therefore can be calculated as

$$\tau = \mu \left(\frac{\partial u}{\partial y} \right)_w = b \quad (7.2)$$

From boundary conditions, we can determine the two constants in Equation 7.1. The third constant can be determined from U at center, which is obtained by solving the Navier-Stokes (N-S) equations. However, CFD-ACE+ solves the N-S equation to get cell volume average value. If we use this average velocity to compute the shear stress, we will get the stress to be lower than the real value. Therefore, we add one more condition to determine the third constant. This new condition is:

$$U = \bar{U} + \delta \quad (7.3)$$

\bar{U} is an average value obtained from CFD solutions. δ is the difference between the real value and numerical solution. The value U can be determined from:

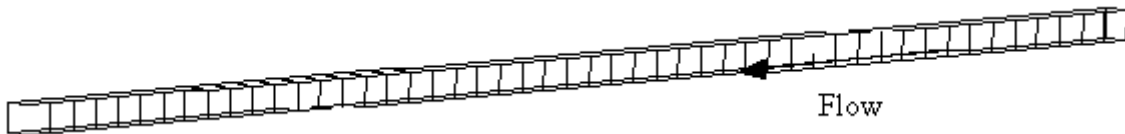
$$\bar{U} = \frac{1}{v} \int U dv \quad (7.4)$$

where v is cell volume. We use U to compute shear stress and put it into the boundary condition of the N-S equations in CFD-ACE+.

7.1.2 Model Application for Straight Channel Flow

Figure 7.1 shows the geometry of a microchannel duct chosen for the demonstration test case. Simulations were performed using both a 3-D model and the one-cell model. The analytical solution for the test case was also obtained to assess the accuracy of both the 3-D and 1-D simulations.

One-Cell and Multi-Cell Simulations: A geometric model was created for a 10x10 micron rectangular channel of length 500 microns. Both 3-D and 1-D meshes were generated for the flow domain (Figure 7.1). The 1-D grid had 1x1x49 cells in the x, y and z directions, respectively. The corresponding 3-D grid structure had 9x9x49 cells. Water at room temperature was used as the fluid flowing inside the microchannel. The fluid inlet velocity was taken as 0.001 m/s. The CFD-ACE+ solver was used to obtain the flow solutions. Symmetry boundary conditions were set on the channel side walls to enable comparison of simulation results with 2-D flow analytical solutions. Simulations were also performed with wall boundary conditions on all the channel walls (3-D flow).



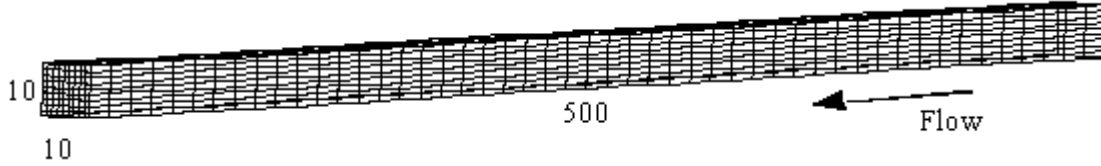


Figure 7.1: Channel geometry and grid for the one-cell and multi-cell simulations

Analytical Solution for Channel Flow: An analytical solution was derived from the Navier-Stokes momentum equation for obtaining the pressure gradient in a 2-D channel flow. The momentum equation breaks down to the form shown in Equation 7.5 for fully developed steady state flow conditions.

$$\frac{d}{dy} \left(\mu \frac{du}{dy} \right) = \frac{dP}{dx} \quad (7.5)$$

Integrating and solving for u we get

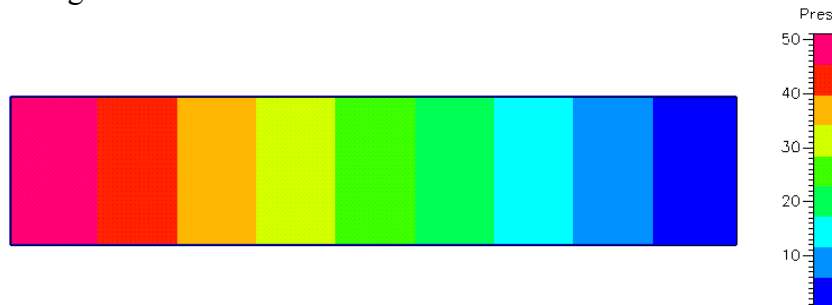
$$u = \frac{1}{2\mu} \frac{dP}{dx} (y^2 - yb) \quad (7.6)$$

where: u = velocity at any cross section of microchannel, dP/dx = Pressure gradient and b = channel height (equal to channel width (w) in this case). Using Equation 7.6 and evaluating the channel mass flow, we get an expression for the pressure gradient along the channel length:

$$\frac{dP}{dx} = \frac{-12\mu}{bw} u \quad (7.7)$$

For this problem, the analytical solution for pressure gradient was calculated as: $dP/dz = 12 * 8.6e-4 * 0.001 / (10e-6)^2 = -103200 \text{ N/m}^3$.

Comparison of Results for 2-D Channel Flow: The pressure distribution along the microchannel is shown in Figure 7.2 for both cases. Table 7.1 compares the channel pressure drop for both cases with the analytical solution. The one cell model solution was much closer to the analytical solution. This shows that the one cell model does better than a coarse grid multi-cell model, for simulating flows in such geometries. Figure 7.3 shows the variation of pressure along the channel length for both the models.



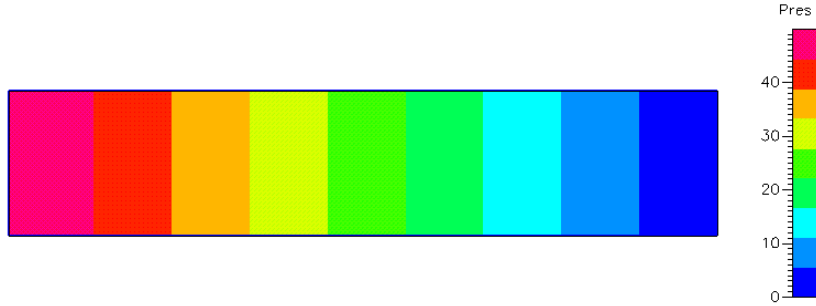


Figure 7.2: Pressure distribution (in Pa) along duct (scaled in Y direction) for one-cell (top) and multi-cell (bottom) models

Table 7.1: Pressure Gradient Along the Microchannel for 2-D Channel Flow

Model	Pressure Gradient (N/m ²)	Error (%)
Analytical	103200	-
Multi-cell	100707.7	2.41
One cell	103192.9	0.007

Comparison of Results for 3-D Channel Flow: Table 7.2 compares the pressure gradient along the microchannel length for both the multi-cell and one-cell model. The pressure gradient predicted by the multi-cell model was larger than the one-cell model results. The variation of pressure along the duct for both models is shown in Figure 7.3

Table 7.2: Pressure Gradient Along the Microchannel for 3-D Channel Flow

Model	Pressure Gradient (N/m ²)
Multi-cell	233703.5
One cell	206304.3

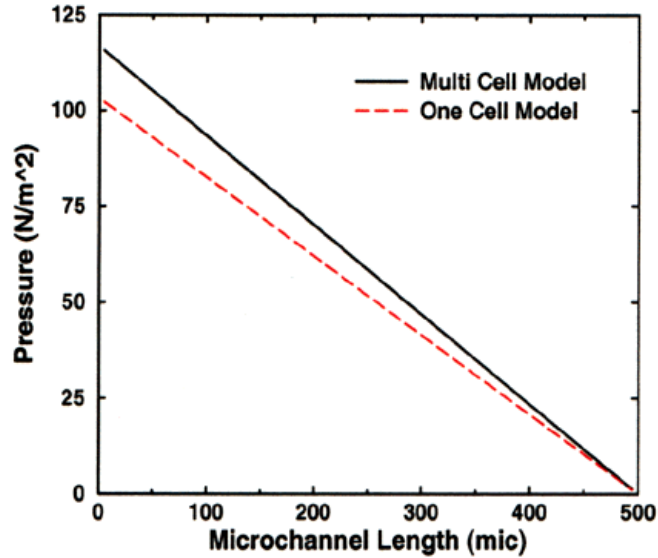


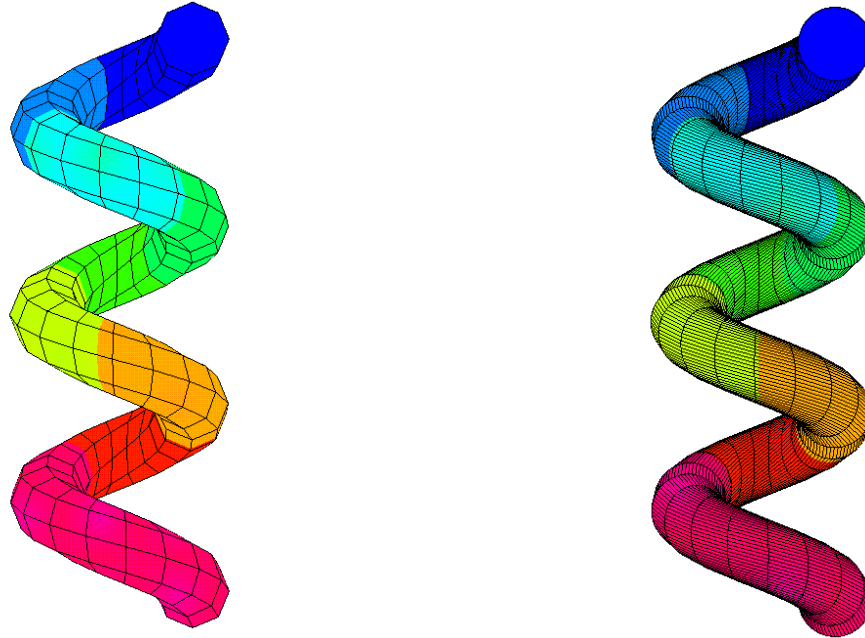
Figure 7.3: Pressure variation along the microchannel length for 3-D flow case

7.1.3 Model Application for Flow in a Spiral Microchannel

Incompressible flow in spiral microchannel was simulated using the one-cell wall model. Polyhedral type cells were created with only one cell at each cross-section in the pipe. In order to apply correct boundary condition for velocity components, a multi-edge structure on the pipe surface was used. A circular parabolic velocity profile was assumed. When the number of edges along the pipe surface are increased, the pressure drop along the pipe and the shear force on the surface is expected to approach the results from analytical solution for a straight circular pipe. Comparisons of pressure drop and shear force for different cases with increasing number of edges are listed below in Table 7.3. Pressure distributions in the spiral channels with two different number of edges are shown in Figures 7.4a and 7.4b. The channel inlet is at bottom of the figure.

Table 7.3: Comparison of Pressure Drop and Shear Force Along Spiral Microchannel for Various One-Cell Models with Analytical Solutions

Number of edge	Pressure drop (N/m ²)	Shear force (N)
4	-16.000	3.200
8	-9.374	2.651
16	-8.316	2.546
32	-8.076	2.521
64	-8.020	2.515
The analytical solution	-8.000	2.513



(a) One-cell model with 8 edges

(b) One-cell model with 64 edges

Figure 7.4: Pressure distribution along a spiral microchannel

7.1.4 Model Application for Flow Through a 90 Degree Bend

The geometry and grid structure of the microchannel bend is shown in Figure 7.5. The fluid used in the simulations was water at room temperature. The inlet velocity of the fluid was 0.001 m/s. The one-cell simulations were performed with and without incorporation of momentum losses at the bend.

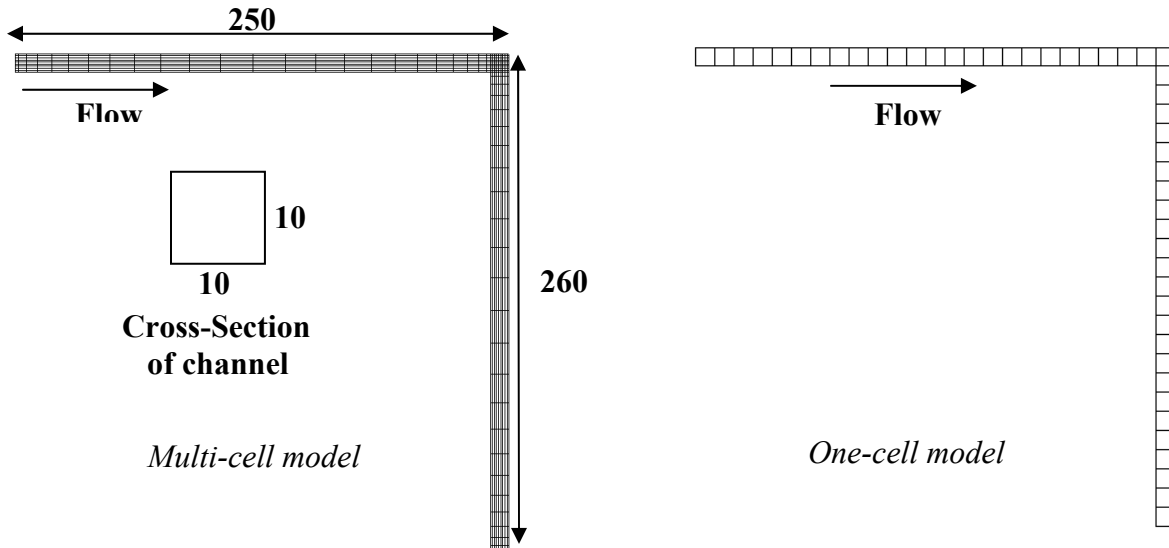


Figure 7.5: Channel geometry and mesh for the bent channel simulations

Without Bending Loss: Figure 7.6 shows the pressure distribution in the microchannel for both the multi-cell and the one-cell model without bending losses. As expected, the one cell model under-predicts the pressure drop in this case as it is not able to fully account for the bending

losses in the microchannel. The pressure variation along the microchannel length for both the models is compared in Figure 7.7a.

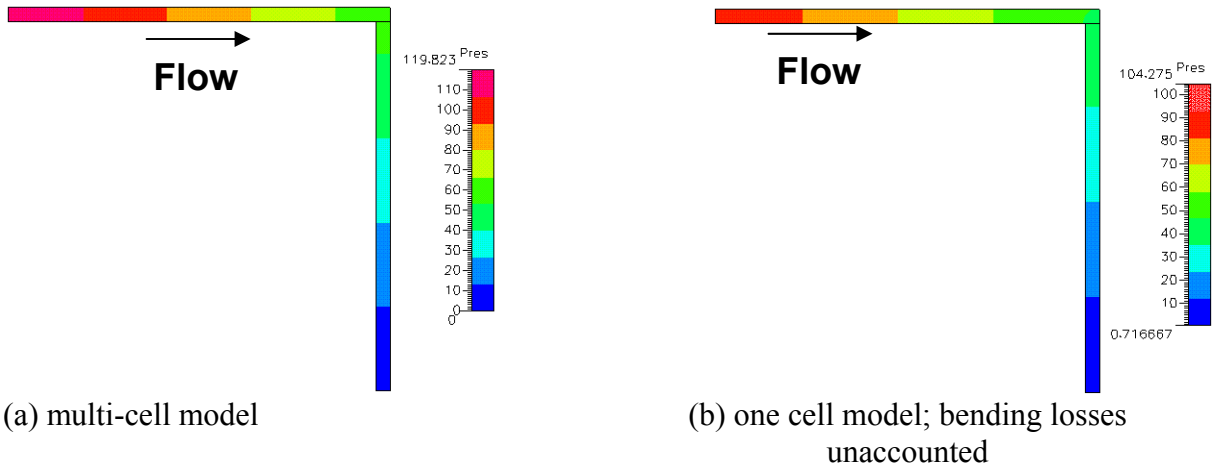


Figure 7.6: Pressure distribution in the microchannel bend

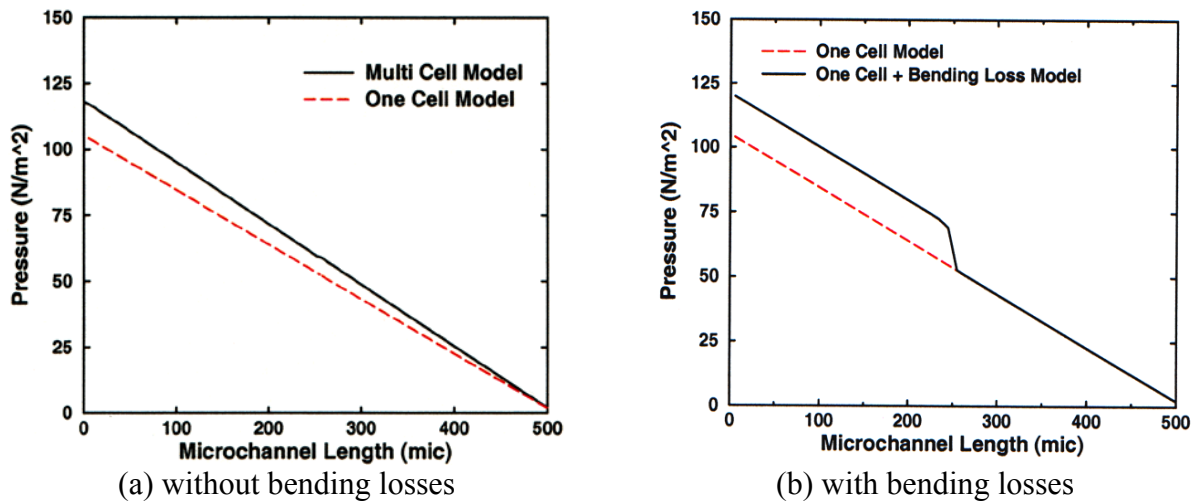


Figure 7.7: Pressure variation along the microchannel length

With Bending Losses: The one cell model was refined to account for the bending losses, through the incorporation of momentum resistance source terms in the computational cells within the bend. Figure 7.7b shows the variation of pressure along the microchannel length for the one cell model with and without the bending loss model. The sharp drop seen in pressure is due to bending losses when the fluid negotiates the bend. The overall pressure drop is now in good agreement with that predicted with the multi-cell model. Figure 7.8, which shows the pressure distribution across the microchannel bend for the modified one-cell model, confirms the much closer agreement between the one-cell and multi-cell simulations.

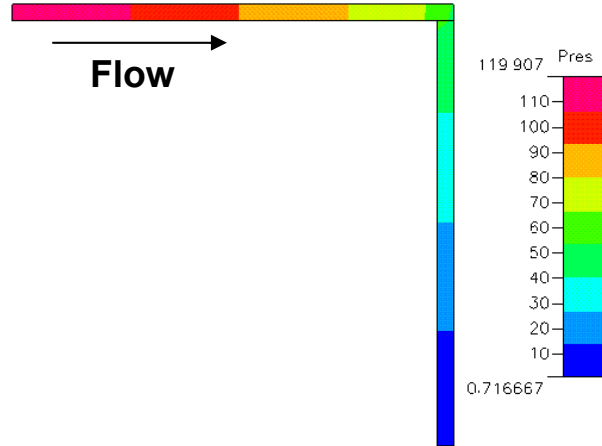


Figure 7.8: Pressure distribution in the microchannel bend predicted with the one-cell model modified to account for bending losses

7.1.5 Reduced-Order Model Library for Flows in Bends

Multi-dimensional modeling of flow through a complicated network of channels in a typical microfluidic device is computationally intensive. If the aspect ratio (length/height) of the channel is very large, a fully developed velocity profile can be safely assumed, since it is shown in literature (Potter and Foss, 1982) that entry length (L_e) for channel flow is $L_e = 0.04 Re$, where Re is the Reynolds number. Therefore, if we neglect entry effects, the system can be modeled as one-dimensional flow with a parabolic velocity profile. This model will work very well as long the walls of the channel are parallel to each other and changes in the shape of the wall are extremely small. However, to simulate pressure drop and shear stresses in non-straight channels, we need to improve the one-dimensional models so that pressure loss due to curvatures, bends, sudden expansions or contractions, etc. can be accounted for properly. Here, we focus on accurately modeling pressure loss in a miter bend in microchannels.

The 1-D models in the previous section were limited to a single specific case in which the pressure losses at the bend for that particular case were calibrated through comparison of the 1-D solution with the corresponding high-fidelity solution. In order to create a library of reduced models for such a case, we performed a systematic study in order to obtain mathematical correlations between the pressure loss coefficients, channel width, bend angle and Reynolds number.

Theory: The one cell wall model described previously does not account for pressure loss due to a bend, since the additional loss is primarily the result of secondary flows. In fluid dynamics, loss is expressed, most conveniently, by an equivalent length of a straight pipe. This length depends on the radius of curvature of the bend. However, in most of applications, a miter bend (bend with a sharp corner) is often used (Fox and McDonald, 1978). This type of bend is also appropriate for microfluidic applications, and hence is modeled in the current study.

In CFD-ACE+, the pressure losses are implemented through a momentum resistance formulation. Momentum resistance is often used to simulate effects of physical obstructions within the flow domain. This resistance is characterized by relating the pressure gradient with velocity through the following formulation:

$$\nabla p = \rho \left(\frac{[K_l]}{2\beta} + \left| \vec{V} \right| \frac{[K_q]}{2\beta} \right) \bullet \vec{V} \quad (7.8)$$

where $[K_l]$ and $[K_q]$ are the coefficient matrix for the linear and quadratic terms, respectively, ρ is the density, β is the porosity of the medium. It is very well known that the losses in a flow system are proportional to the square of the velocity and it is appropriate to assume that $[K_l] = 0$ and $\beta = 1$ (non porous medium). The task, then, is to compute values of $[K_q]$ for various channel dimensions and bend angles.

Method of Approach: A large number of simulations were performed to calculate $[K_q]$ for various channel widths and bend angles. We first simulated pressure drop across a straight channel using a 2-D analysis. A full two-dimensional analysis was then performed with the bend. The difference in the total pressure drop between two systems gave us the pressure drop due to the bend. The values of U_{\max}^2 vs. ΔP were plotted on a log-log chart as shown in Figure 7.9. $[K_q]$ was computed as a function of channel width and angle of bend from the slopes. The simulation of the full geometry (with the bend) was then repeated using the one-cell model. However, a momentum resistance was assigned in the region corresponding to the bend (as shown in Figure 7.10) based on the computed values of $[K_q]$. The results from this simulation are compared with full two-dimensional simulation for various Reynolds number.

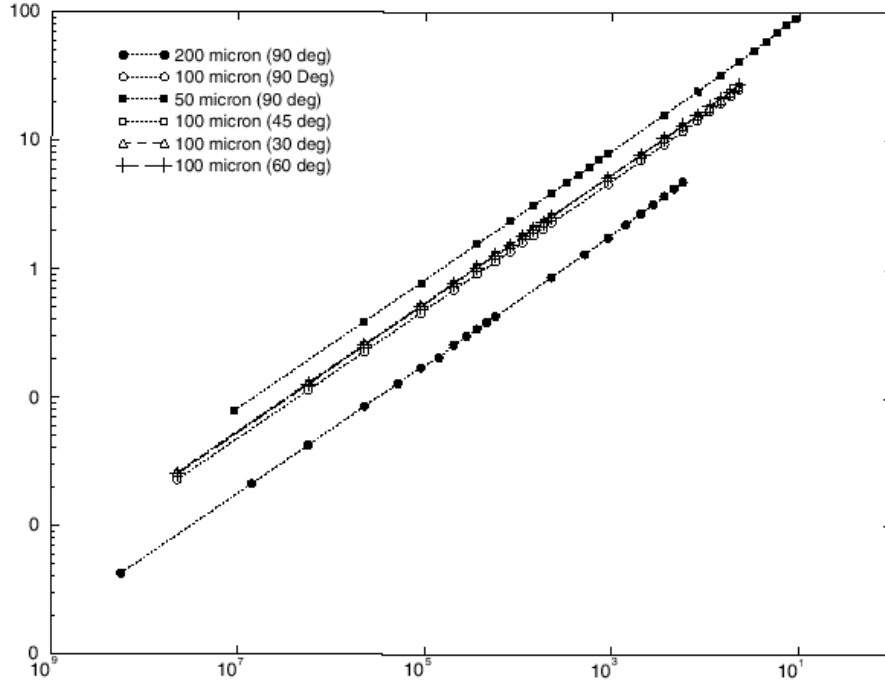


Figure 7.9: Pressure loss (ΔP , Y-axis) due to a bend as a function of U_{\max}^2 (X-axis)

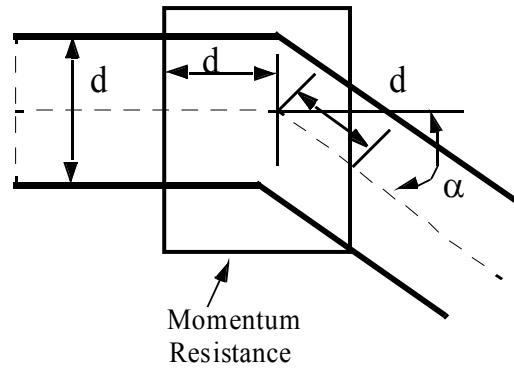


Figure 7.10: Schematic of a miter bend. The momentum resistance is applied in the area of the channel shown inside the box.

Results and Discussion: Figure 7.9 clearly shows that pressure loss due to the bend varies linearly with the square of maximum velocity when shown in a log-log plot. The pressure loss varies significantly with width of the channel and is influenced very little by the angle of the bend. Table 7.4 shows that the results of the high-fidelity 2-D simulation compare reasonably well with corresponding results for the modified 1-D model (with momentum resistance terms) at different Reynolds numbers. This study thus indicates that flow channels with bends can be modeled via momentum resistance formulation accurately. The quadratic coefficient [Kq] in this formulation does not vary much with the angle of the bend. It is a strong function of channel width. A database of [Kq] can be easily developed and incorporated into ACE+, which could be used by MEMS designers to accurately predict pressure drops using the reduced order computational models.

Table 7.4: Comparison of 1-D Model with Momentum Resistance and 2-D Simulations

Re	ΔP (2-D Simulation)	ΔP (1-D Model with Momentum Res.)	% Error
0.01	0.159074	0.167503	5.3
0.1	1.59112	1.67516	5.28
1.0	15.9499	16.7654	5.1
10	163.991	169.811	3.55

7.1.6 Model Applications for Flow Through Microfluidic Valves

The one-cell model was applied for simulating flow through passive microfluidics valves. Multi-cell solutions were also obtained for the valves for comparison. Both solutions were also compared with experimental data on pressure-flow characteristics for the valve.

Method of Approach: The Tesla valve, which was developed on the DARPA/MTO MicroFLUMES project, was chosen as the demonstration valve. A geometric model was constructed for the valve (Figure 7.11). Both 3-D multi-domain structured grids and a 1-D grid were constructed using CFD-GEOM for the valve (Figure 7.12). The 3-D model had 62,238 cells, while the 1-cell model had 196 cells. The pressure values for the valve were set at one outlet ranging from positive 0.06 MPa to negative 0.06 MPa at 0.01 MPa intervals, while the other outlet was consistently kept at a value of 0 Pa. Kinematic viscosity was designated as $8e-7$ kg/ms and the density was set at 1000 kg/m³, corresponding to properties of water. The

resulting mass flow rate for a prescribed pressure drop was computed and compared against corresponding experimental data (Deshpande, et al., 1998).

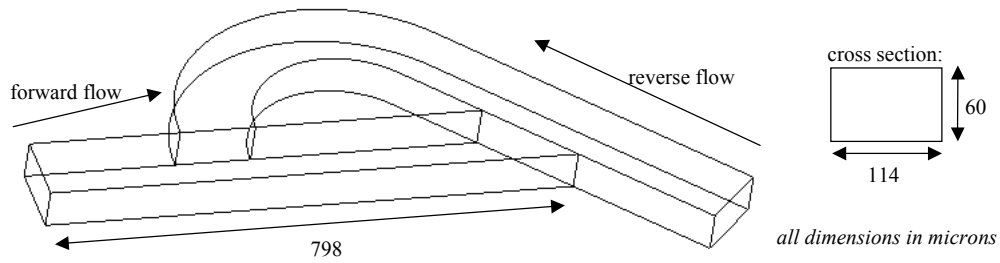
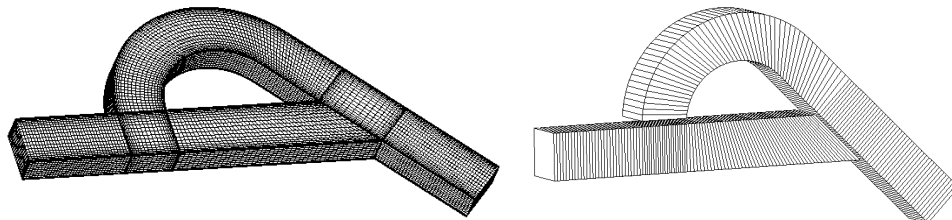


Figure 7.11: Tesla valve geometry and dimensions



a. multi-cell mesh

b. single-cell mesh

Figure 7.12: Multi-cell and single-cell grids for the Tesla valve model

Results: Simulation results for the single-cell and multi-cell models are compared against experimental data in Figure 7.13. Both models show the same qualitative trend as the experimental data, i.e. there is a decrease in fluid flow rate in the reverse direction. This implies that in a continuous flow cycle, the valve can be used for a net transport of fluid in the forward flow direction.

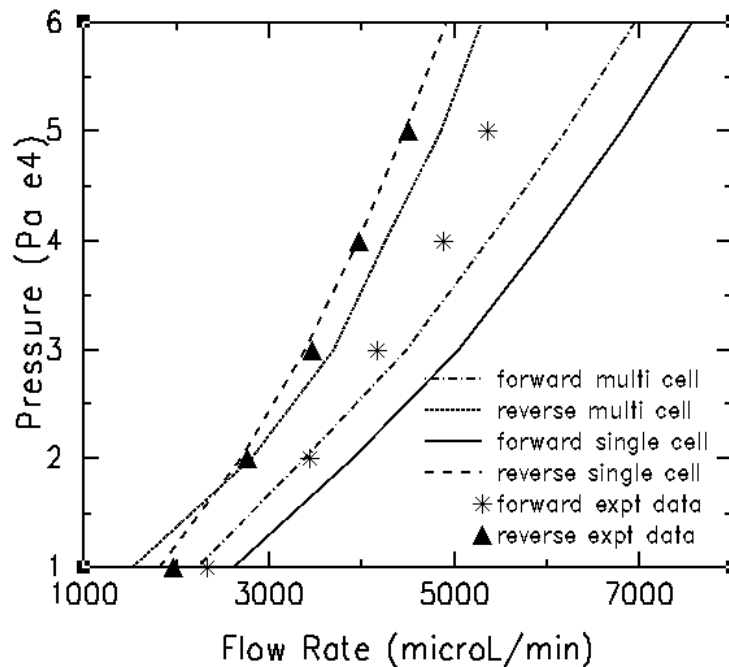


Figure 7.13: Simulated (3-D and 1-D models) and experimental pressure-flow characteristics for Tesla valve

7.2 One-Cell Model for Electrokinetic Flows

The theoretical framework for the one-cell model for electrokinetic flows is identical to that for multi-cell simulations, and has been described in detail earlier in Section 5.1.1. Therefore, here we only present sample cases that demonstrate the ability to simulate electrokinetics flows using the single-cell approach.

7.2.1 Model Application for Straight Channels

In order to test the 1-D cell simulation of electroosmotic and electrophoretic transport of a charged sample, we set up the following 1-D meshes in a channel that is 2 cm long and 0.02 cm high. Figure 7.14 shows the geometry and mesh. The positively-charged sample is initially at the channel left end. The electrical potential are 100 Volt and 0 Volt at the left and right end respectively. The wall potential is set to be -1 , so that the electroosmotic flow will be created from left to right. The charged sample will be carried with the flow. The images in Figure 7.15 clearly show the sample motion.

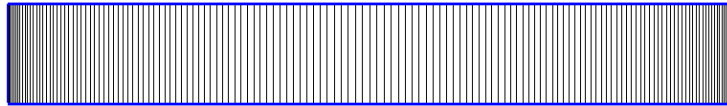


Figure 7.14: 1-D Geometric model for electrokinetic channel flow

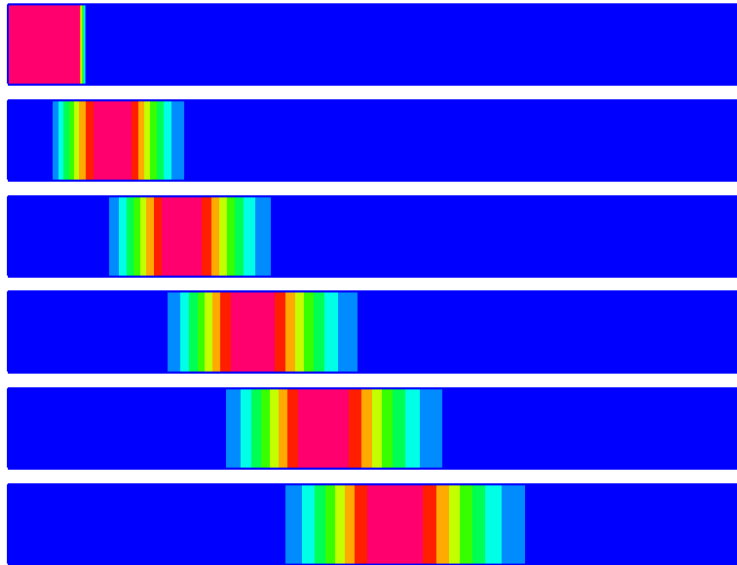


Figure 7.15: Electroosmotic transport of charged sample at different time instants

7.2.2 Model Application for Double S-Shaped Channels

Problem Description: In this problem, the inner radius of circle is 4×10^{-4} m and the thickness of the circle is 10^{-4} m. Two ions, A+ and B+ are injected from the bottom inlet. The potential at the inlet is 100 V and potential at the top outlet is 0 V. The mass fractions of both ions are 10^{-3} . The diffusivities of ion A+ and B+ are 5×10^{-8} and 2×10^{-8} m²/s, respectively. For comparison with corresponding 2-D simulations, we calculated the solution for a 2-D grid at exactly the same conditions as in the 1-D case (see Figure 7.16). The time step dt was 0.001 second.

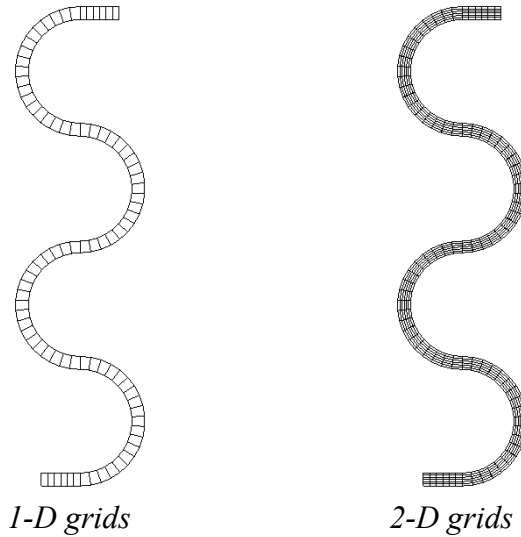


Figure 7.16: Channel geometry and 1-D/2-D grids for the double S-shaped channel

Results and Discussion: The 1-D results are shown below for A^+ and B^- in Figure 7.17. It can be seen that the ion B^+ transports slower than ion A^+ due to the smaller diffusivity value. The 2-D results for B^+ transport are shown in Figure 7.19. A comparison of corresponding images in Figure 7.18 and 7.19 shows that locations of ions at different times are almost same for both cases. The 1-D model predictions therefore seem to be in good agreement with the corresponding 2-D solutions.

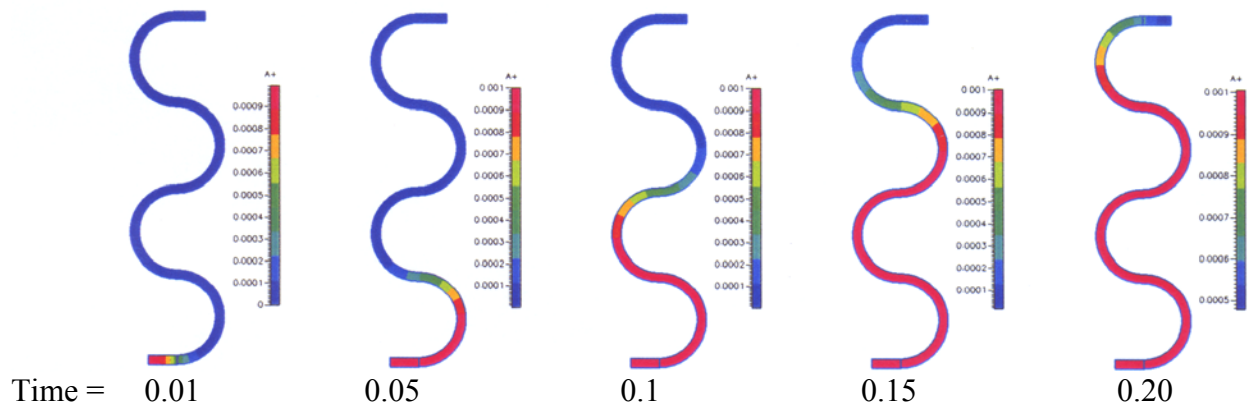


Figure 7.17: 1-D solutions of A^+ concentration contours at different instants (in secs.)

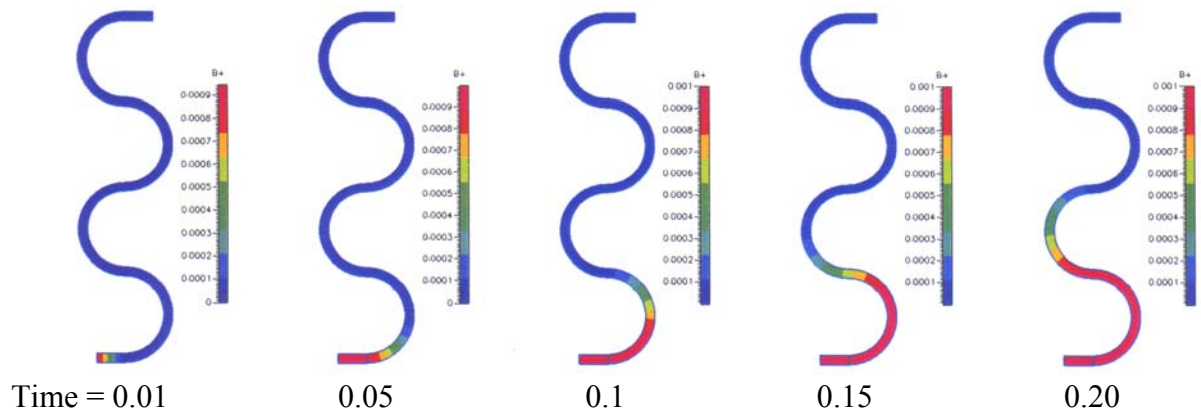


Figure 7.18: 1-D solution of B+ concentration contours at different instants (in secs.)

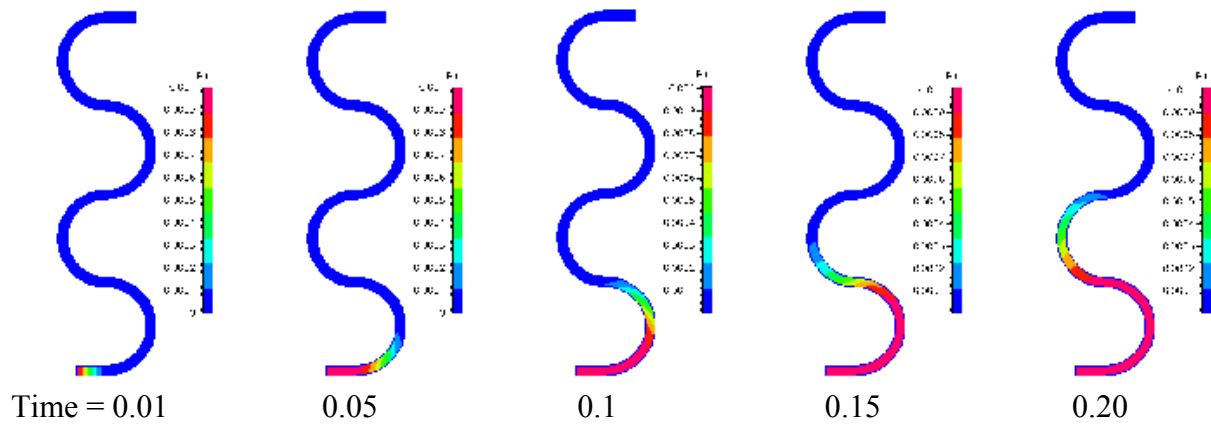


Figure 7.19: 2-D Solutions of B+ concentration contours at different instants (in secs.)

7.2.3 Model Applications for a Bent Square Pipe

Here, sample transport is simulated using the 1-D model. The sample ion A+ is located in a spot at the left bottom pipe initially. The pipe is 1.5 mm long and 1.05 mm high. Figure 7.20 shows the geometry and initial sample location, and Figure 7.21 shows the locations of sample A+ at different time instants.

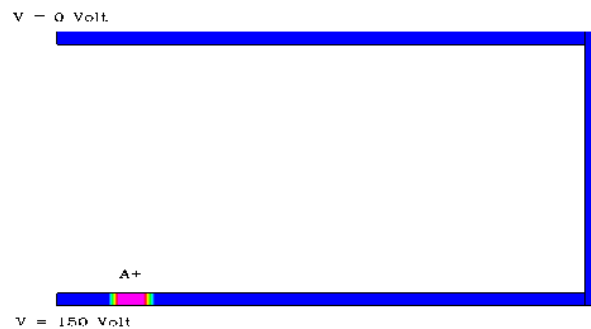


Figure 7.20: Bent square channel geometry and initial location of sample A+.

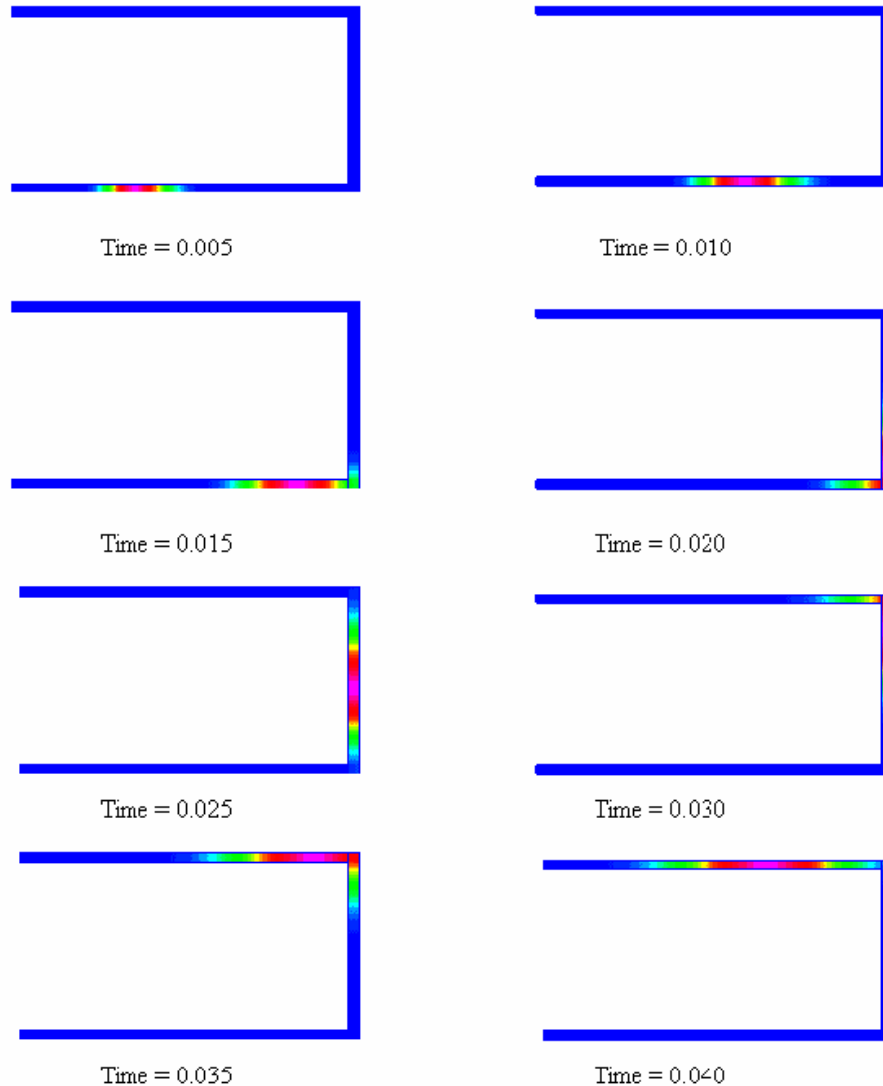


Figure 7.21: Sample locations at different time instants (in secs.) in bent square pipe

7.3 One-Cell Model for Free Surface Flows

7.3.1 Model Description

The reduced 1-D model capability in CFD-ACE+ was extended for Volume-of-Fluid (VOF)-type calculations in CFD-ACE+. The VOF module is used to simulate free surface flow, which occurs during liquid filling in microchannels. A second-order shear stress formulation, based upon the Heleshaw model, is used. The liquid-wall contact angle (which characterizes the extent of hydrophobicity of the surface) and corresponding liquid-front curvature (in the form of a polynomial function) are prescribed in the simulations.

7.3.2 Validation Test Case

The 1-D model is validated against the analytical solution (shown below) for surface tension-driven liquid filling in a straight microchannel (Yang and Przekwas, 1998)

$$L = \left(\frac{ht\sigma \cos \theta}{3\mu} \right)^{1/2} \quad (7.9)$$

where L is the penetration distance of the liquid front, h is the channel width, t is the time, μ is the liquid viscosity and θ is the contact angle. Two numerical test cases with different initial conditions are presented in Figure 7.22. In the first case, the liquid front starts from a static position. For this case, one clearly sees that the numerical solution lags behind the analytical predictions by a fixed penetration distance due to inertial effect. However, the second case corresponding to a start with an initial field based upon the exact analytical solution shows excellent agreement with the analytical curve.

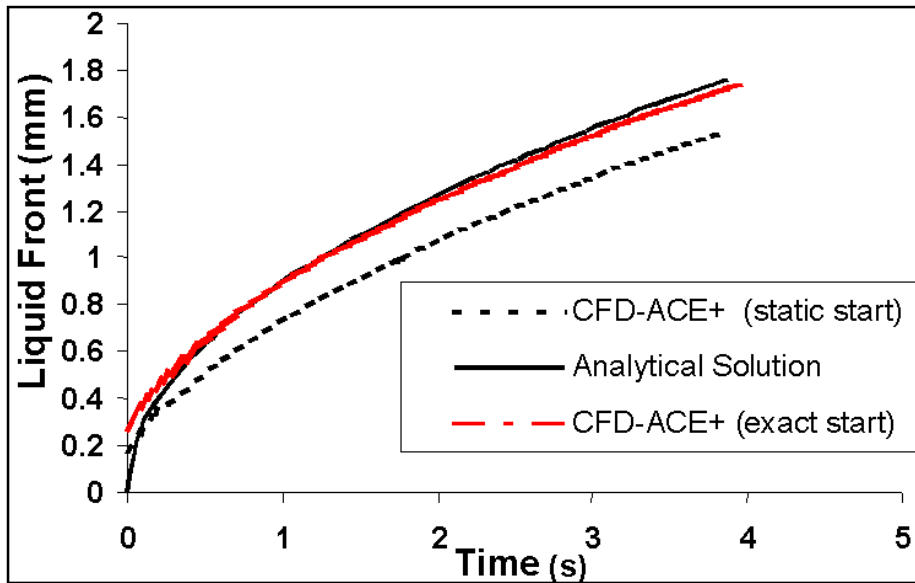


Figure 7.22: 1-D model validation for surface tension-driven liquid filling problem

7.3.3 Comparison Between 1-D and High-Fidelity Simulations

A comparison of results from the 1-D model and a 2-D model for the microchannel liquid-filling test case is shown in Figure 7.23 below. The agreement between the two sets of results is excellent.

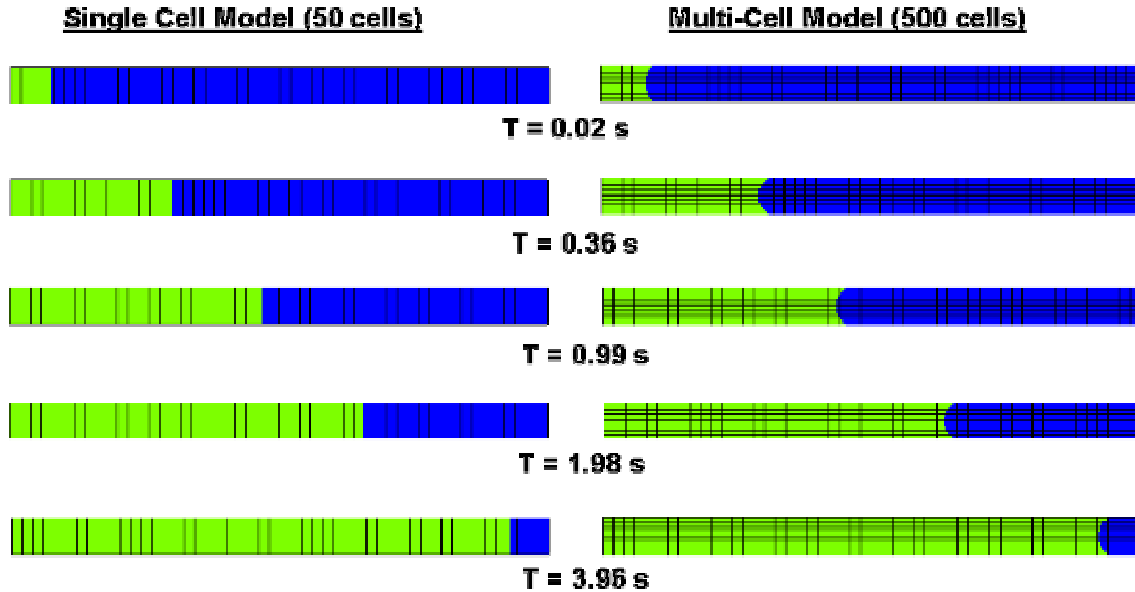


Figure 7.23: Comparison of 1-D and 2-D simulation for microchannel liquid filling

7.3.4 Hybrid One-Cell and Multi-Cell Model Capability

The VOF reduced model was also extended to permit hybrid high fidelity-reduced model simulations. For demonstration purpose, a 2 ½ D model was developed to simulate surface-tension driven filling in a bifurcating microchannel system (see geometry in Figure 7.24) in which the height is much smaller than the channel width. Here, the reduced model assumption was applied to reconstruct the liquid interface along the channel height, whereas a 2-D mesh was used along the width/length. In the reduced model, a second-order shear stress formulation, based upon the Heleshaw model, is used. The liquid-wall contact angle, which characterizes the wettability of the surface, and corresponding liquid-front curvature, in the form of a polynomial function, are prescribed in the simulations. Sample results showing the surface-tension driven filling for a purely hydrophilic case are shown in Figure 7.25.

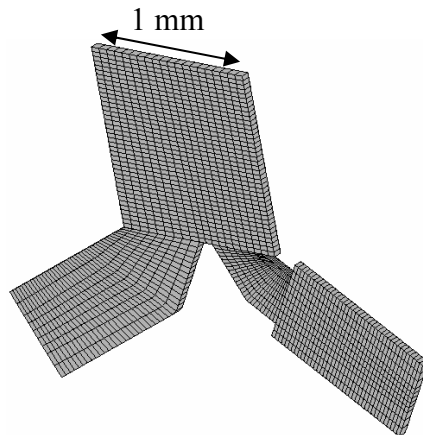


Figure 7.24: Geometric model and mesh for a bifurcating microchannel (45 μm height)

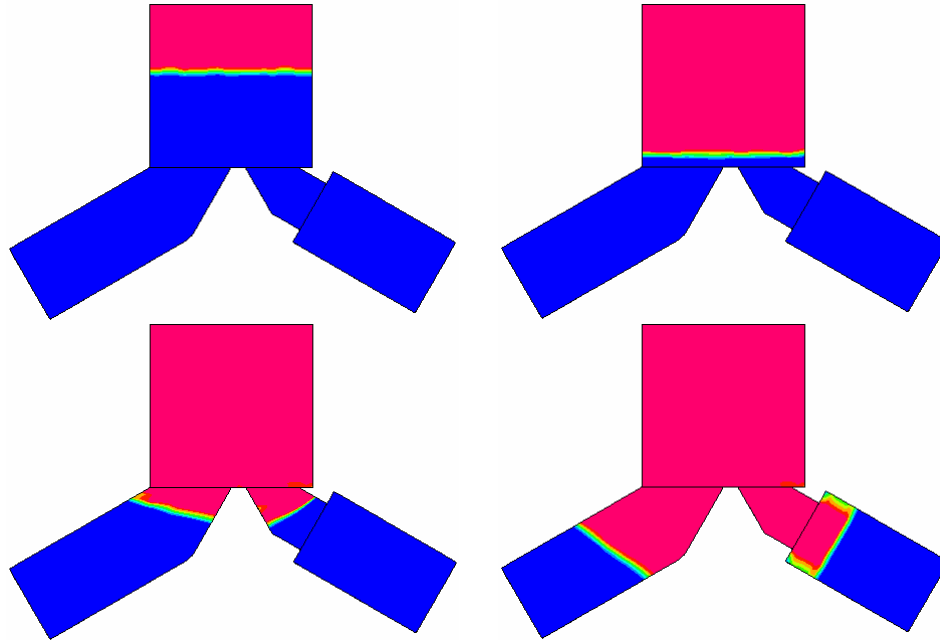


Figure 7.25: Surface tension-driven liquid filling simulation with hybrid model

7.4 Filament Model

7.4.1 Theory

The filament capability enables simulations in domains containing large geometric scale variations without the need to precisely grid the whole domain. Filaments are thread-like structures whose transverse dimension is much smaller than that of the neighboring cells in the base domain. Filaments interact with the base domain in two ways:

- Exchange sources to account for mass, momentum, energy, etc. interactions; and
- Add to cell and cell face blockages in base-domain cells in order to account for the cell face area and volume decrease caused by the presence of the filaments.

The filament concept has been primarily developed to deal with biomicrofluidic and bioMEMS systems that contain embedded objects or components that are pre-dominantly one-dimensional, i.e., long and slender and with transverse length scales much smaller than the isotropic length scales of the multi-dimensional space in which the objects are embedded. In this approach, because the filaments and the background domain are gridded separately, the grid generation tasks are much simpler because the different length scales in filaments domain and background domain are de-coupled. The filaments and background meshes are basically merged together to form a unified simulation environment. During the simulation, physical phenomena such as fluid flow and heat transfer, are solved separately in filament and background, but they interact with each other through source terms which describe the exchange of mass, momentum, energy etc. Although one has to sacrifice some details very close to the filament, the method proves to be very easy to use and very computationally efficient.

7.4.2 Filament Application for Fluid Heating in Microreactor

The application of filament model was demonstrated through simulation of fluid heating in a microfluidic reactor. Fluid heating is accomplished by five heating elements embedded in a solid in the top part of the channel. Filament heating was simulated by imposing a constant temperature of 1000 K at the filaments ends. The results are shown in Figure 7.26. Note the temperature drop in the filament and temperature increase in the solid and the fluid, illustrating the two-way thermal coupling between the filament and surrounding media.

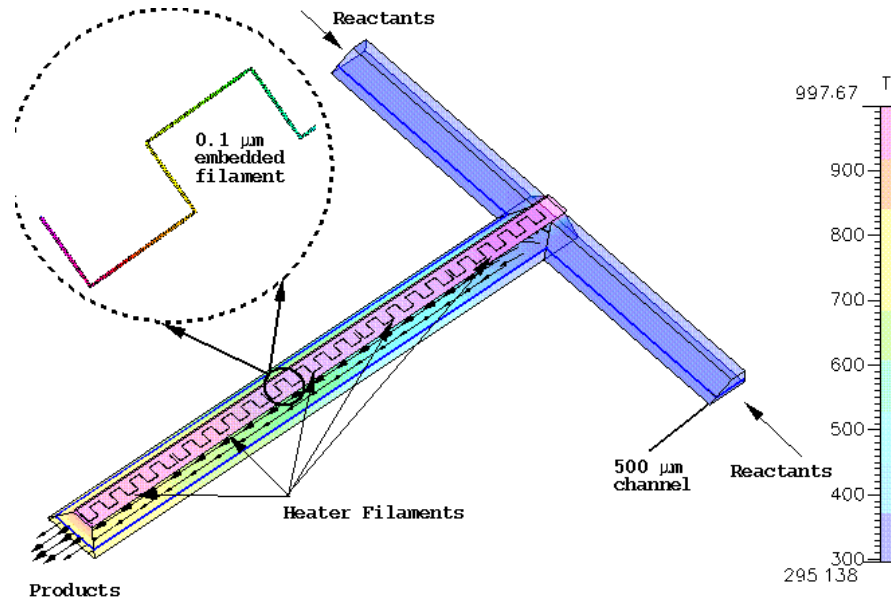


Figure 7.26: Simulation of flow and heat transfer in a microreactor system using filaments

7.4.3 Model Application for a Continuous-Flow PCR System

Problem Description: This next demonstration test case shows the application of filaments for simulation of flow through the embedded object in a continuous flow PCR device. Here the temperature is kept constant over time at different locations in the system and the sample is moved through the individual temperature zones. The time delay for the sample to reach a new temperature depends only on the times needed to transport the sample into the appropriate temperature zone and to heat a fluid element in the capillary. The PCR system simulated is based on a single micro-channel passing repetitively through three temperature zones with temperature of 60 °C, 77 °C and 95 °C, respectively. The channel has a slender shape and its path waves back and forth passing through three temperature zones repetitively. Such a system is a perfect candidate for the filament model.

Method of Approach: In the simulation, the flow channel is simulated as a filament, and the three temperature zones are simulated in the background domain. Figure 7.27 shows the computation grid. The thin thread is the flow channel and the three blocks represent the three different temperature zones. Figure 7.28 shows the temperature distribution inside the channel when the fluid is passing through those temperature zones.

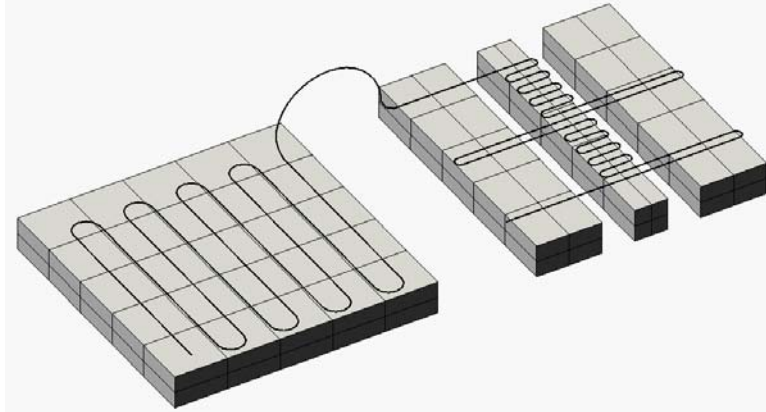


Figure 7.27: Computational domain for continuous flow PCR system

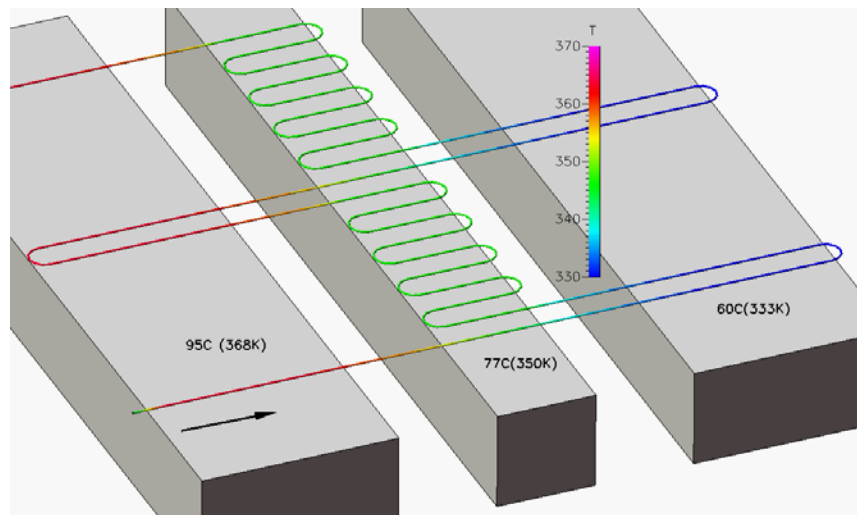


Figure 7.28: Simulation results for continuous flow PCR system

7.4.4 Filament Application for Branching Microfluidic Channels

Branching Filament Capability: One of the major developments was the expansion of filament type from single thread to thread with branches. A double link graph data structure was adapted to represent the filament threads with branches. New grid generation tools have been developed to automatically generate grid cells for different kind of joints as well as regular threads, and connect them together to form a valid computational grid. Currently supported joint types include T-junction, Y-junction and a cross. Figure 7.29 shows a T-junction grid and a tree structure constructed using T-junction.

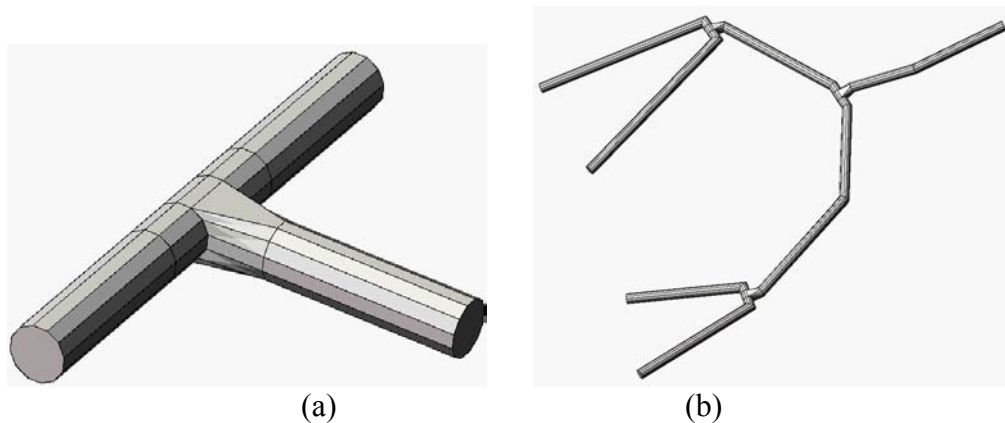


Figure 7.29: (a) T-junction between filaments, and (b) Network of T-junction branches

Sample Applications: Figure 7.30 shows a sample application of the branching filament capability for simulation of heat transfer in a microfluidic bio-chip with a cross joint channel. Heat transfer occurs between the reservoirs through the interconnecting microchannels. Color contour in the figure represent the temperature distribution in the channel and reservoirs.

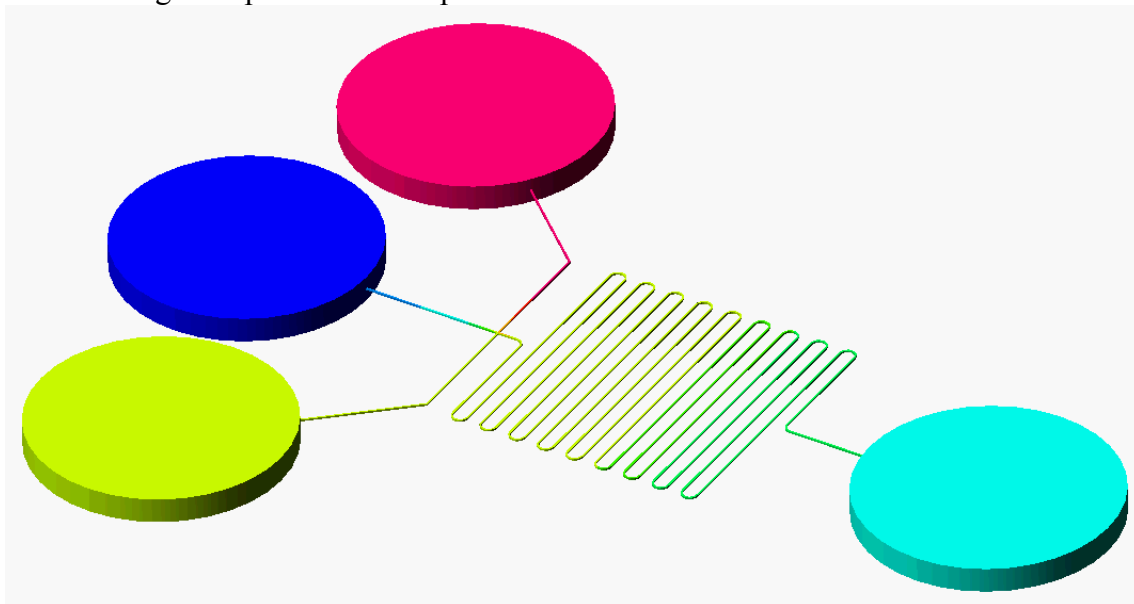


Figure 7.30: Heat transfer between reservoirs and interconnecting channels in a biochip device

A more complex sample problem with branching filaments is shown in Figure 7.31. Here, a high-density chip is cooled by a cooling module with built-in microliquid cooling channels. High density chips usually have a three-dimensional multi-layer structure to hold more transistors in the same volume. The heat generated from a high density chips is significantly higher than a regular single layer chip. Therefore, more powerful cooling mechanism must be introduced to solve the heating problem. The entire cooling module is simulated using the filament model. The microfluidic channels are represented as a set of filaments. The background domain, which is the cooling module body, is simplified as a solid box with heat generated from the top face. Figure 7.31 shows the microchannel geometry, filament grid and

flow direction. Figure 7.32 shows the temperature distribution in the flow channels as well as in the cooling base.

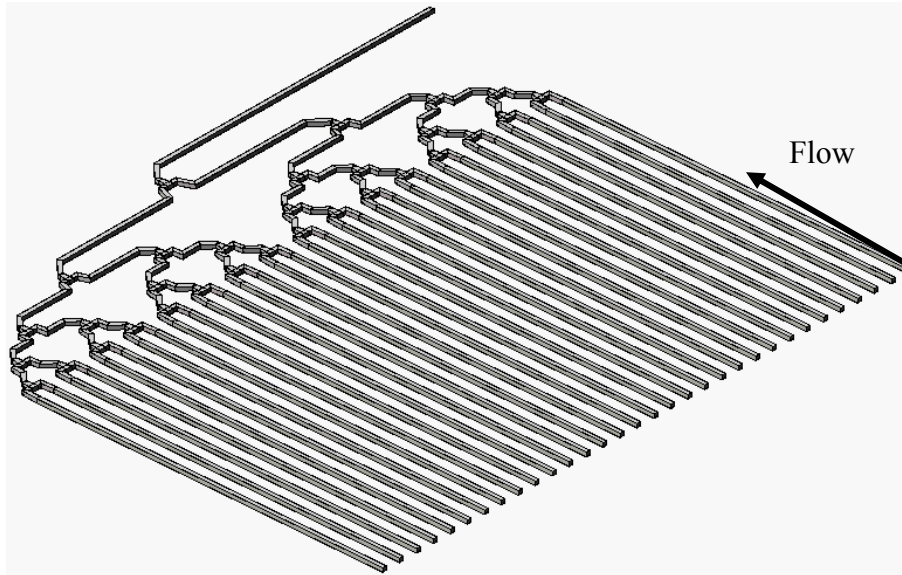


Figure 7.31: Geometry of the microchannels and 1-D filament grid

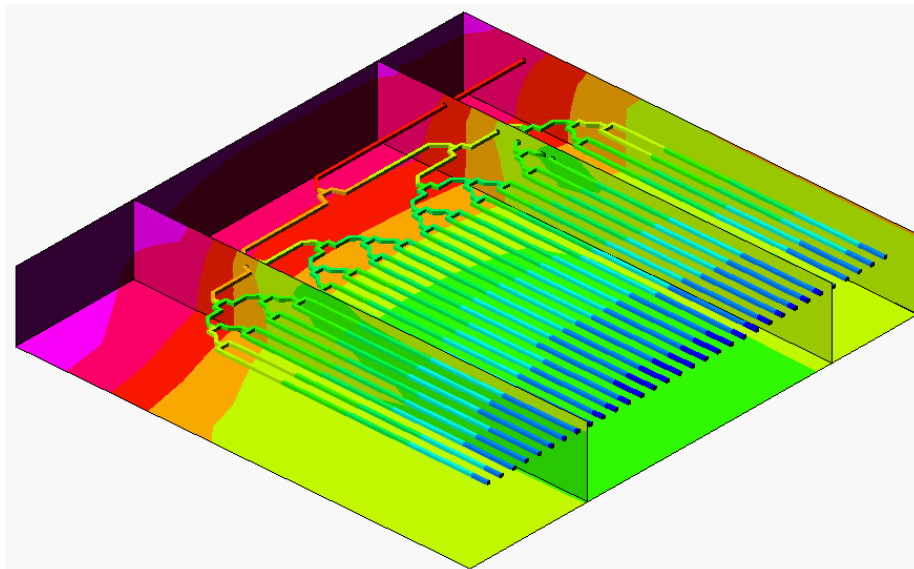


Figure 7.32: Temperature distribution in microchannel network and cooling base

7.5 Serial Coupling Between Multi-Cell and Single-Cell Domains

7.5.1 Model Application for Pressure-Driven Microfluidic Flows

The test case chosen for demonstration of this capability was the static micromixer case, in which flow and mixing were simulated. We simulated both the full 3-D case and the mixed-dimensionality case, which had 3-D elements in the mixing regions and 1-D elements in the supply channels for a single fluid. The 3-D case had 44,280 cells whereas the mixed case had only 27,630 cells (see Figures 7.33a,b). The CPU times for these computations were 71 minutes and 47 minutes, respectively. A comparison of mixing patterns for both cases is shown in

Figures 7.34a and 7.34b. The mixed 3-D model provides a fairly comparable solution with much reduced CPU time.

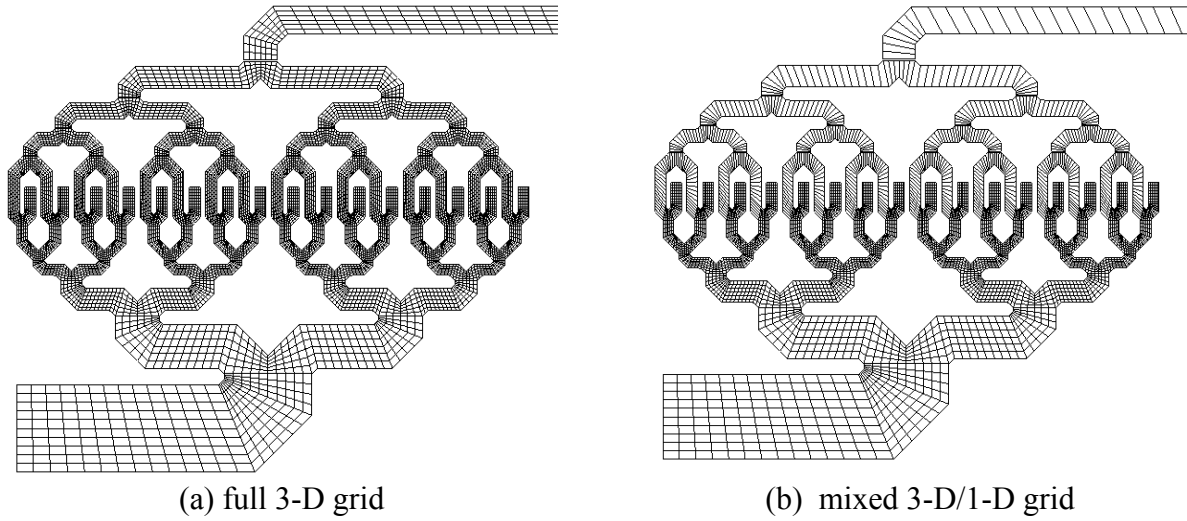


Figure 7.33: Geometric model and mesh for a static micromixer test case

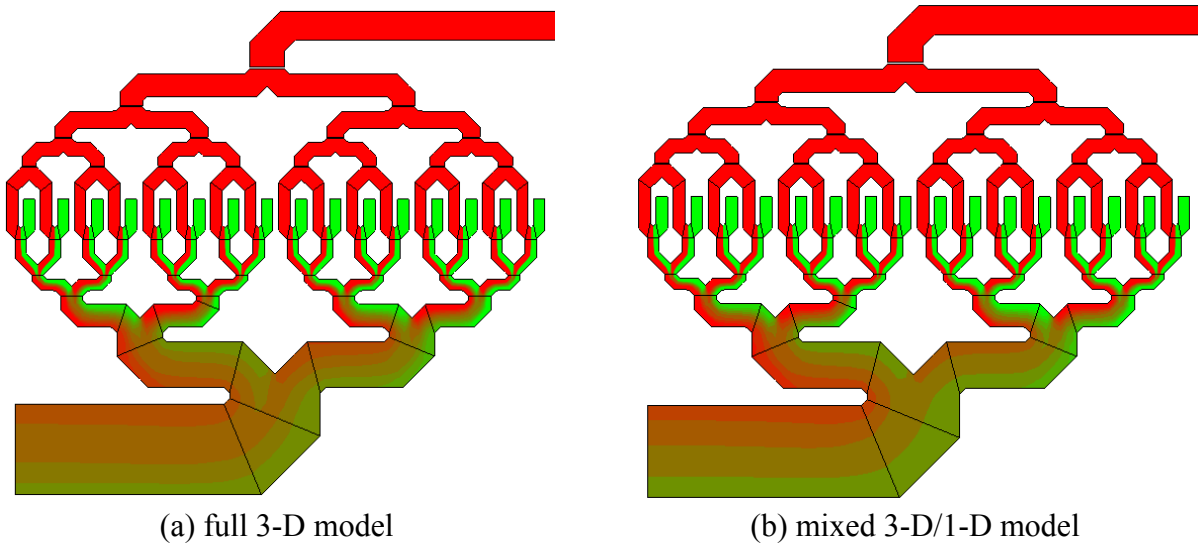


Figure 7.34: Fluid mixing patterns in the static micromixer

7.5.2 Model Application for Liquid Filling Problem

We focussed on testing the coupled 1-D/3-D VOF model in a complex microchannel geometry that cannot be accurately characterized using a purely 1-D approach. The structure comprises of narrow microfluidic channels that connect to a larger well. Although the narrow channels can be accurately modeled using the single-cell approach, liquid filling in the well-shaped cavity needs to be simulated with a hi-fidelity model. Sample results from the coupled 3-D/1-D simulation of liquid filling under a constant flow rate for a purely hydrophillic case are shown in Figure 7.35.

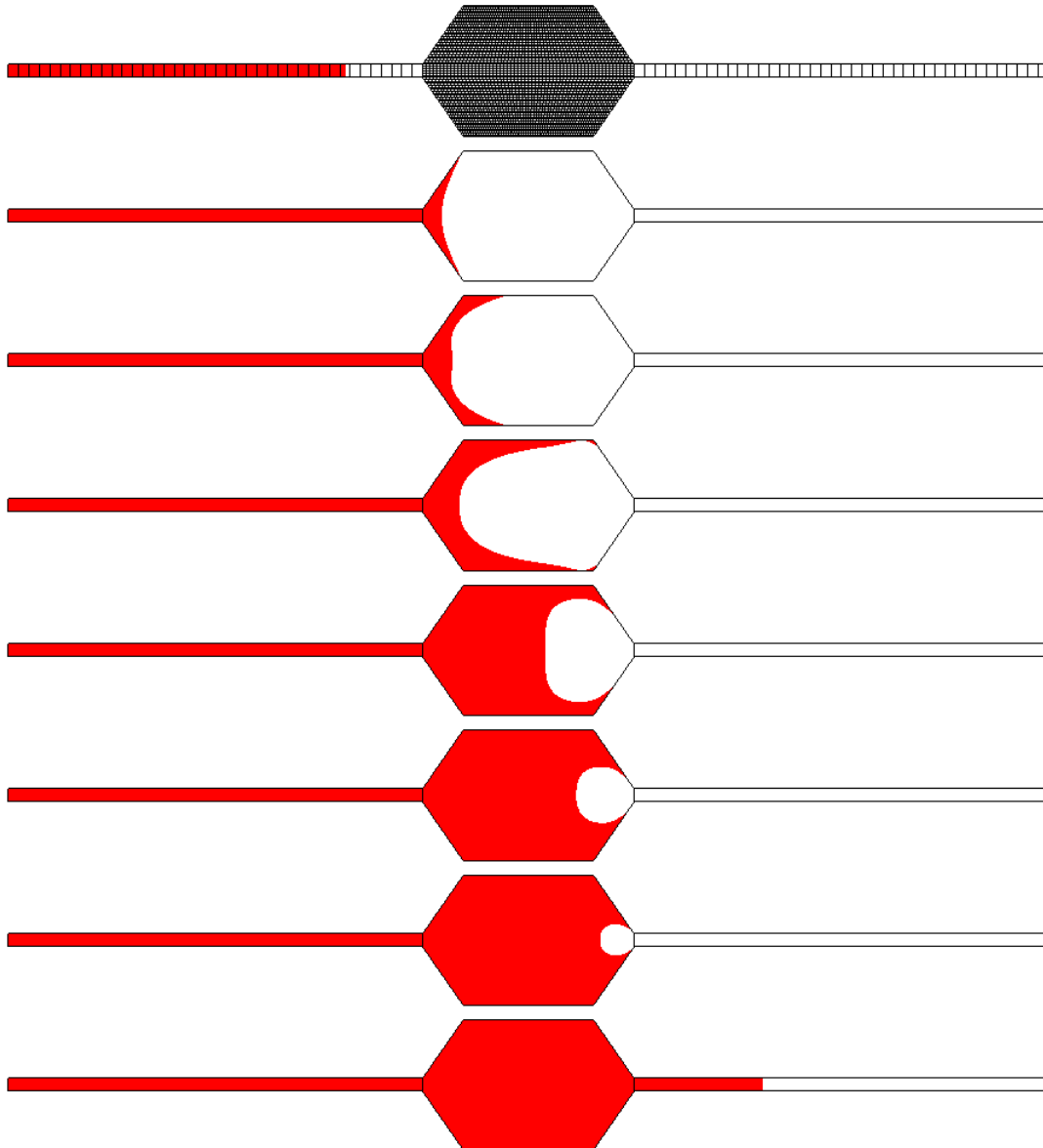


Figure 7.35: Simulation of liquid filling (in red) using a coupled 3-D/1-D approach

7.6 Mixed-Dimensionality Coupled Multi-Cell and 0-D Point Model Simulations

The capability has also been developed for mixed-dimensionality simulation involving hi-fidelity 3-D/2-D models and 0-D network-type lumped-parameter point models. In these simulations, boundary fluxes and/or pressures from the multi-cell simulations are integrated to obtain the equivalent “input parameters” for the network models. The network model solutions are then fed back as boundary conditions into the high-fidelity simulations. The capability to couple CFD-ACE+ with both SABER and SPICE simulators was developed. The coupling methodology and sample problems are described in the following sections.

7.6.1 Coupling between CFD-ACE+ and Analogy SABER

CFD-ACE+ was adapted to make it possible to perform a coupled physical-level (3-D) and system-level (0-D) simulation using the commercial software, SABER. The Analogy Saber circuit simulator is used for system-level, and CFD-ACE+ for 3-D simulation. Both the simulators communicate through CORBA (see Figure 7.36). Additional user subroutines (in C++ and MAST) for SABER handle the communication with ACE+, and provide relevant physical simulation result for input to SABER. The example below shows a circuit in which pressure source is modeled by SABER, and Tesla valve is simulated as a 3-D physical model. Figure 7.37 shows the plot of flow–pressure characteristic obtained in SABER from simulation of this coupled circuit. This task was later discontinued because of the unavailability of SABER for further development (due to its acquisition by Avant).

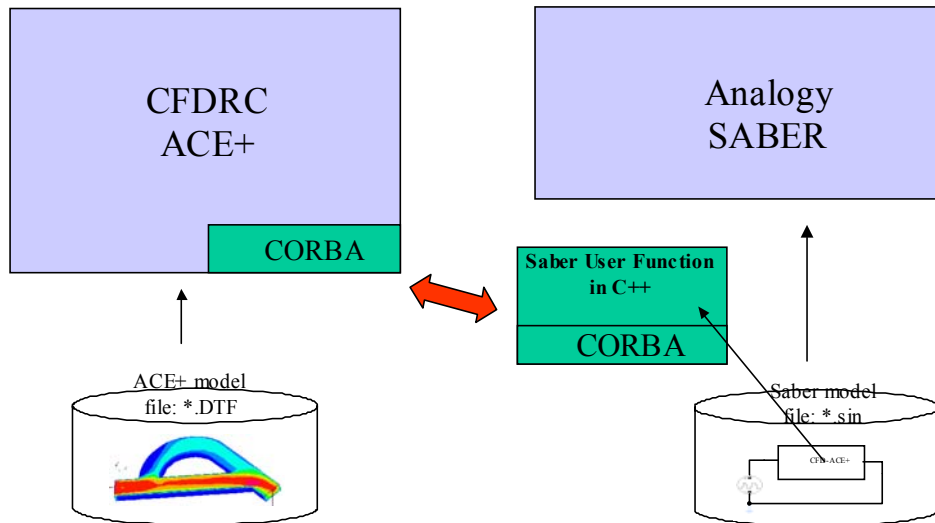


Figure 7.36: Schematic representation of coupling between ACE+ and SABER

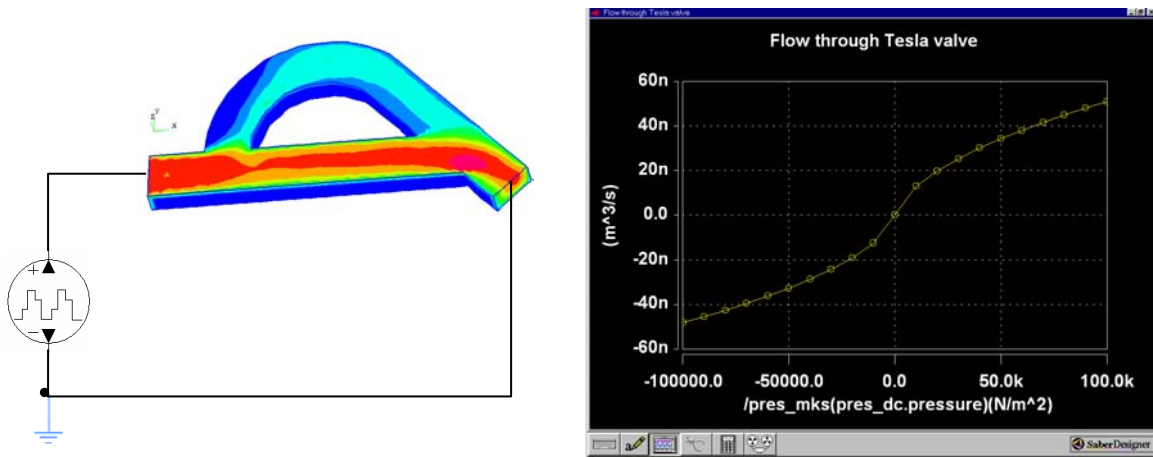


Figure 7.37: Fluidic circuit in SABER coupled with 3-D ACE+ model of Tesla valve (left) and simulated pressure-flow characteristics (right)

7.6.2 Coupling Between CFD-ACE+ and SPICE

SPICE has been interfaced with CFD-ACE to enable mixed-dimensional simulations. SPICE is a network analysis code and uses reduced models for all the individual components in order to predict system behaviour. Often, however, there may be an element in the network which requires full modeling to represent it accurately. For such elements a full-fledged (2-D/3-D analysis, as is appropriate) is done using CFD-ACE+ with full device physics represented.

The latest Berkeley version of SPICE was downloaded, installed and tested in Unix and Linux operating system environments at CFDRC. The freeware version is from the University of California, Berkeley, with the latest release being SPICE3. A variety of preliminary test problems, provided with the software, were first run to ensure that the install is up to the specifications. SPICE has traditionally been run under the Unix and Windows platforms. A large number of workstations, including a number of them in CFDRC, run the Linux operating system and hence it is imperative that SPICE be run with Linux. This was accomplished after a number of installation problems were fixed.

Description of SPICE: In order to describe how SPICE functions, let us consider the simulation of incompressible flow in a fluidic channel with the following variables: P - fluid pressure and V_i - velocities. It should be noted that a code like SPICE does not really care about the actual physics of the problem. It is instructive to look broadly at the way SPICE computes the solutions in order to understand what are the interface quantities that need to be provided at the interface by CFD-ACE+.

A typical circuit simulator like SPICE essentially solve a non-linear system of equations, (e.g. Equation 7.10 shown below) using some form of Newton-Raphson schemes.

$$P(V_i)=0 \quad (7.10)$$

The update for the next step is then obtained (Newton-Raphson) by:

$$V_i^{n+1} = V_i^n - J^{-1}(V_i^n)P(V_i^n) \quad (7.11)$$

Here J is the Jacobean of transformation between the two set of variables,

$$J(V) = \frac{\partial P}{\partial V_i} = \left[\frac{\partial P}{\partial V_i}, \frac{\partial P}{\partial V_i}, \frac{\partial P}{\partial V_i} \right] \quad (7.12)$$

In Equation 7.12, the independent variables at iteration level 'n' will be known along with a initial guess value of $P(V)$. The transformation Jacobian is evaluated at the previous time step making the equation a linear system for the variables F . It should be noted that the physics of the problem hinges critically on the evaluation of the Jacobian. Therefore, an accurate derivation of the Jacobian is necessary to correctly drive SPICE.

Coupling Methodology: The coupling is implemented using CORBA interfaces to facilitate communication between the two codes. A controlling code acts as the mediator between SPICE and CFD-ACE+.

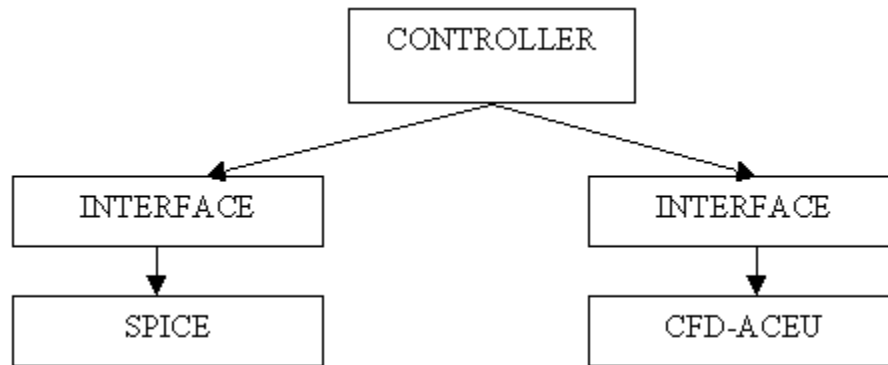


Figure 7.38: Schematic showing coupling between SPICE and CFD-ACE+

For the coupled ACE+ and SPICE3 simulations, the two-level Newton algorithm is applied (see Figure 7.39):

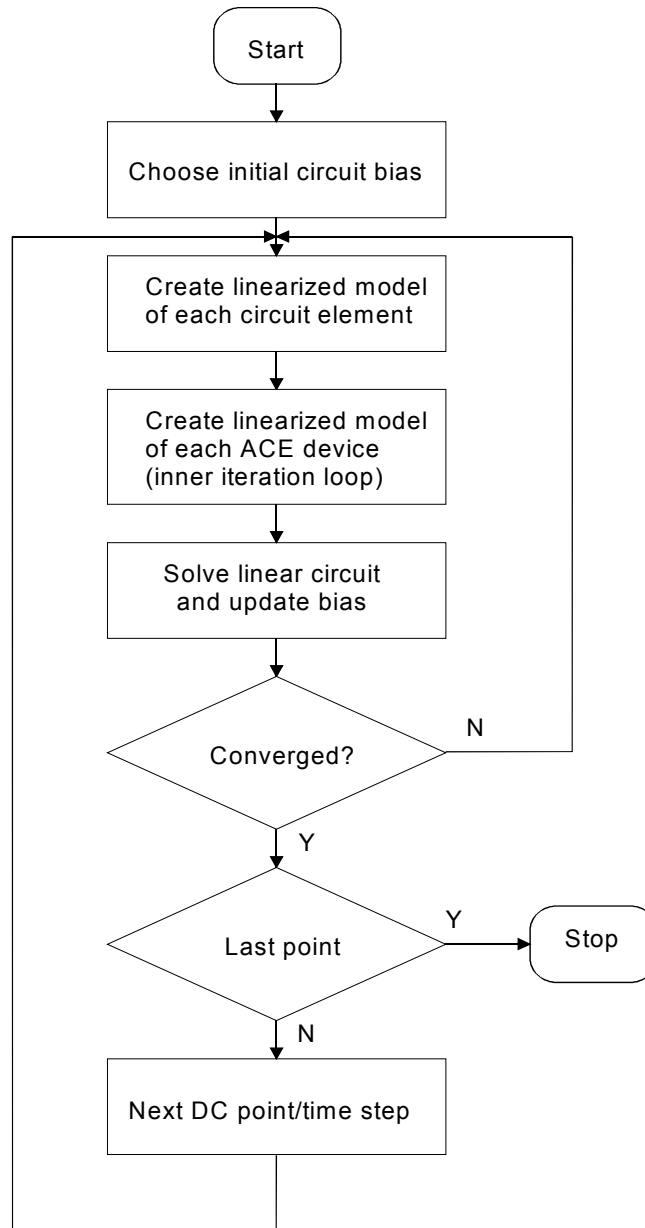


Figure 7.39: ACE+ and SPICE simulation with two-level Newton-Raphson Algorithm

Figure 7.39 hides the actual complexity of this process, as the creation of linearized models of ACE-modelled devices is an iterative process itself. The Jacobian is calculated numerically by sequentially changing each ACE device pin bias by some amount and then calculating the desired quantity. This approach does not require changes in ACE+. However, the currents flowing through the ACE device have to be calculated accurately enough to eliminate random fluctuations of the computed derivatives. Implementation of this algorithm is far from reality and cannot be used for a circuit simulation.

The coupled simulation proceeds as follows:

- Controller calls SPICE Factory and obtains a reference to SPICE
- Spice parses the circuit and returns information about the ACE+ devices to the controller
- Controller calls ACE Factory and spawns appropriate number of ACE instances (one per device)
- For every time step/DC sweep point, a Newton-Raphson iteration loop is run until convergence
- For a given pressure bias, flow in all ACE devices is computed
- Flow vs. pressure derivatives are computed numerically by sequentially changing each ACE device pin bias by 1 Pa. If the bias has moved significantly far from the previous iteration value, the previous iteration derivatives are used.
- All behavioral devices are linearized
- The linearized circuit is solved

The simulation step is chosen automatically by SPICE. In the coupled simulation, the circuit is no longer an electrical circuit. The voltage/current quantities become pressure/flow or temperature/power. However, the values of circuit elements have to be input in electrical units.

Example simulations of the Berkeley micromixer system, based on the coupled ACE+ and SPICE models, are shown in Section 9.

8. PARAMETRIC MODELS, SCRIPTING AND OPTIMIZATION

8.1 Parametric Microfluidic Device Models Using Python Scripting

8.1.1 Python Scripting

Microdevice model geometry/mesh generation using GEOM and GUI is an interactive process that requires high level of expertise and has several shortcomings e.g. models are nonparametric, it is very difficult to make changes to models, it takes too long to setup similar problems, etc. To alleviate these problems, CFDRC has been developing a Python interface to CFD-GEOM for script based geometry and mesh generation, which would enable automated generation of models from parametric templates. Python is an interpreted, interactive, object-oriented programming language with very high level dynamic datatypes and functions. It allows conventional software modules/subroutines/programs (Fortran, C, C++) to be used as functions called from Python script in simple single line statements. Python is an open source free software that is gaining tremendous popularity.

8.1.2 Parametric Model of Tesla Valve Geometry

A sample application of Python scripting for generating a parametric model of a microfluidic device, the Tesla valve, is shown in Figure 8.1. The Python script generated the geometry, structured mesh and boundary conditions in a manner that the model was ready for analysis with CFD-ACE+. The results of the ACE+ runs are described later in Section 8.3.

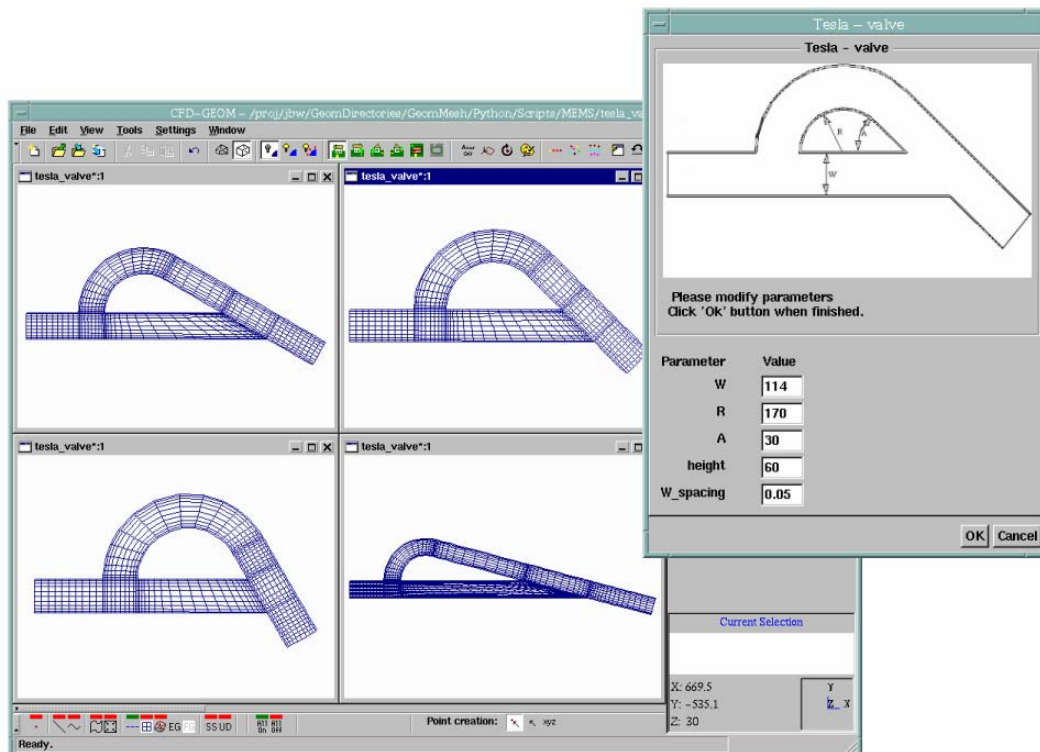


Figure 8.1: Construction windows of Python-generated parametric Tesla valve Models

8.1.3 Parametric Model of Helical Microfluidic Mixing Chamber

Here, we describe a parametric 3-D model of a helical microfluidic mixing chamber, developed using the Python scripting feature of CFD-GEOM. The model allows the user to change the length, diameter, pitch and the number of coils of the mixing chamber at his discretion, all at the click of a button. Figure 8.2a shows the geometry model set-up and details. Note that, in addition to geometric parameters such as coil diameter and pitch, mesh parameters such as nodes on the circumference can also be altered very rapidly. Sample grids generated using the model are shown subsequently. Figure 8.2b shows a mixing coil with a helix diameter of 5 mm, tube diameter of 0.5 mm and a pitch of 1 mm. In Figure 8.2c, the coil pitch has been increased to 2.5 mm. Figure 8.2-D shows the coil with a helix diameter which is half that of the baseline in Figure 8.2b.

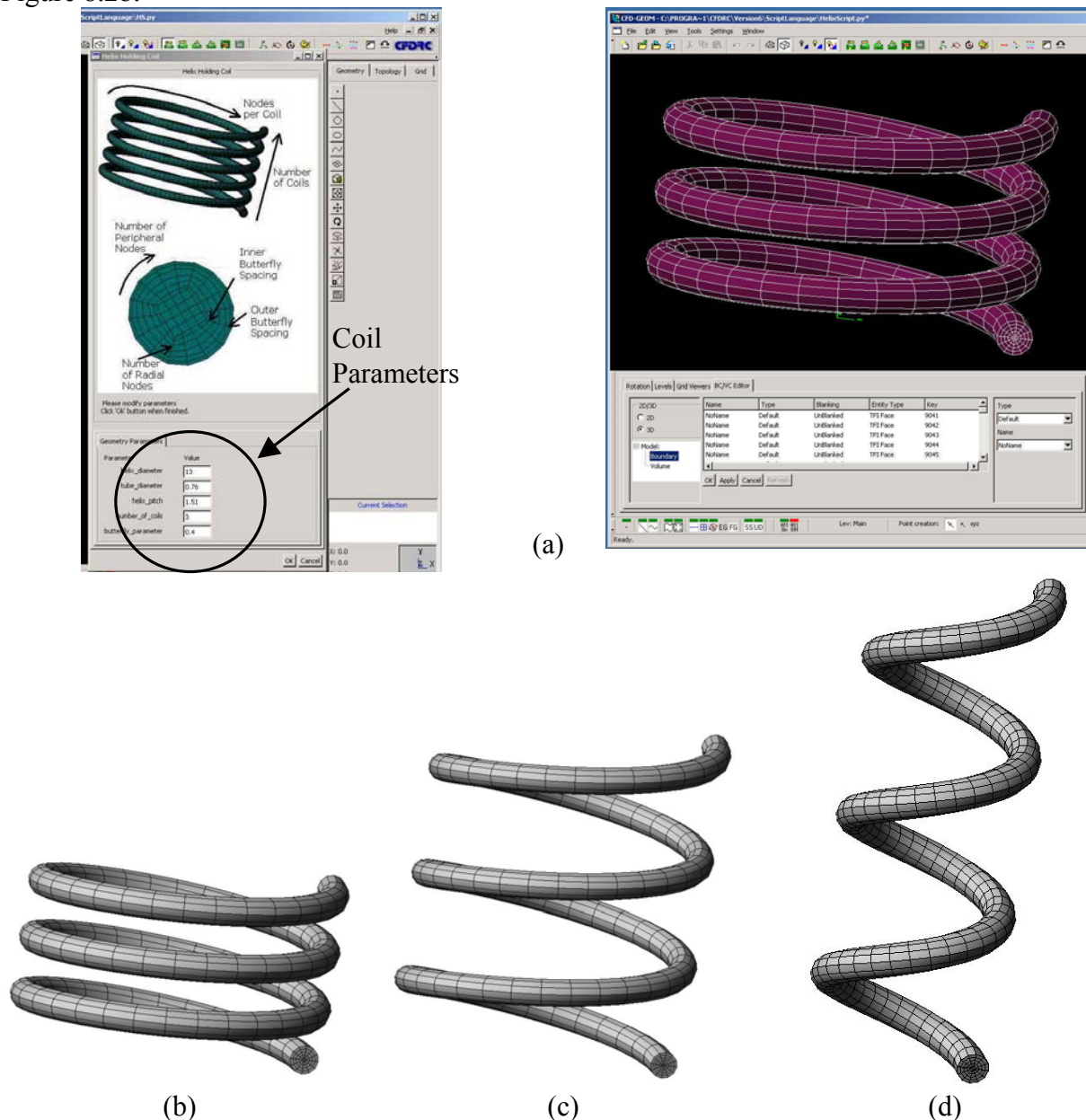


Figure 8.2: (a) Parametric geometry creation set-up; (b) Baseline mixing coil; (c) Mixing coil with 2.5 times pitch; (d) Mixing coil with half the tube diameter

8.1.4 Python Scripting in CFD-Micromesh

Some effort was put in to integrate Python scripting functionality inside CFD-Micromesh. The idea is that this new feature should enable script-based definition of projects with the same functionality, which is currently available through GUI interface. Integration was done via a non-direct connection through CORBA Python binding. This approach makes it possible to control CFD-Micromesh from an external Python GUI, or from any program with a built-in Python interpreter, without the necessity to direct link with CFD-Micromesh. The controller program does not even need to be started on the same computer as the CFD-Micromesh server.

For debugging or demonstration purposes, it is possible to run the GUI of CFD-Micromesh during the script invocation and execution. The operations performed inside the script are immediately reflected by graphical change in the project displayed in GUI. This capability is expected to be useful for training purposes as well. A few basic functions for geometry object manipulation inside layers have been already implemented. Even with this limited set of operations, it has been possible to run a series of demonstration test cases.

Demonstration Case: A sample case, showing the automatic building of microfluidic binary-tree flow splitter, is presented in Figure 8.3. A defined function *genBinaryTreeFlowSplitter* generates such structure with variable number of splits levels and different dimensions. Scripting calls to this function create four splitters at different locations, number of binary-split levels, width of channels, and distances between them. The parameters of the function are: fluid layer from project, x position, y position, number of binary-splits, channels width, and distance between generated channels.

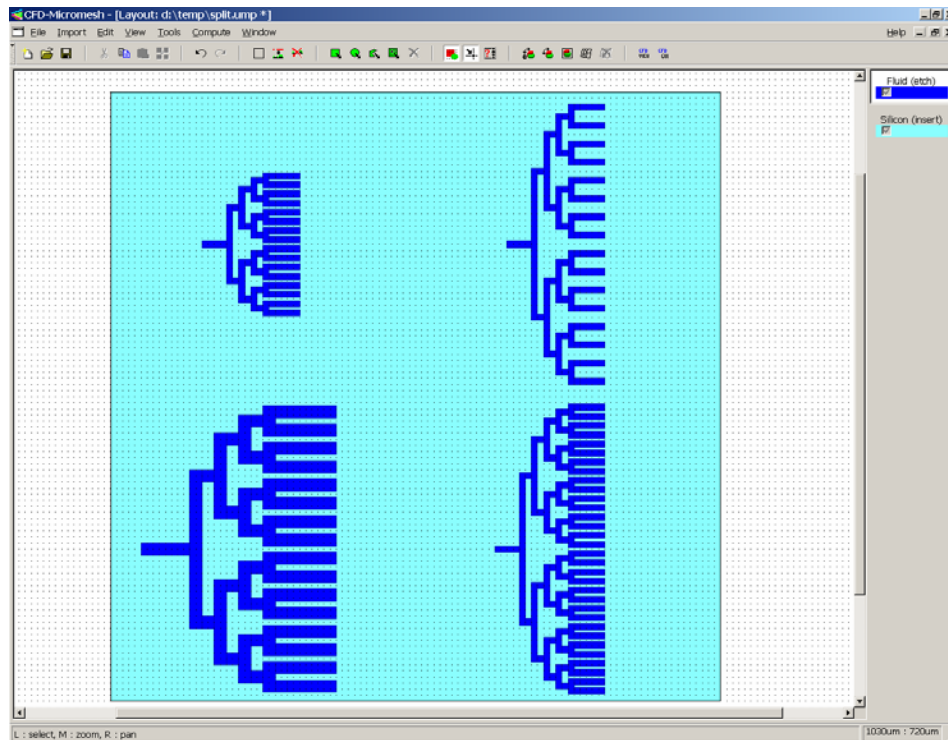


Figure 8.3: CFD-Micromesh GUI showing parametric models of microchannel network

8.2 Simulation Manager for Automated Numerical Design Analysis

8.2.1 Manual Design Analysis Procedures

The numerical design process consists of several disparate steps that need to be meshed together to analyze the possible device variations for a given parameter space. The steps involve grid generation for a given set of parameters (using a grid generator such as CFD-GEOM), analysis of the flow (using a flow solver such as CFD-ACEU) and the repetition of the above process for variation in parameters to arrive at an optimal set of parameters. Typically, an end-user of the software will set up a geometry model, perform the grid generation, set up the solver parameters, run the case, and analyze/visualize the results. Based on the results the user may change certain solver parameters, may change certain grid parameters, and/or make a change to the geometry and rerun the case. This process may be repeated several times. This interactive process may consist of a great number of steps to be performed by the device designer.

Most GUI driven grid generators work from a bottom to top building of grid starting from points and going on to build lines, edges, surfaces and finally grid volumes. Once a grid is generated, even a simple parametric variation of the underlying geometry will still involve a lot of human interaction and work for each grid to be studied during the optimization process. It is necessary to move away from the GUI-based grid generation and flow solution control in order to integrate the various components into one umbrella.

8.2.2 Automated Script-Driven Simulation Methodologies

Figure 8.4 shows the hierarchy of processes that can be controlled by scripting. The scripting process starting with points and nodes to the finished grid and boundary conditions. The key advantages of the Python based scripting system are as follows:

- Parametric / Optimization studies
 - Starting from existing models
 - Starting from scratch
 - Customized applications
- Reuse
 - Libraries of components
 - Reuse existing models

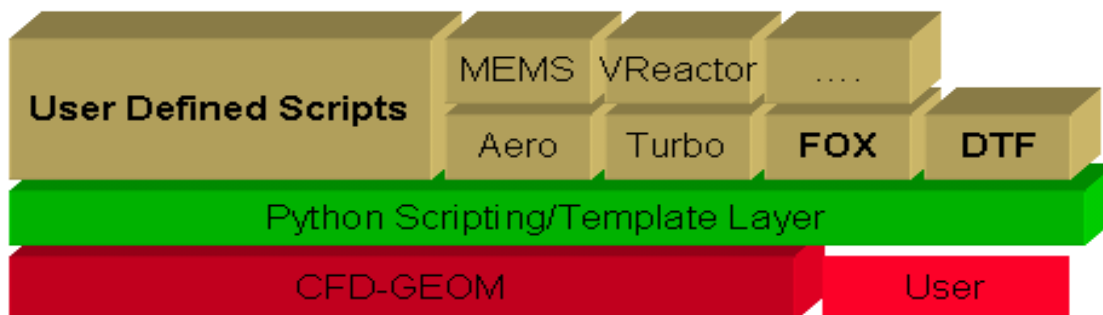


Figure 8.4: Hierarchy of processes controlled by scripting

The next step in the optimization process is the study of the flow field. In the CFD-ACE+ Simulation Manager environment there are several optimization modules including: one

parameter Brent algorithm and multiparameter Powell and simplex algorithms. In the 2003 release a robust least-squares Gauss-Newton algorithm will be implemented. The CFD-ACE+ suite of engineering analysis tools consists of a set of interactive programs (CFD-GEOM, CFD-GUI, CFD-VIEW) and one batch oriented program, i.e. the flow solver itself. The Simulation Templates facilitate an automation of the manual process of geometry and grid generation, simulation and analysis of results and subsequent modification of input parameters for the next round of simulations. This automation is achieved by controlling all analysis tools from one central application, i.e. the Simulation Manager. A Simulation Template is a textual description of all steps involved in an engineering simulation. All steps put together form a script or 'simulation recipe'. In order to enable easy interpretation of the script by all CFD-ACE+ tools, it is written in Python. The template or script is executed in the Simulation Manager, and all CFD-ACE+ tools follow the script instructions automatically.

8.2.3 Simulation Templates

A Simulation Template may contain instructions just for the geometry/grid part of the simulation, i.e. control the CFD-GEOM tool, it may contain instructions just for the CFD-ACE+ solver, or it may control a combination of both tools (in this release the CFD-VIEW tool has not been integrated yet). The script is based on Python scripting language, and many programming constructs such as loops and conditional statements are supported. This gives a lot of freedom to the end-user and templates can potentially be used for many applications.

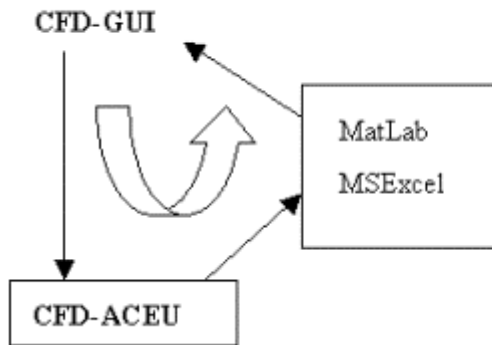
With this in mind, the main applications of the script templates are:

- Modification of boundary and/or volume condition parameters in DTF files
- Automated geometry and grid creation
- Parametric Analysis, and
- Optimization

Figure 8.5 shows the schematic of the design process. The Simulation Manager simplifies the process by invoking all of the elements required (solver, controller, etc.) repeatedly to move through the parametric design space. Scripting in Simulation Manager provides tools for creating customized simulation environments and performing automated design optimization. Using scripts written in Python, a user has:

- complete access to all geometry and grid generation capabilities in CFD-GEOM
- ability to set boundary and volume condition values for the CFD-ACE solver
- access to several multi-variable optimization algorithms and one single variable optimizer
- ability to run CFD-GEOM, the CFD-ACE solver, and optimizers in background mode

Traditional Design Optimization



Design Optimization by Simulation Templates

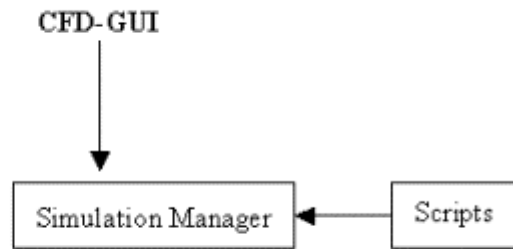


Figure 8.5: Schematic of the steps involved in the design processes

8.2.4 Application of Simulation Manager for Parametric Simulations

A high-fidelity model of flow and heat transfer over a heated beam in a 2-D microfluidic channel (Figure 8.6) was developed using CFD-ACE+. The simulation manager was used to facilitate automated grid generation and perform multiple simulations. The main objective here was to demonstrate the applicability of the simulation manager for rapid numerical parametric studies on microfluidic devices and systems.

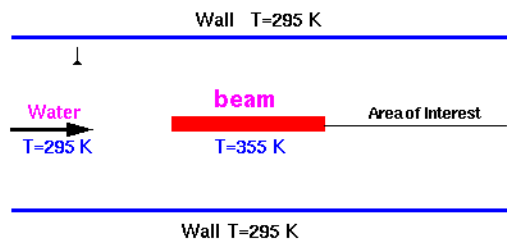


Figure 8.6: Configuration of 2-D planar microchannel and beam

Model Details: Flow inside the channel was modeled as 2-D single-phase, incompressible laminar flow. Fixed velocity and temperature boundary conditions were applied at the inlet. Constant pressure was imposed at the exit. Constant temperatures were prescribed on the beam and channel surfaces. The computational grid was generated using Python Geometric Script Templates. Simulations were executed using the Python simulation manager, which allows users to automatically perform multiple simulations with changes in the geometry, grid and flow conditions.

Results: Six simulations were carried out using a second-order upwind scheme with inlet velocity $U_{in}=0.001, 0.002, 0.005, 0.01$ and 0.02 m/sec. Figure 8.7 shows the temperature contours for the different inlet velocities. For the first three lower velocity cases, the temperature downstream of the beam increases with flow velocity, both near the beam end and further downstream, due to the strong effect of viscous diffusion. When the flow velocity is greater than 0.005 m/sec., convection dominates, resulting in overall lower temperatures around the beam, but higher values at downstream regions.

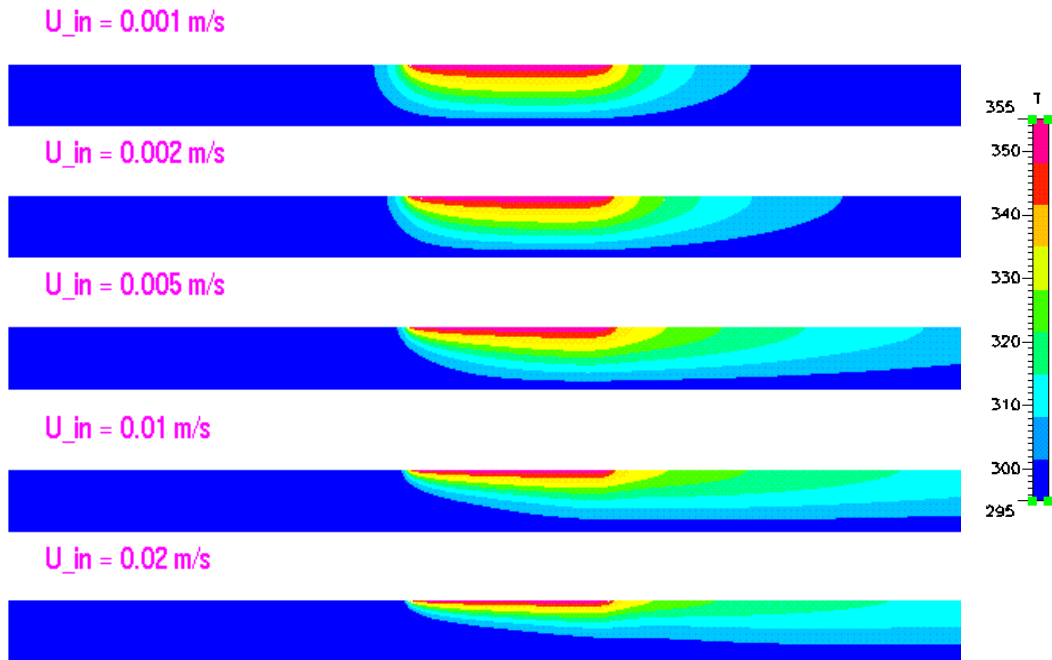


Figure 8.7: Temperature contours in the microchannel

8.3 Numerical Optimization of Tesla Valve

Here, we describe an optimization run for the Tesla valve considered earlier based on a cost function comparing the forward and backward flow rates. Three geometries shown in the figure were considered, and five cases with varying pressures, with forward and backward flow for each case were included in the simulation manager – a total of 3 CFD-GEOM runs and 30 CFD-ACEU runs. The scripting panel in Figure 8.8 shows the geometric angle variation between the three geometries, and the pressure variation for the five solver cases for each geometry.

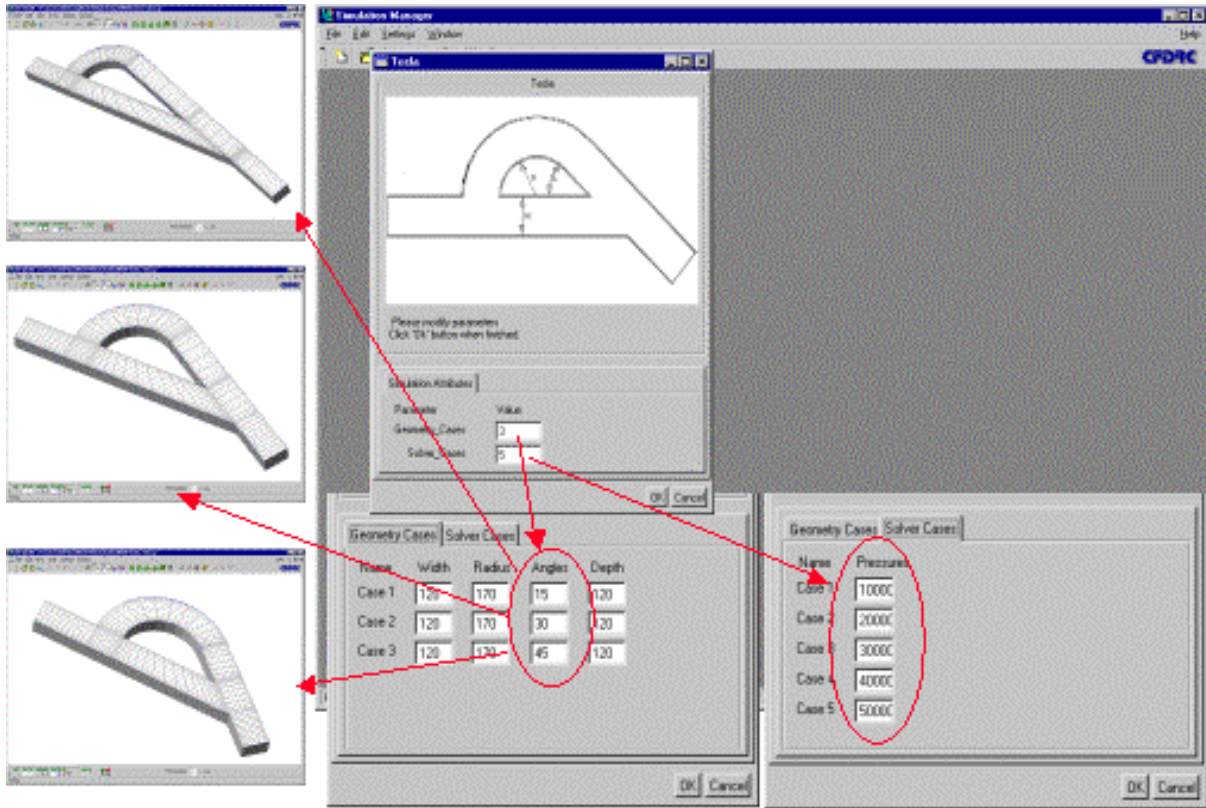


Figure 8.8: Tesla valve optimization using the Simulation Manager

Figure 8.9 shows the resulting optimization by plotting the net cost function (in this case, $\text{flow}_{\text{for}} - \text{flow}_{\text{back}} / 0.5(\text{flow}_{\text{for}} + \text{flow}_{\text{back}})$) for the Tesla valve. The scripting for the input plotter is also included in the simulation manager.

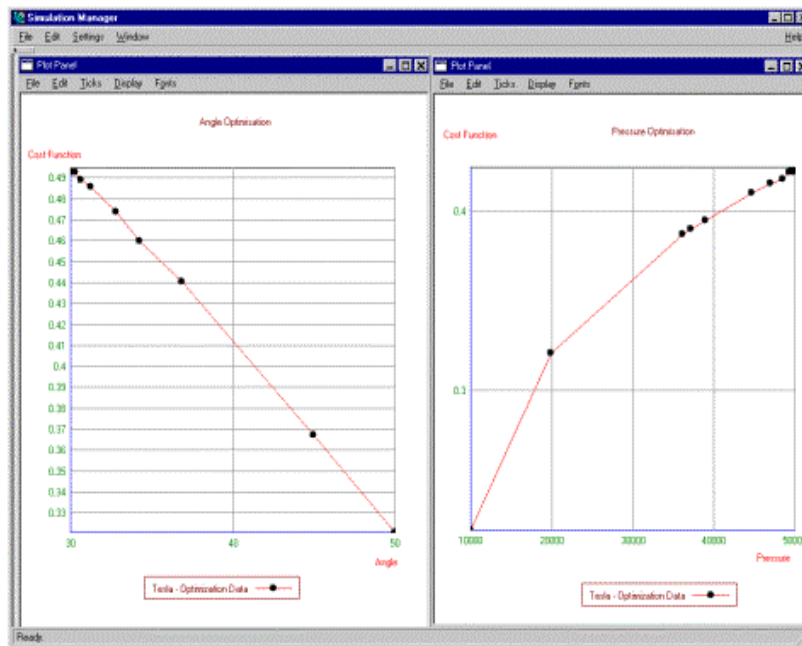


Figure 8.9: Tesla valve angle optimization (left) based on cost function (right)

8.4 Numerical Optimization of the DNA Biochip Device

8.4.1 Problem Description

We describe another sample optimization test case involving microfluidic flow and DNA hybridization in a DNA biochip device. DNA hybridization occurs on along the surface of the posts within the biochip. The objective of this work is to find the optimum post radius given a cost function that takes accounts for the fact that increased binding with an increase in the post radius comes at the cost of increased pressure drop in the system. This increase in pressure drop with increasing radius will cause the pump driving the fluid to work harder. The objective is to maximize DNA hybridization without making the pressure drop too high.

8.4.2 Customized GUI for DNA Chip Optimization Problem

A parametric 2-D model of the DNA biochip was developed. A customized simulation environment was developed for performing design analysis of the DNA chip. The GUI, created by the Python script, allows the user to set up the analysis (see geometry model set-up in Figure 8.10). This custom GUI is a simplified interface that allows the user to modify only the parameters that affect the performance of the DNA chip. In the first tab, the user enters the file name they wish to use for the simulation and specifies inlet mass flow rate and DNA solution concentration using familiar units. The geometric parameters, affecting pillar diameter and spacing, can be adjusted in the second tab. Note that both geometric and mesh parameters can be altered very rapidly.

When the user presses OK, the script calls CFD-GEOM to create the geometry and (unstructured) grid according to the values specified in the GUI. After the grid generation process is complete, the script sets inlet mass flow rate and concentration values. The CFD-ACE+ solver is then called by the script to solve the flow and binding in the DNA chip. At the end of the run, the user can plot the surface concentration of DNA as a function of time, which is a measure of the hybridization efficiency of the DNA chip.

Use of an automated optimization algorithm can provide optimal design solutions with very less user interaction. The optimizer requires a quantitative measure of the design performance (cost function). Starting with an initial design configuration, the optimizer tries a new design, then uses the results to select a better design. This iterative process continues until there is little improvement in the design. Simulation Manager currently provides the Optimization Template (see Figure 8.11), a GUI-driven script that allows users to perform automated design optimization without having to write Python script.

8.4.3 Model Setup

The DNA Chip is modeled as a 2-D problem with a symmetry plane. Figure 8.12 shows the full geometry, however the calculations take advantage of the inherent geometric symmetry of the chip. Dimensions of the various parts of the model are given in Figure 8.12. The chip is assumed to have a thickness of 0.10 mm.

There are a total of 23 posts (11.5 for each side of the symmetry plane) in the model where the probe molecules can bind. The surface concentration of the probe DNA is assumed to be 1×10^{-9} M. The inlet concentration of target DNA molecules is 200×10^{-9} M, carried in by an inlet flow

rate of 75 $\mu\text{L}/\text{min}$. This translates to an inlet velocity boundary condition of 0.00625 m/sec. The binding constants for target-probe interactions are $K_a = 8 \times 10^5 \text{ M}^{-1}\text{s}^{-1}$ and $K_d = 0$.

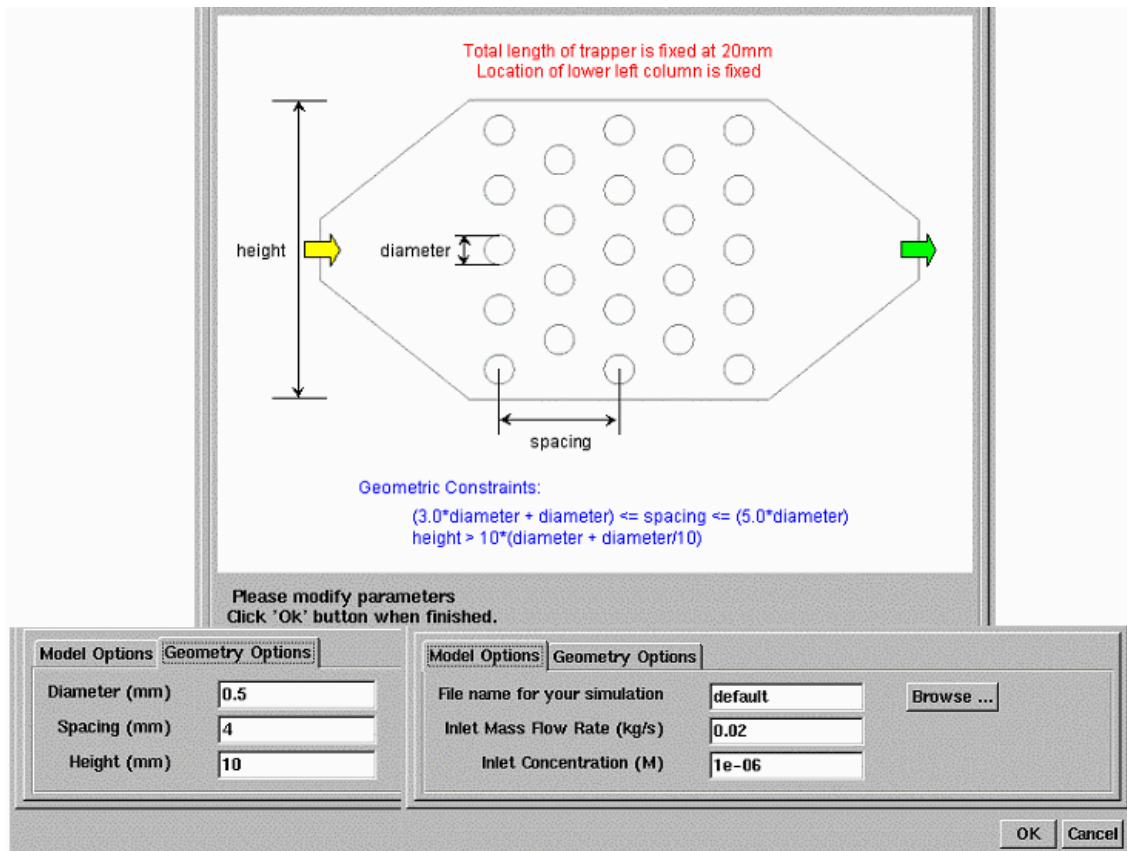


Figure 8.10: Customized template designed for the DNA biochip problem. The 2 panels below show fields for entering geometric parameters as well as model options.

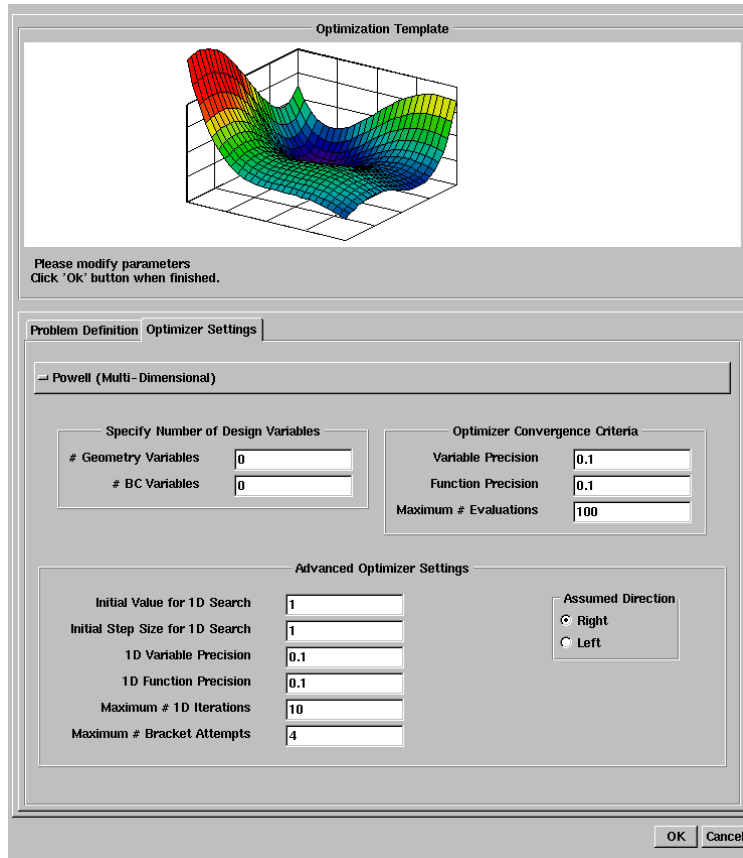


Figure 8.11: Optimizer-GUI image shows GUI for running general optimization simulations

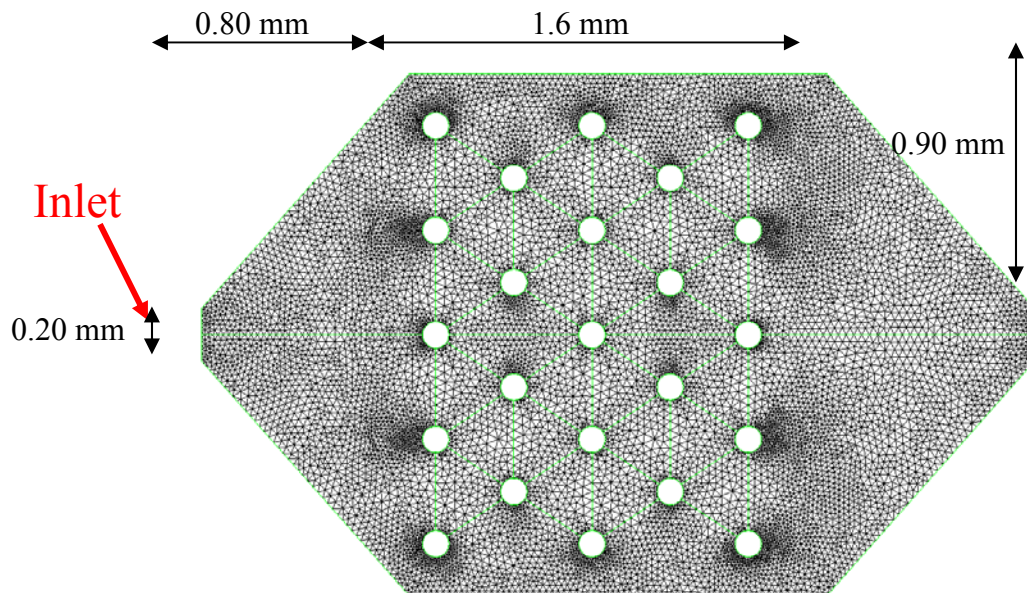


Figure 8.12: Geometry of the DNA chip and computational mesh

8.4.4 Solution Procedure

The optimization was performed using SimManager and the available optimization modules. A cost function was developed using the criteria stated in Section 8.4.1. Basically, the optimal post radius is one that will balance the surface bind and the system pressure drop. To that end, the following cost function is proposed.

$$\text{Cost} = w\Delta P + (1-w)(-\log(A_{\text{total}} \bar{C}_{\text{surface}})) \quad (8.1)$$

The first term in the cost function is the weighted pressure drop. The second term in the cost function is a bit less obvious. Since the product of the total area and the average surface concentration of the bound DNA will be very small, on the order of say 10^{-9} , the base 10 logarithm will be a negative number (say -9). Placing the negative number in front of the logarithm makes this number positive. If this number decreases, then the total amount of bound DNA increases. The cost function was then minimized using the post radius as the variable. A weighting parameter $0 < w < 1$ is used to balance the contribution of each component of the cost function. For our purposes “w” was arbitrarily chosen to be 0.30.

The optimization was performed using the Brent’s method module available in the SimManager. Brent’s method is similar to the secant method, in that no explicit numerical calculation of the derivative is performed. A flowchart of the optimization is given in Figure 8.13 below.

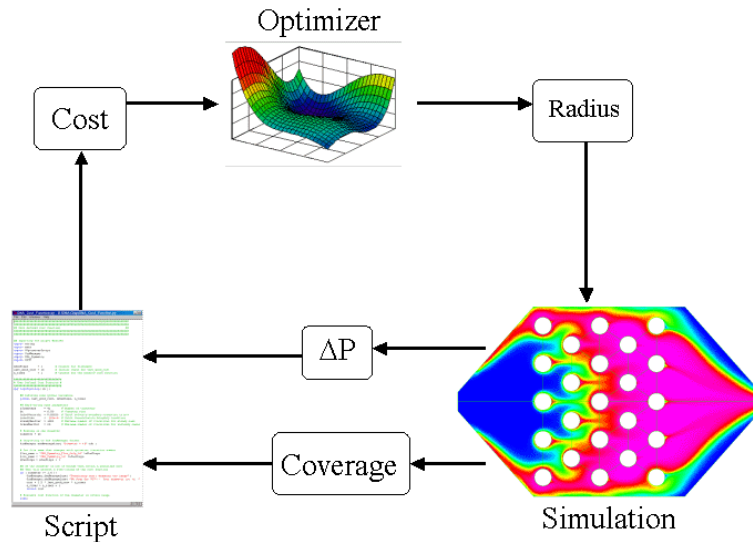


Figure 8.13: Flowchart for the DNA chip optimization process

At the beginning of each iteration, a check is performed on the radius to make sure a real geometry can be created. The device geometry is then created using the parametrized model, and subsequently gridded. The grid in the region of the posts must vary to allow for the size change in the post radius. Some heuristic rules were developed for the generation of a high quality grid around the posts.

After the grid is generated, a solution for only the flow is generated. This is because only one full flow solution is required for each radius. The time dependent DNA binding simulations use the flow solution as an initial condition. Once the flow solution is obtained, the pressure drop across the chip can be computed. The transient solution for the DNA binding is then obtained.

Once the transient simulations are complete, the total surface coverage and resulting cost function is calculated. The cost is then given to the optimizer and the optimizer generates a new radius for the simulation module. This process continues until an optimal design solution is obtained.

8.4.5 Optimization Results

The variation in cost function during the optimization procedure is plotted in Figure 8.14. The simulations predict an optimum post radius of 0.089 mm for the DNA biochip based on the chosen weighting function and model parameters. Sample target DNA concentration contours within the biochip at an intermediate time step during the simulation for the optimized geometry are shown in Figure 8.15.

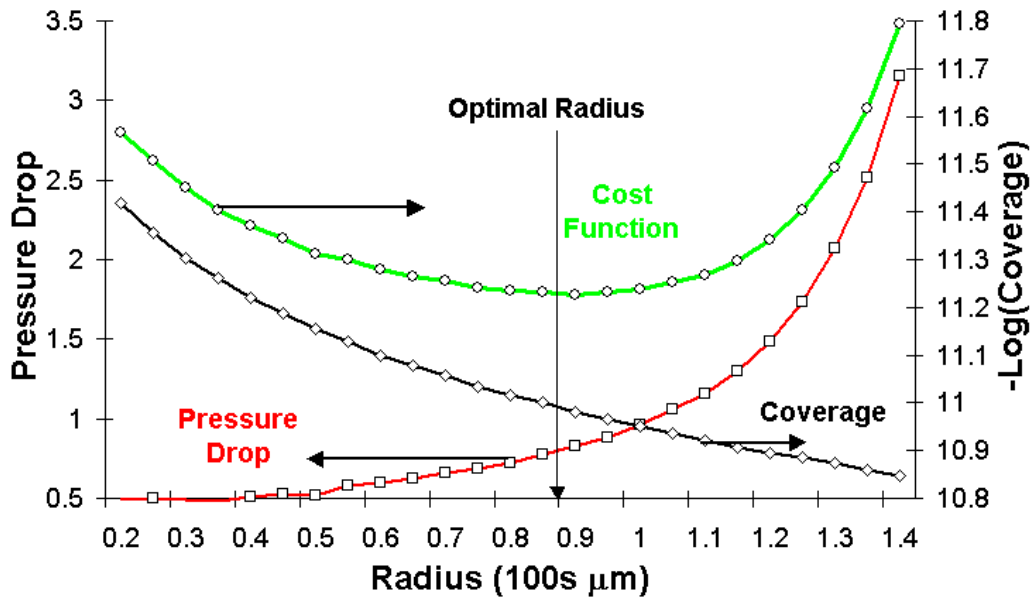


Figure 8.14: Plot of cost function and cost function components during optimization

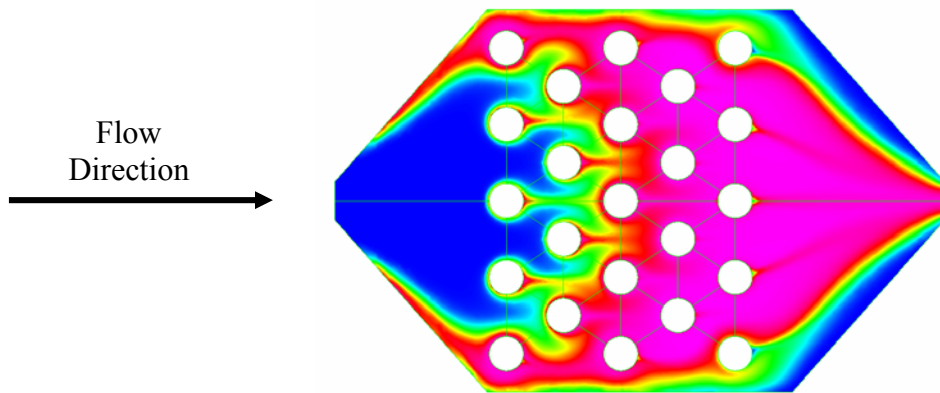


Figure 8.15: Target DNA concentration in the optimized biochip

9. DEMONSTRATION AND APPLICATION FOR BIOMICROFLUIDIC DEVICES AND INTEGRATED SYSTEMS

The developed capabilities were applied for several demonstration studies on various kinds of biomicrofluidics devices and integrated systems for various companies, national labs and academic research labs during the course of the project. They were as follows:

Biomicrofluidic Device and Process Design Studies

1. Analyte delivery and binding in fluidic cell of the CANARY B-cell biosensor (MIT Lincoln Labs)
2. Electrokinetic sample injection and pinching in a cross-channel configuration (Aclara Biosciences)
3. DNA transport in electrokinetic DNA chip (Nanogen, Inc.)
4. Sample stacking in a straight channel (Aclara Biosciences)
5. Impact of sheath flow on electrokinetic transport (Applied Biosystem)

System-Level Studies on Integrated Biomicrofluidic Systems

6. Sample mixing in micromixer system (U. C. Berkeley)
7. Sample transport and separation in capillary electrophoresis biochip system (U. C. Berkeley)
8. Sample injection and separation in Protein Labchip system (Agilent)
9. Flow and heat transfer in biodiagnostic microfluidic system (ISTAT Corp.)

Study details are outlined in the following sections.

9.1 CANARY B-Cell Biosensor

This section summarizes the work performed in the simulation of the CANARY B-cell biosensor system developed at MIT Lincoln Laboratory (DARPA/DSO - Tissue-Based Biosensors program). The BIOCHEM module in CFD-ACE+ was used to help analyze and suggest the design criteria for maximizing surface binding of antigen to B-cells.

9.1.1 Problem Description

The general objective of this project was to aid the MIT-Lincoln Laboratory research team in analyzing the functionality, and optimizing the design, of the CANARY Biosensor system. Antigen is injected into a rectangular, duct-like microfluidic chamber with flush mounted sensors on exposed surfaces. The antigen is convected and diffused towards the sensors where it binds with the B-cell patch. Biomolecular binding is influenced by a complex interplay of antigen transport properties and kinetic rates (diffusivity, association and dissociation constants), assay protocol and flow cell geometry. Small alterations in the assay protocol or flow-cell geometry can often facilitate and tremendously enhance antigen binding. Additionally active antigen transport to the B-cell surface (gravitational, electrostatic, magnetic etc.) can increase the interaction and binding probability of an antigen with its B-cell receptors.

Specifically, the objectives of this study were to:

1. Develop geometric models of the microfluidic cell in the CANARY system
2. Simulate and analyze the transport and surface binding kinetics of antigen/B-cell in the CANARY biosensor system
3. Conduct design optimization studies on the biosensor system by varying
 - (a) Sample Injection Protocol
 - (b) Flow Cell Geometry
 - (c) Drift velocity
 - (d) Hydrodynamic Forcing

9.1.2 Stage I Studies

The project was divided into two distinct Stages. During Stage I (funded by MIT Lincoln Labs on their DARPA/DSO project), the focus was on flow/sample injection protocol and device geometry. Three different buffer flow stop modes were tried with continuous flow providing the baseline. Sample results are shown in Figure 9.1. The simulations demonstrated that continuous buffer flow yielded higher short term (around 1sec) binding levels (see Figure 9.2). However, under the slow settling effect of captive sample, stopped flow modes eventually produced much higher binding levels (at around 10 sec or more).

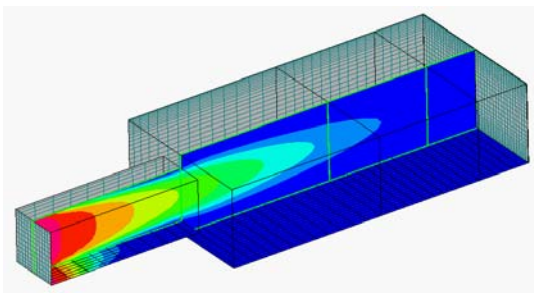


Figure 9.1: Contours illustrating the convective-diffusive motion of antigen from the inlet chamber into the flow chamber.

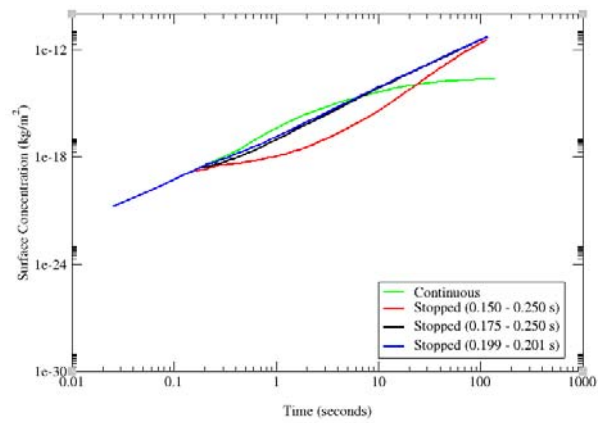


Figure 9.2: Effect of flow injection protocol (stopped vs. continuous buffer flow) on surface binding

Next geometric obstacles were introduced in the flow path to enhance binding. A rectangular chamber was chosen as the baseline configuration. The geometry parametrics can be grouped into two major categories: (a) flow obstacles; and (b) flow tortuosity. The following flow obstacles configurations were studied:

1. Rectangular fins (Figure 9.3);
2. Cylindrical Posts
3. Square Posts
4. Cup or Cut-away Post.

The effect of flow tortuosity (degree of bending/turning of streamlines) on antigen mixing, and hence binding, was assessed using: (1) Helical (Figure 9.4); (2) Planar-helical; and (3) Recess designs.

A comparison of all the designs studied is shown in Figure 9.6. Obstacles generally worked well, with the cylindrical post (Figure 9.5) and cup designs showing the best binding levels. This was on account of the intercept of high speed (central) flow. On the other hand, increased tortuosity actually led to decreased overall binding for the flow mode and time frame considered (< 100 secs).

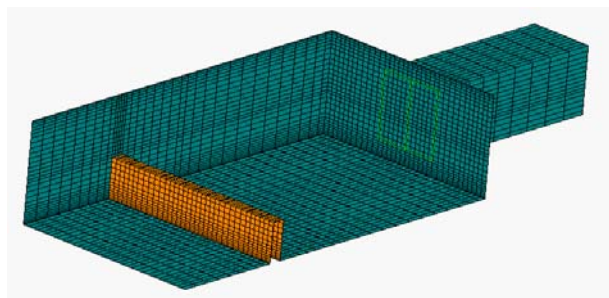


Figure 9.3: B-Cells on fin-type obstacle

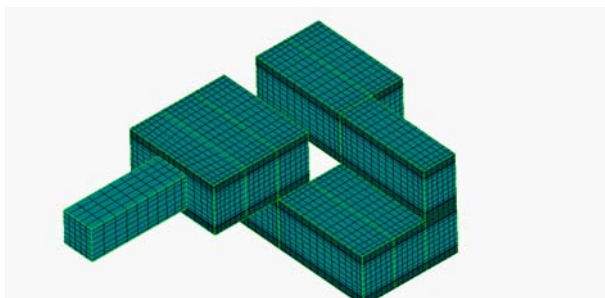


Figure 9.4: Helical snake geometry

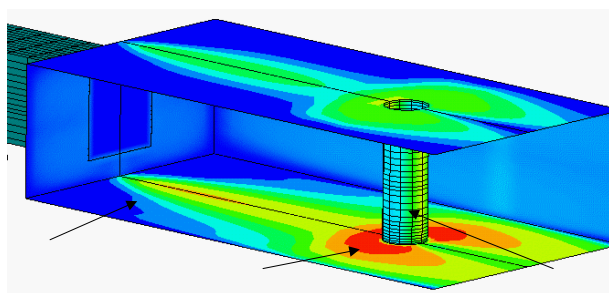


Figure 9.5: Post geometry with surface coverage

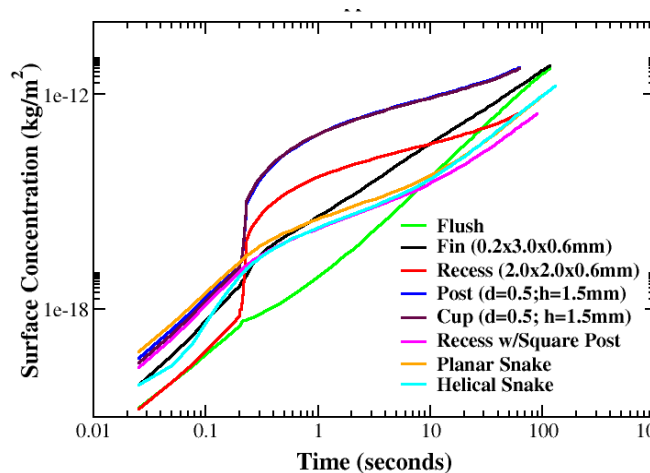


Figure 9.6: Comparison of surface coverages. Post and cup designs show maximum signal.

9.1.3 Stage II Studies

Diffusion-driven delivery (through the viscous boundary layer) of antigen to binding surfaces is often insufficient for real time detection of agents. To counter this, additional drift velocities are employed to drive the antigen towards the wall (Figures 9.7 and 9.8) using gravitational, electrophoretic, magnetic or other means. The primary objectives during Stage II of the work was to quantify the effect, on antigen binding, of (a) lateral (drift) velocity field and (b) hydrodynamic forcing. Both studies used 2-D, flush mounted sensors under continuous flow.

Effect of Lateral Drift Velocity: A set of eight parametric simulations were performed to study the role of settling or drift velocity on binding rates. Four different settling velocities (0, 1, 10, 100 microns/sec) were used in conjunction with two different flow rates (0.5 & 5.0 microL/sec). Simulations showed a nearly linear growth in binding, with increasing downward drift. As expected, the binding enhancement was more pronounced in the smaller throughput simulations (Figures 9.9 and 9.10).

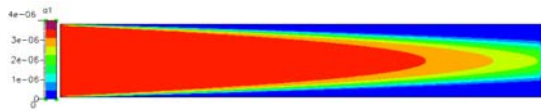


Figure 9.7: Antigen transport - no lateral force

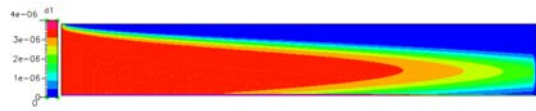


Figure 9.8: Antigen transport under lateral force

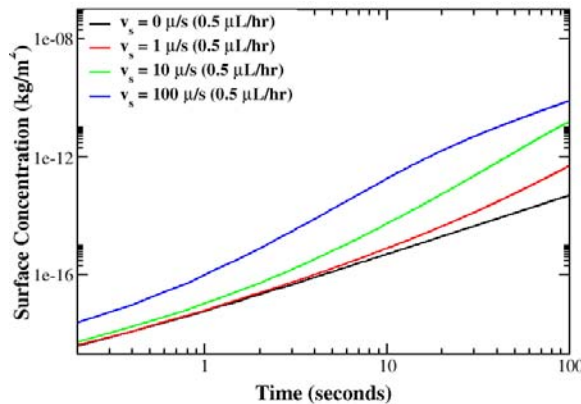


Figure 9.9: Binding enhancement due to lateral force -slow flow.

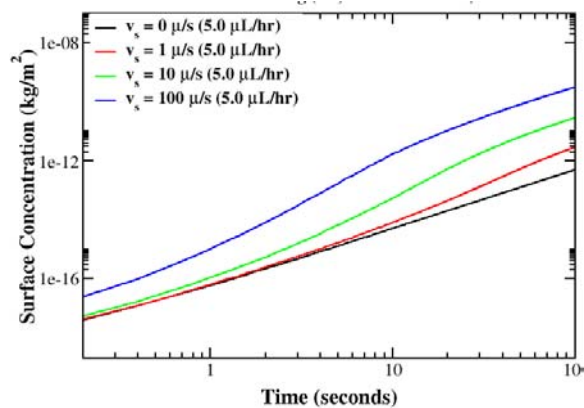


Figure 9.10: Binding enhancement due to lateral force- fast flow.

Effect of Hydrodynamic Forcing: Hydrodynamic forcing involves the "squeezing" or "driving" of the antigen sample toward the sensor by means of a high speed buffer flow. The two main parameters are (a) secondary flow ratio and (b) secondary flow angle. Eight parametric simulations were performed to carefully study the effect of both parameters. Two primary (0.1 and 1.0 $\mu\text{L}/\text{sec}$) and two secondary (100, 1000 $\mu\text{L}/\text{sec}$) flow rates were used along with two forcing flow angles (45 and 90 degrees).

A large flow ratio is desired to focus the sample into a narrow region near the wall. However, this also implies rapid flushing of the analyte. In addition, the importance of gravity is dependent on the absolute values of the velocities (at low enough velocities appreciable sedimentation could occur). The streamline contours, for the flow ratio of 100 and forcing angle of 45 & 90 degrees, are shown in Figures 9.11 and 9.12. A recirculation zone caused by the detachment of the high-speed (secondary) flow boundary layer can be readily seen as the dominant flow feature. Driven by sedimentation, there is an accumulation of the antigen in the primary channel just ahead of the recirculation region. Correspondingly, peak surface coverages also occur in this region, slightly upstream of the junction. Examining the time evolution of the averaged surface binding (across the entire bottom surface, shown in Figures 9.13 and 9.14), it is seen that absolute magnitude of the primary flow rate is the most important, followed by the secondary flow rate ratio in determining short-term signals. Longer-term signals are predominantly controlled by secondary flow rates.

Another major factor controlling flow and hence binding, during hydrodynamic forcing, is the angle at which the secondary flow meets the primary flow. Forcing angles of 45 and 90 degrees were chosen. Flow streamlines show a similar recirculation pattern, albeit more upstream than the 45 degree study. Surface averaged binding evolution with time indicates that the 90 degree case performs slightly better.

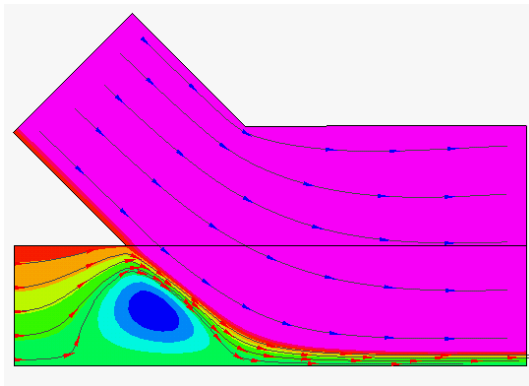


Figure 9.11: Hydrodynamic forcing - 45 degree

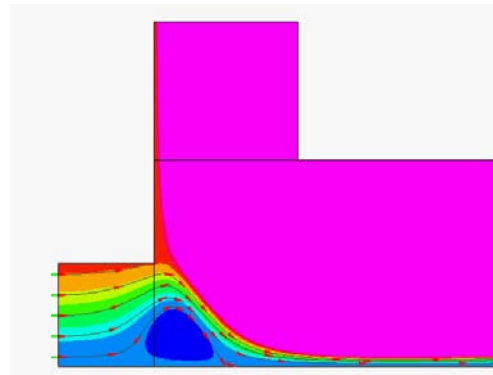


Figure 9.12: Hydrodynamic forcing 90 degree

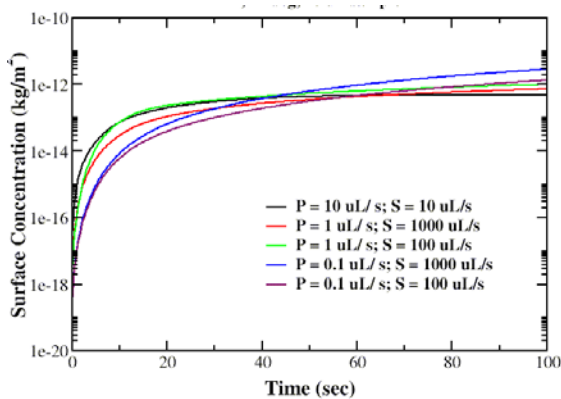


Figure 9.13: Effect of forcing flow ratios on surface coverage

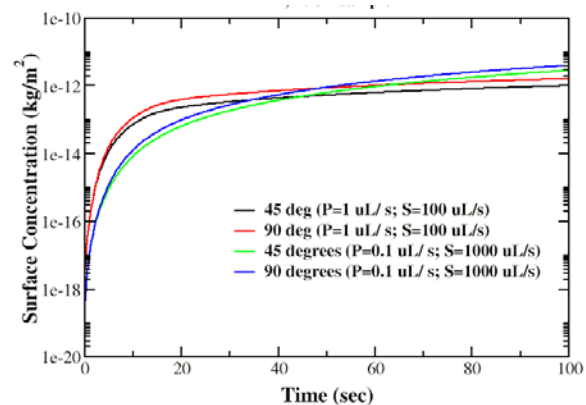


Figure 9.14: Effect of forcing flow angle on surface coverage

9.1.4 Conclusions

CFDRC successfully performed numerical design analysis and optimization studies on the CANARY biosensor system being developed by MIT Lincoln Laboratory. Diffusion-based delivery (through the viscous boundary layer) of antigen to binding surfaces was found to be insufficient for real time detection of agents. Using computer simulations, several design alternatives were analyzed with the aim of enhancing sample arrival rate at the sensor surface. The design alternatives encompassed flow obstacles, drift velocities and hydrodynamic forcing or focusing. While considering a range of flow obstacles, including fins, posts etc., *the pedestal region of the cylindrical post was found to yield maximal binding rates*. Imparting lateral velocity (by any of gravitational, electromagnetic, electrophoretic, etc. means) was found to linearly increase the antigen presentation and hence binding rates. *The most promising approach was to use a high-speed secondary flow to force the antigen toward the sensor wall.*

9.2 Electrokinetic Sample Injection and Pinching in a Cross-Channel

9.2.1 Problem Description

A short study was carried out to demonstrate the capabilities of the electrokinetics modeling capability developed in CFD-ACE+ during this project to Aclara BioSciences, Inc. The specific goals are to simulate and analyze sample injection and pinching in a cross channel configuration

under the influence of an electric field. The objective was to study the shape and strength of a signal (sample concentration) during the injection and separation process.

9.2.2 Method of Approach

A schematic of cross channel configuration is shown in Figure 9.15. It consists of a straight separation channel connecting Reservoirs R1 and R3, and an injection channel at 90 degrees, connecting reservoirs R2 and R4. The sample is placed in R4. As shown in Figure 9.15, due to isotropic etching, the cross channels have a trapezoidal form. The injection process consists of three steps:

- Step 1: Filling of the injection channel
- Step 2: Pinching
- Step 3: Injection with pullback

To perform the injection process, the voltages applied at each of the reservoirs are changed during different steps. The corresponding values are shown in Table 9.1

Table 9.1: Applied Voltage (V) and Time (sec) During Injection Process

	R1	R2	R3	R4	Time Duration (sec)
Step 1	0	500	0	0	0 - 25
Step 2	940	1320	0	1005	25 - 26
Step 3	0	630	1800	630	26 - 36

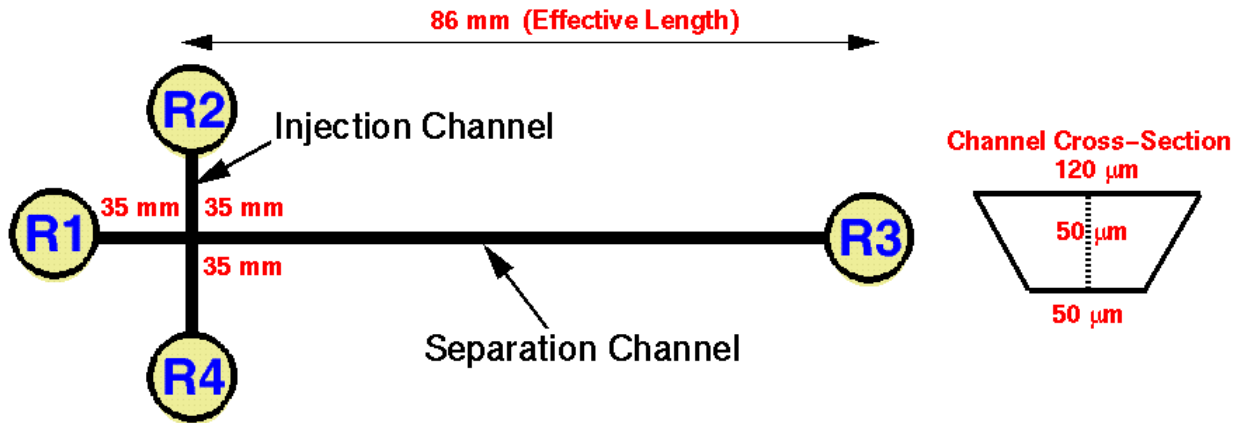


Figure 9.15: Cross-channel system for sample injection and pinching

Geometry and Grid Generation: Two-dimensional geometric models of the cross-channel configuration and two-specie stacking system in a simple rectangular channel were developed using CFD-GEOM. The flow domain was divided into approximately 27000 cells using a structured mesh.

Transport Equation for Mass Transfer: To model electrophoretic phenomena, the equations governing advection, diffusion and electromigration of a charged specie in an electric field is solved. The conservation equation for a given specie i is expressed as:

$$\frac{\partial c_i}{\partial t} = -(\nabla \cdot \mathbf{J}_i) + r \quad (9.1)$$

where the flux vector \mathbf{J}_i is given by:

$$\mathbf{J}_i = \mathbf{V}c_i - z_i\omega_i c_i \nabla\phi - D_i \nabla c_i \quad (9.2)$$

In the above equation, c_i is the concentration, D_i is the diffusion coefficient, z_i is the valence and ω_i is the electrophoretic mobility of the i^{th} specie. \mathbf{V} is the velocity vector and ϕ is the electric potential. The production rate term, r , is neglected since the equilibrium assumption is made.

Governing Equation for External Electric Field: The next step is to calculate the electromigration term. For this, one needs to calculate the electric field

$$\mathbf{E} = -\nabla\phi \quad (9.3)$$

where ϕ is the potential. This is achieved by solving the Laplace equation for potential:

$$\nabla \cdot (\sigma \nabla \phi) = 0 \quad (9.4)$$

where the electrical conductivity σ is defined as:

$$\sigma = F \sum_i z_i^2 \omega_i C_i \quad (9.5)$$

Here, F is the Faraday constant.

Boundary Conditions: The ion concentration values provided by Aclara were specified at the inlet. The zero gradient condition was used for the species at the exit. The zero-flux condition is imposed at all the solid walls. For the electric field, the applied voltage during various steps of the injection process as shown in Table 9.1 was prescribed. All the walls were assumed insulated.

Initial Condition and Properties: During Step 1 of the injection process, the initial ion concentration was assumed zero. For subsequent steps, the ion distribution at the end of the previous step was used as the initial condition. The ion was assumed negatively charged with the mobility of $4.0 \text{ m}^2/\text{Vs}$. Density and kinematic viscosity of the buffer solution was assumed 1000 Kg/m^3 , and $1.0\text{e-}06 \text{ m}^2/\text{s}$, respectively. Electroosmotic flow was neglected.

Solution Procedure: The electrokinetics module in CFD-ACE+ was used to solve the governing equations. The drift velocity of the ionic species was calculated based on local electric field and added suitably in the convection term. This module solves the transport equations for multiple species.

9.2.3 Results and Discussions

The potential distribution along the separation channel axis for all 3 steps is shown in Figure 9.16. Sample filling (Step 1), pinching (Step 2) and subsequent injection (Step 3) in the cross-channel predicted by the model is illustrated in Figures 9.17, 9.18 and 9.19, respectively. The shaded region represents sample concentrations greater than 90% of the initial well concentration.

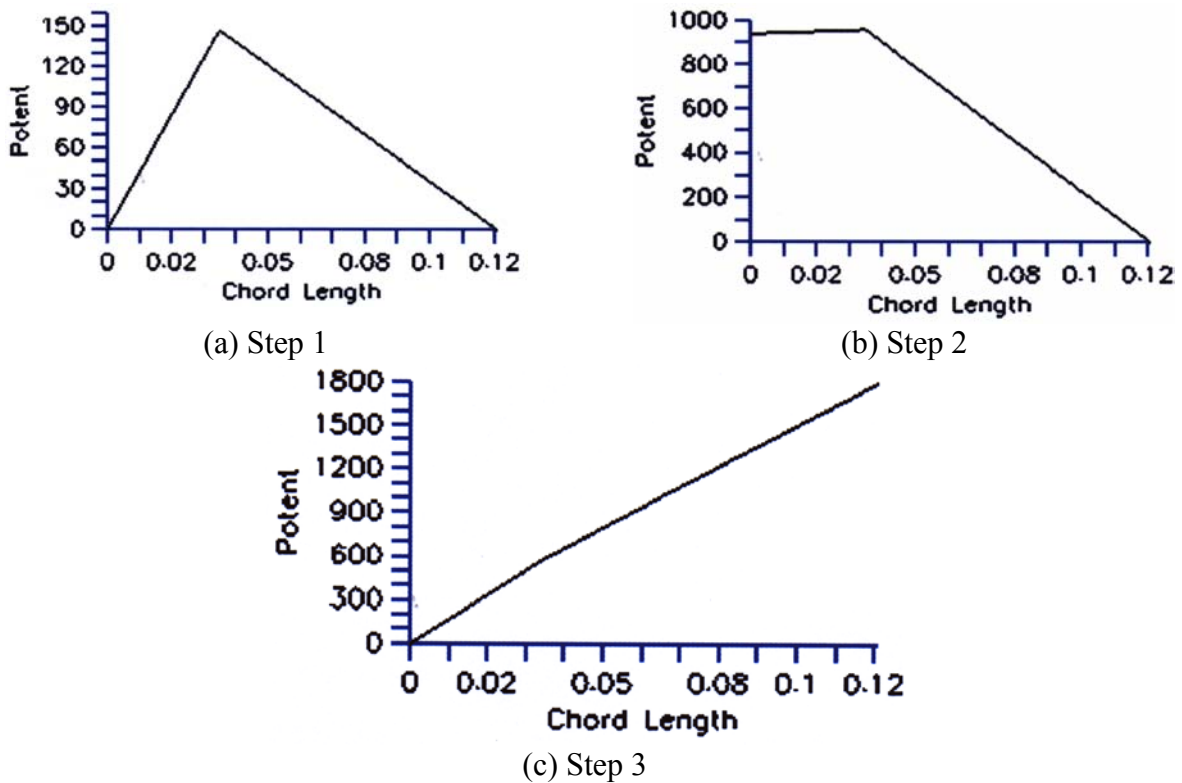


Figure 9.16: Potential distribution along the axis of the separation channel

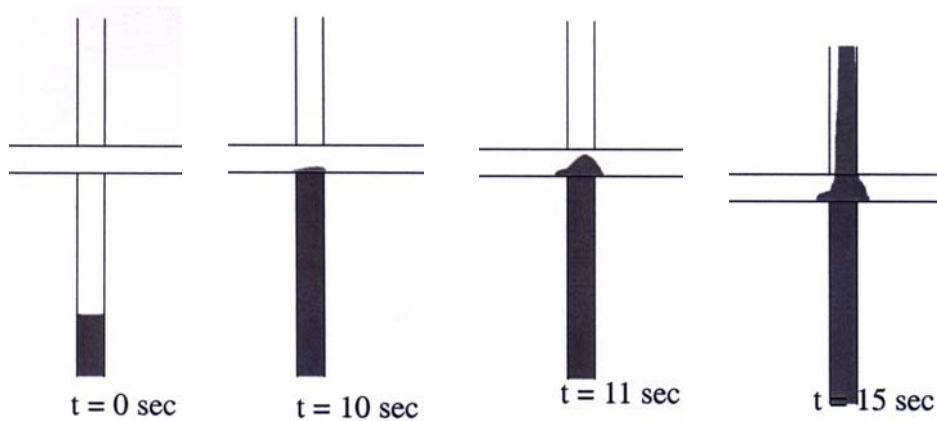


Figure 9.17: Sample filling in cross during step 1

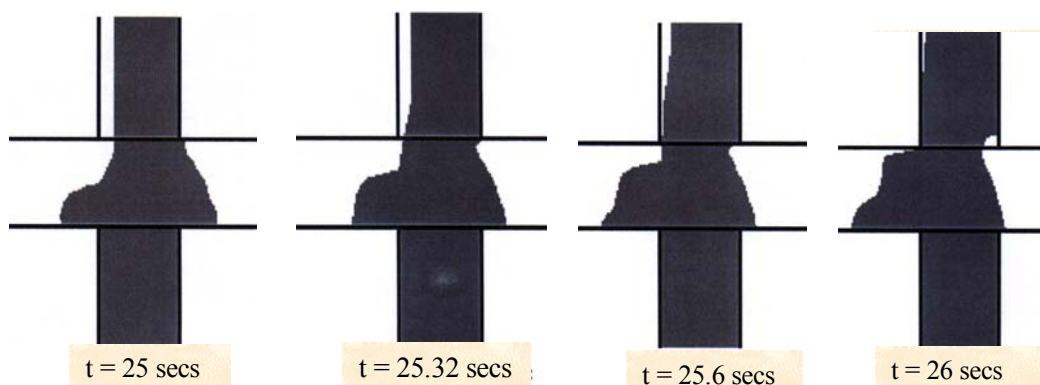


Figure 9.18: Sample pinching in the cross-channel during step 2

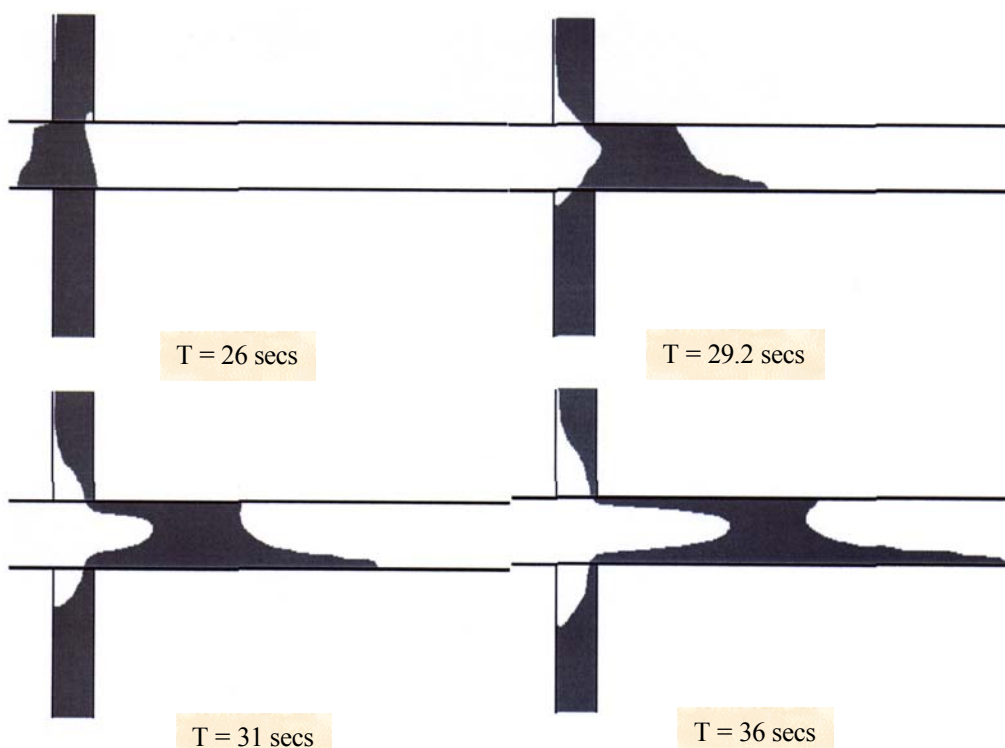


Figure 9.19: Sample injection in the cross-channel during step 3

Step 1: During Step 1, the sample is pulled from reservoir R4 to R2 due to electrophoresis. The injection channel experiences uniform electric field and hence the sample moves with constant velocity till it reaches the cross. The electric field is highly distorted in this region due to channel geometry and causes sample bulging. However, sample continues to move past the intersection to Reservoir R2 (see Figure 9.17).

Step 2: Once the voltages are switched to the Step 2 setting, the voltage at the intersection is slightly greater than that of R1. The net effect is an almost zero electric field on the left side of the separation channel and a very high electric field on the right side (from intersection to R3). The sample plug at the intersection experiences higher electrophoretic force from the right side than from the left side. As seen in Figure 9.18, this causes the sample to squeeze.

Step 3: Here, the voltage at the intersection is slightly more than that applied at R4 and R2. Hence, the net electric field along the injection channel is almost zero and the sample starts moving from the cross towards reservoir R3 (see Figure 9.19).

9.2.4 Summary of Results

This study demonstrates how the developed computational design tool can be used to analyze electrophoretic separation in microchannels. The model predicts that the shape of the sample plug at the intersection is a strong function of the electric field at the cross of the injection channel. This, in turn, depends on the geometry (length and cross-sectional shape of the separation and injection channels) and the applied voltage. A uniform plug shape, which is important for biomolecular separation processes, can therefore be achieved by manipulating these parameters.

9.3 Electrokinetic DNA Chip

9.3.1 Problem Description

The problem considered here involves mass transport of DNA and ionic species under a electric field in an aqueous solution on a generic electronic DNA biochip. Electrochemistry reactions at the microelectrodes provide electric current and electric field in aqueous solution, and DNA molecules move towards microelectrodes due to electrophoretic transport (see Figure 9.20a). Target DNA are transported and concentrated at one or more test sites on the microchip. The accumulation of DNA at each test site promotes rapid hybridization of the sample DNA with complementary capture probes derivatized at the test site. In contrast to the passive hybridization process, the electronic transport process has the distinct advantage of significantly accelerating the rate of hybridization. To remove any unbound or non-specifically bound DNA from each site, the polarity or charge of the site is reversed to negative, thereby forcing any unbound or non-specifically bound DNA back into solution away from the capture probes. In addition, since the test molecules are electronically concentrated over the test site, a lower concentration of target DNA molecules is required, thus reducing the time and labor otherwise required for pre-test sample preparation.

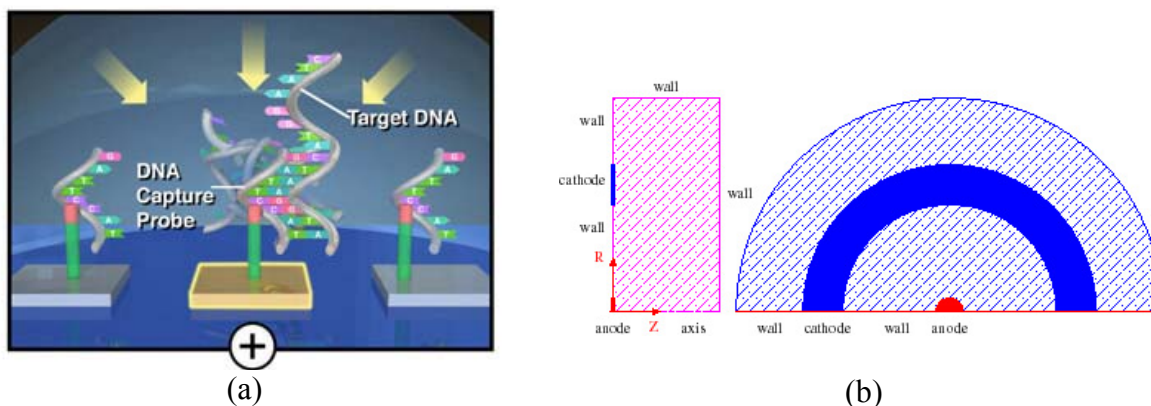


Figure 9.20: (a) Schematic illustration of DNA transport and hybridization on a DNA Chip; (b) Geometry of the flow cell chip (provided by Nanogen)

Here, we outline the results from a feasibility study on modeling multi-species transport on the DNA chip. Specific issues that we addressed in this study were:

- How does DNA concentration change in time near the anode?
- How does the H⁺ distribution change in time in the solution?
- What is the pattern of the electric field?

9.3.2 Method of Approach

The geometry of the computational domain is sketched in Figure 9.20b. The aqueous solution is contained in a cylinder-shaped flow cell. The microelectrodes are located on the bottom of the cylinder with a circular disk shaped anode in the center and an annular disk shaped cathode. Geometric dimensions were provided by Nanogen. Cylindrical coordinates (R, θ, Z) are chosen with the axis of symmetry shown in Figure 9.20b. The electrolyte solution is 1 mM sodium phosphate of density $\rho = 103 \text{ kg/m}^3$ at pH 7.4. A 1 nM single-stranded DNA sample is mixed in this solution. In addition to the ssDNA, five ionic species (Na^+ , H_2PO_4^- , HPO_4^{2-} , H^+ and OH^-) were considered in the analysis.

A structured axisymmetric grid generated by CFD-GEOM was used. Appropriate clustering of the grid near the edges of the electrodes is done in order to resolve the solution adequately in these regions. The Laplace equation (Eq. 9.4 and 9.5) was solved everywhere in the bulk fluid to compute the electric potential. This is because, except for the thin double layer adjacent to the electrodes, electroneutrality is satisfied everywhere else in the bulk solution. At the electrodes, however, the Poisson equation for electrostatic potential is solved to obtain the electric field distribution. The electromigration equation, which accounts for advection, electric drift, and diffusion (Eqs. 9.1 and 9.2), is also solved to describe DNA and ionic species transport. The governing equations are appropriately modified to take into account the ionization reactions for phosphate buffer. The generation of H⁺ and OH⁻ was considered at the electrodes. Conductivity of the aqueous solution was calculated as a function of species concentration.

The ECHEM module was used for the simulations. Two kinds of problems were simulated. The first problem involved choosing the boundary condition where a fixed electric potential is applied across the electrodes, i.e., $V=0$ at the cathode and $V=1$ at the anode. In the second, we prescribed a constant electric current density.

9.3.3 Sample Results and Discussion

DNA Concentration Near Anode: Sample results showing DNA accumulation near the anode are presented in Figure 9.21 for the simulations with a fixed electric current of 10 nA. Figure 9.21a shows the DNA concentration distribution on the anode. The results show a more uniform DNA distribution over the anode as compared to the case with constant electric potential (not shown here). The DNA concentration contours are plotted in the vicinity of the anode in Figure 9.21b at $T = 1$ second. In contrast to the fixed electric potential results, once again a more uniform DNA accumulation is observed.

Variation of H⁺ Concentration: The variation of H⁺ on the electrode plane is shown in Figure 9.22 for the fixed potential case. Since the hydrogen ions are trapped at the cathode and created

at the anode, H^+ concentrations are higher than its initial value throughout the flow cell, particularly near the electrode.

Electric Field Distribution: In the simulations, electroneutrality is not assumed everywhere throughout the flow cell. Instead of solving the Laplace equation, the more general Poisson equation is used. However, it is found that the coupling between the electric field and species concentration is pretty weak because a dilute solution is considered. As a result, the electric field seems insensitive to the species concentration as time proceeds, and electric field contours near both the cathode and anode do not seem to change with time.

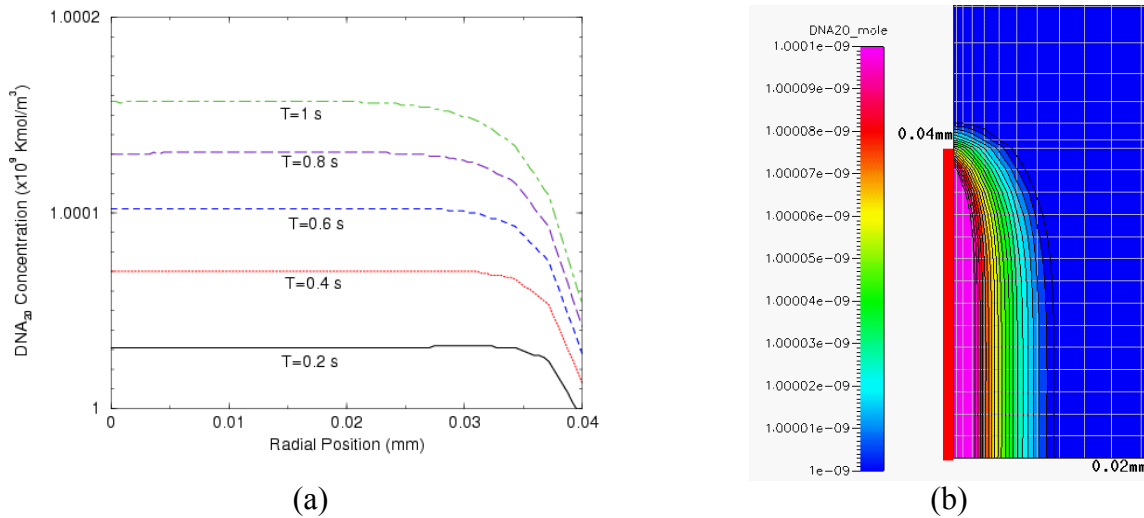


Figure 9.21: (a) Distribution of DNA concentration at the anode; (b) DNA concentration contours near the anode at T = 1 second.

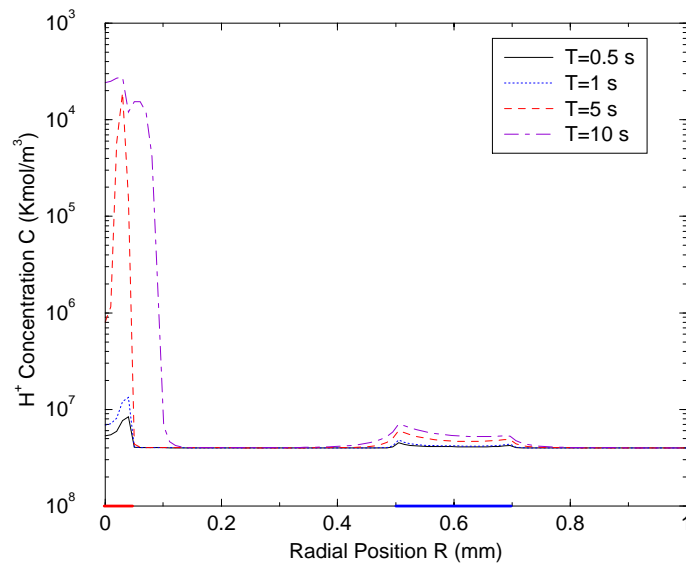


Figure 9.22: H^+ concentration along the electrode plane at different time instants for the fixed potential simulations

The most important factor that affects the molecular transport is the local electric field. Figure 9.23 shows such a profile of both E_R and E_Z along the electrode plane for the fixed potential case. Note that a huge electric field is generated near the edges of the electrode. It is in these high electric field regions that species (DNA) transport is most significant.

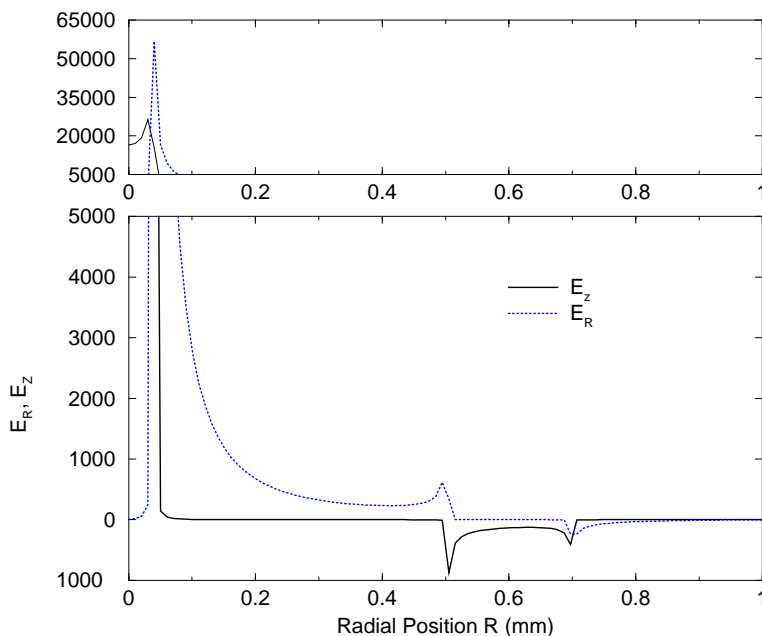


Figure 9.23: Radial variation of electric field components E_R and E_Z along the electrode plane for $T=0.5s$.

9.3.4 Summary and Conclusions

In this feasibility study, we demonstrated the capability to successfully simulate and characterize DNA transport and the electrochemistry of the aqueous electrolyte species on a DNA chip under different modes of operation (constant potential, constant current). Simulations revealed the underlying mechanisms for the concentration of DNA molecules near the anode. Due to the large electric field generated at the edges of the electrodes, DNA molecules are trapped at the anode. The constant current simulations show more uniform DNA distributions in this region as compared to the constant potential case. The study clearly demonstrates how the simulations can be used for design analysis and optimization of electrokinetic DNA hybridization biochips.

9.4 Stacking of Species in a Glass Microchannel

9.4.1 Problem Description

The problem considered in this study is the stacking of species in a glass microchannel. A two-species system is considered here. Stacking is accomplished by sandwiching the sample between a leading and trailing electrolyte of lower electrophoretic mobility and different ionic conductivity. Since the ionic concentrations are significantly different between the electrolyte and sample, electric conductivity and the electric field vary by several orders of magnitude. This causes the front and back edges of the sample to move at different velocities and results in stacking. The chosen electrophoretic system consisted of TAPS as the trailing and leading ion, and fluorescein as the sample. Both the ions are negatively charged. The study objective is to

simulate this sample stacking process so that a uniform, thin, concentrated sample plug can be obtained during the injection process. The study was performed in collaboration with Aclara Biosciences.

9.4.2 Method of Approach

A two-dimensional analysis was performed on a rectangular channel 100 μm wide and 1 cm long. A 2-D geometric model of the channel was developed using CFD-GEOM. The flow domain was divided into approximately 1000 cells. The initial concentration profile provided by Aclara (see Figure 9.24) was assumed for the Fluorescein and TAPS ions. The following physical properties were also assumed:

- Density of the buffer = 1000 Kg/m^3
- Kinematic viscosity of the buffer = 1.0e-06 m^2/s
- Electrophoretic mobility of TAPS = 2.5e-08 $\text{m}^2/\text{V s}$
- Electrophoretic mobility of fluorescein = 5.5e-08 $\text{m}^2/\text{V s}$

The channel was assumed to be filled with a sieving gel (POP6) that self coats along the sides of the channel. Hence, electroosmosis was not considered. The electrical conductivity was calculated using a linear approximation:

$$\sigma = (\sigma_{\text{TAPS}}/1.0\text{e-}02)*1.0\text{e-}02 + (\sigma_{\text{fluorescein}}/1.0\text{e-}04)*1.0\text{e-}04 + 1.0\text{e-}06 \text{ S/m.} \quad (9.6)$$

For computation of the electric field, 0 V and 100 V were applied at the inlet and exit, respectively. All the walls were assumed insulated. The simulation is performed by solving the advection-diffusion transport equation for TAPS and fluorescein, simultaneously with the potential equation for electric field distribution.

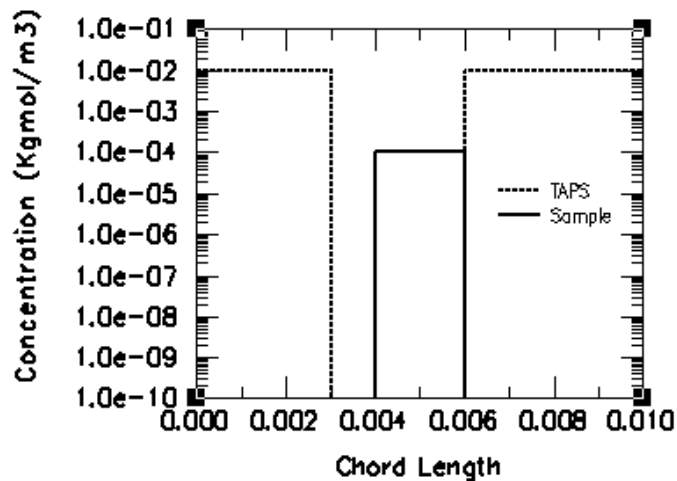


Figure 9.24: Initial concentration of TAPS and sample in straight channel

9.4.3 Sample Results and Discussion

Figures 9.25-9.28 show the spatial variation in sample concentration and electrical conductivity along the channel axis at times $t = 0.2, 0.6, 5$ and 10 seconds, respectively. Simulations indicate that at time $t = 0.2$ secs, the electrophoretic motion has just set in. There is a large variation in

electrical conductivity due to the variation in ionic species concentration (see Figure 9.25b). In the region between the sample and trailing electrolyte, conductivity varies almost by four orders of magnitude. This results in a large electric field. However, at the leading edge of the sample, the electric field is relatively weak due to higher ionic concentration (uniform potential distribution). Subsequently, the leading and trailing edges of the sample start to move at different velocities and cause sample stacking at the leading edge (Figure 9.25a).

As shown in Figure 9.26b, this trend continues at $t = 0.6$ secs. We observe that there is an accumulation of the sample at the trailing edge also. However, as time progresses, this accumulation stops and stacking occurs only at the leading edge. At time $t = 5$ secs, stacking continues to occur, and the electric field at the sample trailing edge continues to decrease due to the transport of TAPS and fluorescein ions by electrophoresis. At time $t = 10$ secs, we stop the computations, fill up the entire channel with TAPS solutions and continue the simulation. This is done to simulate sample motion in actual experiments where TAPS ions from the side channels (not considered here) flow into the injection channel as the sample moves away from the intersection. As shown in Figure 9.28b, we observe that the electric conductivity becomes more or less uniform, except in the small region where the sample is stacked. Here, the conductivity is very large due to large concentration of the sample. The potential varies almost linearly across the channel and the electric field appears uniform. The sample is now transported electrophoretically.

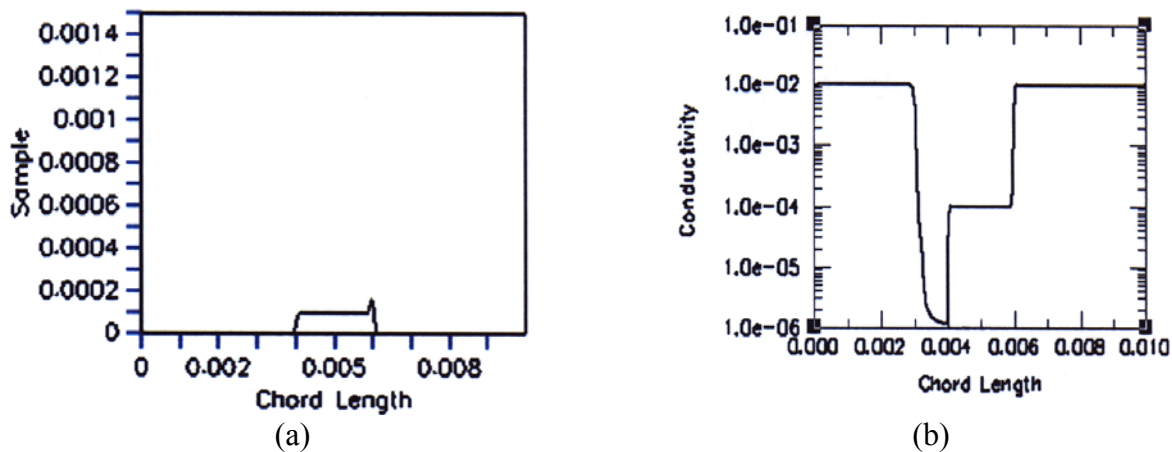
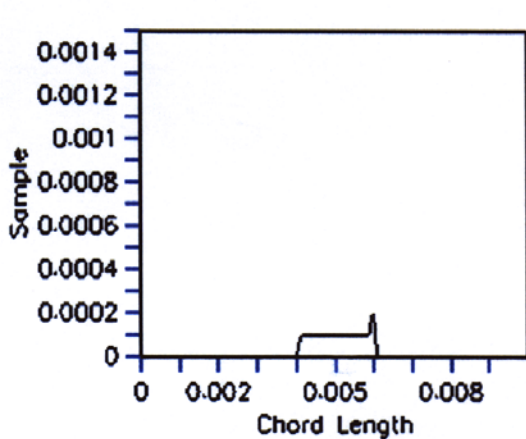
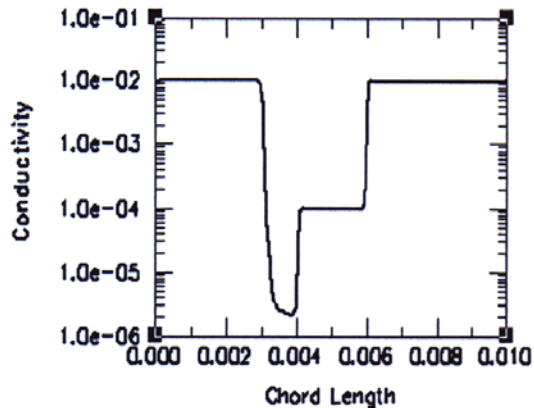


Figure 9.25: Spatial variation in (a) sample concentration (Kgmol/m^3), and (b) electrical conductivity (S/m) along the channel axis at 0.2 secs.

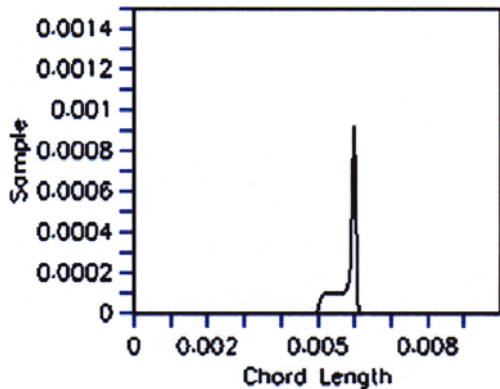


(a)

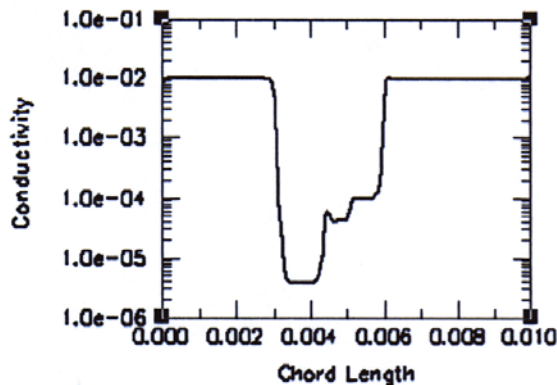


(b)

Figure 9.26: Spatial variation in (a) sample concentration (Kgmol/m^3), and (b) electrical conductivity (S/m) along the channel axis at 0.6 secs.

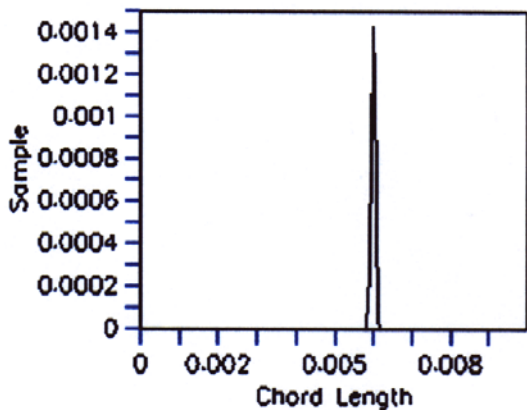


(a)

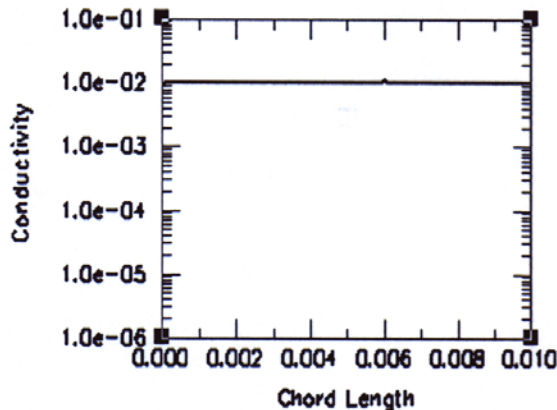


(b)

Figure 9.27: Spatial variation in (a) sample concentration (Kgmol/m^3), and (b) electrical conductivity (S/m) along the channel axis at 5.0 secs.



(a)



(b)

Figure 9.28: Spatial variation in (a) sample concentration (Kgmol/m^3), and (b) electrical conductivity (S/m) along the channel axis at 10 secs.

9.4.4 Summary of Results

The study demonstrates the application of the CFD-ACE+ electrokinetics models for analyze the stacking phenomenon in microchannels. A linear approximation for electrical conductivity as a function of local ion concentration was used to simulate the stacking phenomenon. *Simulations revealed that the efficiency of the stacking depends upon the mobility of the leading and trailing electrolyte and the applied voltage.*

9.5 Impact of Sheath Flow on Electrokinetic Sample Transport

9.5.1 Problem Description

We studied the evolution of a sample plug in a capillary inside a channel under the impact of both electric field and a sheath flow. A schematic illustration of the problem of interest is shown in Figure 9.29.

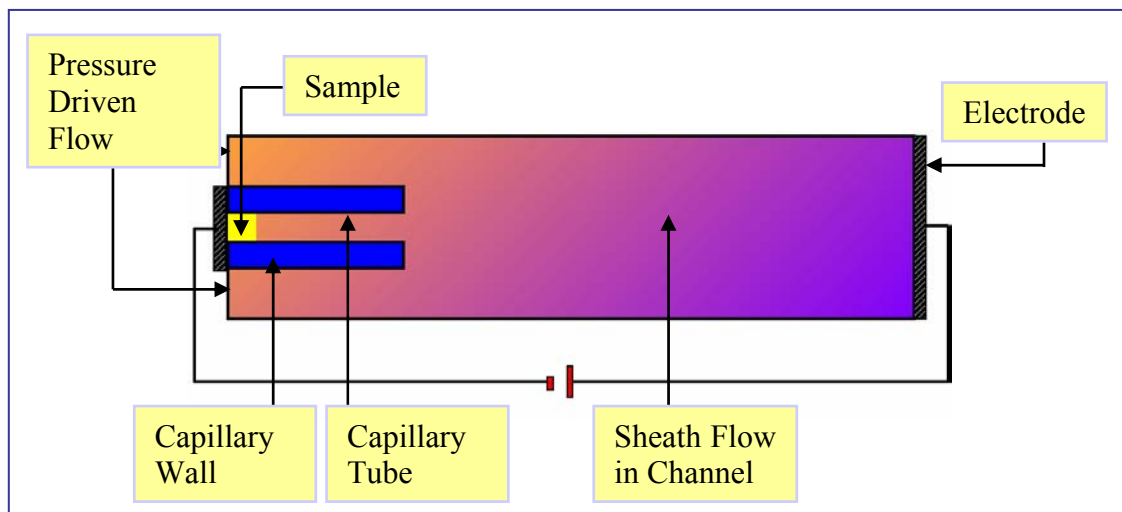


Figure 9.29: Schematic of sample transport in a capillary inside a channel.

9.5.2 Method of Approach

ECHEM2 was used to solve the electrokinetic and hydrodynamic equations simultaneously under a variety of boundary condition corresponding to different physical significance. The total length of the out channel is 1.2mm and the height is 0.3mm. The outer and inner diameters of the capillary are 150 μm and 50 μm , respectively. The length of the capillary is 0.3mm.

The following parameters in the numerical simulation:

$$\text{Sample diffusivity: } D=1E-8m^2/s$$

$$\text{Sample charge: } z = -1$$

$$\text{Electric potential difference: } \Delta V = 100v$$

$$\text{Pressure drop: } \Delta p = 0.01, 1, 5, 20, 40 \text{ N/m}^2$$

The sheath flow is assumed to be for water. Simulations are performed for a plug sample of initial width 60 μm .

9.5.3 Results and Discussion

The sample transport is influenced by electrophoresis and pressure-driven flow in outer sheath channel. When $\Delta p < 10 \text{ N/m}^2$, the entire transport process is electrophoresis-dominant, otherwise it is pressure-driven flow dominant. The relative importance of these two mechanisms is illustrated in the sample results shown below. We are particularly interested in studying the evolution of sample shape after it enters the outer channel. Figures 9.30 and 9.31 show the transient variation in sample concentration in the domain for $\Delta P = 0.01 \text{ Pa}$ and 1 Pa , respectively. There is a significant amount of sample dispersion despite the “focussing” effect the pressure-driven flow is supposed to exert on it. In fact, some of the sample is seen penetrating the region above the capillary in a direction upstream of the flow.

The reason for this becomes clear in Figure 9.32 when one analyzes the electric field contours in that region. Sample electromigration and diffusion in the upstream direction is clearly more prominent than the opposing downstream convective motion. The other extreme case where the sample motion is clearly electrophoresis-dominated is shown in Figure 9.33. Here, the sample appears more focussed along the axis in the flow domain.

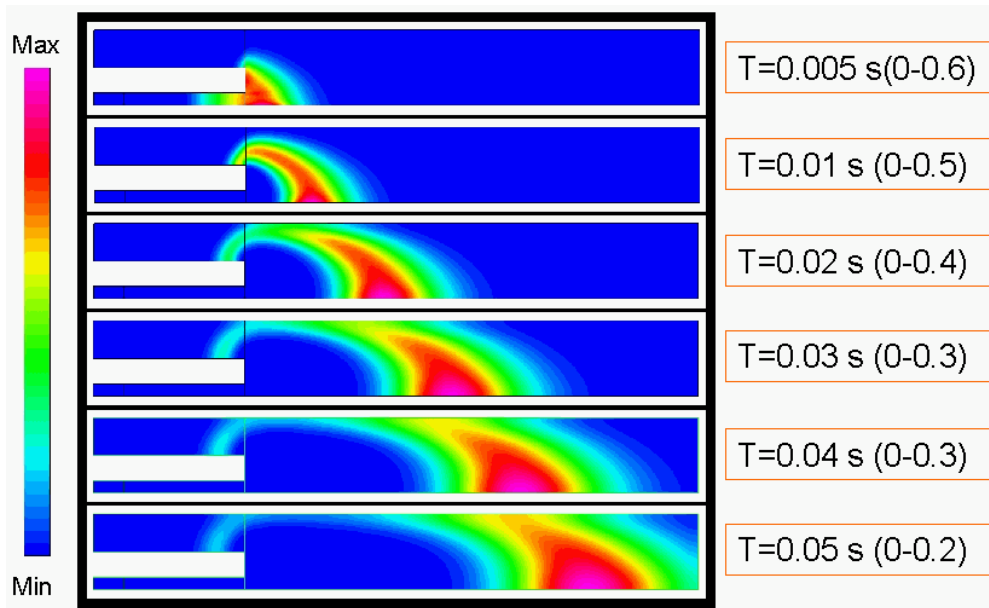


Figure 9.30: Sample dispersion in the domain for the 0.01 Pa case. The time instants and peak sample concentrations are shown adjacent to each plot.

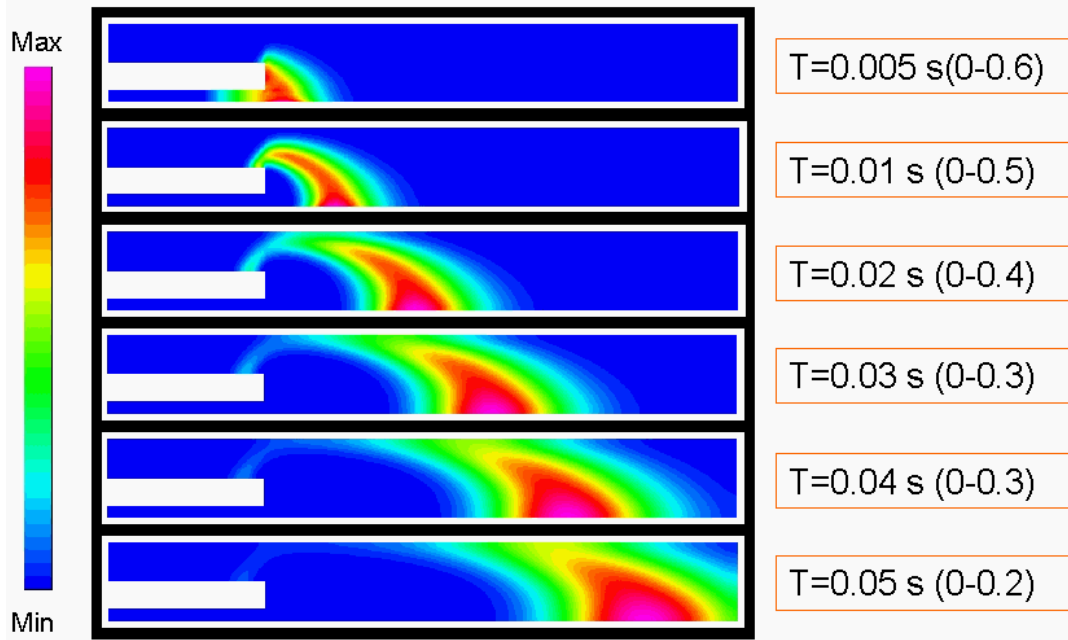


Figure 9.31: Sample dispersion in the domain for the 1.0 Pa case. The time instants and peak sample concentrations are shown adjacent to each plot.

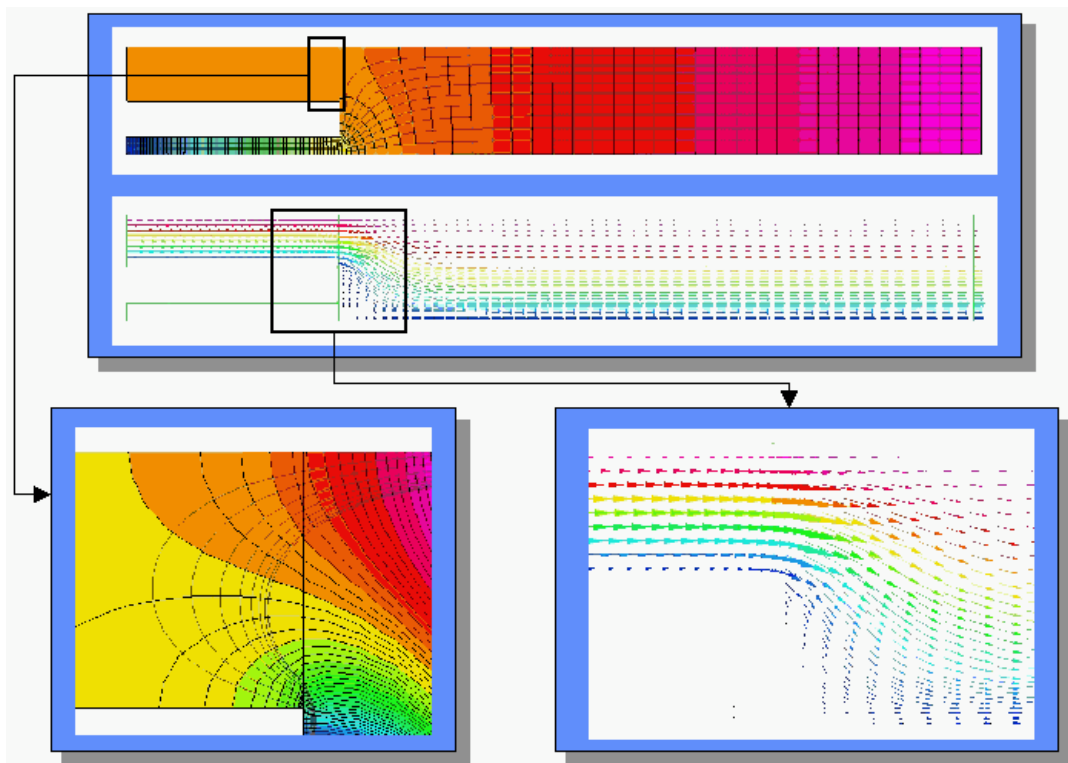


Figure 9.32: Electric field contours and flow vectors in the domain for the 1 Pa case.

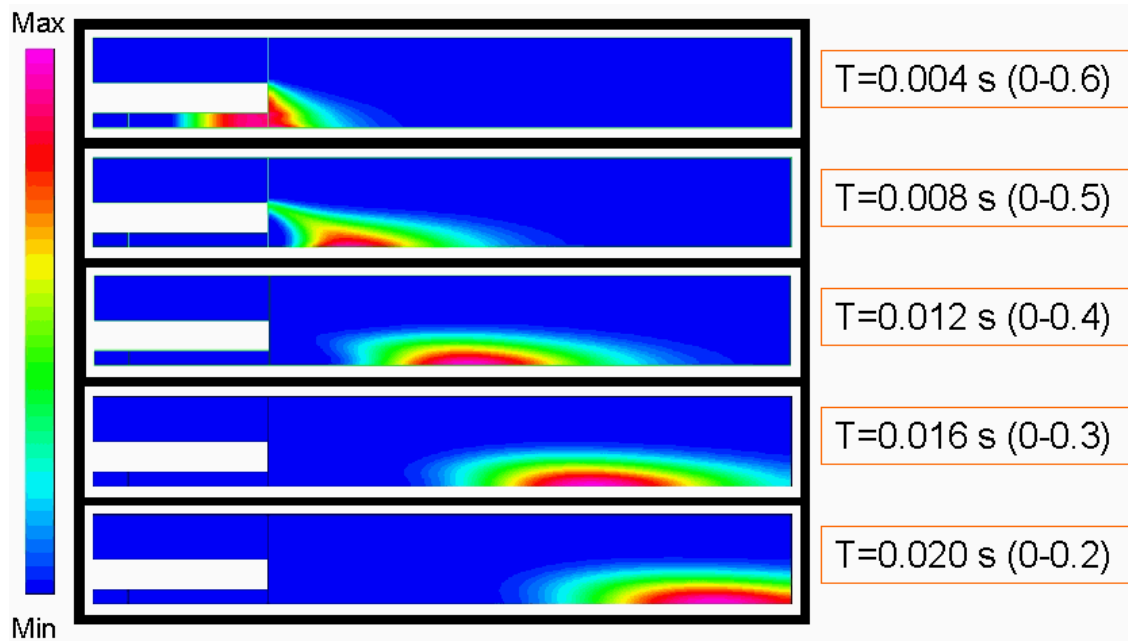


Figure 9.33: Sample dispersion in the domain for the 40 Pa case. The time instants and peak sample concentrations are shown adjacent to each plot.

9.6 Continuous Micromixer System Analysis

9.6.1 Coupled 3-D/1-D/0-D Simulation using ACE+ and SABER

Problem Description: The objective of this study was to apply the developed system-level design tools for simulating and analyzing the performance of the continuous micromixer system being developed at UC Berkeley. As discussed earlier in Section 6.4.1 (see Figure 6.12), this system utilizes pulsatile flow bubble micropumps and microvalves developed at UC Berkeley (Dr. Liepmann's group). The micromixer represents a fully integrated planar system, which consists of 2 bubble pumps, 4 check valves, 3 reservoirs and the mixing channel (Figure 9.34a). Each of these devices are connected via interconnects (or microchannels).

Method of Approach: Modeling of this system via a full-scale 3-D simulation is expected to be very cumbersome and computationally expensive. Hence, we use a mixed-dimensionality, coupled 3-D/1-D/0-D approach in which the 0-D point models are described using SABER. The individual components of this coupled system are described as follows (see Figure 9.34a, b):

- a. Fluidic interconnects: 1-D models (CFD-ACE+);
- b. Valves and bubble pump: 0-D circuit models (SABER);
- c. Mixing channel: 3-D model (CFD-ACE+).

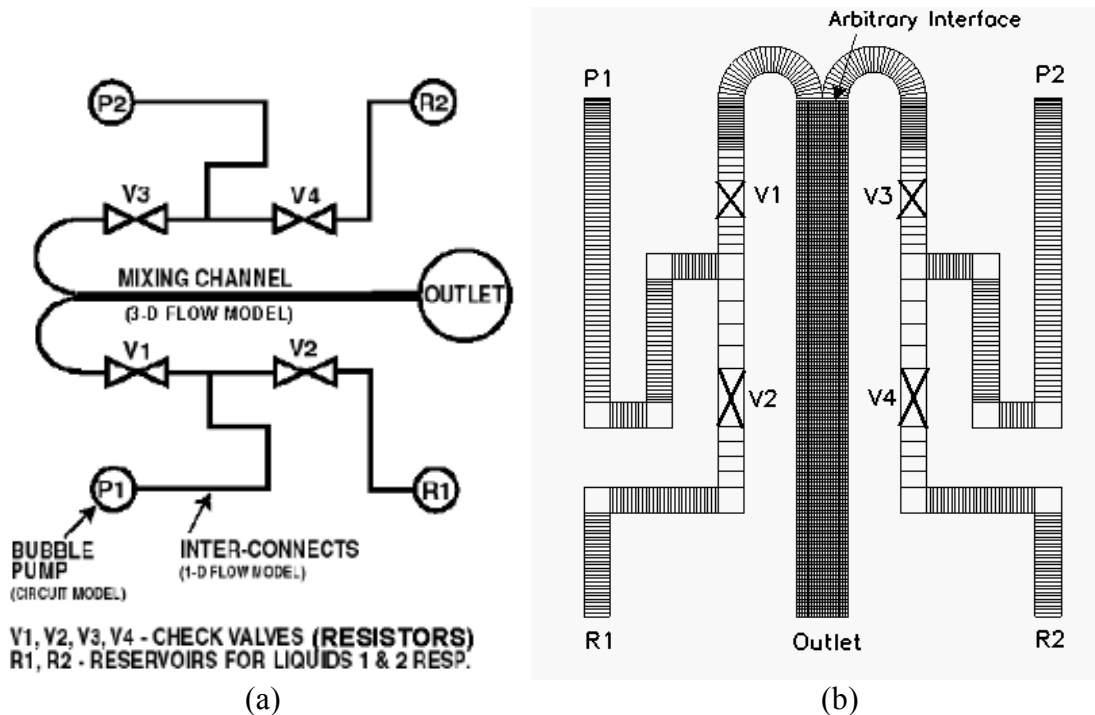


Figure 9.34: (a) Schematic representation of micromixer system model, and (b) Computational domain and mesh used in the analysis

This type of model represents the optimum combination between all 3 modes of modeling in our system-level design tool in terms of computational speed and physical accuracy (since, to our knowledge, there still aren't any accurate reduced models available for characterizing phenomena such as mixing).

All the fluid flow simulations (mixed-dimensional simulations) are performed using CFD-ACE+ coupled with SABER. In the mixed dimensionality simulation, the devices are connected via arbitrary interface type boundary conditions (see Figure 9.34b), for example, the junction between the U-bend (1-D model) and mixing chamber (3-D model).

Sample Results: Preliminary results for the case where the pump frequency is 2 Hz and pressure amplitude is 100 Pa are shown in Figure 9.35. Sinusoidal variations in pump pressure were assumed. The two pumps are modeled as being 90 degrees out of phase. The resulting velocity field pulsations within the mixing chamber are shown in the figure.

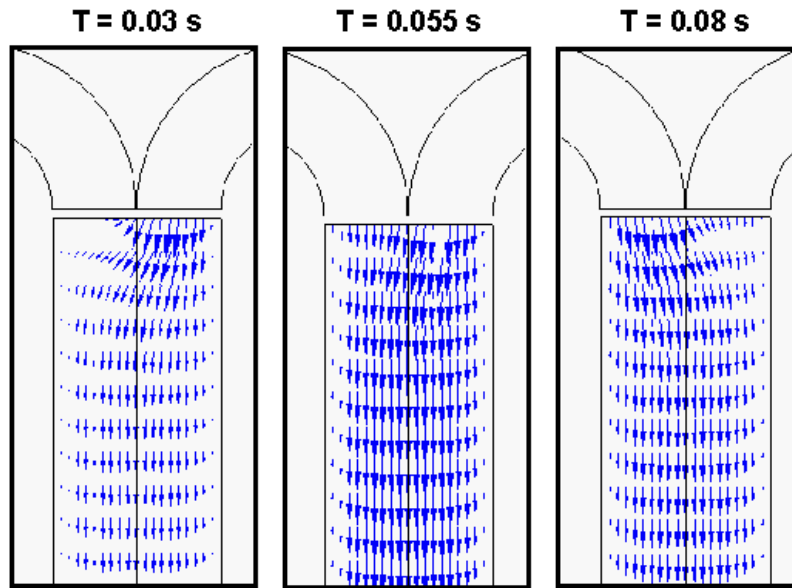


Figure 9.35: Preliminary results from coupled ACE+ and SABER system-level micromixer simulations

9.6.2 System-Level Simulation using ACE+ and SPICE

The system-level simulations of the Berkeley chaotic micromixer system had to be redone using the ACE+ and SPICE interface due to the unavailability of SABER after a certain period of time during the project (as discussed in Section 7.6.1). The micromixer system was simulated using the circuit presented in Figure 9.36, which comprises of 3-D (ACE+) and 0-D (SPICE) elements. The simulations took 17 hrs on a 433 MHz Celeron processor. Simulation results are presented in Figure 9.37.

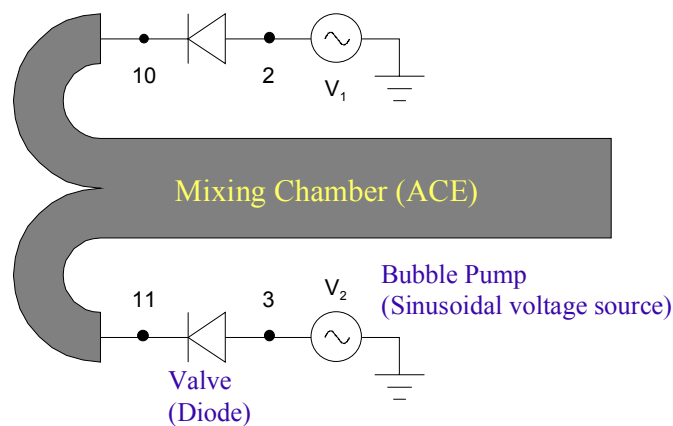


Figure 9.36: Coupled 3-D and 0-D model of Berkeley micromixer system

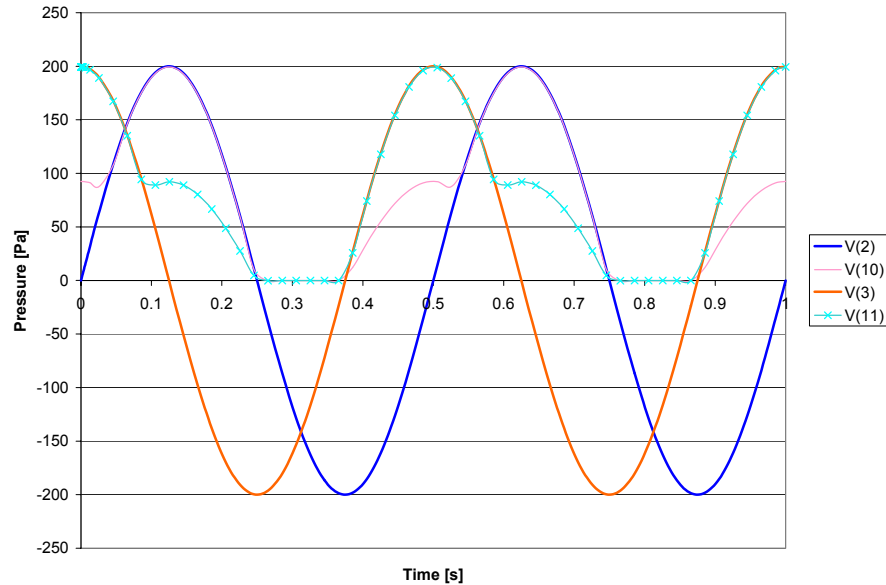


Figure 9.37: Sample ACE+ and SPICE results for the Berkeley micromixer showing pressure-flow variations in the system

9.7 Capillary Array Electrophoresis Chip

9.7.1 Problem Description

This problem was chosen to demonstrate the application of our system-level simulation capability for biomicrofluidic chips which involves microfluidics and electrokinetics. An integrated electrokinetic biochip, designed at U.C. Berkeley, for batch separation/mixing with 11 channels is studied. The layout of a symmetric chip is shown in Figure 9.38a, and the simulation mesh generated by CFD-Micromesh is shown in Figure 9.38b. The chip contains 11 sets of injection and separation capillary channels as well as two optical alignment channel patterned on a 50x75 mm chip. Each channel is about 60 μm long, 60 μm wide and 50 μm deep. Electric potential is applied at each end of the channel to control the injection and separation. In this simulation, we focused on the separation process that occurs after injection step is completed.

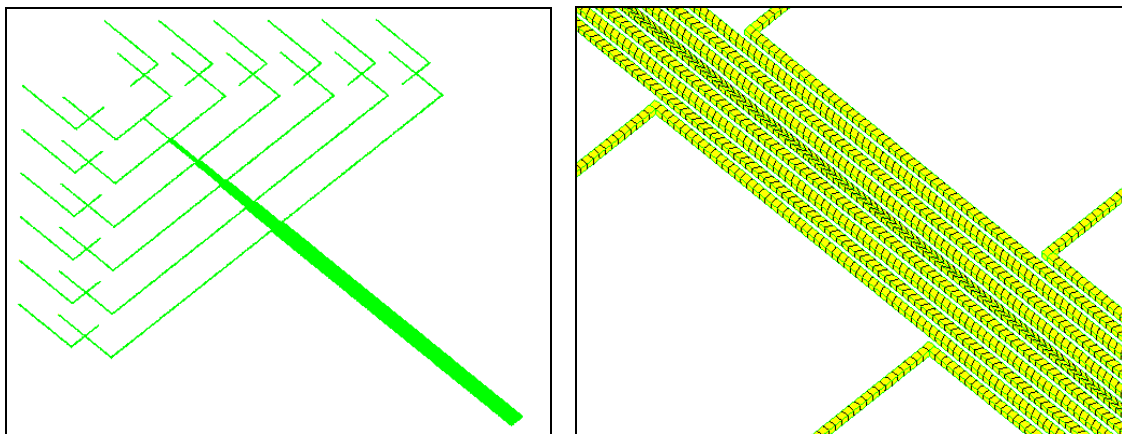


Figure 9.38: (a) Capillary array electrophoresis chips designed and fabricated by UC-Berkeley; (b) Structured one-cell simulation mesh generated by CFD-Micromesh.

9.7.2 Method of Approach

We simulated the injection and separation of six species A-F, with different electrophoretic mobilities, in the system using the EChem module. The species are injected in each pair of separation channels, and a 150V/cm field is applied to drive the species by electrophoresis to the anode. The initial position of each sample is at the intersection of the separation and injection channel after injection is complete.

9.7.3 Sample Results

Typical results for sample evolution at different time are shown in Figure 9.39. The species in each channel move at different speeds due to the different mobilities. Simulations indicate that this multi-channel chip can be used to process all six species simultaneously in each channel, thus enabling a large degree of multiplexing.

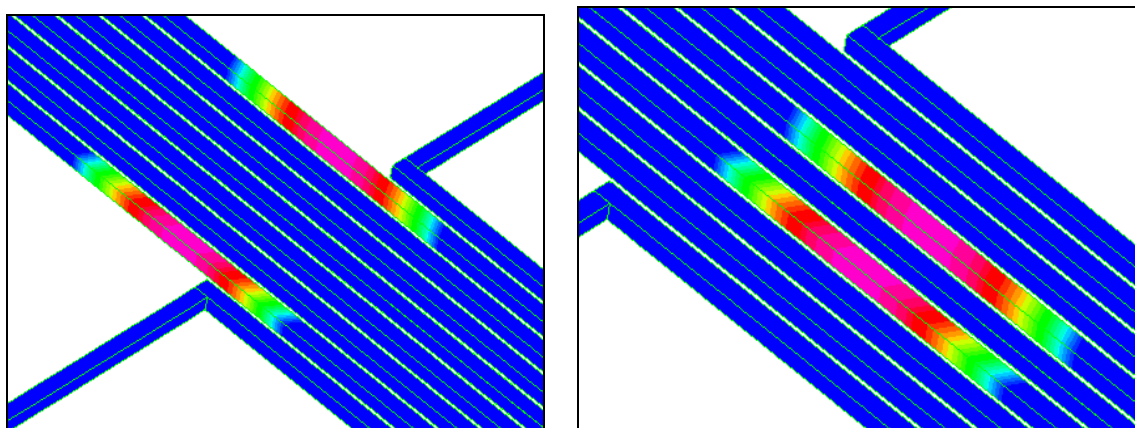


Figure 9.39: Positions of Species C (left) and Species E (right) at T=25s in the capillary electrophoresis chip

9.8 Protein Labchip System

9.8.1 Problem Description

The biochip simulated in this demonstration problem is similar to one used in Agilent 2100 Bioanalyzer, manufactured by Caliper Technology. The geometry of the microfluidic circuit (see Figure 9.40) was based on Agilent's DNA Labchip design, and was taken from the Caliper website (www.calipertech.com). The LabChip contains 16 interconnected reservoirs and micro-channels embedded on a 2 by 2 cm glass chip. From the Caliper website, it is observed that this particular biochip has advantages over traditional research methods. Experiments take less than 30 minutes, and a single integrated process, carried out on a single instrument, replaces multiple manual steps and the need for multiple instruments. These experiments only use nanoliter samples. Human error is virtually eliminated, and researchers get a precise digital readout of data.

In this demo problem, both injection and separation of the sample containing three charged species of differing mobilities, SPA, SPB and SPC, was simulated. Species injection was accomplished using electroosmosis, and the separation was accomplished using electrophoresis. This simulation demonstrated the applicability of CFD-ACE+ for performing virtual experiments

that can be effectively used to design and optimize the biomolecular processes occurring on such biochip systems.

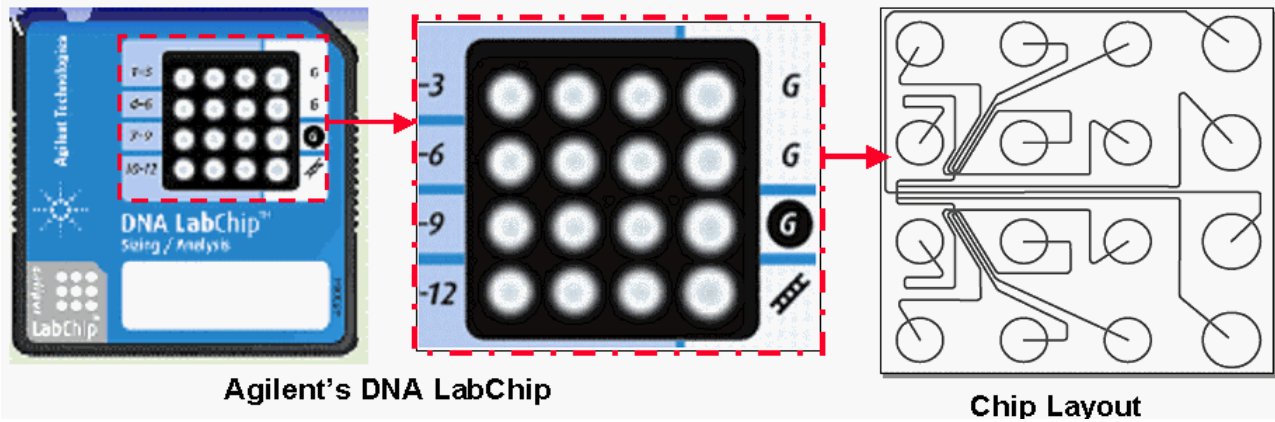


Figure 9.40: Layout of Agilent chip used in demonstration simulations

9.8.2 Method of Approach

A gif image was captured from the Caliper website and read into CFD-Micromesh to create an unstructured grid for the computational domain (as shown in Figure 9.41). All the species used in the simulations were assumed negatively charged. During injection, the species were injected through inlet1 and an electroosmotic mobility of $1.0e-07 \text{ m}^2/\text{Vs}$ was applied. The electric field was maintained between inlets 1 and 2, with inlet 1 grounded and inlet 2 maintained at 1000 V (see inlet location in Figure 9.42). Electrophoresis was inhibited during injection process. Once the sample fills up the injection channel, sample pinching was simulated by applying a voltage between inlets 3 and 4 ($V_4 = 2000\text{V}$). No electric field was applied in the injection channel during this step.

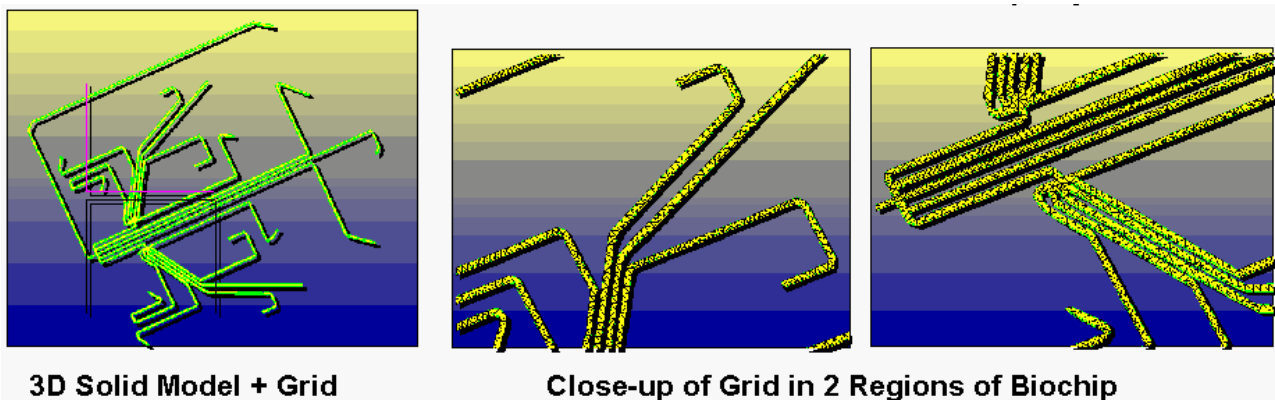


Figure 9.41: Solid model and mesh for the protein Labchip

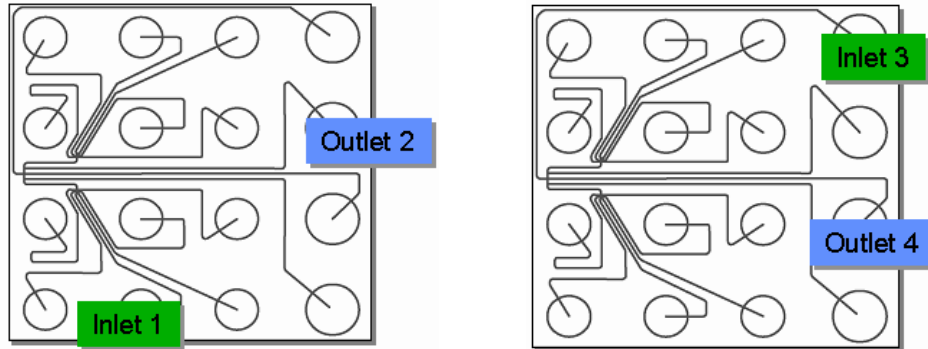


Figure 9.42: Locations of inlets 1 and 3, and outlets 2 and 4 in the Biochip system

9.8.3 Sample Results

Figure 9.43 shows the simulated pinching of the sample in the biochip. Once the sample fills up the injection channel, it is pinched off and moves toward the anode. During this process, all three species migrate with different velocities (due to different mobility) and can be detected at different times at a fixed location in the separation channel. CFD-ACE+ results agree qualitatively with experimental observations.

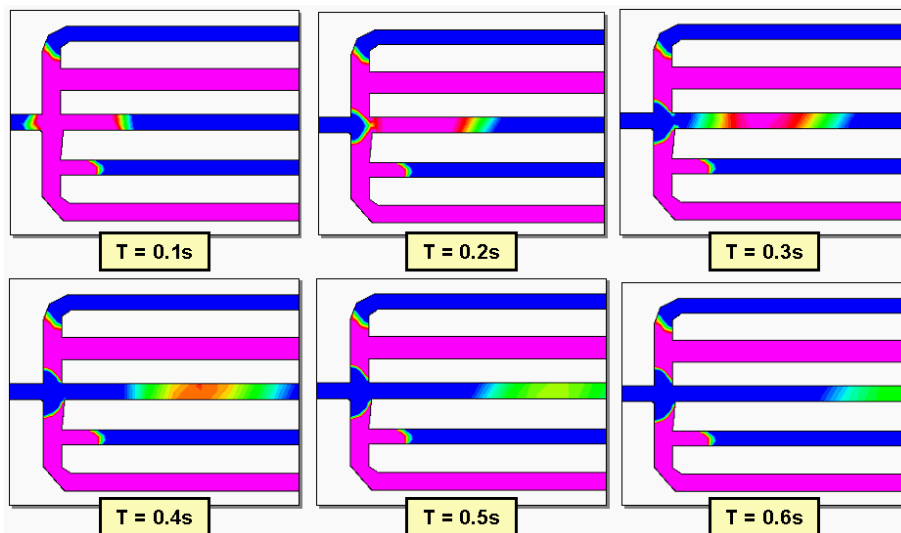


Figure 9.43: Simulated sample pinch-off in the Agilent Biochip

9.9 Microfluidic Biodiagnostic System

9.9.1 Study Objective

I-STAT Corporation currently manufactures and sells portable clinical chemistry analyzers that utilize miniature cartridges to rapidly measure a variety of clinical chemistry values on patient whole blood. Cartridges measure or (calculate) pH, PCO_2 , PO_2 , Sodium, Potassium, Chloride, Urea Nitrogen, Ionized Calcium, Glucose, Bicarbonate, Carbon Dioxide, Hemoglobin, and Hematocrit or select groups of these analytes. The ISTAT biodiagnostic system (Figure 9.44) combines microfluidic and biosensor chip technologies. A 3-D model of the upper portion of their cartridge, showing the miniaturized sensor technology packaged inside the cartridges is shown in Figure 9.45. Each of the miniature cartridges performs a self-calibration and then preprogrammed chemical analyses on a single sample of a patient's whole blood.

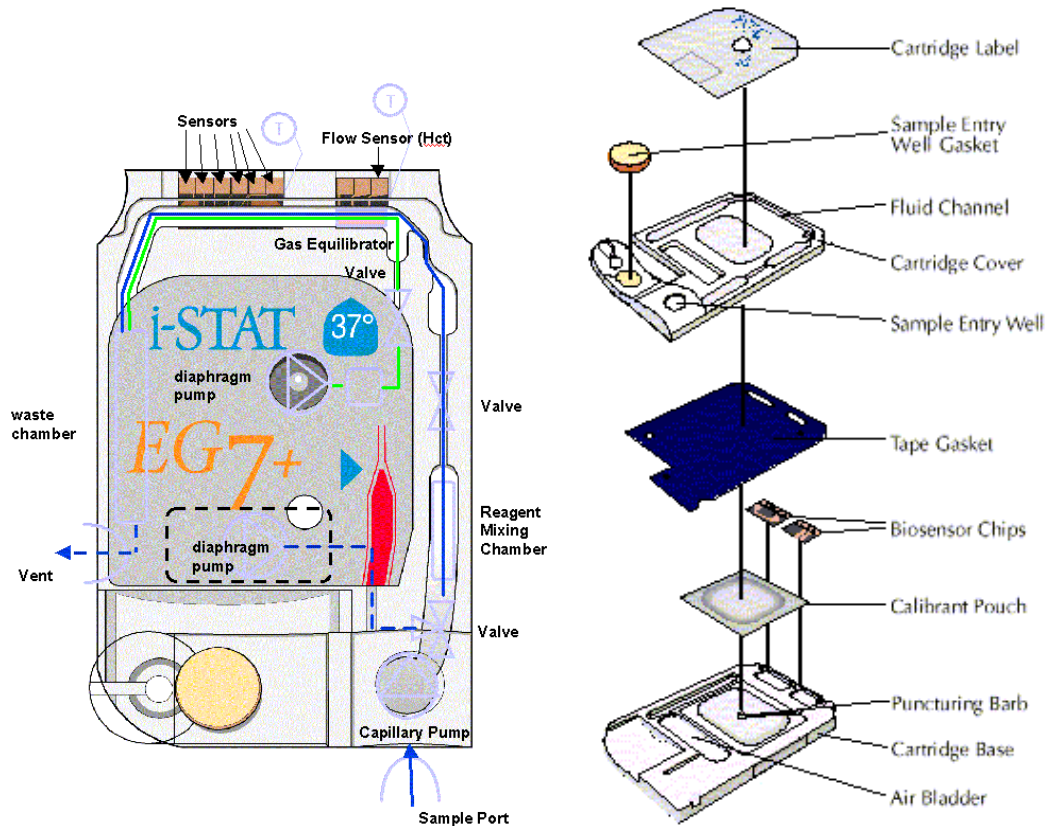


Figure 9.44: Schematics showing the assembled ISTAT biomicrofluidic diagnostic cartridge (left) as well as the sub-assemblies (right)

Since the analyzer is field portable, numerous critical variables must be kept tightly controlled to ensure that the reported results meet published precision and accuracy. One of the most critical variables is the temperature at which the analyses are performed. It was the objective of this study to discover how well the analyzer/cartridge combinations achieved and maintained temperature uniformity along the reaction zone within the cartridges. Finite volume modeling of heat transfer within the various elements in the front portion of the cartridge was performed using CFD-ACE+ to provide insight into how quickly and how uniformly heat distributes.

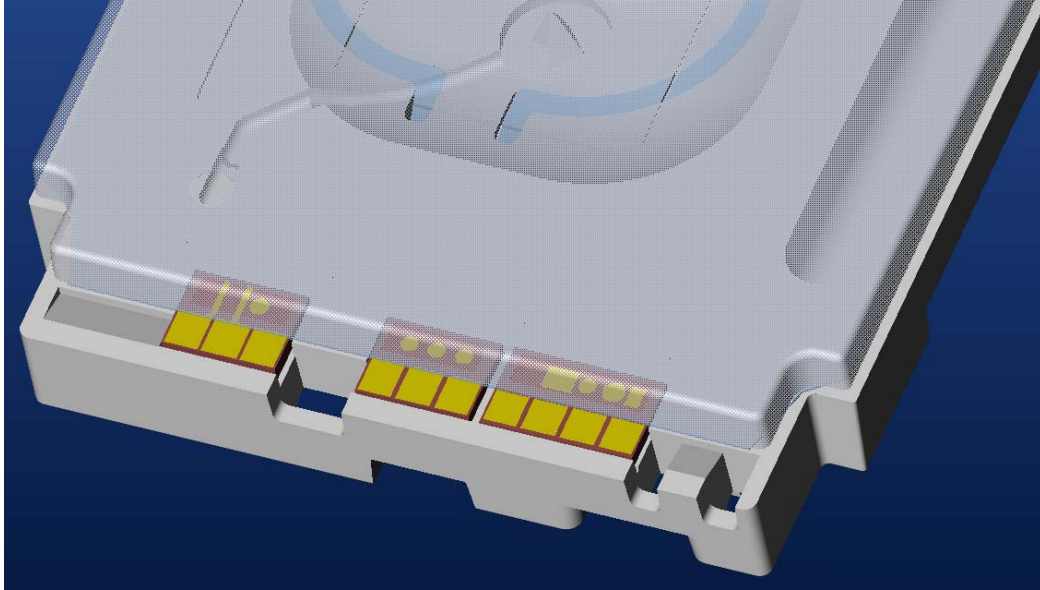


Figure 9.45: See-through solid model of I-STAT cartridge assembly showing blood gas and ion selective electrodes

This study was conducted by the project consultant, Donald Verlee, as a representative of his consulting firm, Microfluidics System Research (MSR), in collaboration with CFDR. His role on this study was to evaluate CFDR's software during the course of the ISTAT demonstration analysis.

9.9.2 Background

For this study, the I-STAT cartridge that was analyzed was a cartridge that measures both blood gases and electrolytes. This particular cartridge has a total of three silicon chips each with multiple electrodes or sensors. The two chips on opposite ends of the flow channel are provided with resistive heaters, which are contacted on the back side of the cartridge. The cartridge is a multi-layer structure that sandwiches these chips as well as an adhesive film layer and calibrant blister between two injection molded plastic components (a cover and base). Channels molded into the interior surfaces of the cover and base define fluid paths illustrated in Figure 9.44.

In a typical assay run, the analyzer advances a plunger up against the center of the cartridge, which causes calibrant in a sealed blister pack to press up against a sharp spike and pierce open. The spike and calibrant well are illustrated in Figures 9.45 and 9.46. As the plunger continues to press against the flexible face of this chamber, the calibrant, now flooding the region under the diaphragm made by the pressure sensitive adhesive layer, advances down the inlet channel flooding the sensor region as well. A capillary break and air bubble are provided to maintain isolation from the sample. To bring the calibrant fluid up to assay temperature and hold the temperature constant, two probes each containing two electrical contacts and a miniature thermistor are brought up from below the cartridge to make electrical contact with heater elements on the silicon (not illustrated) under each of the outside sensors. The silicon in each of these chips rapidly equilibrates to 37 °C (310 K). A PID control loop in the analyzer's software maintains the temperature near the surface of the silicon, under these chips, constant at that temperature.

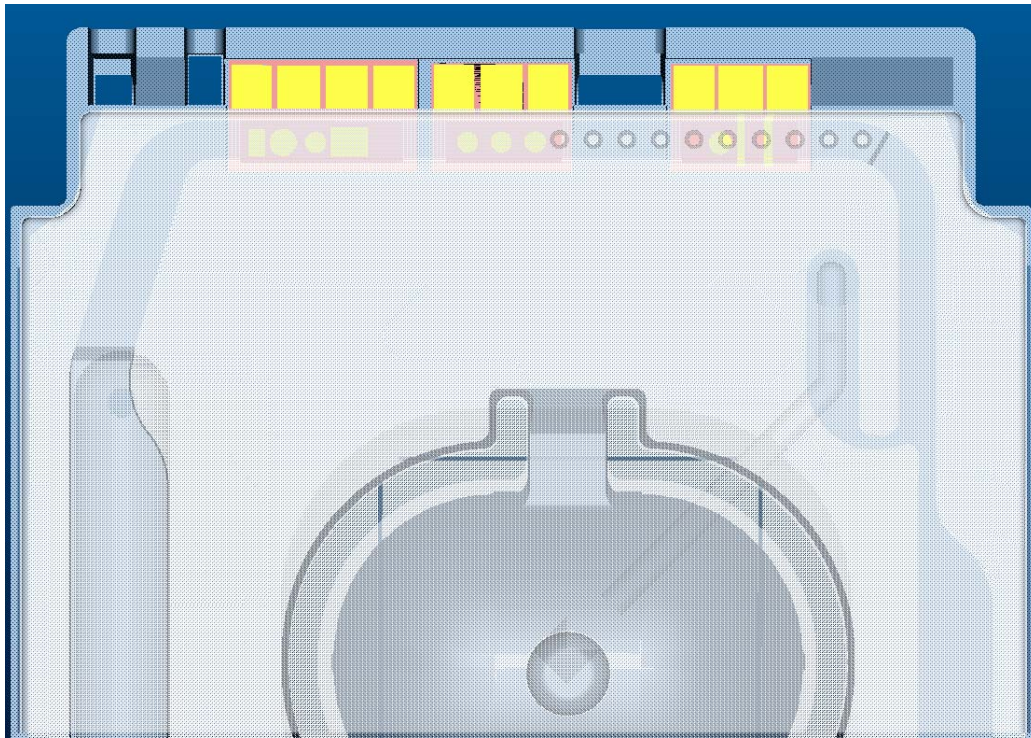


Figure 9.46: Top View of Sensor Half of I-STAT Cartridge

Potentiometric, amperometric and conductometric measurements are taken on each of the electrodes through gold contact pads on the tops of the chips. Once the signal from each of the sensors stabilizes, a reading is made and immediately thereafter, the sample measurement cycle is started. To advance the sample up to the measurement zone, a second plunger presses on a second diaphragm region near the front of the cartridge. This diaphragm pressurizes and advances the sample behind an air bubble up through the detection zone and beyond, into the waste chamber. The advancing air bubble and blood sample wash the calibrant out of the detection zone.

For the second time, the heaters under the two end chips are turned on and are controlled to a constant 310 K. This constant temperature condition is intended to heat the sample to a constant temperature comparable to the temperature the calibrant was measured at. The analyzer then waits for the sensors to stabilize and measurements are made on the sample. Calculations are performed and the resulting concentrations of the measured analytes are reported to the user.

9.9.3 Geometric Modeling and Mesh Generation

The processes occurring in the I-STAT cartridge system were analyzed with the help of CFD-Micromesh and CFD-ACE+ using the following procedure. Accurate solid models of each of the cartridge elements were received from I-STAT, reconstructed in Pro-E and then exported to CFD-GEOM in the IGES format. The complexity of the structures to be meshed threatened the short time schedule allocated for the study. *After spending about 1 week trying to mesh the solid models in CFD-GEOM with slow, limited progress (only 1/3rd mesh was ready by this time), we decided to expedite the solid modeling/mesh generation process by utilizing CFD-Micromesh to break the many complex elements in the cartridge down to discrete voxels. The entire solid*

model and mesh generation task was completed in a 6 hour time period. Both the solid model and the resulting meshed model from CFD-Micromesh are illustrated in Figures 9.46 and 9.47.

As can be seen from Figure 9.47, the mesh created by CFD-Micromesh displays structure or fluid regions right through each of the various layers of the cartridge and reflects the necessary alignment of voxel (*volumetric pixel*) faces on each of the multiple layers of the cartridge. However, since CFD-Micromesh creates structure by projecting “mask” layers into the Z (depth) direction, free standing islands, which at certain depths become “disconnected” from the main layer, are not allowed. Furthermore, structure that projects into the Z dimension at an angle becomes problematic to accurately mesh. This forced us to make slight “adjustments” to the geometry in certain regions (such as the area immediately to the left of the leftmost sensor’s contact pads), to simulate structure that was reasonably close in mass and conservatively close in how temperature would distribute. As it turned out these “adjustments” had little effect on the resulting outcome of the simulation of thermal distribution between the sensors.

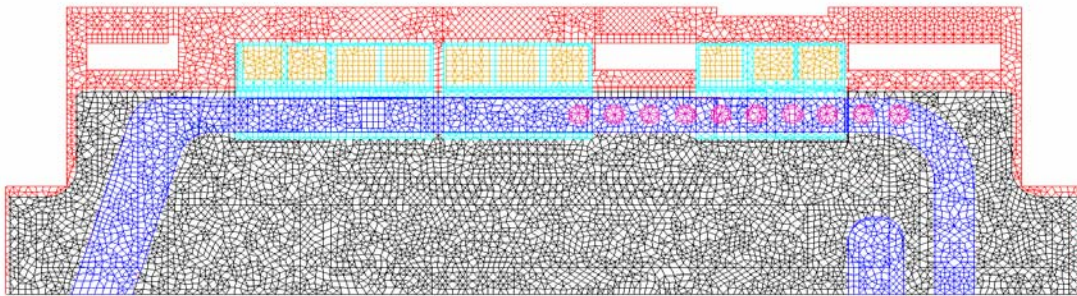


Figure 9.47: Same View of Meshed Results from CFDR’s CFD-Micromesh

9.9.4 Model Parameters

Once we had a representative model of the cartridge discretized and grouped according to material or flow region, the resulting model was analyzed using CFD-ACE+. Table 9.2 illustrates each of the discrete volume regions that were modeled, along with pertinent physical properties that were assigned to them.

Table 9.2: Material properties used in the I-STAT simulations

Cartridge Region	Material	Density (Kg/m ³)	Heat Capacity (J/kg·K)	Thermal Conductivity (W/m·K)	Viscosity (m ² /s)	Initial Temp (°K)
Base	Cycolac T	1270	1300	0.21		293
Cover	Eastar	1040	1400	0.19		293
Gasket	Acrylic	1310	1883	0.16		293
Bottom1	TiW	12900	377	598.0		310
Bottom2	TiW	12900	377	598.0		293
Bottom3	TiW	12900	377	598.0		310
Contact	Gold	19320	132	301.0		293
Sensor 1	Silicon	2330	703	124.0		293
Sensor 2	Silicon	2330	703	124.0		293
Sensor 3	Silicon	2330	703	124.0		293
Cavity	Air	1.1614	1007	0.0263	1.59X10 ⁻⁵	293
Sample	Blood	1080	4175	0.500	non-Newtonian	293
Calibrant	Saline	1080	4175	0.603	9.8X10 ⁻⁷	293

9.9.5 Model Assumptions

Several assumptions were made concerning the design of the cartridge. First, it was believed that the silicon substrate of the two outside chips would quickly reach the desired measurement temperature of 310 K. Furthermore, it was stated that, because of the relatively higher thermal conductivity of both the calibrant and blood sample, the sample would also heat up quickly, and the entire zone between the two sensors would reach a lower but reproducible temperature distribution to assure consistent results from the center chip. To achieve this result it was believed that both of the top and bottom plastic layers would act as insulators, keeping the fluid under test at a constant temperature.

With regards to physical processes, rather than conduct a coupled flow and heat transfer analysis on the cartridge or channel fluids, a simplifying assumption was made that I-STAT scientists intended to achieve static flow conditions during the measurement phase of each assay. The fact that fluid drift does occur not only introduces a complexity that requires further assumptions, but also makes the likelihood of uniform thermal distribution in the fluid channel less probable. It was decided that for the initial analyses, fluid flow in the channel would be deferred, to present ideal “best case” scenario results to verify the assumptions that went into the cartridge design and assay programming. If desired, coupled heat transfer and fluid flow could be conducted at a later date on the model as constructed under a separate project from I-STAT.

Heat transfer into fluids can be simulated in CFD-ACE+ as simple conduction, or more accurately as conduction, convection, and/or radiation. Both convective and radiative heat transfer were ignored for the case of heat transfer into the liquids in the channel, but were not ignored for heat transfer away from the cartridge sensor contacts to air. Our rationale for these assumptions are as follows:

- Convective heat transfer by natural convection occurs when surfaces conducting heat cause density differences in the fluid adjacent to the surface. The density differences set up convective flow along or away from the heated surface. In very small spaces such as the fluid channel and air spaces over the channel, this flow is negligible because the density differences over these distances are small.
- Heat transfer by radiation is a photometric phenomenon that is governed exclusively by photometric properties. Effective radiative heat transfer requires a high emissivity source and high photometric absorbance at the radiation wavelengths in the fluid that photometric energy is being transferred to. When compared to conductive heat transfer, at 310 K, radiative transfer is negligible.
- The air gap distances, contact points and conditions outside of the cartridge were known only approximately. Emissivity values for gold, silicon and TiW were found, but no values for either plastic were found. The largest temperature differences will exist between the silicon sensor/metal surfaces and the air. Rather than assume that heat transfer from these surfaces will be adiabatic conduction to an infinite sink, conservative approximations were made of the heat transfer coefficient from the gold contacts to the air immediately adjacent to them using a formula found in Perry and Chilton’s Handbook for Chemical Engineers. This was used to more closely approximate the heat transfer from gold to air. Of all the assumptions, this one is the most tentative and unverified, but seem to have relative little effect.

- The plastic surfaces were modeled as adiabatic walls for all of our analyses. A more accurate boundary condition assumption would have been to model the plastic surfaces as dissipating heat by conduction, convection and radiation. However, the air within the narrow gaps between the cartridge and the handheld instrument could not be accurately modeled in the limited time, and reasonable heat transfer coefficients could not be easily approximated with the data available to us.

9.9.6 Solution Procedure

The simulations of heat transfer in the sensor region of the I-STAT cartridge system was conducted in the five separate stages to mimic and adequately resolve the various individual phenomenon occurring during those stages.

Stage I: For the first simulation, 50 time points of 0.1 sec each were simulated with the initial temperature values for all volumes, except the TiW layer under the two outside sensors, set to a value 293 K. The TiW voxels, and the air immediately adjacent to them, were set at a constant, isothermal 310 K.

Stage II: The second simulation began where the first ended at (T=5 sec) and continued the original simulation in 1 sec increments out to 2 minutes.

Stage III: During this stage of the simulation, the model was “manipulated” to mimic the effect of transient flow on the temperature profiles within the cartridge. Rather than attempt to simulate blood following the calibrant through the sensor region (with the complexity of starting with two independent fluids and a meniscus between them, one possessing non-Newtonian viscosity characteristics, and an unknown starting temperature distribution) we chose instead to attempt to “reset” the temperature value of all of the fluid voxels in the channel to 293 K, leaving the cartridge and sensors at the temperature they had heated up to. To accomplish this, we attempted to “freeze” the temperature of each voxel in place while we “flowed” heat loss down the channel. This was accomplished by resetting the thermal conductivity values of the plastic solids to 1/1000X their actual values and the silicon and metals to 1/100,000X their actual values, while simultaneously resetting the thermal conductivity all of the fluid volumes to 2000X their actual values. The boundary condition of the fluid channel inlet was reset to isothermal 293 K, and the simulation was started from where it had finished on the second simulation and allowed to run for ~2.4 sec. The result of this simulation accomplishes the objective of resetting all of the fluid elements while leaving the plastic and silicon temperature profiles relatively undisturbed.

Stage IV: The fourth simulation reverted all of the thermal conductivity values back to their actual values, and picked up from the final condition achieved at the end of the third simulation. Once again, 50 time points of 0.1 sec were simulated with all of the boundary conditions left as they were at the end of the third simulation. The fluid inlet and outlet boundary condition temperatures were approximated to follow the values predicted for the fluid in the channel during the second simulation.

Stage V: The fifth simulation extended the results at the end of the fourth simulation out to 1 minute at 1-second intervals.

9.9.7 Results and Discussion

Figures 9.48a, b show thermal distribution plots superimposed on a rendering of the cartridge. In these plots, it is quite evident that a sharp temperature gradient exists at the start of heating and even after 2 minutes still exists around the silicon sensors.

Figure 9.49 shows the transient variation in temperature distribution in the cartridge during the calibrant liquid heating phase. Figure 9.50 shows the progression in temperature distribution near the sensors and in the channel during the flushing of the calibrant and introduction of sample in the channels. Transient variation in sample fluid temperature within the channel during sample heating is shown in Figure 9.51.

At the onset of the study, the expected result was that the outside silicon sensors would quickly heat up and transfer heat to the fluid in the channel. It was assumed that the plastic would act as an insulator and that the warm silicon surface would quickly transfer heat to the fluid, heating it between the two sensors. As expected the two outside silicon sensors warmed up very quickly to 310 K. However, several totally unexpected results are evident in all of the plots above.

- The aqueous fluids heat up at the same rate as the plastic layers.
- Heat propagates relatively quickly above and below the hot sensor areas, but very slowly laterally down the fluid channel, and away from the sensor area.
- Heat transfers across the plastic to the center sensor slowly, and follows the pattern that the center sensor heats up first, and then transfers the heat to the fluid and the plastic surrounding the channel slowly.
- Significant thermal gradients exist for up to 2 minutes into the analysis.
- A hot cartridge heats up the fluid more readily than a room temperature one, leading one to believe that variance in the starting temperature might lead to significant variance in the final assay temperature if all cartridges are heated for the same time period.

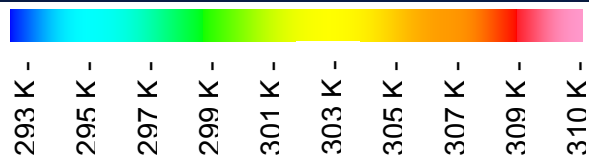
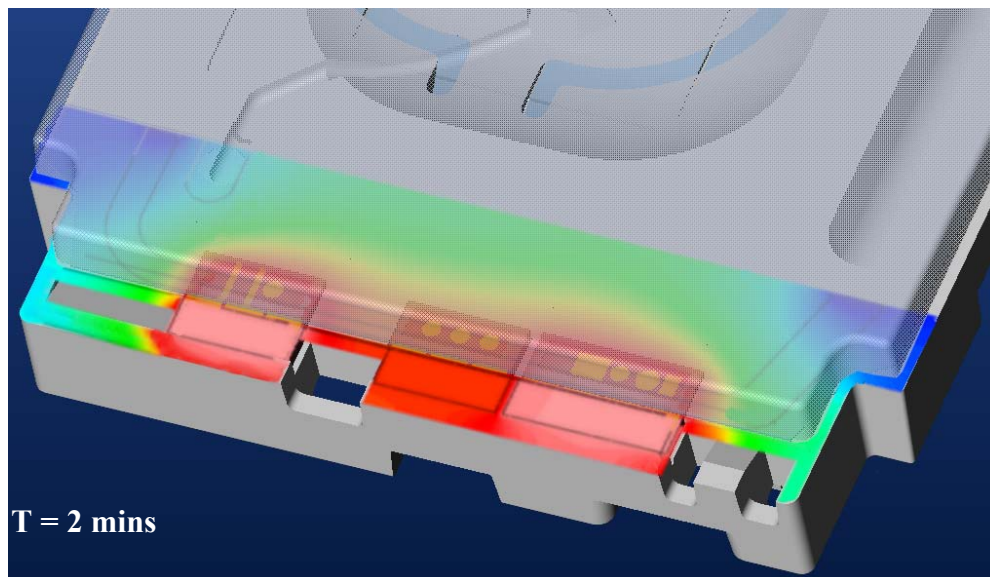
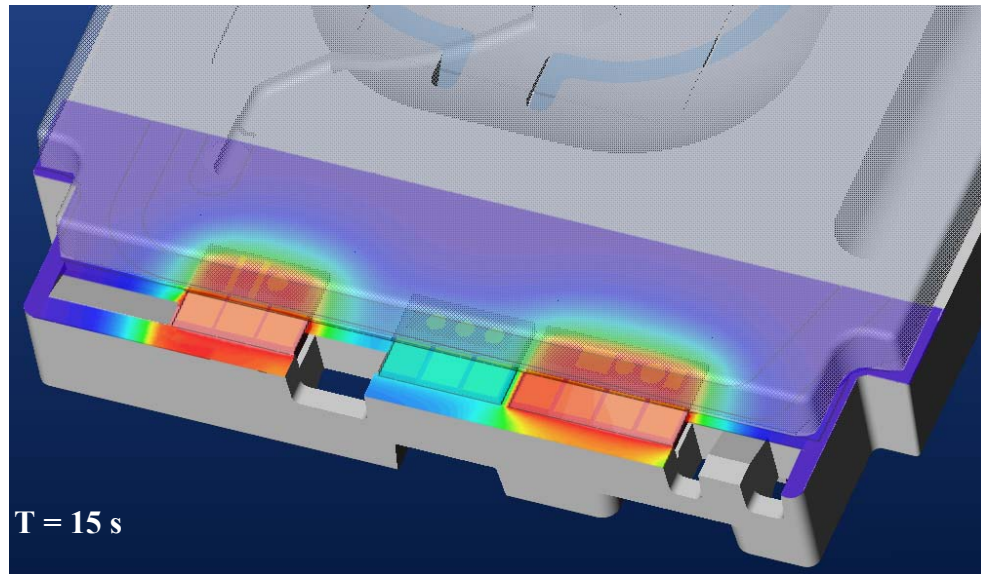


Figure 9.48: Temperature Distribution in Cartridge at 15 Seconds and 2 Minutes after Calibrant Heating in the Channel. The plots show horizontal planes through the sensor and through the channel.

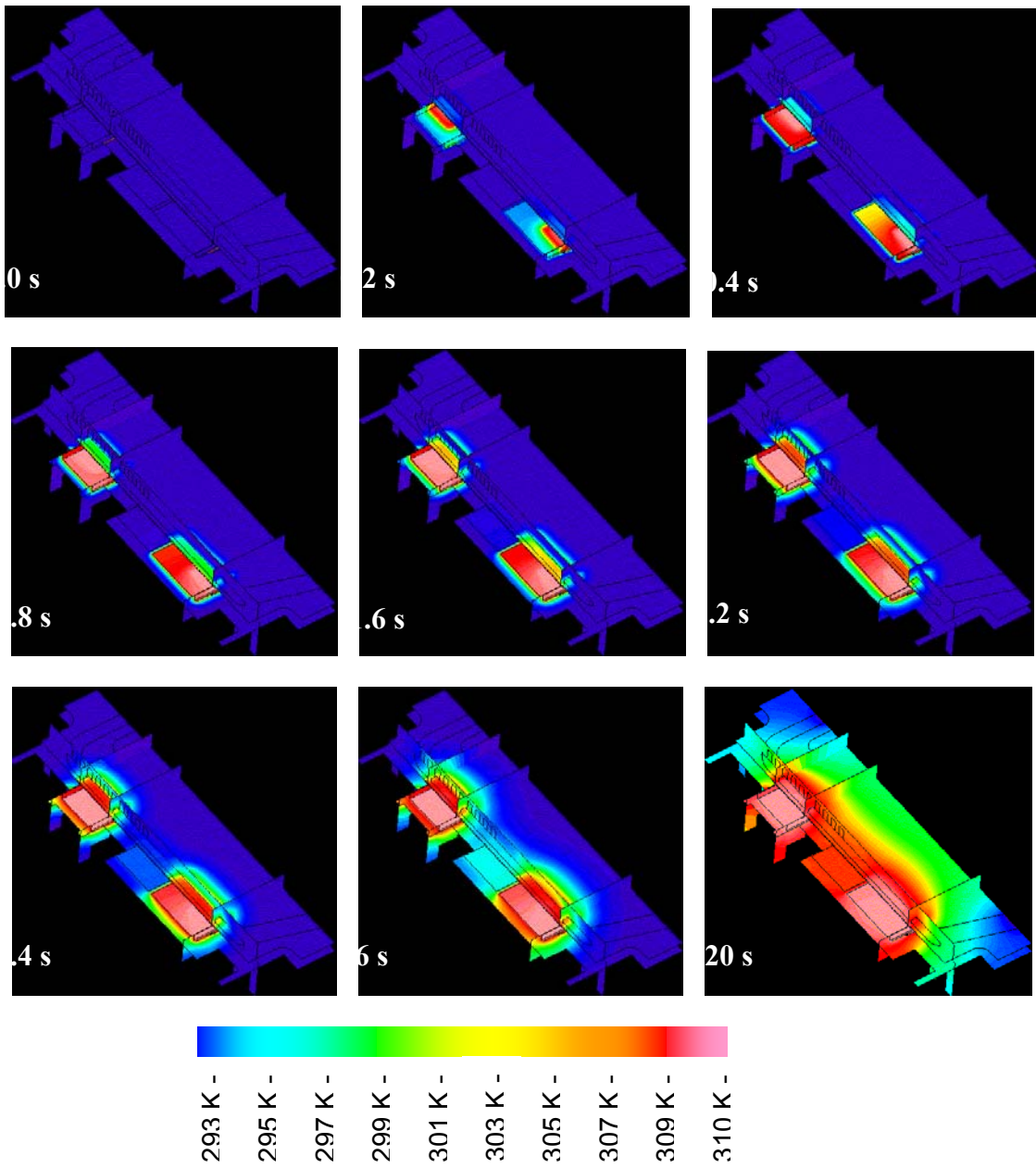


Figure 9.49: Transient Temperature Profiles during Calibrant Fluid Heating

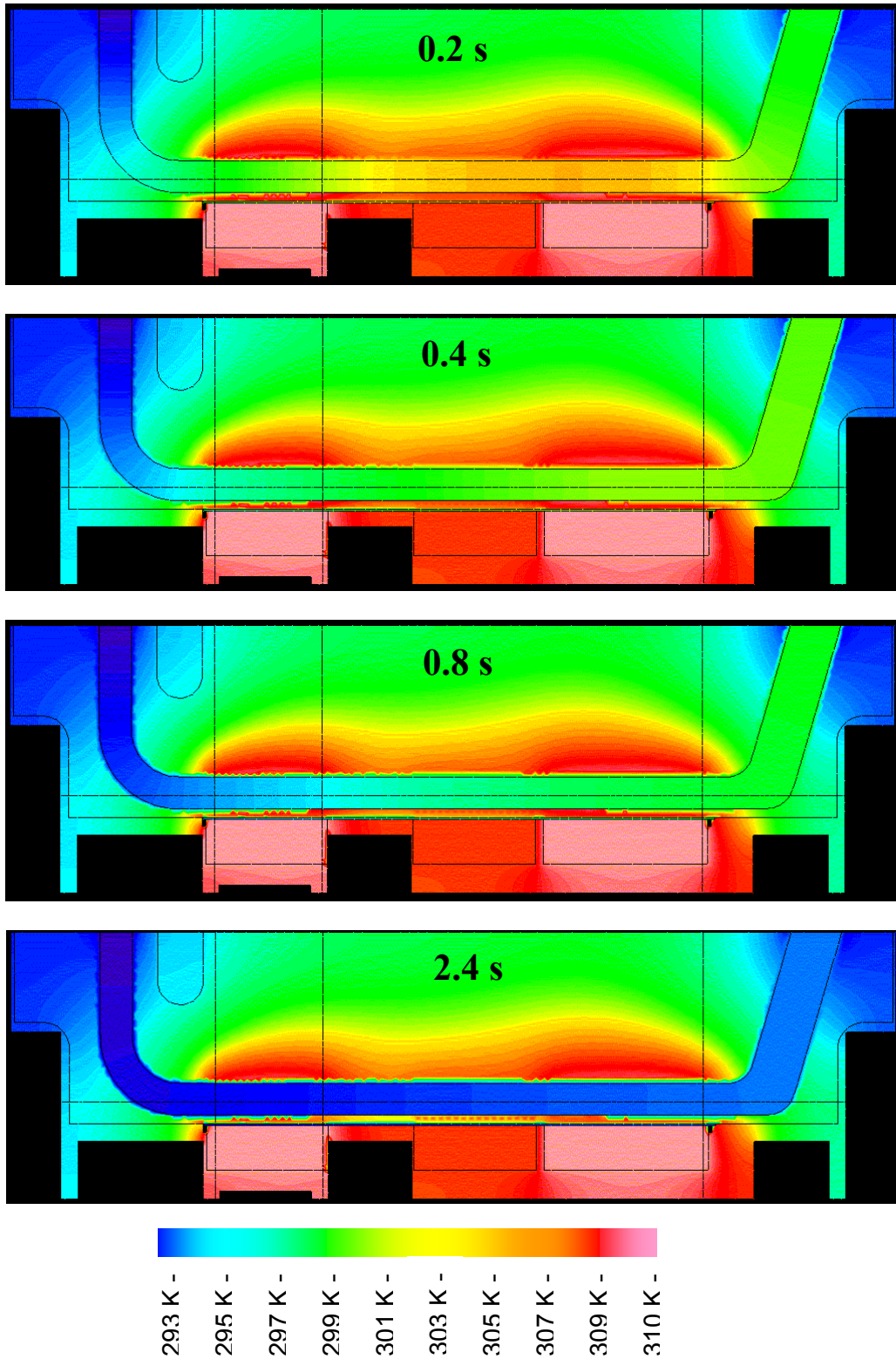


Figure 9.50: Transient Temperature Profiles in Channel during Calibrant Flushing and Sample Introduction

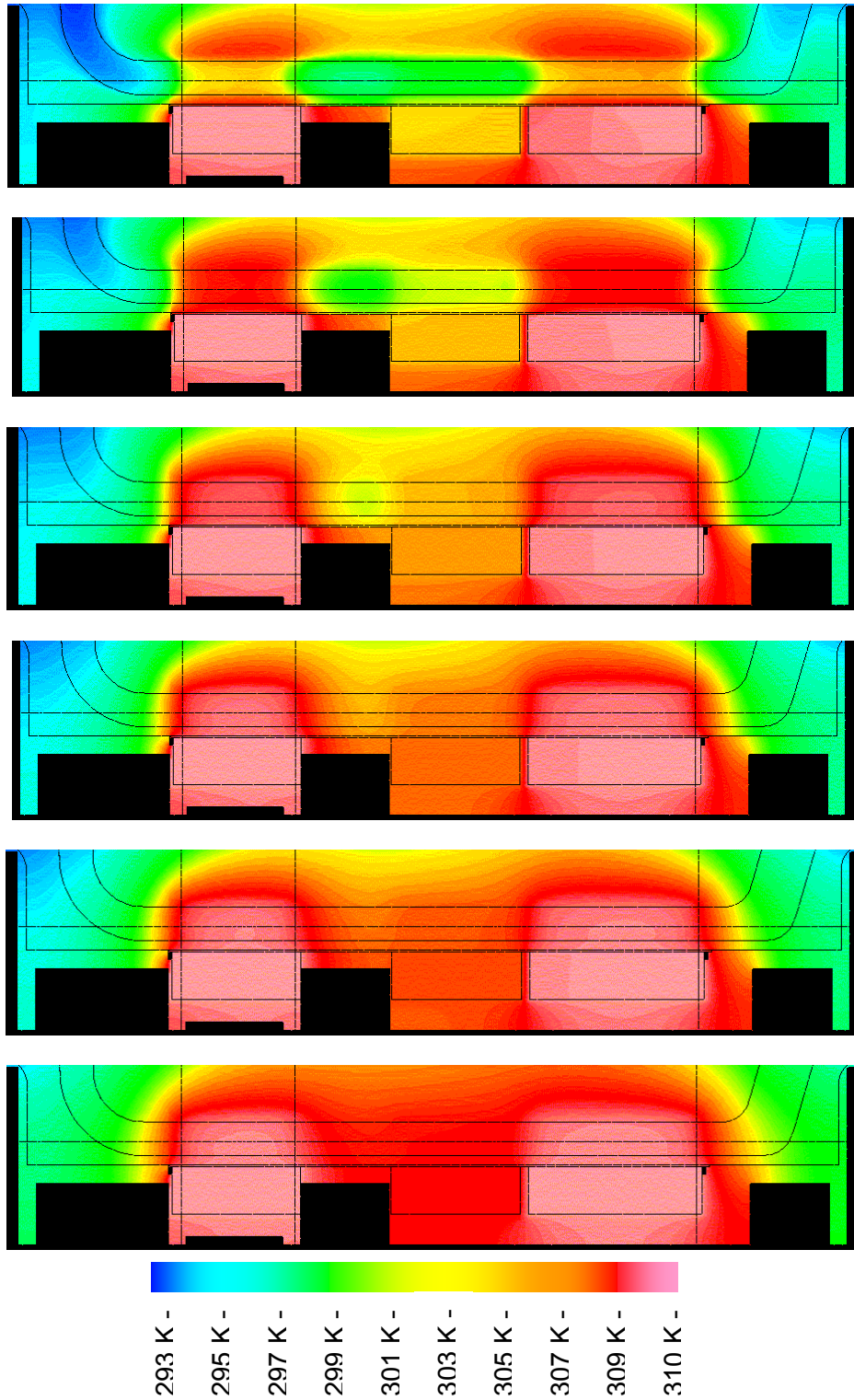


Figure 9.51: Transient Temperature Profiles during Sample Heating in Channel

So what caused these unexpected results? In retrospect, the bulk thermal properties of the various materials point to the causes. First let us make some order of magnitude observations. Silicon and the metals have from 200 to ~1200 times the thermal conductivity of blood or the calibrant liquid! This explains the rapid heat distribution and equilibration within these materials. The plastics have only ~2/5 to ~1/3 the thermal conductivity of blood or calibrant! To truly be a thermal insulator the plastic would have to exhibit ratios comparable to air, which has less than 1/20 the thermal conductivity.

Blood and calibrant have 4-6 times the heat capacity of any of the rest of these materials! This significantly higher capacity to store heat somewhat nullifies the slightly more rapid thermal conductivity.

The last observation that helps to explain the slow propagation of heat down the channel comes from an inspection of the simplified equation of heat transfer frequently used by chemical engineers.

$$Q = U A \Delta T \quad (9.7)$$

In Equation 9.7, Q is the heat flux, A is the area that heat fluxes across, ΔT is the temperature differential ($T_2 - T_1$) that motivates the heat transfer, and U is a generalized heat transfer coefficient (resistance to heat transfer) that is usually empirically determined for the collection of materials and fluids through which the heat is flowing. Although more exact equations of heat transfer exist, we can see from this simplified equation that heat transfer is directly proportional to the cross sectional area A through which heat is propagating. A careful inspection of the previous thermal plots show that the surface area of the sensors present a large cross sectional area for propagating heat up and down through the cartridge, but the cross sectional area of the channel in which the heated fluid resides is small by comparison. Thus, the heat that is forced to propagate through this narrow cross sectional area, progresses laterally through the cartridge much more slowly.

9.9.8 Conclusions and Recommendations

Gradients and slower than expected heat propagation are not necessarily indications that these are major sources of variance for assay results. Indeed if heat propagates in this manner repeatedly cartridge after cartridge, then relatively little variance in final assay results will be observed. The results presented here, however, do suggest that larger than expected thermal gradients through the fluid during analysis might be contributing to assay variability. However these simulations have not been empirically verified with actual cartridge data. Therefore, while they may be useful in suggesting qualitative performance, they should not be used to quantitatively predict assay performance.

These analyses do suggest at least the following two approaches to achieve rapid and uniform heat distribution:

First Recommendation: Consider if a small bar of aluminum were insert-molded into the plastic along the base of all three sensors, so that it presented a high thermal conductivity floor for resting the sensors on, and it came to the surface along the fluid channel under the adhesive film. If the sensors were adhesive bonded into placed in their respective cavities so that they

rested on, or in close proximity to this aluminum bar, then the aluminum element would serve as a heat pipe to rapidly distribute heat to the center sensor and the floor of the fluid channel. The heat would propagate down the aluminum bar with the same speed that it propagates through the silicon. It would also present a much larger surface area to the fluid channel.

Second Recommendation: A second, and less expensive, alternative would be to implement an assay programming change. Consider oscillating a portion of the fluid under test back and forth over the sensor region to mix and distribute the heat in the fluid more evenly. Ideally this fluid slug could be capped at both ends with an insulating air slug. But if that is not possible, simply adding oscillating fluid movement should still "mix" the heat up in the fluid channel and cause more uniform thermal distribution.

Results from the study indicate the need for further simulation and analysis using a coupled fluid flow/heat transfer approach in order to:

- Evaluate the effect of slow fluid drift on heat transfer and thermal distribution;
- Verify that the two proposed remediations will work; and,
- Validate the predicted thermal distribution profiles and further understand their impact on assay variability.

10. PROJECT SUMMARY

This report has presented the current status and results of the DARPA BAA 97-39 project aimed at developing, demonstrating and validating a mixed-dimensionality simulation tool for virtual prototyping of biomicrofluidics devices and integrated systems. All of the project objectives have been met successfully. Many new, advanced biomicrofluidics simulation capabilities have been developed and validated through comparison with analytical solutions and experimental data. The developed software has been successfully commercialized and demonstrated on various different types of biochip devices and integrated systems. A summary of newly developed simulation capabilities and software commercialization efforts undertaken to ensure technology transfer to the biomicrofluidics community is presented below. A list of recommendations and plans for further work is outlined at the end of the section.

10.1 Software Capabilities Developed

The key software capabilities developed either partially, or entirely, on the current project are as follows:

Automation of Model Set-up

- (a) CFD-Micromesh model generator for fast geometric modeling and fully automated mesh generation from 2-D layouts and fabrication process specifications for 3-D microfluidics devices and systems.
- (b) Automated multi-block structured mesh in CFD-Micromesh from layout and processes;
- (c) Adaptive oct-tree grids in CFD-Micromesh;
- (d) Interoperability between CFD-Micromesh and CalTech's multi-process SEGS etch (isotropic/anisotropic) and deposition simulator.

Microsystem Fabrication Process Simulations

- (a) Multi-process 3-D isotropic and anisotropic etch and deposition simulator, SEGS;
- (b) Genetic algorithm to permit the synthesis of mask-layouts with variable geometric complexity

Specialized Algorithms for Biomicrofluidics Applications

- (a) Higher-order accuracy scheme for species transport;
- (b) Improved computational speed of VOF with surface tension capability.

Biomolecular Reaction Models:

- (a) Surface-immobilized enzyme-catalyzed reactions;
- (b) Cooperative protein-ligand volumetric reactions;
- (c) Biomolecular surface adsorption phenomena (first-order and second-order kinetics; competitive and non-competitive binding; reversible and irreversible binding);
- (d) Biomolecular receptor-ligand surface interactions (first-order and second-order kinetics; non-competitive binding; cross-reactivity; reversible and irreversible binding);
- (e) Virtual sequences programming capability for biochemical assays.

Electrochemistry Models

- (a) Acid-base equilibrium reactions with autoionization of water;
- (b) Ionization equilibria involving ampholytes;
- (c) Sample stacking in a multiple ionic species system;
- (d) Electrokinetic DNA transport and electrolyte dissociation.

Reduced-Order Models and Mixed-Dimensionality Capability

- (a) Mixed-dimensionality 3-D/1-D/0-D (compact models) CFD-ACE+ and SPICE interface;
- (b) 1-D models for incompressible pressure-driven microchannel flows and flows in bends;
- (c) 1-D models for electroosmotic flows and electrophoretic multi-species transport;
- (d) 1-D ionization electrochemistry model;
- (e) 1-D and Hele-shaw model for free surface flows (with surface tension);
- (f) Multi-physics filament models for multi-scale analysis in CFD-ACE+.

Parametric Models, Scripting and Optimization

- (a) Parametric microfluidic device model libraries (Tesla valve, helical microfluidic mixing coil, DNA chip, microchannel network, etc.) using PYTHON-based scripting in CFD-GEOM and CFD-Micromesh;
- (b) Simulation manager for automated numerical design analysis (parametric studies)
- (c) Simulation-based optimization methodologies.

10.2 Commercialization and Technology Transfer

CFDRC has been actively involved in software commercialization and technology transfer activities to ensure that the technology developed (CAD tools/capabilities) and experience gained during the course of the current project is made available to the biomicrofluidics community. Commercialization and technology transfer activities related to the current project can be broadly classified into the following three categories: Software, Services and In-House Applications. Specific activities and accomplishments in all three categories are outlined below.

10.2.1 Software Commercialization Efforts

Incorporation in Commercial Software: All of the capabilities developed within the framework of CFD-ACE+ during the course of the current project have been commercialized and made available to the biomicrofluidics community through CFD-ACE+ Version 6.6, released in July 2001. Alpha and Beta versions of the software were released to a few select biomicrofluidics companies (Aclara, Applied Biosystems) and universities (UC Berkeley) in order to obtain user feedback on the developed modules. A detailed independent evaluation of the software features was also conducted by two different CFD-ACE+ users:

- (a) Project consultant, Don Verlee, President of Microfluidics Systems Research, who is simultaneously working on the ISTAT problem while evaluating the relevant CFD-ACE+ capabilities; and
- (b) Goran Goranovic, PhD student, Microelectronics Center, Technical University of Denmark, who spent 1 month at CFDRC working on biomicrofluidics problem of relevance to his PhD research.

Their suggestions and recommendations were taken into consideration prior to software release.

Specialized Training Courses/Tutorials: We have developed several CFD-ACE+ tutorials which focus on our multiphysics modeling capabilities in the areas of BioMEMS and microfluidics. Several additional tutorials are in preparation based upon the cases that were simulated during the course of the project. CFDRC is also conducting specialized master classes during its annual Users Conference to train software users in areas such as MEMS, Electrochemistry, Biochemistry, etc.

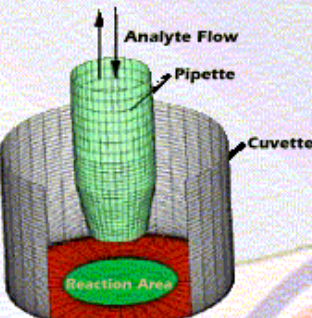
Software Marketing: CFDRC has aggressively participated as an exhibitor in several relevant conferences/expos (total 18), in the US and overseas, during the past 3 years in order to market the biomicrofluidics software capabilities. The complete list of exhibitions is as follows:

- MD&M West Expo (Anaheim, CA, January, 1999)
- IMRET III (Frankfurt Am Main, Germany, April, 1999)
- MD&M East Expo (New York, NY, June, 1999)
- CFDRC's 2nd Workshop on Multidisciplinary Design & Simulations Tools for Micro- and Biomed. Fluid Applications (Berlin, Germany, June, 1999)
- IBC's BioMEMS Conference (San Francisco, August 1999)
- IBC's Chips to Hits Conference (Berkeley, CA, November, 1999)
- MD&M West Expo (Anaheim, CA, January, 2000)
- MSM '2000 (San Diego, CA, March, 2000)
- MicroTAS, 2000 (Enschede, Netherlands, May, 2000)
- MD&M East (New York, NY, May, 2000)
- CFDRC's 3rd Workshop on Interdisciplinary Design and Simulation Tools for Micro- and Biomedical Fluidic Applications (Wendelsheim, Germany, June, 2000)
- IBC's Chips to Hits (Philadelphia, PA, November, 2000)
- MD&M West Expo (Anaheim, CA, January, 2001)
- MSM 2001 (Hilton Head, SC, March, 2001)
- Protein Microarray Technology Conference (San Diego, March, 2001)
- MD&M East Expo (New York, NY, June, 2001)
- Second Annual BioMEMS & Biomedical Nanotechnology World 2001 (Columbus, OH, September, 2001) IBC's Chips to Hits (San Diego, CA, October, 2001)

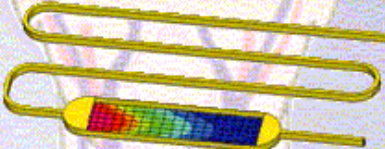
CFDRC has also run several advertisements in the Medical Devices and Diagnostics Industry magazine. A sample advertisement is shown in Figure 10.1.

ACCELERATE

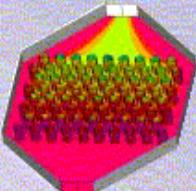
your Design Cycle and Lower Costs with CFDRC Design and Analysis Software and Services for Biomedical Diagnostic Systems & Devices



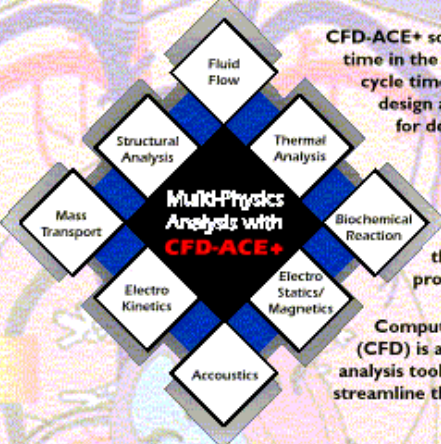
Optical Biosensor



Blood-Glucose Monitoring Device



DNA Filtration Chip



Multi-Physics Analysis with CFD-ACE+

CFD-ACE+ software enables reduce time in the product development cycle time by providing a virtual design and testing environment for devices performance.

You can save time and money by optimizing your designs and cutting down on the need for extensive physical prototyping.

Computational Fluid Dynamics (CFD) is also recognized as an analysis tool by the FDA, helping to streamline the approval process.

CFD Research Corporation offers software licenses, excellent customer support and technical guidance.

Continuous Flow PCR Systems

Blood-Gas Sensing Devices

Microfluidic Mixers, Valves, Pumps

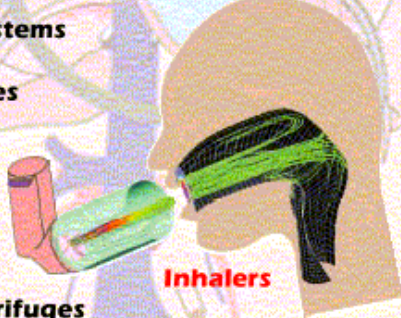
Electrophoretic Devices

Particle Separators, Centrifuges

Enzyme-Based Biosensors

Cardiovascular Devices & Medical Imaging Systems

Contact Us with Your Challenging Design Problems!



Inhalers



Figure 10.1: Advertisement for CFD-ACE+ Multiphysics Software

10.2.2 Software Commercialization Success

CFDRC's marketing efforts have resulted in the successful commercialization of our multiphysics software for biomicrofluidic applications at several companies, national labs and reputed universities. A partial list is given below:

Companies

1. Abbott Labs Hospital Products;
2. Motorola Biochip Division, CTRL and PSRL;
3. Aclara Biosciences;
4. Agilent;
5. Johnson and Johnson Lifescan;
6. Symyx Technologies;
7. YSI, Inc;
8. Applied Biosystems (formerly PE Biosystems);
9. Micronics;
10. Cohesion Technologies;
11. Sequenom;
12. Honeywell Tech Center;
13. Orchid;
14. Samsung;
15. LG Electronics;
16. IMM-Mainz;
17. Mesosystems Technologies

National Labs

18. NIST;
19. Sandia National Labs;
20. Fraunhofer IBMT

Universities

21. Stanford (Kovacs, Santiago);
22. U. C. Berkeley (Majumdar, Liepmann);
23. UCLA (Chi Ming Ho);
24. Univ. of Cincinnati (Ahn);
25. Univ. of Washington (Forster);
26. U. C. Santa Barbara (Meinhart)
27. Univ. of Vanderbilt (Rosselli)

Several other software licensing opportunities are currently being pursued.

10.2.3 Software-Based Commercial Services

In addition to licensing commercial software to the biomicrofluidics community, CFDRC is also providing a wide range of software-based commercial services. These include: advanced user support for software use; advanced multiphysics courses related to software applications in biomicrofluidics; design analysis and optimization services. The following sections describe the services offered.

Advanced User-Support: CFDRC is providing advanced user support to biomicrofluidic companies such as Aclara, Sequenom, Motorola, YSI, Inc and Applied Biosystems. This activity is aimed at accelerating their usage of biomicrofluidics modeling capabilities in CFD-ACE+ for improved device and/or process design.

Advanced MultiPhysics Courses: CFDRC has developed a series of advanced biotechnology industry-specific multiphysics software courses. The objective of these courses is to facilitate rapid learning and build confidence in using the mixed-dimensionality multiphysics software capabilities for biomicrofluidic applications in existing and new users of CFD-ACE+. Several relevant test cases and tutorials based on the work done in the current project have been included in following multiphysics courses:

1. Modeling of Microfluidics in Biochip/BioMEMS Devices
2. Design of Biochemical Assays in Microfluidic Systems
3. Electrokinetic and Electrochemistry Applications in Microfluidic Systems

The first set of courses have been scheduled for April 16-17, 2002 in Huntsville, AL. Several additional courses will be offered at later dates at various East/West-coast locations

Biomicrofluidics Design Analysis Services: CFDRC has begun marketing the design analysis services, in the form of consulting projects, to the biomicrofluidics community using software capabilities developed during the current project. Several preparatory steps have been taken, which include the hiring of various engineers with diverse experience in areas related to biomicrofluidics and bioMEMS, and expansion of CFDRC's biofluids lab facilities (see Figure 10.2) so as to provide the following complementary experimental services:

- (a) Gathering of biomolecular input data (biofluids rheology in microchannels, biomolecular binding kinetics, etc.)
- (b) Providing model validation data (high-speed/low-speed flow visualization, micro-PIV, etc.)
- (c) Device performance testing (pressure-flow characteristics, mixing efficiency, etc.).

Several design analysis projects were obtained and completed during the course of this project, which are described in the next section.



Figure 10.2: CFDRC's biofluids lab facility

10.2.4 Projects and Success Stories Resulting from Consulting Services

The following projects involving design analysis of biochip/biosensor devices or follow-up developmental work resulted either directly or indirectly from the work performed and capabilities developed on the current project.

Privately-Funded:

- a. Performance evaluation of microfluidic glucose monitoring system – Abbott Medisense: We evaluated SpectRx's biophotonic continuous glucose monitor (Figure 10.3) for interstitial fluid samples for Abbott Medisense during the course of this study. Our multiphysics simulations showed, counter-intuitively, that the SpectRx technology had a high potential for success. *Based on the recommendations resulting from our analysis, a strategic alliance was established between Abbott Medisense and SpectRx for commercialization of the glucose monitoring technology*
- b. Performance evaluation of a vein filter (using multi-scale filament capability) – Johnson and Johnson Cordis: We studied the impact of a novel vein filter design on venous blood flow patterns, and compared it's performance to that of other leading commercial designs available in the market. The filament model developed on the project was used to perform a multi-scale analysis, because the filter thickness was approximately 2% of the vein diameter (Figure 10.3). *Based on the recommendations resulting from our analysis, a decision was made to pursue further product development at Cordis.*

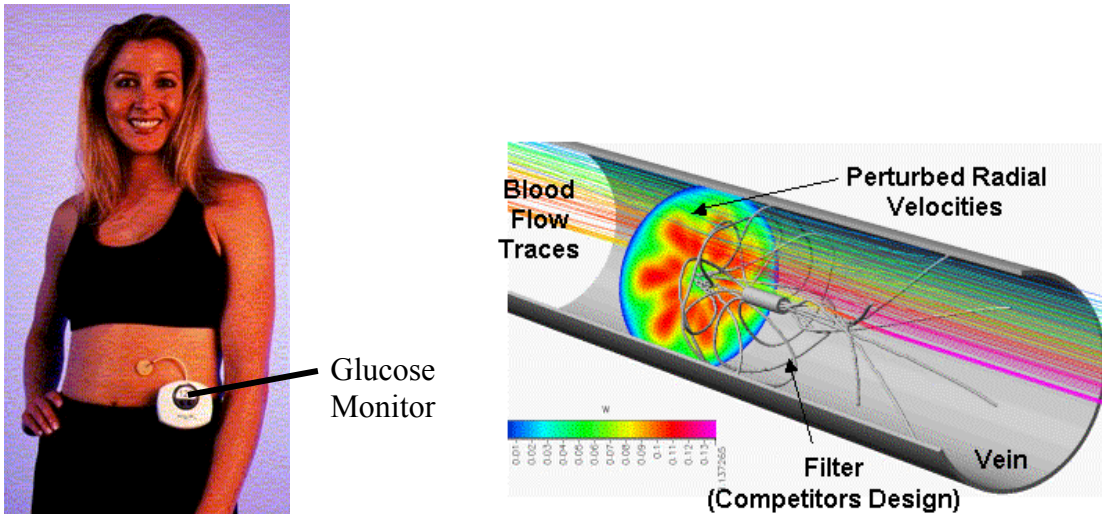


Figure 10.3: Glucose monitoring system analyzed for Medisense (left) and sample results from multiscale vein filter analysis for J&J Cordis (right)

- c. CFD-ACE+ customization for design analysis of microfluidic glucose monitoring system - YSI, Inc.;
- d. Design analysis of mixing efficiency in the Motorola Biochip hybridization chamber - Motorola Biochip Division;
- e. Design analysis of a biosensor system for rapid detection and identification of bacteria - Utah State Univ. (originally developed through DARPA/DSO funding from M. Donlan);
- f. Air flow past a microscale heater (using multi-scale filament capability) - Aradigm Corp.

Government-Funded:

- a. Design optimization of the CANARY biosensor analyte delivery system - MIT Lincoln Labs (funded in part by DARPA DSO, Alan Rudolph): Here, our multiphysics simulations revealed flow cell configurations and process parameters that would potentially enable signal enhancement by several orders of magnitude, especially early in the detection process (see Figure 9.6), an almost **15-fold increase in device sensitivity**. MIT Lincoln Labs, in the April 2000 DARPA PI Meeting, reported. Details of our study are presented in detail in Section 9.1;
- b. System-level modeling of various biosensor systems for chem-bio agent detection - Lockheed Martin/Biopraxis (DARPA SPO funding, Steve Buchsbaum): As part of this study, we analyzed the biomolecular reactions and mixing phenomenon that governed the detection time in the microbead assay-based automated pathogen detection system at Lawrence Livermore National Labs (Figure 10.4). **Our simulations suggested an improved mixing protocol, involving sample cycling, which would decrease the detection time from 30 to approximately 10 minutes.**

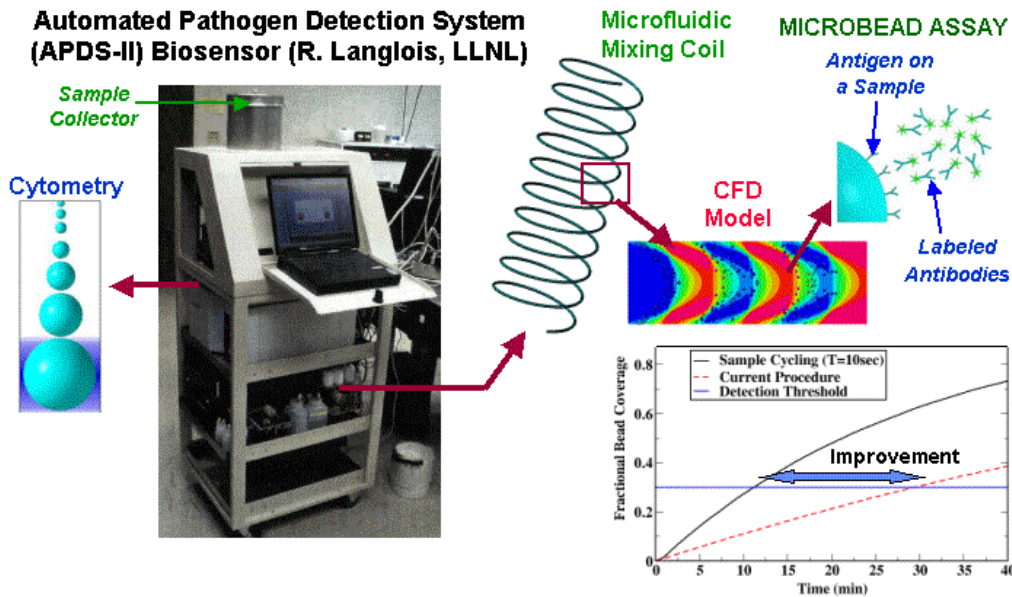


Figure 10.4: Design analysis of APDS-II biosensor system being developed at LLNL

- c. Design analysis and optimization of a structurally programmable biomicrofluidic system for clinical diagnostics - subcontract from Univ. of Cincinnati (DARPA MTO BioFLIPS program);
- d. Design analysis and optimization of a biochip system for nosocomial agents - subcontract from Motorola PSRL (NIST/ATP and Motorola funding);
- e. Combined experimental-numerical study of protein adsorption on biomaterial surfaces in microfluidic systems - subcontract from Clemson (DARPA MTO SIMBIOSYS program);
- f. Design analysis and coupled microscale-nanoscale simulation of DNA hybridization in microcantilever biosensor systems – subcontract from U. C. Berkeley (DARPA MTO SIMBIOSYS program);
- g. Further development of biochemistry and electrochemistry modules and their application for investigating new fundamental biomicrofluidics phenomena – subcontract from Stanford (DARPA MTO SIMBIOSYS program);
- h. Development of simulation software for characterization of microsphere-based bio-analytic systems (funded by NSF Biotechnology program).

10.2.5 In-House Applications

In addition to providing software and design services to external clients, the Biomedical Technology branch at CFDR is working towards facilitating a series of innovative device development in-house efforts in the area of biomicrofluidics. All of the conceptual design analysis and testing (computational and experimental) work will be done at CFDR. Device fabrication will be subcontracted out to groups with the necessary microfabrication facilities. The basis for these efforts will be the mixed-dimensionality multi-physics biomicrofluidics software

capabilities developed on the current project, experimental lab facilities, prior experience of newly hired employees in the bioMEMS/biodiagnostics area and CFDRC's prior experience with medical device development (NIH-funded hemodialysis catheter and pediatric spacer projects). Upon successful demonstration of prototype device function, CFDRC will pursue device commercialization through licensing of associated intellectual property (patents, device master records, design history file, etc.) to interested parties.

The following proposals are either in preparation or are currently being evaluated by funding agencies:

1. A PDMS-based enzymatic microreactor system to extract potable water from urine – in collaboration with LA Tech and submitted in response to DARPA/DSO Water Harvesting solicitation;
2. A novel mesoscale electrostatic device for harvesting water from atmospheric humidity - submitted in response to DARPA/DSO Water Harvesting solicitation;
3. Development of a microfluidic mixing system for microbead assay-based devices – submitted as part of an SBIR Phase II proposal to NSF;
4. Microfluidic biochip for actively-controlled crystallization of macromolecules – in collaboration with NASA Marshall/UAH (in preparation for NASA).

10.3 Plans for Further Research, Development and Improvement

During the final phase of the project, we received a great deal of feedback on our current biomicrofluidics modeling capabilities from existing and potential future clients. We also obtained information on necessary capabilities that were missing in our software suite which could not be developed on the current project. Based on this feedback, we have prepared the following list of areas for further research, model development and CFD-ACE+ software improvement:

1. Coupling between the biochemistry and electrokinetics modules in CFD-ACE+;
2. Development of 1-D biochemistry and pressure-driven species transport models;
3. Coupling between the bio-electrochemistry module and VOF module;
4. Development of nanoscale models for improved description of enzyme kinetics, protein adsorption and biomolecular reactions in microfluidic systems;
5. Development of biomolecular databases (analyte properties, bio-reaction kinetics, etc.);
6. Coupling of microparticle transport and electrokinetics models to enable dielectrophoresis simulations;
7. Extension of microparticle model for simulation of macroparticle transport;
8. Coupling of biochemistry module with particle transport models to enable simulation of microbead assays;
9. Coupling of electromagnetics module with particle transport models to enable magnetic manipulation of micro- and nanoparticles in biofluidic systems; and
10. Expansion of microfluidic device and component libraries.

We will continue to pursue development efforts in these areas with existing resources from CFDRC, government and industry.

REFERENCES

- Bird, Stewart and Lightfoot, Transport Phenomena, New York, Wiley, 1960
- Christel L.A. et al “High Aspect Ratio Silicon Microstructures for Nucleic Acid Extraction,” Solid State Sensors and Actuators Workshop, Hilton Head, SC, June 7-11, 1998.
- Crane, “Flow of Fluids Through Valves, Fittings and Pipe”, Technical Paper No. 410, New York, 1986.
- Deshpande, M., Gilbert, J., Bardell, R., and Forster, F., “Design Analysis of No-Moving-Parts Valves for Micropumps,” DSC-Vol. 66, MEMS, ASME, 1998.
- Ermakov, S. V. and Righetti, P. G., “Computer Simulation for Capillary Zone Electrophoresis: A Quantitative Approach”, *J. Chromatogr., A*, 667, pp. 257-270, 1994.
- Fox, R. W. and McDonald, A. T., Introduction to Fluid Mechanics, John Wiley & Sons, New York, 1978.
- Fung, Y. C., Biomechanics: Mechanical Properties of Living Tissues, 2nd edn., Springer-Verlag, New York, 1993.
- Hall, C. L., Slack, S. M., and Turrilo, V. T., “A computational analysis of FXa generation by TF:FVIIa on the surface of rat vascular smooth muscle cells. *Ann. Biomed. Eng.* **70**, 129-134, 1998.
- Herr, A. E., Molho, J. I., Santiago, J. G., Mungal, M. G. and Kenny, T. W., Electroosmotic capillary flow with nonuniform zeta potential. *Anal. Chem.* **72**, 1053-1057, 2000.
- Herr, A. E., Molho, J. I., Kenny, T. W., Santiago, J. G., Mungal, M. G. and Garguilo, M. G., “Variation of capillary wall potential in electrokinetic flow”, *Transducers '99*, Sendai, Japan, 1999.
- Kovacs, G. T. A. (1998) *Micromachined Transducers Sourcebook*. McGraw-Hill, New York.
- Long, D., Stone, H. A. and Ajdari, A., “Electroosmotic flows created by surface defects in capillary electrophoresis”, *J. Colloid and Interface Sci.* **203**, 383-391, 1998.
- Lu et al., *J. Colloid Interface Science*, v168, pp. 152-161, 1994.
- Makhijani, V. B, Cokelet, G. R., and Clark, A. Jr. (1990) Dynamics of oxygen unloading from sickle erythrocytes. *Biophys. J.* **58**, 1025-1052.
- Marshall, A. G. (1978) *Biophysical Chemistry - Principles, Techniques and Applications*. John Wiley & Sons, New York.

McWhorter P.J. "Intelligent Microsystems: Key to the Next Silicon Revolutionn", MST News, 4/1999.

Patankar, N. A. and Hu, H. H., "Numerical Simulation of Electrosmotic Flow," Anal. Chem., V.70, pp 1870 - 1881, 1998.

Potter, M. C. and Foss, J. F., Fluid Mechanics, Great Lakes Press, Inc., MI, 1982.

Popel, A. S., "Theory of Oxygen Transport to Tissue", *Crit. Rev Biomed. Eng.* **17(3)**, 257-321, 1989.

Probstein, R., Physicochemical Hydrodynamics, Butterworth Publishers, 1989.

VanDoormal, J. P. and Raithby, G. D. (1984) Enhancements of the SIMPLE method for predicting incompressible fluid flows. *Numer. Heat Transf.* **7**, 147-163.

Vay, J. R., Measurement of Oxygen Saturation and Hemoglobin Diffusivity in Hemoglobin Solutions with a Microscope Spectrophotometer, MS Thesis, Univ. of Rochester, Rochester, New York, 1986.

APPENDIX A

SPECIALIZED NUMERICAL ALGORITHMS FOR BIOMICROFLUIDICS APPLICATIONS

Advanced numerical algorithms were implemented in CFD-ACE+ during the course of the project to reduce numerical dispersion while simulating species mass transport and to significantly speed up free surface volume-of-fluid (VOF) simulations in the presence of surface tension. Both of these capabilities were identified as critical for successful application and commercialization of the developed biomicrofluidics modeling capabilities. Both capabilities are briefly described below.

A.1 Higher-Order Accuracy Scheme for Species Transport

A higher-order accuracy scheme was implemented in CFD-ACE+ to combat the problem of numerical dispersion that occurs during simulation of dilute species transport. This is a key capability required to minimize the impact of numerical artifacts on the simulation of biochemical assays in microfluidic systems. It was decided to implement a Total Variation Diminishing (TVD) scheme with 2nd order accuracy for unstructured polyhedral meshes and 3rd order for structured grids. The TVD schemes have been developed for shock capturing for high-speed aircraft aerodynamics. We have implemented them for low speed flows to capture species concentration, thermal, flow and other discontinuities for both steady and transient flow simulations.

To test the impact of the higher-order accuracy schemes on CFD-ACE+ predictions, flow and mixing in the static micromixer, being developed at the Imperial College by Dr. Andreas Manz's group (shown earlier in Figure 2.2), was simulated using both 1st order and higher order schemes. Results are shown below in Figure A.1. The higher order scheme results apparently match experimental data quite well as was communicated to us by the Imperial College group upon review of the results.

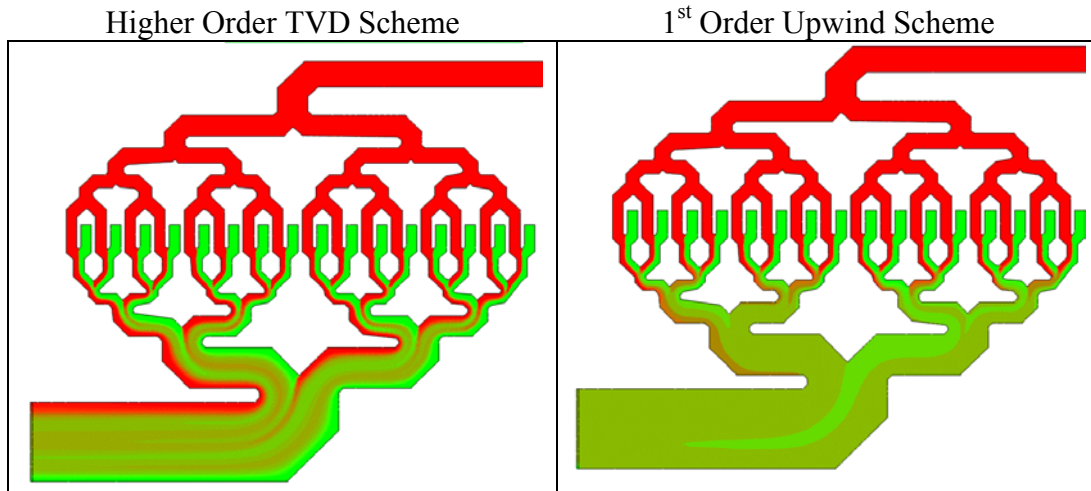


Figure A.1: Comparison Between 1st Order and Higher Order Scheme for Static Micromixer Case

A.2 Improved Computational Speed of VOF with Surface Tension Capability

The volume-of-fluid (VOF) with surface tension capability in CFD-ACE+ is a key design capability needed for simulating liquid filling and emptying of microchannels, which in turn is needed for designing microfluidic channels and interconnects in biofluidic chip systems. The VOF simulations with CFD-ACE+ earlier were extremely slow (each simulation requiring approximately 1 week or more) when used with the surface tension capability turned on. This was due to the generation of artificially high air flow velocities near liquid interface, which would force the time steps used in the transient simulations to be extremely small in order to satisfy CFL criteria.

The two major developments that have been implemented in the VOF module in CFD-ACE+ over the past six months are as follows:

- (i) Replacement of Backward-Euler time-integration scheme used to evolve the Volume-Fraction Equation with a Forward-Euler time-integration scheme;
- (ii) Addition of viscous damping in the immediate vicinity of the liquid-gas interface.

The first development markedly increases the robustness and improves the convergence of the solution algorithm, especially for problems in which the source term depends on the interface geometry (including problems with dominant surface-tension forces). This is because the source term no longer changes from iteration to iteration in the outer-iteration loop of the SIMPLEC algorithm.

The second development markedly improves the robustness and increases the time-step of the solution algorithm, especially for problems with dominant surface-tension forces. This is because the damping reduces the magnitude of the velocity component that is tangential to the interface, which could be an order or more greater than the magnitude of the corresponding normal component. Elimination of these tangential velocities is legitimate since they are produced by numerically generated noise in the evaluation of the surface curvature from the volume fraction data. Since the time-step in the solution algorithm is confined by a CFL constraint, reducing the tangential velocities increases the time-step by one or more orders of magnitude.

PROJECT BIBLIOGRAPHY

1. V.B. Makhijani, J. Raghavan, A. Przekwas and A. Przekwas, "Simulation of Biochemical Reaction Kinetics in Microfluidic Systems", In: Microreaction Technology: Industrial Prospects, IMRET3 Proceedings of 3rd International Conference on Microreaction Technology, W. Ehrfeld (Ed.), Springer-Verlag, Heidelberg, Germany, pp: 441-450, 2000.
2. A. Przekwas, D. M. Wang, V. B. Makhijani and A. J. Przekwas, "Microfluidic Filtration Chip for DNA Extraction and Concentration", In: Microreaction Technology: Industrial Prospects, IMRET3 Proceedings of 3rd International Conference on Microreaction Technology, W. Ehrfeld (Ed.), Springer-Verlag, Heidelberg, Germany, pp: 488-499, 2000.
3. V. B. Makhijani, J. Raghavan and A. J. Przekwas, "Multi-Disciplinary Computational Design and Analysis Tool for Microfluidic Biosensor Devices", Proceedings of 2nd Annual International Conference on Biosensor Technologies in Pharmaceutical and Biotechnology Discovery, San Diego, CA, May 6-7, 1999.
4. V. B. Makhijani, J. Raghavan, M. G. Giridharan, S. Krishnamoorthy, M. M. Athavale and A. J. Przekwas, "Multi-disciplinary Simulation Tools for Bio-microfluidic Systems", Proceedings of IBC's 6th Annual Chips to Hits'99 Conference, Berkeley, CA, Nov. 2-5, 1999.
5. V. B. Makhijani, "Multi-Disciplinary Computational Design Tools for Microfluidic Bio-Diagnostic Devices", Proceedings of Advanced Technology Applications for Combat Casualty Care (ATACCC99) conference, Ft. Walton Beach, FL, October, 1999.
6. A. Przekwas, M. M. Athavale, V. B. Makhijani, A. Klein, P. Bartsch, "Computational Simulation of Bio-Microfluidic Processes in Integrated DNA-Biochips", Proceedings of DECHEMA Conf. On DNA-Chiptechnologie Anwendung und Nutzung, January 24-25, 2000, Frankfurt aM.
7. Z.Q. Tan, M. Furmanczyk, M. Turowski, and A. Przekwas, "CFD-Micromesh: A Fast Geometrical Modeling and Mesh Generation Tool for 3D Microsystem Simulations", Proc. Int. Conf. MSM 2000, San Diego, CA, March 27-29, 2000.
8. Cin-Young Lee and Erik K. Antonsson, "Variable Length Genomes for Evolutionary Algorithms", Proc. of Genetic and Evolutionary Computation Conference, (GECCO-2000), Las Vegas, NV, July 8-12, 2000.
9. Lin Ma and Erik K. Antonsson, "Mask-Layout and Process Synthesis for MEMS", Proc. Int. Conf. MSM 2000, San Diego, CA, March 27-29, 2000.
10. Cin-Young Lee and Erik K. Antonsson, "Self-Adapting Vertices for Mask Synthesis", Proc. Int. Conf. MSM 2000, San Diego, CA, March 27-29, 2000.

11. V. B. Makhijani, J. Raghavan and A. J. Przekwas, "Computational Fluid Dynamics Model of Competitive Multi-Protein Surface Adsorption", Proc. IMRET 4, AICHE Spring 2000 Meeting, Atlanta, GA, March 5-10, 2000.
12. V. B. Makhijani, J. Raghavan, A. J. Przekwas, M. Margulies and G. Kumar, "Computational Analysis of Mass Transport-Limited Binding Kinetics in an Optical Biosensor System", Proc. IMRET 4, AICHE Spring 2000 Meeting, Atlanta, GA, March 5-10, 2000.
13. A. J. Przekwas, V. B. Makhijani, M. M. Athavale, A. Klein, P. Bartsch, "Computational Simulation of Bio-Microfluidic Processes in Integrated DNA-Biochips", Proc. Micro-TAS 2000, Enschede, Netherlands, May 14-18, pp. 561-564, 2000.
14. V. B. Makhijani and A. J. Przekwas, "Multi-Physics Modeling Tools for Microfluidic Devices", 3rd Workshop on Interdisciplinary Design and Simulation Tools for Micro- and Biomedical Fluidic Applications, Wendelsheim, Germany, June 27-28, 2000.
15. V. B. Makhijani, "Multi-Scale, Multi-Physics Computational Modeling of Sensors for Biowarfare Agent Detection", ATACCC2000, September 25-27, Ft. Walton Beach, FL.
16. S. Sundaram, J. Raghavan and V. B. Makhijani, "Micro-Fluidic Analysis of Flow And Surface Binding in a Bio-Sensor System," Proc. AICHE Annual Meeting, 2000, Los Angeles CA.
17. Cin-Young Lee and Erik K. Antonsson, "Dynamic Partitional Clustering Using Evolution Strategies", Proc. The Third Asia-Pacific Conference on Simulated Evolution And Learning (SEAL), Nagoya, Japan.
18. A. J. Przekwas and V. B. Makhijani, "Mixed-Dimensionality, Multi-Physics Simulation Tools for Design Analysis of Microfluidic Devices and Integrated Systems", In: Technical Proc. 4th International Conf. on Modeling and Simulation of Microsystems, Hilton Head, SC, Laudon, M and Romanowicz, B, (Eds.), Computational Publications, Cambridge, MA, pp. 198-201, 2001.
19. S. Krishnamoorthy, J. J. Feng and V. B. Makhijani, "Analysis of Sample Transport in Capillary Electrophoresis Microchip using Full-Scale Numerical Analysis", In: Technical Proc. 4th International Conf. on Modeling and Simulation of Microsystems, Hilton Head, SC, Laudon, M and Romanowicz, B, (Eds.), Computational Publications, Cambridge, MA, pp. 206-209, 2001.
20. Cin-Young Lee and Erik K. Antonsson, "A Framework for Mask-Layout Synthesis Implementing a Level Set Method Simulator", In: Technical Proc. 4th International Conf. on Modeling and Simulation of Microsystems, Hilton Head, SC, Laudon, M and Romanowicz, B, (Eds.), Computational Publications, Cambridge, MA, pp. 438-441, 2001.
21. Lin Ma and Erik K. Antonsson, "Robust Mask-Layout Synthesis for MEMS", In: Technical Proc. 4th International Conf. on Modeling and Simulation of Microsystems, Hilton Head,

- SC, Laudon, M and Romanowicz, B, (Eds.), Computational Publications, Cambridge, MA, pp. 128-131, 2001.
22. Cin-Young Lee and Erik K. Antonsson, "Adaptive Evolvability via Non-Coding Segment Induced Linkage", Proc. Genetic and Evolutionary Computation Conference (GECCO 2001), San Francisco, CA.
 23. A. K. Singhal and V. B. Makhijani, "Growing Role of Multi-Physics Simulations for Rapid Development of Microreaction and Bioanalytical Systems ", In: Proc. 5th International Conference on Microreaction Technology (IMRET5), Strasbourg, France, May 27-30, 2001.
 24. S. Krishnamoorthy, J.J. Feng & V. B. Makhijani, "Full-Scale Computational Study Of Electrophoretic Systems", In. Proc Electrochemical Society 2001 Joint International Meeting San Fransisco, CA, Sept. 4, 2001.
 25. Feng, J. J., Blosch, E., Krishnamoorthy, S. and Makhijani, V. B., "Computational Analysis of Electrokinetic Transport in Lab-On-a-Chip Systems", In: Proc. IBC's 8th Annual International Microtechnology Event, Chips to Hits '01, San Diego, CA, Oct. 28th – Nov. 1st, 2001.
 26. Cin-Young Lee, Lin Ma and Erik K. Antonsson, "Evolutionary and Adaptive Synthesis Methods", In: Formal Engineering Design Synthesis, Chapter 8, Erik K. Antonsson and Jonathan Cagan, editors, Cambridge University Press, 2001.
 27. Erik K. Antonsson, "Microsystem Design Synthesis", In: Formal Engineering Design Synthesis, Chapter 5, Erik K. Antonsson and Jonathan Cagan, editors, Cambridge University Press, 2001.